Terahertz-driven manipulation of electron bunches using dielectric-lined waveguides

A thesis submitted to The University of Manchester for the degree of

Doctor of Philosophy

in the Faculty of Science and Engineering

2021

Vasileios Georgiadis

Department of Physics and Astronomy

Contents

Word Count: xx,xxx

List of Figures

List of Tables

Abstract

Vasileios Georgiadis

Doctor of Philosophy

The University of Manchester

Terahertz-driven manipulation of electron bunches using dielectric-lined waveguides

September 2021

In this thesis the characterisation and implementation of dielectric-lined waveguides (DLW) for Terahertz (THz) driven acceleration and manipulation of electron bunches is presented. THz-driven particle accelerators are very promising for unprecedented control over the phase space of charged particle bunches compared with conventional radio frequency technologies. The modes in a DLW were exploited, allowing certain frequencies to propagate at phase velocities less than the speed of light, achieving extended collinear interaction with electron beams.

Here, the first proof-of-principal THz-driven acceleration of relativistic electrons is demonstrated, using the CLARA beamline. Narrowband THz pulses were tuned to the phase velocity-matched operating frequency of the DLW, inducing multicycle energy modulation to 35 MeV, 60 pC, 6 ps-long chirped bunches and energy gain of up to 10 keV to 2 ps-long bunches. The linear and cubic coefficients of 47.3 keV/ps and 0.4 keV/ps^3 were determined for the chirped bunch.

Furthermore, THz-driven ultrafast deflection of 100 keV electrons was demonstrated. A DLW was driven by single-cycle THz pulses, achieving a time-dependent deflection. A streaking speed of 28 mrad/ps was measured. The experimental results were supported with simulations, enabling the 3.6 ps bunch duration to be determined.

The phase-matching capability of the DLW structures was experimentally investigated through time-frequency analysis, measured in a time-domain THz spectroscopy experiment. From the analysis, the propagation constant of the LSM modes were determined, and supported by a model.

These proof-of-principal results establish a route to all-optical control, characterisation and acceleration of ultrafast electron bunches, directly applicable to different energy regimes, thus making a key milestone for future THz-driven electron manipulation and acceleration.

Declaration

No portion of the work referred to in the thesis has been submitted in support of an application for another degree or qualification of this or any other university of other institute of learning.

Copyright Statement

i The author of this thesis (including any appendices and/or schedules to this thesis) owns certain copyright or related rights in it (the "Copyright") and s/he has given The University of Manchester certain rights to use such Copyright, including for administrative purposes.

ii Copies of this thesis, either in full or in extracts and whether in hard or electronic copy, may be made only in accordance with the Copyright, Designs and Patents Act 1988 (as amended) and regulations issued under it or, where appropriate, in accordance with licensing agreements which the University has from time to time. This page must form part of any such copies made.

iii The ownership of certain Copyright, patents, designs, trade marks and other intellectual property (the "Intellectual Property") and any reproductions of copyright works in the thesis, for example graphs and tables ("Reproductions"), which may be described in this thesis, may not be owned by the author and may be owned by third parties. Such Intellectual Property and Reproductions cannot and must not be made available for use without the prior written permission of the owner(s) of the relevant Intellectual Property and/or Reproductions.

iv Further information on the conditions under which disclosure, publication and commercialisation of this thesis, the Copyright and any Intellectual Property and/or Reproductions described in it may take place is available in the University IP Policy (see http://documents.manchester.ac.uk/DocuInfo.aspx?DocID=24420), in any relevant Thesis restriction declarations deposited in the University Library, the University Library's regulations (see http://www.library.manchester.ac.uk/about/regulations/) and in the University's policy on Presentation of Theses.

List of Publications

Journal Publications:

1. **V. Georgiadis**, A.L. Healy, M.T. Hibbert, G. Burt, S.P. Jamison, D.M. Graham, "Dispersion in dielectric-lined waveguides designed for terahertz-driven deflection of electron beams", *Applied Physics Letters*, vol.118, no.14, p.144102, 2021.

2. M.T. Hibberd, A.L. Healy, D.S. Lake, **V. Georgiadis**, E.J. Smith, O.J. Finlay, T.H. Pacey, J.K. Jones, Y. Saveliev, D.A. Walsh, E.W. Snedden, R.B. Appleby, G. Burt, D.M. Graham, S.P. Jamison. "Acceleration of relativistic beams using laser-generated terahertz pulses", *Nature Photonics* 14, p. 755–759 (2020)

Conference Publications:

1. Keynote presentation

   V. Georgiadis, M. Hibberd, A. Healy, D.Lake, G. Burt, S. Jamison and D. Graham, "Characterizing the accelerating mode of a dielectric-lined waveguide designed for terahertz-driven manipulation of relativistic electron beam," in *2019 44th International Conference on Infrared, Millimeter, and Terahertz Waves (IRMMW-THZ)*, pp. 1-2, IEEE, 2019.

2. Oral Presentation

   M. Hibberd, A. Healy, D. Lake, **V. Georgiadis**, E. Smith, O. Finlay, *et al.*, "Terahertz-driven acceleration of a relativistic 35 MeV electron beam," in *2019 44th International Conference on Infrared, Millimeter, and Terahertz Waves (IRMMW-THz)*, pp.1-2, IEEE, 2019.

3. Keynote presentation

   V. Georgiadis, A. Healy, M. Hibberd, G. Burt, S. Jamison, D. Graham, "Characterizing a terahertz-driven dielectric-lined waveguide for electron beam manipulation," in *2018 43rd International Conference on Infrared, Millimeter, and Terahertz Waves (IRMMW-THZ)*, pp. 1-2, IEEE, 2018.

Poster Presentations:

1. Poster presentation at the Henry Royce Institute Opening Celebration held at The University of Manchester, Manchester, UK. **V. Georgiadis**, M.T. Hibberd, S.P. Jamison, D.M. Graham. "Developing a terahertz-driven dielectric-lined waveguide for electron beam manipulation".

2. Poster presentation at the 10th International Particle Accelerator Conference held at the Melbourne Convention & Exhibition Centre, Australia. X.Y. Liu, M. Dehler, R. Ischebeck, C. Lombosi, V. Guzenko, V. Schlott, T. Feurer, M. Hayati, Z. Ollmann, D. Rohrbach, S. Jamison, A. Healy, D. Lake, T. Pacey, D. Graham, M. Hibberd, **V. Georgiadis**. "Proof of principle test of THz driven deflector structures".

Acknowledgements

First and foremost, I would like to express my sincere gratitude to my supervisor, Dr. Darren Graham, for providing me this great opportunity to join your group, and for your continuous support and guidance throughout this project. From the time we had the interview, until now, you have been the perfect mentor, your research skills, knowledge, work ethic and manner have had a huge influence on my development as a researcher but also as a person. I will always be grateful for believing in me. I would also like to extend my gratitude to ASTeC and my ASTeC co-supervisors, Prof. Steven Jamison and Dr. Edward Snedden as well as to the rest of the academics of the group, Prof. Rob Appleby and Prof. Graeme Burt. Without our discussions, I would not have pursued the research in the way I did.

Special thanks go to Dr. Morgan Hibberd and Dr. Daniel Lake for your huge contribution to my time as a researcher. Your passion for science and your countless hours of experimental help in my early stage of my project, have been important and I have enjoyed working with both of you. I also thank my fellow PhD students Oliver Finlay, Christopher Shaw, Adam Shorrock and Abas Roble and everyone at the Cockcroft Institute for being great people to work with and making my experience an enjoyable one. I would also like to express my special appreciation to Rachel Green, for all of your support and encouragement throughout this journey, and for always being there when I needed you the most.

Lastly, I would like to thank my family to let you know how much I appreciate everything you have done and continue to do for me. To my parents, Rea and Costas, I am eternally grateful for your unconditional love and support and I would not be where I am today without you both. To all my brothers and sisters, who every one of you support me and inspire me in your own unique way, thanks for everything we have shared over the years.

Chapter 1

Introduction

There is a growing interest in the use of lasers to reduce the scale and cost of today's particle accelerators, with the ultimate dream of producing compact laboratory-sized accelerators for versatile x-ray sources and medical treatment. Intense ultrafast terahertz (THz) pulses are extremely promising for the realisation of such accelerators. THz radiation can provide accelerating field gradients on the order of multi-GV·m^{-1}, exceeding the breakdown threshold limiting conventional radio frequency (RF) based schemes. This is because of a higher breakdown threshold, which scales with surface electric field, $E_s \propto f^{1/2}\,\tau^{-1/4}$ [1], where f is the operating frequency and τ is the pulse duration. Therefore, scaling to higher frequencies and shorter pulse durations is desirable.

This thesis covers the implementation and the modelling of dielectric-lined waveguides, which have been designed to be used for the manipulation of charged particles. By the term manipulation, deflection or acceleration of a particle beam is referred. The particle beam interacts with the electromagnetic radiation that drives the structure, resulting in compression or stretching of the beam in time and space, or resulting in acceleration, depending on the mode of operation. The parameters of these structures have been tailored so that they operate at THz frequencies and are phase velocity matched with the velocity of the particle beam. In this chapter, an introduction to the terahertz radiation and particle accelerators is given. The end of this chapter provides an outline of the rest of this thesis on a chapter by chapter basis.

1.1 Terahertz radiation

Terahertz (THz) radiation refers to the region of the electromagnetic spectrum which lies between the microwave and infrared spectral regions as illustrated in Figure 1.1. The THz frequency range is usually defined as the region from 0.1 to 10 THz, ranging to wavelengths from 30 μm to 3 mm. This corresponds to photon energies between 0.4 meV to 41 meV, and an equivalent temperature range of 4.8 K to 480 K. This range is also described as the 'THz gap' because it is a relatively unexplored area of research with a rapid development of coherent THz sources within the past two decades. The range of applications of THz radiation is fast expanding with some applications ranging from communication systems to medical imaging, material characterisation, biomedical and pharmaceutical studies as well as security screening.

The most common application of THz radiation is in spectroscopy, where it is employed to probe and characterise numerous materials in a non-contact, non-destructive way [2–4]. As illustrated in Figure 1.1, several physical phenomena occur at THz frequencies, such as intermolecular and lattice vibrations as well as plasma oscillations and molecular rotations. The THz field cycle is approximately three orders of magnitude slower than for optical light, thus matching the natural timescale of those collective modes. These molecular transitions are specific to the molecule, enabling spectroscopic fingerprinting in the THz range. For example, the THz range covers the two modes of intermolecular motion in the dielectric spectrum of water [5], while also covering a broad range of absorption features. This makes THz waves transparent to most dry dielectric materials, and combined with the longer wavelength and low photon energy, THz radiation can be very useful in security screening.

The definition of the THz band is not standardised in the literature, and it can be extended up to 30 THz. However, the frequency range of interest of the work carried out in this thesis and relevant schemes mentioned from the literature, will be below the 10 THz mark, falling into the submillimetre-wave category.

The reason why investigation of materials in the THz regime is relatively new is the lack of coherent, table-top, cost-effective and energy efficient THz sources [7–9]. At the end of the 1960s and in the early 1970s, the first tunable far-infrared radiation

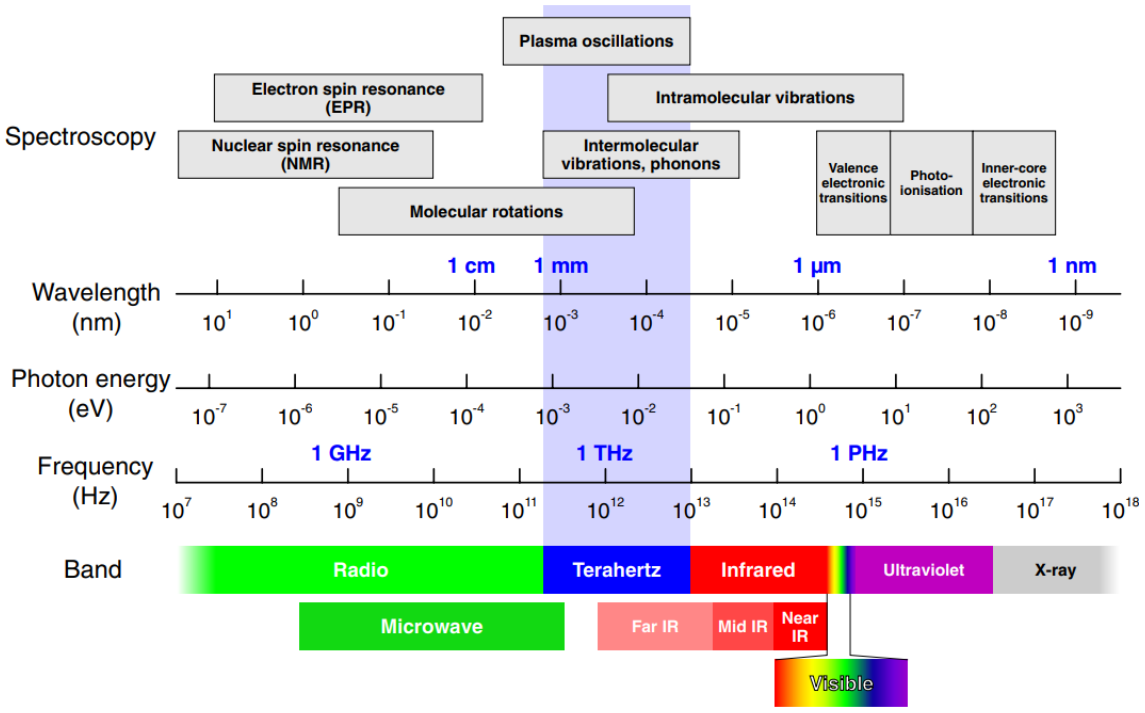

Fig. 1.1: The electromagnetic spectrum, showing the THz band occupying the frequency range from 0.1 to 10 THz and wavelength range from 30 μm to approximately 3 mm. Figure taken from [6].

produced by optically pumping a nonlinear crystal, was reported [10,11]. Since then, tremendous development has been made in THz technologies regarding sources and new methods of detection. The increasing interest in the development of novel and attractive THz sources, has triggered the in-depth studies of mechanisms of THz field generation via a number of techniques. Quantum cascade lasers [12], laser-driven THz emitters [13, 14], free electron based sources such as the free electron laser [15] is just an example of the technologies that have been recently developed. In this thesis, the main focus will on laser-driven THz emitters, where the utilisation of optical methods has been the major technique for the generation of, broadband and narrowband THz pulses.

1.2 Particle acceleration and manipulation in current machines

A particle accelerator is a machine that produces and propels a beam of charged particles, such as protons or electrons, at high velocities, close to the speed of light [16]. Particle accelerators come in many forms applying a range of technical principles. All are based upon the interaction of electromagnetic fields with electric charge, in order to accelerate, deflect, focus, stretch or compress a distribution of charged particles.

Conventional particle accelerators are usually classified by their operational frequency range. From betatrons where static electric fields induced by a varying magnetic field oscillating at 50 to 60 Hz is used, to radio frequency (RF) cavities which operate in the gigahertz (GHz) range. RF cavity accelerators are a well established and successful technology, often considered as the workforce in the accelerator physics world. The Large Hadron Collider (LHC) is currently the world's largest in scale and most powerful particle accelerator [17]. The LHC is part of the CERN research facility, located near Geneva, and designed to deliver mass collision energies up to 14 TeV. It consists of a 27 km ring of superconducting magnets, kept at a temperature of -271.3 °C, with a number of accelerating structures. This is considered a significant improvement since the first accelerators built in the 1930s, which were capable of reaching energies on the order of 1 MeV. However, using the same technology, future particle accelerators will continue to scale in size and cost in the pursuit of higher beam energies and improvement of beam quality.

The LHC is an exceptional example of a very high energy machine used for particle physics experiments which aims in a better understanding of matter and of the origins of the universe. However, smaller scale particle accelerators are widespread scientific tools that drive experimental progress in a broad range of disciplines. Accelerators are the key component for some devices, like synchrotron radiation, capable of taking images at the angstrom scale with femtosecond resolution. Proven to be the most powerful microscope, particle accelerators have been established as a powerful tool for research in material science, chemistry, molecular biology and life sciences [18].

Accelerators have also become a commercial tool used widely for medical applications. Thanks to the development of radioisotope production, radiopharmaceuticals are used in major clinical areas for diagnosis and/or therapy. Moreover, accelerators are employed as radiation sources for various applications, namely neutron radiography, neutron activation, cancer therapy by neutrons, protons and light heavy ions. Electron accelerators are also used to sterilise medical equipment and toxic disposables [19].

1.3 Thesis outline

Overall this thesis reports on the characterisation and implementation of THz-driven dielectric-lined waveguide (DLW) structures used for charged particle manipulation. The manipulation of electron beams at two energy regimes have been investigated in this work, at 100 keV which falls under the sub-relativistic regime and at 35 MeV which falls in the relativistic regime. The presented scheme can be adapted over a range of particle velocities, by tailoring the geometry of the DLW structure, and the input THz radiation.

Chapter 2 provides a literature review with relevant schemes, beginning with novel particle accelerator concepts, which are not THz-driven. Moreover, a discussion of the recent developments in THz-driven accelerators and other experiments is provided. Finally, recent developments in laser-driven strong field THz sources reported in the literature, is also covered.

Chapter 3 presents the background theory used to both interpret and analyse the experimental results obtained. The chapter covers the nonlinear optics, starting with the nonlinear wave equation and the second order nonlinear polarisation term. Consequently, the generation of THz radiation through optical rectification of ultrafast pulses in nonlinear crystals and through the inverse spin Hall effect in spintronics sources is discussed. In addition, the underpinning theory of hollow metallic and dielectric-lined waveguides is outlined, closing with the equation of motion of charged particles in the presence of electromagnetic radiation.

Chapter 4 describes the experimental techniques, covering the three ultrafast laser systems and the two electron beam facilities. Moreover, an overview of the equipment and DLW structure design is included. In addition, a description of the

simulation techniques and tools used for the numerical solution of the propagation constant of the supported modes in a DLW and for the THz-electron interaction, are also included. The THz-electron interaction is quantified by solving the equation of motion with numerical methods in an iterative algorithm, in order to track the time evolution of the particle trajectories.

Chapter 5 details the experiments conducted for the determination of the propagation characteristics of the 100 keV DLW structure. The propagation constant of the DLW structure was measured by employing a custom-built THz time-domain spectrometer and by using the experimental cut-back technique. From the analysis, the operational frequency as well as the the phase-matching capability were determined. The experimental results were then compared with the theory, by evaluating the propagation constant as described in Chapter 4.

Chapter 6 reports the experimental demonstration of THz-driven acceleration of relativistic electron beams, at the CLARA facility. The DLW structure designed for the manipulation of 35 MeV electron beams, was driven by narrow-band THz pulses, interacting with the co-propagating electrons, monitoring the energy spectra on a camera. A model was used in order to interpret the observables and characterise the longitudinal phase space of the electron beam. Moreover, the propagation constant of the DLW structure was measured and compared with a model.

Chapter 7 presents the experiment where the aim was to characterise the temporal profile of the 100 keV electron beam, in an all-optical control and metrology concept. The DLW structure was employed as a streaking device, which was driven by single-cycle THz pulses. The transverse profile of the electron beam was monitored on a downstream detector, as a function of the relative phase between the electron beam and the THz pulse. The experimental observables were then compared to simulations, in order to evaluate and extract the temporal profile of the 100 keV electron beam.

Finally, Chapter 8 contains the conclusions of the results of the experimental work and discusses further work. The next generation of DLW structures is discussed and how they can become competitive in the field of novel acceleration techniques.

Chapter 2

Literature review

In this chapter, an overview of the literature relevant to the topics discussed in this thesis is provided. An introduction to novel particle accelerator schemes is included, followed by a discussion of recent developments in Terahertz-driven particle beam manipulation, including acceleration and deflection. Furthermore, a review of high power laser-driven Terahertz (THz) sources is provided, focussing on the optical techniques developed for efficient generation of THz radiation.

2.1 Novel particle accelerators and manipulators

As accelerators have found very attractive applications for research, medical and industrial purposes, there has been a growing interest in acceleration schemes that can deliver high-energy, compact particle beam facilities. As briefly mentioned in §1.2, radio-frequency (RF) cavities used in accelerators such as the LHC, are reaching their physical limits. This limit is linked to the electrical breakdown of the cavity surface. As Wang *et al.* [1] have reported, the breakdown threshold for X-band structures, was estimated to be on the order of 100 MV/m. The breakdown rate is dependent on the RF pulse length τ, and the center frequency f, as has been reported by Grudiev *et al.* [20], and it scales as $E_s \propto f^{1/2}\,\tau^{-1/4}$. Therefore, typical accelerating fields have been operated below this limit.

Different alternatives to RF acceleration have been developed over the last decades, in order to increase the maximum achievable accelerating gradient, while also trying to downscale the size and the cost of future accelerators. One approach was to implement different alloys in standard RF cavities which feature a higher

breakdown threshold. An example is the superconducting cavities, where a superconducting material allows an RF resonator to store energy with low energy loss. An example is the niobium superconducting resonant cavities, which are kept at approximately 2 K [20], featuring low rate of energy loss with accelerating gradients reported up to 45 MV/m [21]. However, this concept operates at radio frequencies, meaning the size is limiting the scalability to high energy accelerators, and also the manufacturing and the operation of these machines' proved to be costly [22].

A different approach in order to achieve higher accelerating gradients whilst reducing the size and the cost, was to utilise higher frequency electromagnetic fields. In particular, plasma-based accelerators have made considerable progress in the past decades [23,24], ranging from laser-driven wakefield acceleration (LWKA) to plasma wakefield acceleration (PWKA). LWKA was first proposed by Tajima *et al.* in 1979 [25], where high-intensity laser pulses at centre wavelength of 1 μm created a plasma wakefield, resulting in the acceleration of electrons which are trapped in the wake. This concept proved to be very promising as peak accelerating gradients greater than 100 GV/m have been reported [26]. This figure was at least an order of magnitude greater than what conventional RF accelerators could provide. Nevertheless, due to the operating wavelength, the beam quality was poor as only a small fraction of the particle bunch was accelerated, resulting in an energy spread. More recently, several attempts have been made in order to increase the control over the plasma and consequently improve the resulting beam quality [27, 28].

PWKA was first proposed by Chen *et al.* in 1985 [29], and experimentally demonstrated by Rosenzweig *et al.* in 1988 [30]. In a PWKA, two particle bunches are employed with a time delay, the first called the drive bunch and the second called the witness bunch. The two bunches are injected into a cold plasma, with the higher-charge drive bunch causing charge density perturbations in the plasma, a wakefield [31, 32]. If the witness lower-charge bunch follows at a proper phase, it gets accelerated as a result of the longitudinal electric field in the wakefield. As the acceleration structure is plasma, an ionised gas, there is no damage threshold, thus higher accelerating fields may be supported by this scheme. This approach can in principle deliver ultra-short, high charge and high current with low emittance and narrow energy spread beams, however, it requires a separate source of high energy particles in order to generate the wakefields.

Moreover, various dielectric laser accelerator (DLA) schemes have been proposed [33–37], with the most notable work demonstrated by Peralta *et al.* [38]. In this work, dielectric sub-micrometre structures were employed as the accelerating cavities, driven by commercially available high-power laser systems. Optical or near-infrared laser pulses can be advantageous in the aspect of low loss and high damage threshold in dielectric materials, providing peak accelerating gradients of up to 151.2 GeV/m [38]. The dielectric structures act as a phase mask, in order to enhance the interaction with the particle bunch. However, due to the operating frequencies of this scheme, these structures require precise control of the spatial alignment and timing of injected bunches while challenging fabrication tolerances are also presented. Therefore, whilst GV/m accelerating fields have been achieved, this has been at the expense of low particle transmission [38, 39].

2.2 Developments in THz-driven particle beam manipulation

As RF accelerators are limited by the cavity damage threshold, and DLA suffer from challenging fabrication tolerances and low particle transmittance, THz radiation falls in the ideal millimetre-scale wavelength regime. Therefore, THz-driven acceleration allows simpler structure fabrication, whilst providing the picosecond-long cycle that are well suited for the manipulation of the entire particle bunch. Moreover, laser-driven THz sources providing peak electric fields exceeding 1 GV/m have been reported by Shalaby *et al.* [40], making THz-driven acceleration very promising for novel particle accelerators. Furthermore, scaling accelerators from RF to THz can benefit from the femtosecond timing synchronisation. Electron beams and THz sources, generated from the same laser system, would intrinsically reach temporal synchronisation, and remove the need for locking electronics.

For efficient THz-driven particle manipulation, several schemes have been proposed and developed over the last two decades. Here only works with experimental demonstration of THz-particle interaction are discussed. THz-driven acceleration was first demonstrated by Nanni *et al.* [41], where a sub-relativistic electron beam of energy 60 keV was accelerated by 6 keV over a 3 mm long interaction out of the total 10 mm-long circular dielectric-lined waveguide (DLW) structure. The DLW

structure was employed as the accelerating cavity, driven by single-cycle THz pulse with a centre frequency of 0.45 THz and pulse energy of 10 μJ. A segmented waveplate was used in order to convert the linearly polarised THz pulse into a radially polarised pulse, and it was then coupled with a linearly tapered horn, in order to excite the accelerating mode of the waveguide. An average accelerating gradient of 2.5 MeV/m, corresponding to a peak on-axis electric field at 8.5 MV/m was reported. The accelerating gradient was claimed to be scalable to multi-GeV/m for THz pulses of 10 mJ pulse energy. The interaction was limited due to the mismatch between the electron velocity and the phase velocity on the centre frequency of the driving THz pulse in the DLW structure.

This work was followed up with the development of the segmented THz electron accelerator and manipulator (STEAM) device in 2018 [42]. Two linearly polarised THz pulses are injected from opposite sides of the device, consisted of a multi-layered rectangular metallic waveguides, filled with dielectric slabs of varying thickness and length. With this scheme, the THz pulse is phase velocity matched with the particle bunch at each stage, by tailoring the thickness and the length of the dielectric filling each layer. In this demonstration, the STEAM device was consisted of three layers, reporting an acceleration of 30 keV, corresponding to a peak electric field of 70 MV/m. The STEAM device has also the capability of dynamically switching between accelerating, streaking, focusing and compressing modes, depending on the relative delay of the two driving THz pulses. The two devices have been combined together towards the development of an all-optical electron gun [43–45]. The THz-particle interaction was limited by the fixed number of layers to a length of 1 mm. In principle, this could be increased by adding more layers, provided more THz energy was available to accommodate the extra segments.

Curry *et al.* have implemented an inverse free-electron laser (IFEL) scheme in order to accelerate a relativistic electron beam of energy 4-9 MeV, driven by THz pulses [46]. A curved parallel plate waveguide in conjunction with a 30 cm-long undulator was employed as the accelerating cavity, observing a peak-to-peak induced energy modulation of up to 150 keV. The scaling of the modulation was linear with the THz field amplitude. However, the dispersion and diffraction of the THz pulse in the waveguide, as well as the coupling efficiency, was found to affect the strength of the interaction for different waveguide spacings. It was also reported

that the accelerating gradient scaled inversely with the beam energy, therefore this scheme would not be directly applicable for scaling to future high-energy, relativistic acceleration.

Furthermore, THz pulses have found applications not just on the acceleration of electron beams, but also on the metrology and bunching. THz radiation can be employed in novel devices for the characterisation of the temporal profile of an electron beam but also for the compression and the transverse focussing. Metallic resonators or ultra-thin metallic sheets have been employed by a number of groups. Kealhofer *et al.* have demonstrated streaking and velocity bunching of a sub-relativistic electron beam, by using 30 μm-thick, butterfly-shape aluminium slits, driven by single-cycle THz pulses [47]. Streaking speeds up to 8 μrad/fs was reported. A single laser system was employed for the electron photo-excitation, and THz generation for the two interaction points, achieving an intrinsic timing synchronisation of the order of few-femtoseconds. In follow up works, streaking and control of the beam was reported by using an ultrathin aluminium sheet, in a resonator-free concept [48, 49].

Zhao *et al.* have used a rectangular-shape, 50 μm-thick metallic resonator, driven by single-cycle THz pulses for the streaking of a relativistic, few femptosecond electron beam [50]. Similarly, a single laser system was employed for both electron photo-excitation and THz generation. However, an RF buncher and an RF deflector was used, introducing further timing jitter. Time stamping was achieved, with a reported streaking speed of 5.1 μrad/fs and with a temporal resolution much higher of what RF metrology methods offer.

In a follow up work from this group, THz-driven dielectric tubes were implemented, which allowed recording the complete time information of an ultrashort relativistic electron beam [51]. A circular polarised THz pulse was injected into the tube, and the co-propagating electron beam was swept and deflected helically resulting in a time mapping. Compression of the electron beam was also demonstrated [52]. This scheme also featured a wide dynamic range, applying for a wide range of electron beam lengths.

Metrology of a relativistic electron beam of energy 3.1 MeV was demonstrated by Li *et al.* [53], with femtosecond resolution. A parallel plate waveguide, machined out of 100 μm thick CuAu braze foil was used. This concept featured wide-band

dispersion-free geometry, unlike the aforementioned metallic resonators. The structure was illuminated at normal incidence by a single-cycle THz pulse, reporting a maximum streaking speed of 7.4 μrad/fs and timing accuracy of 0.41 fs.

The wide range of works, shows the drive towards understanding and exploiting the potential of THz pulses through structures that mediate interactions for control over the temporal, energy and spatial properties of electron beams. However, the key challenge is to increase the THz-electron interaction length for optimum efficiency. It was proven, that the interaction length was often limited by the dispersion induced by the structure, when a broadband pulse was employed. In order to calculate the optimum bandwidth and thereby, maximise the interaction, knowledge of the propagation characteristics of the structure is required.

In this thesis, two rectangular-shaped DLW structures were employed as the accelerating and the streaking cavities, driven by multi-cycle and single-cycle THz pulses, respectively. The propagation constant of the DLW structures was experimentally measured and compared with a model. Consequently, interactions with relativistic and sub-relativistic electron beams were explored and modelled.

2.3 High power laser-driven THz sources

Another key challenge for scalable, competitive THz-driven particle acceleration and manipulation, is the availability of high-power, table-top THz sources. Here, only laser-driven THz sources will be discussed, as methods of developing all-optical particle sources is of interest.

The development of laser-driven, table-top THz sources has been a fast expanding area of research over the last decades [54]. Generally, there is no optimal THz source, or a standard THz generation method. Each area of research or each industrial application has different requirements. For example, for a THz time-domain spectroscopy experiment, a low energy, broadband pulse is needed, in order to study the underlined physical phenomena, over a wide range of frequencies. However, in telecommunications, narrowband THz signals are required. Different THz sources or generation techniques can be used to access different region of the spectral range, with the desired bandwidth, and energy conversion efficiency. THz-driven acceleration always benefits from strong THz electric fields. However, the optimal spectral

content can vary for each scheme.

The generation of THz radiation by optical rectification (OR) consists of a nonlinear crystal and ultrashort laser pulses. OR is a second-order nonlinear optical process, where a quasi-DC signal is generated from the interaction of the frequencies components within the bandwidth of the ultrashort laser pulse. Here, the quasi-DC transient is the THz pulse, and generation of quasi single-cycle THz pulses was reported as early as 1971 [11,55]. Media suitable for OR are semiconductors, such as GaAs, GaP or ZnTe, ferroelectric crystals like $LiNbO_3$ (LN) or $LiTaO_3$ and organic crystals such as DAST, DSTMS, OH1 and BNA. The parameters of the emitted THz radiation also depend on the pump laser pulse duration, centre wavelength and pulse energy. Figure 2.1 taken from [54], depicts an overview of the highest pulse energies and peak electric field strengths achieved. The short vertical lines show the frequencies of the spectral peaks.

In this thesis, laser systems which have Ti:sapphire as an active medium are of interest, as they are well established and commercially available. Ti:sapphire laser systems are able to deliver high power, high repetition rate, ultrashort laser pules, at a centre wavelength of approximately 800 nm [56]. The LN crystal has been an attractive THz source, as it can deliver higher pump-to-THz energy efficiency, comparing to the rest of the inorganic crystals [8,13,54]. For the efficient THz generation via OR in a LN crystal, an optical technique was proposed by Hebling *et al.* [57], called pulse-front-tilt (PFT). This technique allowed overcoming the limitations due to lack of phase matching of the pump and the emitted THz pulse inside the crystal.

With the development and optimisation of the PFT technique, significant increase in efficiency and THz pulse was achieved. Wu *et al.* [58] have reported the generation of 0.2 mJ single-cycle THz pulses at room temperature (RT) (reference 60 in Figure 2.1). A Ti:sapphire laser system was employed, able to deliver Joule-level pulse energy of sub-50 fs pulse duration. The LN was pumped in a PFT technique, with a reported pump-to-THz conversion efficiency of 0.3%. The peak electric field strength at the focal spot was measured to be approximately 4 MV/m.

Higher conversion efficiency was demonstrated by Fulop *et al.* in 2014 [59] (reference 63 in Figure 2.1). The generation of single-cycle THz pulses of 0.4 mJ energy at RT was reported, with a corresponding efficiency as high as 0.77%. Nevertheless, this group employed a custom-made Yb:YAG based laser system, delivering laser

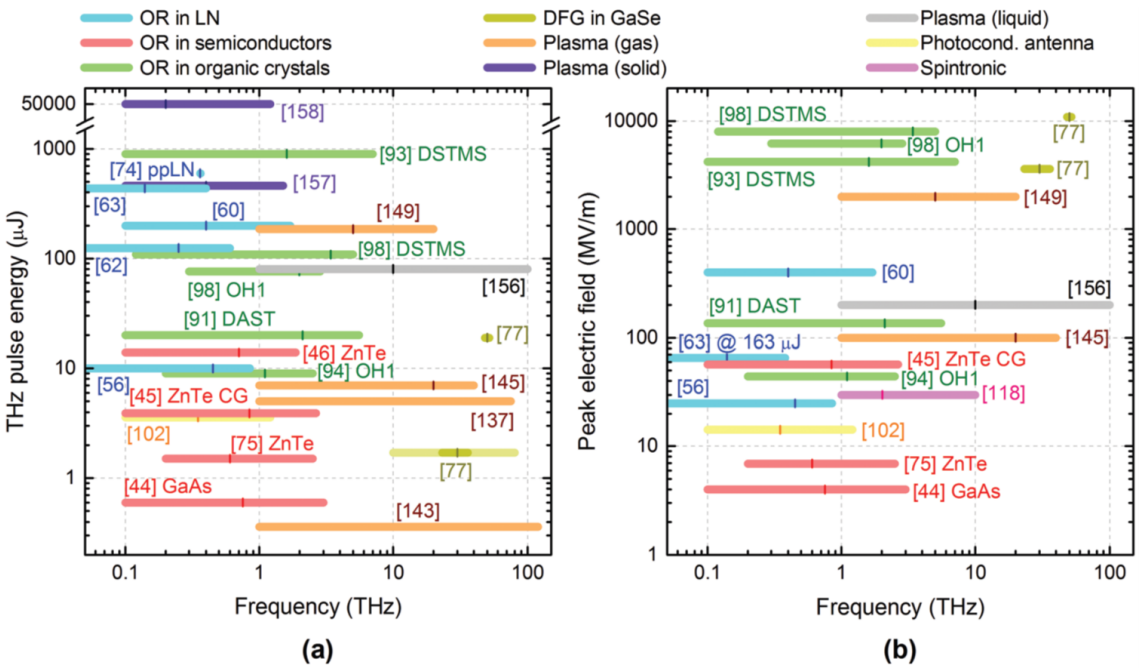

Fig. 2.1: Spectral coverage and some of the highest reported experimental values of (a) THz pulse energy and (b) peak electric field strength for a range of THz sources and techniques.. Figure taken from [54]. References in brackets can be found in [54].

pulses of 1030 nm centre wavelength, 785 fs pulse duration and up to 60 mJ pulse energy. In a separate experimental series, the enhancement of the conversion efficiency was investigated by cooling the LN crystal to cryogenic temperatures. An enhancement of a factor of 3 was measured compared to RT measurements. The use of cryogenic cooling, longer pump wavelength and temporally longer pump pulses contributed to suppressing the effects limiting the efficiency of THz generation.

Huang *et al.* [60] have demonstrated the highest energy efficiency, with a cryogenically cooled LN crystal at a lower pump pulse energy. A Yb:KYW laser system was employed emitting pulses with a centre wavelength of 1030 nm, 680 fs pulse duration and up to 2 mJ pulse energy. A maximum enhancement of 3.3 was measured when cooling the LN at 150 K, corresponding to a conversion efficiency of 3.8%±0.4%. However, such high efficiency could not be demonstrated at higher pump energies.

Even though the PFT technique is considered as the prominent technique for intense THz generation via OR in a LN crystal, it proved to be experimentally challenging. A diffraction grating and an imaging system are required, and the accuracy and precise alignment of these optical components are crucial as imaging

errors can lead to spatial distortions of the THz beam quality [61]. Poor THz beam quality makes diffraction-limited focussing a challenge, resulting in not exploiting the full potential of the source. Alternatives have been attempted via bringing into contact or etching a diffraction grating onto the LN crystal surface [62–65].

Other promising sources for intense THz generation, that can be implemented in a collinear excitation geometry, are organic crystals. Shalaby *et al.* [40] have demonstrated generation of single-cycle THz pulses from DSTMS and OH1 crystals via OR at room temperature (reference 98 in Figure 2.1). A Ti:sapphire laser system in conjunction with an optical parametric amplifier system, was used to pump the organic crystals, at 1.5 μm and a pulse energy of 3.8 mJ for DSTMS and at 1.35μm, 3.5 mJ for OH1. Despite the small size of the crystals (<5 mm radius), and the moderate pump pulse energy, THz pulses of energy of 109 μJ and 75 μJ were generated, corresponding to conversion efficiency of 2.86% and 2.14%, respectively. A concept of optimising the emerging THz beam quality and brightness by tweaking the pump wavefront-divergence was applied, achieving a diffraction-limited focusing. As a result, peak electric field strengths of 8.3 GV/m for DSTMS and 6.2 GV/m for OH1 were measured at the focal spot.

The highest THz pulse energy generated via OR in a nonlinear crystal was reported by Vicario *et al.* [66]. THz pulses of energy as high as 0.9 mJ were generated by a large area, 400 mm^2, partitioned DSTMS crystal (reference 93 in Figure 2.1). In this work, in order to avoid the inevitable irregular pump beam profile, and the shot-to-shot energy fluctuation induced by an Optical Parametric Amplifier (OPA) system [40, 67], a Cr:forsterite laser system was employed, delivering laser pulses at 1250 nm of 95 fs pulse duration and 30 mJ pulse energy. The conversion efficiency was reported to be a record high 3% at room temperature.

Organic crystals could pave the way for laser-driven, efficient intense THz pulse generation. However, due to phase matching and absorption conditions, pumping at higher than 800 nm wavelengths is required [67, 68]. Laser systems operating at that wavelength range are non-standard, and not available at higher energies. Moreover, organic crystals have been proved to exhibit lower damage threshold than inorganic crystals and due to the crystal growth technique complexity, the availability of large area crystals is limited and also the affordability makes it less favourable.

For THz time-domain spectroscopy experiments, a low energy, broadband source

is sufficient in order to probe the material characteristics in the THz regime. Spintronic emitters are metallic heterostructures, consisting of ferromagnetic and non-ferromagnetic thin films. This source rely on the conversion of an ultrafast spin photocurrent into a transverse charge current upon an ultrafast pulse excitation. The thin films are deposited on a substrate which is optically transparent to the pump pulse [69]. The spintronic emitters can be excited by low laser pulse energy, in the order of a few nanoJoules, generating THz pulses with a gap-less bandwidth, covering the range from 1 to 30 THz when excited by a 10 fs long pulse [70]. This was because metallic films exhibit featureless refractive index in the THz regime [71]. Moreover, as the metal films are on the order of nanometres thickness, much thinner than the wavelengths involved, there is no phase matching condition to be met. Furthermore, these emitters can be implemented in a collinear geometry, inexpensive, independent of the pump wavelength [72], and the emerging THz polarisation can be controlled by applying an external magnetic field pattern [70, 73].

In this thesis, a number of Ti:sapphire laser systems were employed as the drive pump laser, for the THz generation and the photo-excitation of electron beams, when applicable. For the THz time-domain spectroscopy experiments, spintronic sources were used, in order to measure and determine the propagation characteristics of the DLW structures. Furthermore, intense THz pulses were generated via OR in a PFT method in LN crystal at RT.

Chapter 3

Background theory

In this chapter, the main underlying theory behind the physical processes explored within this thesis is included. An overview of the generation and detection of freely propagating THz pulses based on nonlinear optical phenomena is discussed as well as guided wave theory. Starting with a brief introduction to nonlinear optics, the chapter focusses on THz generation through optical rectification of ultrafast laser pulses and through the inverse-spin Hall effect. Phase matching schemes such as the pulse-front tilt combined with chirped-pulse beating for the generation of multi-cycle THz pulses are also included.

The propagation of electromagnetic waves is also discussed, starting with Maxwell's equations in free space, to derive the wave equation. Then, the Hertz potentials are introduced, in order to solve the wave equation with dielectric-lined boundaries. As a result, the dispersion relation and the field pattern for the supported modes are derived, using the transverse resonance technique, closing with the interaction of charged particles with co-propagating electromagnetic radiation.

3.1 Nonlinear optics

Nonlinear optics is the study of phenomena that occur as a consequence of interaction of electromagnetic radiation within material systems, resulting in modification of its optical properties. In a nonlinear medium, most commonly a crystal, the polarisation responds nonlinearly to an applied electromagnetic field, typically observed at high light intensities, provided by laser systems.

For example, Second Harmonic Generation (SHG) and Sum/Difference Fre-

quency Generation (SFG/DFG) occur as a result of the atomic response that scale quadratically with the strength of the applied field. On the other hand, Pockels' effect is a linear electro-optic effect, where the refractive index of a medium is modified in proportion to the applied electric field strength [3].

The propagation of electromagnetic wave can be described by Maxwell's equations [74]

$$\nabla \cdot \mathbf{D} = \rho, \tag{3.1}$$

$$\nabla \cdot \mathbf{B} = 0, \tag{3.2}$$

$$\nabla \times \mathbf{E} = -\frac{\partial \mathbf{B}}{\partial t}, \tag{3.3}$$

$$\nabla \times \mathbf{H} = \frac{\partial \mathbf{D}}{\partial t} + \mathbf{J}, \tag{3.4}$$

where $\mathbf{E}$ is the electric field vector, $\mathbf{D}$ the electric displacement vector, ρ the charge density, and $\mathbf{J}$ the current density. $\mathbf{D}$ is given by

$$\mathbf{D} = \epsilon_0 \mathbf{E} + \mathbf{P}, \tag{3.5}$$

where $\mathbf{P}$ is the induced polarisation of the medium and ϵ_0 the electric permittivity in vacuum. The magnetic flux density $\mathbf{B}$, is related to the magnetic field strength $\mathbf{H}$, via

$$\mathbf{B} = \mu_0 \mathbf{H}, \tag{3.6}$$

where μ_0 is the magnetic permeability in vacuum. For the case where there are neither free charges $\rho = 0$, nor current density $\mathbf{J} = 0$, taking the curl of Equation 3.3 and using Equation 3.6, yields

$$\nabla \times \nabla \times \mathbf{E} + \mu_0 \frac{\partial^2 \mathbf{D}}{\partial t^2} = 0\,. \tag{3.7}$$

Using the vector calculus identity, $\nabla \times \nabla \times \mathbf{E} = \nabla(\nabla \cdot \mathbf{E}) - \nabla^2 \mathbf{E}$, in Equation 3.7, and substituting Equation 3.5, the wave equation is obtained

$$-\nabla^2 \mathbf{E} + \frac{n^2}{c^2} \frac{\partial^2 \mathbf{E}}{\partial^2 t} = -\frac{1}{\epsilon_0 c^2} \frac{\partial^2 \mathbf{P}}{\partial^2 t}, \tag{3.8}$$

where $c = 1/\sqrt{\mu_0 \epsilon_0}$ is the speed of light. Equation 3.8 states that the nonlinear response of the medium acts as a source term, in the form of a driven wave equation. If the right-hand side of Equation 3.8 is equal to zero, then it reduces to the wave equation of free waves, propagating with velocity c/n, where n is the refraction index of the medium.

The time dependent polarisation of a system $\mathbf{P}$(t), or the dipole moment per unit volume, depends on the strength of an applied time varying electric field $\mathbf{E}$(t). For the linear case, the induced polarisation is given as

$$\mathbf{P}(t) = \epsilon_0 \, \chi^{(1)} \mathbf{E}(t), \tag{3.9}$$

where $\chi^{(1)}$ is the linear electric susceptibility of the medium. However, for a nonlinear system, the optical response can be described by expressing the polarisation as a power series in terms of $\mathbf{E}$(t) as

$$\begin{aligned} \mathbf{P}(t) &= \epsilon_0 \left(\chi^{(1)} \mathbf{E}(t) + \chi^{(2)} \mathbf{E}^2(t) + \chi^{(3)} \mathbf{E}^3(t) + ... \right) \\ &\equiv \mathbf{P}^{(1)}(t) + \mathbf{P}^{(2)}(t) + \mathbf{P}^{(3)}(t) + ..., \end{aligned} \tag{3.10}$$

where $\chi^{(2)}$ and $\chi^{(3)}$ are the second and third order of nonlinear electric susceptibilities, respectively. For the scope of the thesis, only physical processes that occur as a result of the second-order nonlinear polarisation, $\mathbf{P}^{(2)}(t) = \epsilon_0 \, \chi^{(2)} \mathbf{E}^2(t)$, will be discussed.

Nevertheless, a crystalline solid such as crystals, have periodic lattice structures, making them spatially not isotropic [2]. Therefore, the second-order susceptibility can be expressed through tensor formalism by [74]

$$\mathbf{P}_i^{(2)}(\omega_n + \omega_m) = \epsilon_0 \sum_{jk} \sum_{nm} \chi_{ijk}^{(2)}(\omega_n + \omega_m, \omega_n, \omega_m) E_j(\omega_n) E_k(\omega_m), \tag{3.11}$$

where the indices i, j and k are the Cartesian components, and n, m are integers. In Equation 3.11, the discrete representation of the applied broadband field can be expressed by

$$\mathbf{E}(\mathbf{r},t) = \sum_n \mathbf{E}(\omega_n) e^{-i\omega_n t}. \tag{3.12}$$

When the frequencies involved are much smaller than the resonance frequency of the crystal, then the nonlinear susceptibility is independent of the frequencies of the applied field allowing the permutation of the spatial indices, without permuting the frequencies involved. This permutation symmetry is also known as the Kleinman's symmetry [3, 74]. When the Kleinman's symmetry is valid, the indices j and k are interchangeable, and the nonlinear susceptibility can be simplified from a 3x3x3 matrix to a contracted 3x6 matrix by combining the last two integers into one l, according to

jk:	11	22	33	23, 32	31, 13	12, 21
l:	1	2	3	4	5	6

The nonlinear polarisation $P^{(2)}(\omega_3 = \omega_1 + \omega_2)$, can then be described by the matrix

$$\begin{pmatrix} P_x^{(2)}(\omega_3) \\ P_y^{(2)}(\omega_3) \\ P_z^{(2)}(\omega_3) \end{pmatrix} = 4\epsilon_0 \begin{pmatrix} d_{11} & d_{12} & d_{13} & d_{14} & d_{15} & d_{16} \\ d_{21} & d_{22} & d_{23} & d_{24} & d_{25} & d_{26} \\ d_{31} & d_{32} & d_{33} & d_{34} & d_{35} & d_{36} \end{pmatrix} \times \begin{pmatrix} E_x(\omega_1)\, E_x(\omega_2) \\ E_y(\omega_1)\, E_y(\omega_2) \\ E_z(\omega_1)\, E_z(\omega_2) \\ E_y(\omega_1)\, E_z(\omega_2) + E_z(\omega_1)\, E_y(\omega_2) \\ E_x(\omega_1)\, E_z(\omega_2) + E_z(\omega_1)\, E_x(\omega_2) \\ E_x(\omega_1)\, E_y(\omega_2) + E_y(\omega_1)\, E_x(\omega_2) \end{pmatrix}, \tag{3.13}$$

where $d_{il} = \frac{1}{2}\chi_{il}^{(2)}$ is the nonlinear optical coefficient.

For a fixed crystal geometry, and for an optical polarisation geometry where the applied field is typically linearly polarised along a crystal axis, the nonlinear polarisation can be simplified to a scalar form

$$P^{(2)}(\omega_3) = 4\epsilon_0 d_{\text{eff}} E(\omega_1) E(\omega_2), \tag{3.14}$$

where $P(\omega) = |\mathbf{P}(\omega)|$, $E(\omega) = |\mathbf{E}(\omega)|$ and d_{eff} is the effective nonlinear coefficient, obtained from the d_{il} matrix in Equation 3.13.

3.2 Generation of THz radiation

3.2.1 Optical rectification

Optical rectification (OR) is a second-order nonlinear optical effect. It is difference frequency generation, where the limit of the difference of the frequencies involved tends to zero, $\lim_{\omega_2 \to \omega_1} \omega_3 = 0$. Typically, mode-locked femtosecond laser pulses are used to generate THz radiation from nonlinear crystals via optical rectification. The bandwidth of the THz-radiation pulse is determined by difference frequency generation by all frequencies within the bandwidth of the femtosecond laser pulse [3].

In a simple mathematical view, when the applied field consists of two frequency components, ω_1, ω_2, of amplitude E_1 and E_2, respectively, then the second-order polarisation is given by

$$P^{(2)}(t) = \epsilon_0 \chi^{(2)} \left(E_1 \sin[\omega_1 t] + E_2 \sin[\omega_2 t]\right)^2 . \tag{3.15}$$

Expanding the bracket in (3.15), and using the trigonometric identity $\sin A \sin B = (\cos(A-B) + \cos(A+B))/2$ and $\sin^2\theta = (1-\cos 2\theta)/2$, the nonlinear polarisation can be expressed by

$$\begin{aligned} P^{(2)}(t) = \frac{1}{2}\epsilon_0 \chi^{(2)} (& E_1^2(1-\cos[2\omega_1 t]) && \text{SHG} \\ & + E_2^2(1-\cos[2\omega_2 t]) && \text{SHG} \\ & + E_1 E_2(\cos[(\omega_1+\omega_2)t]) && \text{SFG} \\ & - E_1 E_2 \cos[(\omega_1-\omega_2)t])) && \text{DFG}, \end{aligned} \tag{3.16}$$

where each component of the expression is labelled by the name of the physical process it describes.

For the case of an optical pulse, the electric field can be expressed by a time-dependent electric field, with an intensity profile described with a Gaussian distribution by

$$E(t) = E_0 \exp\left[-\ln 4 \frac{(t-t_0)^2}{\Delta\tau^2}\right] \exp\left[-i\,\omega_0\,t\right], \tag{3.17}$$

where $\Delta\tau$ is the FWHM duration of the intensity profile, and ω_0 the centre frequency of the pulse. In the assumption where the pulse duration is much longer than the optical period, $\Delta\tau \gg \omega_0^{-1}$, and the dispersion of the nonlinear susceptibility is negligible near the optical frequencies, then the induced polarisation by OR will have a time-dependent profile, proportional to the optical pulse envelope, given by

$$P^{(2)}(t) \propto E_0^2 \exp\left[-2\ln 4 \frac{(t-t_0)^2}{\Delta\tau^2}\right]. \tag{3.18}$$

The time varying nonlinear polarisation acts as the source of THz radiation. The THz radiation generated by OR of ultrashort laser pulses rises from the difference frequency mixing between all of the different frequency components present in a single ultrashort laser pulse. The temporal profile of the radiated THz pulse is proportional to the second time derivative of $P^{(2)}(t)$, as Equation 3.8 suggests. It becomes clear from the time-bandwidth product, for a Gaussian pulse where, $\Delta\tau \cdot \Delta\omega \approx 0.44$, that for a pulse duration $\Delta\tau$ of 100 fs, the transform-limited spectral FWHM bandwidth is approximately 4.4 THz.

Nonlinear phenomena such as OR, SHG and SFG/DFG can occur only in noncentrosymmetric crystals [3, 4, 74]. As Equation 3.13 denotes, for a centrosymmetric crystal, an inversion symmetry would dictate zero values for the nonlinear optical coefficient matrix, $d_{ijk} = 0$, for all i, j and k [74]. Therefore, THz generation via OR is possible if the crystal is noncentrosymmetric or the symmetry is broken by a strong electric field [3].

3.2.2 Phase matching

For substantial optical to THz energy conversation efficiency, three major factors need to be considered; nonlinear coefficient of the medium, absorption of both optical and THz frequencies in the medium, and the coherent length of the OR process.

The first parameter is reliant on the crystal of choice, and the crystal orientation with respect to the linear polarisation of the pump beam [3]. For example, Zinc

Telluride (ZnTe) is a III–V semiconductor, with a zincblende structure and it is widely used for THz generation via OR. Zincblende crystals demonstrate a cubic structure with a $\bar{4}3m$ point group symmetry, with non-zero nonlinear coefficient elements $d_{14} = d_{25} = d_{36}$. THz generation via OR of femtosecond pulses, has been reported from (100) [75], (110) [76] and (111)-oriented crystals [77], featuring zincblende structure.

The second parameter can be understood by considering the fact that when the photon energy is less than the band gap of the nonlinear medium, then the pump laser pulse is able to propagate though the bulk for a longer distance. Equivalently, low absorption in the THz regime in the medium is required, to allow successful cumulative generation throughout the bulk. Therefore, it is important for the medium to exhibit low optical and THz absorption for efficient THz emission via OR.

The coherent length can be explained through the phase matching condition. Phase matching condition can be understood as the conservation of energy and momentum in the nonlinear process. If the nonlinear crystal was dispersionless, then the resulting bandwidth of the THz radiation would solely depend on the pulse width of the incident laser pulse. However, nonlinear crystals are generally dispersive materials, featuring different refractive index at frequencies ω_1, ω_2 and ω_3, involved in the OR process.

Defining the electric fields involved, propagating in the $+z$ direction, (for j=1, 2, 3) to be

$$E_j(z,t) = A_j\, e^{i(k_j z - \omega_j t)}, \tag{3.19}$$

where $k_j = n_j\, \omega_j / c$ is the wavenumber and A_j the amplitude, then according to Equation 3.14, the amplitude of the nonlinear polarisation yields

$$P^{(2)}(\omega_3) = 4\epsilon_0 d_{\text{eff}} A_1 A_2 e^{i(k_1 - k_2)z}. \tag{3.20}$$

Substituting Equations 3.19, 3.20 into the wave equation 3.8, and rearranging, the relation is obtained [74]

$$\frac{d^2 A_3}{dz^2} + 2ik_3 \frac{d\, A_3}{dz} = \frac{-4 d_{\text{eff}} \omega_3^2}{c^2} A_1 A_2 e^{i(k_1 - k_2 - k_3)z}. \tag{3.21}$$

The first term on the left-hand side in Equation 3.21 can be neglected, as the 'slowly varying amplitude' approximation is made. This approximation applies in cases where the fractional change of A_3 in a distance of the order of an optical wavelength is much smaller than unity, $\left|\frac{d^2A_3}{dz^2}\right| \ll \left|k_3\frac{dA_3}{dz}\right|$.

With the slowly varying approximation taken into consideration, the amplitude of the radiated THz wave ω_3, at the exit of the nonlinear crystal of length L is obtained by

$$A_3(L) = \frac{2id_{\text{eff}}A_1A_2}{k_3c^2}\int_0^L e^{i\Delta k\, z}dz = \begin{cases} \dfrac{2id_{\text{eff}}A_1A_2}{k_3c^2}\left(\dfrac{e^{i\Delta kL}-1}{i\,\Delta k}\right), & \Delta k \neq 0 \\ \dfrac{2id_{\text{eff}}A_1A_2}{k_3c^2}L, & \Delta k = 0 \end{cases} \tag{3.22}$$

where the quantity $\Delta k = k_1 - k_2 - k_3$, is the wavevector mismatch. As can be seen from Equation 3.22, for the case where $\Delta k = 0$, the amplitude increases linearly with z, and the intensity increases quadratically with z, respectively. This condition is called perfect phase matching. The radiated wave sustains a fixed phase with respect to the nonlinear polarisation, extracting energy more efficiently from the incident waves ω_1 and ω_2.

When the condition of perfect phase matching is not satisfied, $\Delta k \neq 0$, the intensity of the generated wave is given by the magnitude of the time-averaged Poynting vector [74]

$$I_3 = \frac{8\,d_{\text{eff}}^2\omega_3^2 I_1 I_2}{n_1n_2n_3\epsilon_0c^2}L^2\text{sinc}^2\left[\frac{\Delta k\, L}{2}\right], \tag{3.23}$$

where $I_i = 2n_i\epsilon_0 c|A_i|^2$, is the intensity of the corresponding wave ω_i. The emitted intensity via OR is proportional to $\text{sinc}^2\left[\Delta kL/2\right]$, as illustrated in Figure 3.1. As the product $|\Delta k|L$ increases, the efficiency of the OR decreases. When perfect phase matching condition is fulfilled, $\Delta k = 0$, the intensity maximises.

When the phase mismatch leads to a phase equal to π, then the intensity drops to zero. The coherence length, L_c, is defined as the distance over which the optical pulse propagates before leading the THz wave by a $\pi/2$ phase shift

$$L_c = \frac{\pi}{\Delta k}. \tag{3.24}$$

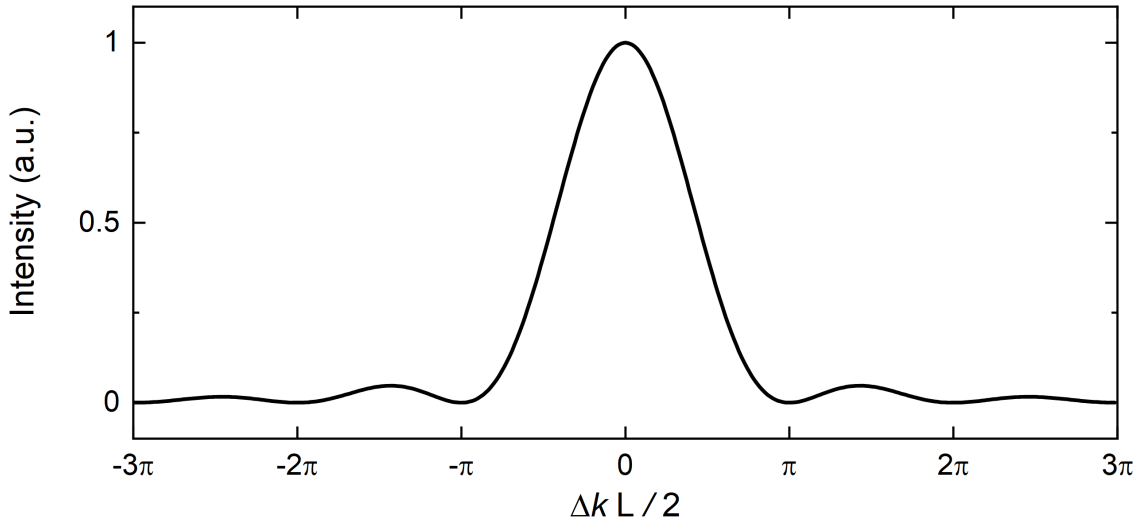

Fig. 3.1: Effect of the wavevector mismatch on the emitted intensity.

Therefore, efficient THz generation via OR in nonlinear crystals at a given frequency, is achieved for crystals that are equal in thickness or thinner than the coherence length.

Perfect phase matching condition requires conservation of energy and momentum in the OR process, which can be described by

$$\begin{aligned} \omega_{O,1} - \omega_{O,2} &= \omega_{\mathrm{THz}} \\ k_{O,1} - k_{O,2} &= k_{\mathrm{THz}}, \end{aligned} \tag{3.25}$$

where $\omega_{O,i=1,2}$ and $k_{O,i=1,2}$ refer to the optical frequencies and wavevectors respectively, and ω_{THz} and k_{THz} refer to the frequency and wavevector of the generated THz wave. Dividing the two relations in Equation 3.25, yields [2]

$$\frac{\partial \omega_O}{\partial k_O} = \frac{\omega_{\mathrm{THz}}}{k_{\mathrm{THz}}} \Rightarrow v_{g,O} = v_{p,\mathrm{THz}}, \tag{3.26}$$

where $v_{g,O}$ is the group velocity of the optical beam and $v_{p,\mathrm{THz}}$ the phase velocity of the THz beam in the nonlinear crystal. From Equation 3.26, it is understood that phase matching is achieved when the optical group velocity is equal to the phase velocity of the generated THz wave.

3.2.3 Pulse-front-tilt

Collinear phase matching occurs intrinsically in specific crystals. For example, the group refractive index near the optical wavelength 800 nm in ZnTe, matches well with the THz refractive index [4]. This makes ZnTe an attractive nonlinear crystal for THz generation via OR of laser pulses.

Lithium Niobate ($LiNbO_3$, LN), is another attractive nonlinear crystal for THz generation. LN is an inorganic crystal with a trigonal crystal structure and a $3m$ point group symmetry, featuring higher nonlinear coefficient than ZnTe and higher energy band gap [4]. The high band gap of 4 eV, makes the LN optically transparent to wavelengths between 350 nm-5200 nm, preventing multiphoton absorption which leads to optical damage of the crystal and saturation of the THz generation process [65]. Doping of the crystal with Magnesium Oxide (MgO), further increases the resistance to optical damage. MgO-doped LN crystals will be extensively employed as THz source in this thesis.

Nevertheless, collinear phase matching cannot be achieved for OR in LN crystals, as there is a substantial mismatch between the optical group, n_g^O, and the THz phase, n_p^{THz}, refractive indices [2, 4]. Therefore, a phase matching scheme, known as Pulse-Front-Tilt (PFT), is employed. The PFT scheme was first proposed by Hebling *et al.* [57], in 2002, for efficient THz pulse generation via OR in LN crystals.

Due to the refractive index mismatch, the THz wave is generated in a Cherenkov cone. Therefore, velocity matching can be achieved by tilting the intensity front of the pump beam by an angle γ where [4, 57]

$$\frac{c}{n_g^O}\cos\gamma = \frac{c}{n_p^{\mathrm{THz}}}. \tag{3.27}$$

With this scheme, the intensity front of the pump beam travels collinearly with the THz wave with the same velocity, with different propagation directions. For efficient extraction of the produced THz radiation, the LN crystal is grown in a prism shape, with a prism angle equal to γ.

As Tokodi *et al.* have demonstrated [78], the PFT can be realised with a diffraction grating in a $4f$ lens configuration. The Chrenkov angle γ can be described in terms of the diffraction order m, the diffraction angle θ_d, and the grating groove

period p as [78, 79]

$$\tan\gamma = \frac{m\lambda_0 p}{n_g^O \beta_1 \cos\theta_d}, \tag{3.28}$$

where λ_0 is the central pump wavelength and $\beta_1 = f_2/f_1$ the magnification factor of the two lenses for the pump-pulse front. Equation 3.28 takes into account the grating equation and the angular dispersion introduced by the grating and the nonlinear crystal.

Consequently, in order to obtain optimal THz beam quality and optical-to-THz conversion efficiency, the tilt angle of the grating image inside the LN crystal θ, should match the pump-pulse front angle γ [61, 79]. The tilt angle θ is given by

$$\tan\theta = n_p^O \beta_2 \tan\theta_d, \tag{3.29}$$

where n_p^O is the optical phase refractive index in LN, and β_2 the magnification factor of the lenses for the diffraction grating image. When the magnification factors coincide, then the phase matching condition described in Equation 3.27, is fulfilled.

Figure 3.2 depicts the calculated magnification factor β_1, for diffraction gratings of different groove density (dashed lines), and β_2 (solid line), as a function of the diffraction angle θ_d. The calculations have been replicated from the work of Hirori *et al.* [79], as an example. The parameters used, are denoted in a text box, also taken from the parameters used from the same work. As can be seen, for a particular diffraction grating, the optimal magnification factor and the diffraction angle can be identified graphically. A combination of two lenses is then chosen to satisfy $\beta = f_2/f_1$.

The optimal magnification factor and the incident angle at the grating θ_i are given by [78]

$$\beta = \frac{f_2}{f_1} = \frac{1}{\sqrt{\alpha}}, \tag{3.30}$$

$$\sin\theta_i = \frac{\lambda_0}{p}\left(1 - \frac{\alpha}{n_p^O\, n_g^O}\right), \tag{3.31}$$

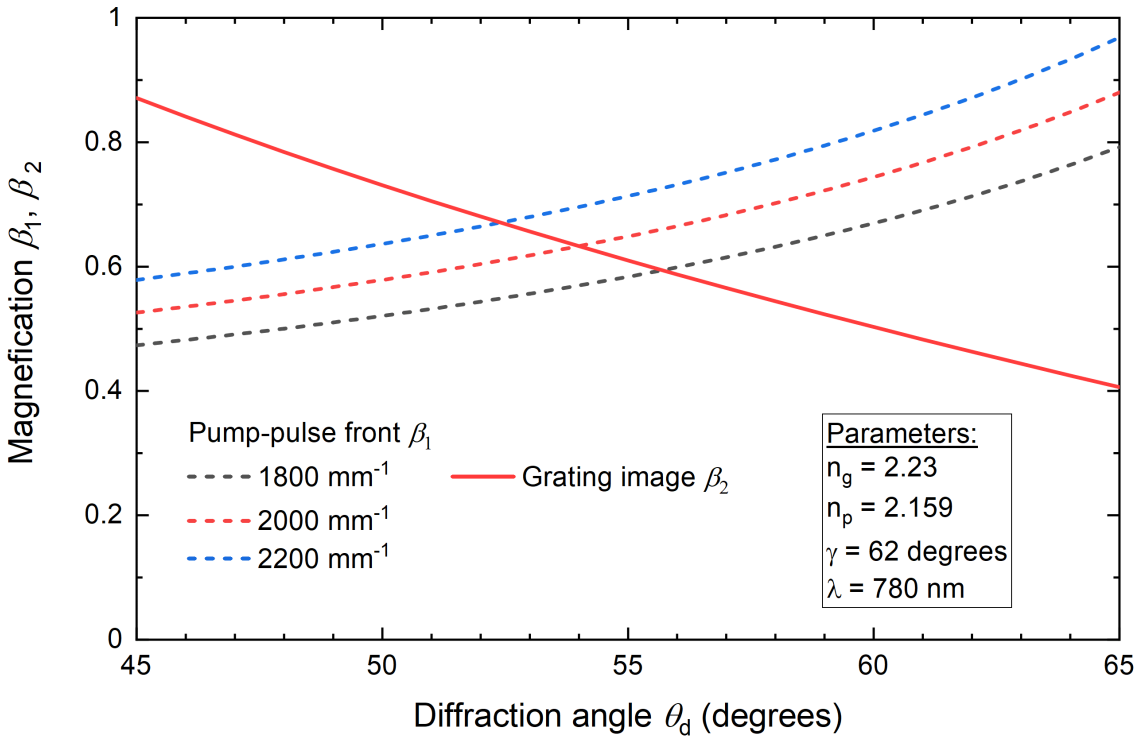

Fig. 3.2: Pump-pulse front magnification β_1, for diffraction gratings of different groove density (dashed lines) with the grating image β_2, as a function of the diffraction angle.

where the α parameter is given by [78]

$$\alpha = \frac{n_p^2\, n_g p}{2\lambda_0}\sqrt{\frac{\lambda_0^2}{n_g^2 p^2 \tan^4\gamma} + \frac{4}{n_p^2}} - \frac{n_p^2}{2\tan^2\gamma}. \tag{3.32}$$

3.2.4 Chirped pulse beating

Optical rectification of laser pulses in nonlinear crystals, typically produces single-cycle, broadband THz pulses. For the generation of frequency-tunable, narrow-band THz radiation in free space, the Chirped Pulse Beating (CPB) scheme is employed. Generation of narrow-band THz pulses using CPB was first demonstrated by Weling *et al.* [80]

CPB is typically realised by two linearly chirped optical laser pulses, with a relative time delay, and a nonlinear optical mixer. The spectral content of a linearly chirped pulse is temporally broadened, with the instantaneous carrier frequency linearly swept in time. The linear frequency chirp in optical pulses, can be produced by introducing Group Velocity Dispersion (GVD). When an optical pulse propagates

through a dispersive medium, a frequency-dependent phase modulation is applied. The phase chirp can be expressed as a Taylor expansion series about the center frequency ω_0 as

$$\phi(\omega) = \phi(\omega_0) + \phi'(\omega_0)(\omega - \omega_0) + \frac{1}{2}\phi''(\omega_0)(\omega - \omega_0)^2 + \frac{1}{6}\phi'''(\omega_0)(\omega - \omega_0)^3 + ... \quad (3.33)$$

where ϕ', ϕ'', ϕ''' are the derivatives of the phase with respect to the angular frequency, and are known as the group delay, second-order dispersion (or GVD), third-order dispersion (TOD), etc.

GVD can be induced with a diffraction grating pair configuration, given by [81]

$$\text{GVD} = \frac{1}{\mu} = \frac{\partial^2\phi(\omega)}{\partial\omega^2} = \frac{4\pi^2 c\, b}{\omega_0^3 d^2}\left(1 - \left(\frac{2\pi\, c}{\omega_0\, d} - \sin\gamma\right)^2\right)^{-3/2}, \quad (3.34)$$

where μ is the carrier frequency sweep rate, ω_0 the center frequency of the optical pulse, b the perpendicular separation between the diffraction gratings, d the grating grove period and γ the angle of incidence. The time duration modulation of the chirped pulse is obtained by [80, 82, 83]

$$T_1 = T_0\left(1 + \frac{4}{\mu^2\, T_0^4}\right)^{1/2}, \quad (3.35)$$

where T_0 is the Fourier limited $1/e$ half width of the field and T_1 the stretched $1/e$ of the field half width.

The temporally stretched optical pulse is then split into two identical pulses, and one pulse is delayed by a variable interval τ_s with respect to the other. The two pulses are interferometrically recombined, so that the spectra overlap in the time domain. The interference between the two pulses results in a quasi-sinusoidal intensity modulation at the beat frequency given by [82]

$$f_0 = \frac{\tau_s}{\pi T_0 T_1} \cong \frac{\mu\tau_s}{2\pi}, \quad (3.36)$$

The approximation in Equation 3.36 applies applies for τ_s relatively smaller to the stretched pulse duration. As can be seen, f_0 is proportional to the time delay

between the two chirped pulses, and inversely proportional to the GVD induced.

The resulting quasi-sinusoidal optical modulation, excites a nonlinear crystal, and through OR, THz radiation of center frequency f_0 is produced, with a corresponding of 1/e full width bandwidth of [80, 82]

$$\Delta f = \frac{\sqrt{8}}{2\pi T_1} \cong \frac{\sqrt{2}\, T_0 \mu}{\pi}. \tag{3.37}$$

With the CPB scheme, THz pulses of tunable bandwidth Δf, and tunable center frequency f_0 can be produced, offering the ability of driving the structure at the operating frequency and optimal bandwidth. CPB will be used in Chapter 6, where the THz-electron bunch interaction is explored at different center frequencies of the driving THz pulse.

3.2.5 Spintronic emitters

Spintronic emitters are a relatively new THz source, introduced in 2013 [84]. The exact emission mechanism that takes place is not yet fully understood, and still under study. Nevertheless, a comprehensive study has been carried out by Seifert *et al.* [70].

The principle of operation of a spintronic emitter, is depicted in Figure 3.3. A heterostructure consisting of a ferromagnetic (FM) and a non-ferromagnetic (NM) metal thin film, is illuminated by an ultrafast optical laser pulse. Absorption of the laser pulse in the metallic layer promotes electrons to energy states above the Fermi level, thus creating a non-equilibrium carrier distribution, changing as a result their mobility and scattering rate which differ in the FM and NM layers. Spin-up and spin-down electrons (blue and red in Figure 3.3, respectively) have very different transport properties as well [85, 86]. As a result the majortiy spin-up electrons travel faster than the minority spin-down electrons [87], inducing a spin-polarised longitudinal current along the z-direction, j_s.

Upon entering the NM layer, spin-orbit coupling deflects spin-up and spin-down electrons in opposite directions [88–90], by a mean angle γ, as illustrated in Figure 3.3. This is also known as the inverse spin-Hall effect (ISHE) [91]. The result of the ISHE is the conversion of the longitudinal spin current density j_s, into an ul-

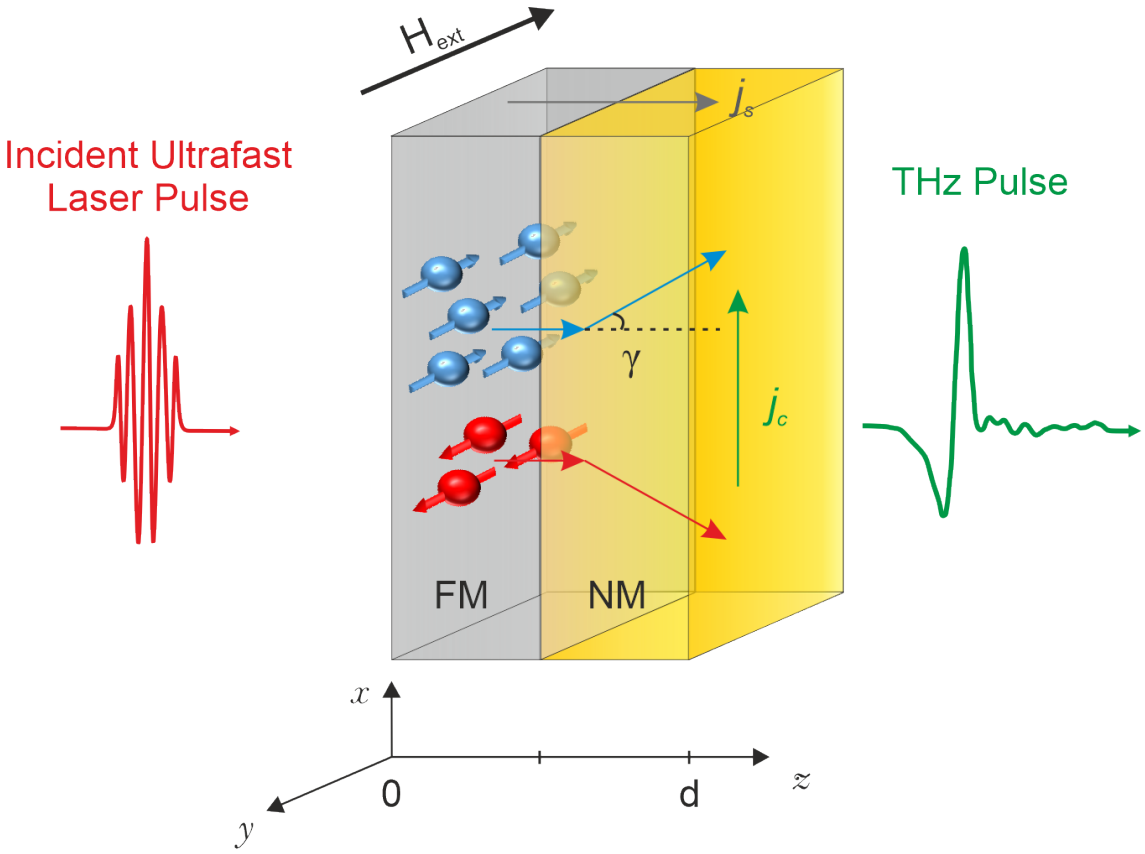

Fig. 3.3: Illustration of the metallic THz emitter and its principle of operation. The process involves an ultrafast laser pulse which induces a spin-polarised current j_s along the z-direction which is transformed into a transverse charge current j_c via ISHE, acting as a source of THz radiation. The metal stack is biased by a constant magnetic field, H_{external}, antiparallel to the y-direction.

trafast transverse charge current density j_c, along the x-axis. This mechanism acts as a source of THz radiation [70, 92], with a corresponding charge current density j_c described by

$$j_c = \sin[\gamma]\, j_s. \tag{3.38}$$

The amplitude of the emitted electric field is governed by the generalised Ohm's Law, given by

$$E(\omega) = Z(\omega)\, e \int_0^d dz\, \sin[\gamma(z)]\, j_s(z, \omega), \tag{3.39}$$

where d is the metal film thickness, e the elementary charge and $Z(\omega)$ an impedance

which describes the conversion of the current into electromagnetic radiation efficiency. The quantity $1/Z(\omega)$ may be interpreted as the effective conductivity of the metal stack [84].

The radiation emitted by spintronic samples via ISHE, has been shown to be in the THz regime, with a polarisation perpendicular to the sample magnetisation and it is independent of the polarisation of the pump beam [70]. THz radiation is emitted in both directions of the spintronic sample.

3.3 Waveguide theory

In this section, the dispersion relation as well as the EM field patters of the supported modes in a rectangular-shape metallic waveguide is presented, followed by how the implementation of a dielectric lining would change the propagation characteristics.

3.3.1 Hollow metallic waveguide

When electromagnetic (EM) waves are confined to the interior of a waveguide, then certain boundary conditions apply. The boundaries of metallic waveguides are assumed as perfect conductors, thus $\mathbf{E} = 0$ and $\mathbf{B} = 0$ inside the material, hence the boundary conditions at the inner wall are [93, 94]

$$\begin{aligned} \mathbf{E}^{\parallel} &= 0, \\ \mathbf{B}^{\perp} &= 0. \end{aligned} \tag{3.40}$$

The electric and magnetic fields of a monochromatic wave travelling through a transmission line in the positive direction of the z-axis have the generic form of

$$\mathbf{E}(x, y, z, t) = \mathbf{E}_0(x, y)e^{i\omega t - \gamma z}, \tag{3.41}$$

$$\mathbf{B}(x, y, z, t) = \mathbf{B}_0(x, y)e^{i\omega t - \gamma z}, \tag{3.42}$$

where $\gamma = \alpha + i\beta$, is the complex propagation constant. The real part of γ is the extinction coefficient, whereas the imaginary part is the propagation constant. $\mathbf{E}_0(x, y)$ and $\mathbf{B}_0(x, y)$ need to satisfy the source-free ($\mathbf{J}$=0, $\mathbf{P}$=0) Maxwell's equations, subject to the boundary conditions described in Equation 3.40. The six resulting equations,

can be arranged to obtain the four transverse field components in terms of E_z and H_z as [95]

$$\begin{aligned} H_x &= \frac{1}{{k_c}^2}\left(i\omega\epsilon\frac{\partial E_z}{\partial y} - \gamma\frac{\partial H_z}{\partial x}\right), \\ H_y &= \frac{-1}{{k_c}^2}\left(i\omega\epsilon\frac{\partial E_z}{\partial x} + \gamma\frac{\partial H_z}{\partial y}\right), \\ E_x &= \frac{-1}{{k_c}^2}\left(\gamma\frac{\partial E_z}{\partial x} + i\omega\mu\frac{\partial H_z}{\partial y}\right), \\ E_y &= \frac{1}{{k_c}^2}\left(-\gamma\frac{\partial E_z}{\partial y} + i\omega\mu\frac{\partial H_z}{\partial x}\right), \end{aligned} \tag{3.43}$$

where ${k_c}^2 = k^2+\gamma^2$. The supported modes in a hollow rectangular-shape waveguide, can be classified into two categories, depending on whether the longitudinal electric or magnetic component has a non-zero value. The Transverse Electric (TE) modes are characterised by $E_z = 0$ and the Transverse Magnetic (TM) modes by $H_z = 0$, where the electric/magnetic field lies only on the transverse plane, respectively.

For a hollow rectangular-shape waveguide of height b and width w, as illustrated in Figure 3.4, the longitudinal field component $H_z(x, y)$ or $E_z(x, y)$ subject to boundary conditions, is solved by separation of variables, given by [93, 95]

$$\text{TE}_{mn}\text{ modes:}\quad H_z(x,y) = H_0\cos\left[\frac{m\pi}{w}x\right]\cos\left[\frac{n\pi}{b}y\right], \quad (m,n = 0,1,2,...) \tag{3.44}$$

$$\text{TM}_{mn}\text{ modes:}\quad E_z(x,y) = E_0\sin\left[\frac{m\pi}{w}x\right]\sin\left[\frac{n\pi}{b}y\right], \quad (m,n = 0,1,2,...) \tag{3.45}$$

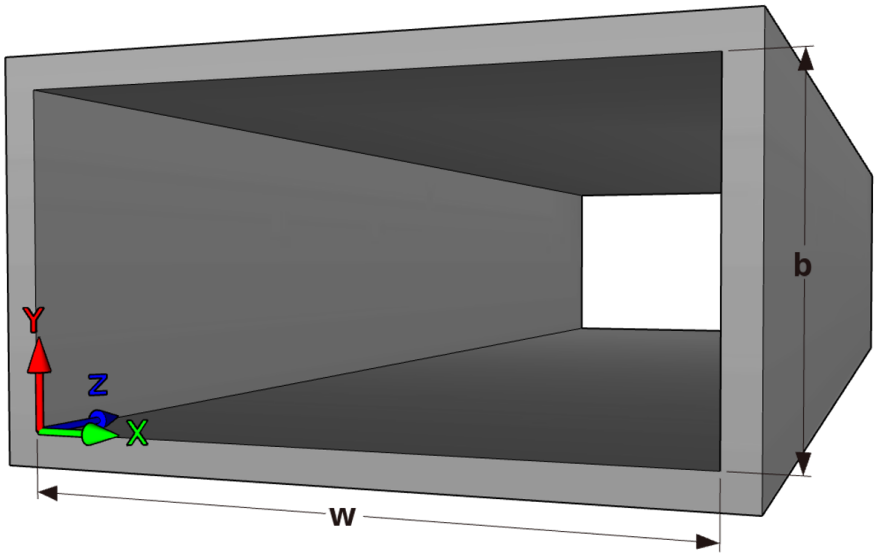

Fig. 3.4: Hollow rectangular-shape waveguide.

where the m, n indices denote the eigenmode. The propagation constant is obtained via [93, 94]

$$\gamma = \sqrt{{k_c}^2 - k^2} = \sqrt{\left(\frac{m\pi}{w}\right)^2 + \left(\frac{n\pi}{b}\right)^2 - \left(\frac{\omega}{c}\right)^2}. \tag{3.46}$$

which is a function of frequency. A figure of merit is introduced, the cut-off frequency f_c, defined by

$$f_c = \frac{c}{2\pi}\, k_c = c\sqrt{\left(\frac{m}{2w}\right)^2 + \left(\frac{n}{2b}\right)^2}. \tag{3.47}$$

For frequencies $f < f_c$, the propagation constant is purely real and instead of a travelling wave, the wave is exponentially attenuating, also known as evanescent modes. Therefore, the frequency of a travelling wave must be higher than f_c. The phase and group velocities are also functions of frequency, given by

$$v_p = \frac{\omega}{\beta} = \frac{c}{\sqrt{1 - (f_c/f)^2}}, \tag{3.48}$$

$$v_g = \frac{\partial\,\omega}{\partial\beta} = c\sqrt{1 - (f_c/f)^2}, \tag{3.49}$$

The transverse EM field pattern of the supported TE/TM, can be obtained by substituting Equation 3.44/3.45 into Equations 3.43 [95]

Quantity	TE_{mn} mode	TM_{mn} mode
E_z	0	$B\sin\left[\frac{m\pi}{w}x\right]\sin\left[\frac{n\pi}{b}y\right]e^{-\gamma z}$
H_z	$A\cos\left[\frac{m\pi}{w}x\right]\cos\left[\frac{n\pi}{b}y\right]e^{-\gamma z}$	0
E_x	$\frac{i\omega\mu n\pi}{{k_c}^2 b}A\cos\left[\frac{m\pi}{w}x\right]\sin\left[\frac{n\pi}{b}y\right]e^{-\gamma z}$	$\frac{-i\beta m\pi}{{k_c}^2 w}B\cos\left[\frac{m\pi}{w}x\right]\sin\left[\frac{n\pi}{b}y\right]e^{-\gamma z}$
E_y	$\frac{-i\omega\mu m\pi}{{k_c}^2 w}A\sin\left[\frac{m\pi}{w}x\right]\cos\left[\frac{n\pi}{b}y\right]e^{-\gamma z}$	$\frac{-i\beta n\pi}{{k_c}^2 b}B\sin\left[\frac{m\pi}{w}x\right]\cos\left[\frac{n\pi}{b}y\right]e^{-\gamma z}$
H_x	$\frac{i\beta m\pi}{{k_c}^2 w}A\sin\left[\frac{m\pi}{w}x\right]\cos\left[\frac{n\pi}{b}y\right]e^{-\gamma z}$	$\frac{i\omega\epsilon n\pi}{{k_c}^2 b}B\sin\left[\frac{m\pi}{w}x\right]\cos\left[\frac{n\pi}{b}y\right]e^{-\gamma z}$
H_y	$\frac{i\beta n\pi}{{k_c}^2 b}A\cos\left[\frac{m\pi}{w}x\right]\sin\left[\frac{n\pi}{b}y\right]e^{-\gamma z}$	$\frac{-i\omega\epsilon m\pi}{{k_c}^2 w}B\cos\left[\frac{m\pi}{w}x\right]\sin\left[\frac{n\pi}{b}y\right]e^{-\gamma z}$

where A and B are arbitrary constants. The characteristic wave impedance of a TE/TM mode is defined by calculating the ratio of the transverse electric and magnetic field

$$Z_{\mathrm{TE}} = \frac{E_x}{H_y} = \frac{-E_y}{H_x} = \frac{k\eta}{\beta}, \tag{3.50}$$

$$Z_{\mathrm{TM}} = \frac{E_x}{H_y} = \frac{-E_y}{H_x} = \frac{\beta\eta}{k}, \tag{3.51}$$

where $\eta = \sqrt{\mu/\epsilon}$ is the intrinsic impedance of the material filling the waveguide which in this case is vacuum. The wave impedance is frequency dependent, and it also depends on the geometry of the waveguide.

3.3.2 Dielectric-lined waveguide

The addition of two dielectric slabs to a rectangular waveguide, lined at the top and the bottom, as illustrated in Figure 3.5, modifies the relations and figures of merit mentioned in §3.3.1. The cross-section of a dielectric-lined waveguide (DLW) can be divided into three homogeneous subregions, based on the permittivity of each component, namely the two dielectric components and the vacuum component.

As the DLW is symmetric about the XZ-plane, it is convenient to portray the half cross-section of the DLW, as depicted in Figure 3.6, split into 2 subregions.

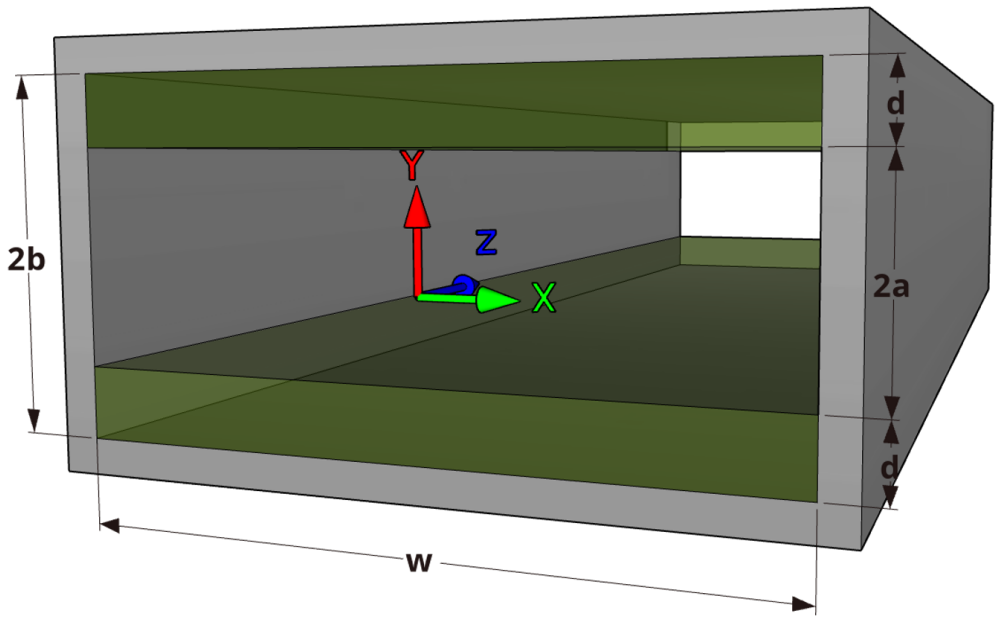

Fig. 3.5: Dielectric-lined waveguide.

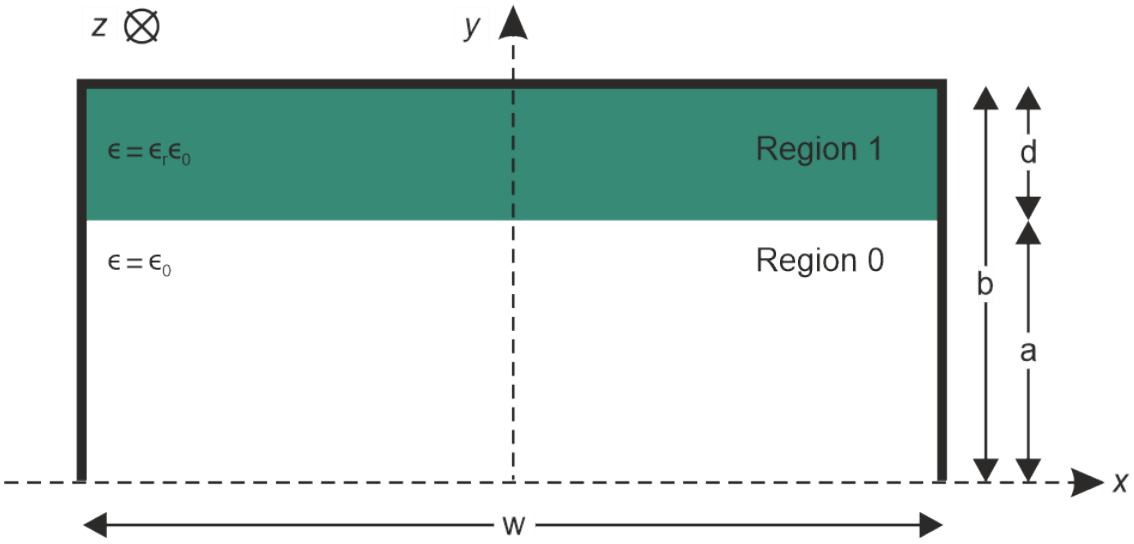

Fig. 3.6: Half cross-section of the DLW. The two subregions are determined by the corresponding permittivity, with Region 0 defining the vacuum component of $\epsilon = \epsilon_0$, and Region 1 defining the dielectric component of $\epsilon = \epsilon_r\epsilon_0$.

Region 0 corresponds to the vacuum component of $\epsilon = \epsilon_0$ and half height of a, while Region 1 corresponds to the dielectric component of $\epsilon = \epsilon_r\epsilon_0$ and thickness d. The equivalent half height of the hollow waveguide would be $b = a + d$.

A new set of boundary conditions are introduced due to dielectric-vacuum interface at $y = a$. The supported modes in a DLW are neither TE nor TM modes as discussed for a hollow metallic waveguide, but a hybrid combination of the two [94]. The supported modes are classified to Longitudinal Section Electric (LSE), where there is no electric field component normal to the dielectric-vacuum interface, and Longitudinal Section Magnetic (LSM), where there is no magnetic component normal to the dielectric-vacuum interface. For the scope of the thesis, only the analysis for the LSM modes will be discussed here.

For the solution of the LSM modes, the transverse resonance technique is employed, with the use of an electric Hertz vector potential. Since the divergence of the magnetic field for a homogeneous source-free region is equal to zero, $\nabla \cdot \mathbf{H} = 0$, assuming a $e^{i\omega t}$ time dependence, the magnetic field can be expressed as the curl of an electric type Hertz vector potential [94]

$$\mathbf{H} = i\omega\epsilon\nabla \times \mathbf{\Pi}_{\boldsymbol{e}}, \tag{3.52}$$

and from Equation 3.4 the electric field yields

$$\mathbf{E} = \nabla \times \nabla \times \mathbf{\Pi_e}, \tag{3.53}$$

where

$$\mathbf{\Pi_e}(x, y, z) = \hat{y}\, \psi_e(x, y) e^{-\gamma z} \tag{3.54}$$

is the electric type Hertz vector potential. Wave propagation along the z-direction is assumed, with a propagation constant of $\gamma = \alpha + i\beta$, which must be the same in both regions. With the implementation of the dielectric slab, the relative permittivity becomes a function of y, in the form of a step function, defined by

$$\epsilon_r(y) = \begin{cases} 1, & 0 < y < a \\ \epsilon_r, & a < y < b \end{cases} \tag{3.55}$$

Because of the discontinuity of the relative permittivity along the dielectric-vacuum interface, the Hertz vector potential is directed along the same direction, which in this case is the y-direction.

The solutions for the LSM modes can be classified into symmetrical (even) and anti-symmetrical (odd) modes. Even and odd refer to the way the E_y component varies with y about the symmetry plane at $x = 0$. For the even modes

$$\left.\frac{\partial E_y}{\partial y}\right|_{x=0} = 0, \tag{3.56}$$

and, since E_z is proportional to this derivative, the tangential electric field vanishes on the $y = 0$ plane for the even solutions. Therefore, an electric wall in the XZ-plane can be implied. A Hertz vector potential is defined, for each region, satisfying the boundary conditions, given by

$$\Psi_{enm} = \begin{cases} A_{nm} \sin\left[\dfrac{m\pi}{w}\left(x + \dfrac{w}{2}\right)\right] \cos\left[k^0_{y_{nm}} y\right], & 0 < y < a \\ B_{nm} \sin\left[\dfrac{m\pi}{w}\left(x + \dfrac{w}{2}\right)\right] \cos\left[k^1_{y_{nm}} (b - y)\right], & a < y < b \end{cases} \tag{3.57}$$

where A_{nm}, B_{nm} are amplitude constants and $k^0_{y_{nm}}$, $k^1_{y_{nm}}$ the transverse propagation constants in Region 0 and Region 1, respectively. For the odd modes,

$$\left.\frac{\partial E_y}{\partial y}\right|_{x=0} \neq 0, \tag{3.58}$$

meaning, there is a non-zero tangential component of the electric field, on the $y = 0$ plane. Consequently, a magnetic wall is implied in the XZ-plane, with the Hertz vector potential defined as

$$\Psi_{enm} = \begin{cases} A_{nm} \sin\left[\dfrac{m\pi}{w}\left(x + \dfrac{w}{2}\right)\right] \sin\left[k^0_{y_{nm}} y\right], & 0 < y < a \\ B_{nm} \sin\left[\dfrac{m\pi}{w}\left(x + \dfrac{w}{2}\right)\right] \cos\left[k^1_{y_{nm}}(b - y)\right], & a < y < b \end{cases} \tag{3.59}$$

As only propagating waves are considered, the imaginary part of the propagation constant will be considered, $\gamma = i\beta$. The transverse propagation constants can be expressed in terms of the longitudinal propagation constant as

$$k^0_{y_{nm}} = \sqrt{k^2 - \left(\frac{m\pi}{w}\right)^2 - {\beta_{nm}}^2}, \tag{3.60}$$

$$k^1_{y_{nm}} = \sqrt{\epsilon_r k^2 - \left(\frac{m\pi}{w}\right)^2 - {\beta_{nm}}^2}, \tag{3.61}$$

for both symmetries. The notation (m, n) will be omitted for conciseness. The EM field components of the LSM mode can then be obtained by substituting Equation 3.57 and 3.59 into Equation 3.52 and 3.53.

Even modes

For the even modes ($n = 0, 2, 4, ...$), the EM field components are given by

$$E_x = \begin{cases} A\dfrac{m\pi}{w} k^0_y \cos\left[\dfrac{m\pi}{w}\left(x + \dfrac{w}{2}\right)\right] \sin\left[k^0_y y\right] e^{-i\beta z}, & 0 < y < a \\ B\dfrac{m\pi}{w} k^1_y \cos\left[\dfrac{m\pi}{w}\left(x + \dfrac{w}{2}\right)\right] \sin\left[k^1_y (b - y)\right] e^{-i\beta z}, & a < y < b \end{cases} \tag{3.62}$$

$$E_y = \begin{cases} A{k_c}^2 \sin\left[\dfrac{m\pi}{w}\left(x + \dfrac{w}{2}\right)\right] \cos\left[k^0_y y\right] e^{-i\beta z}, & 0 < y < a \\ B{k_c}^2 \sin\left[\dfrac{m\pi}{w}\left(x + \dfrac{w}{2}\right)\right] \cos\left[k^1_y (b - y)\right] e^{-i\beta z}, & a < y < b \end{cases} \tag{3.63}$$

$$E_z = \begin{cases} A(-i\beta)k_y^0 \sin\left[\frac{m\pi}{w}\left(x+\frac{w}{2}\right)\right] \sin\left[k_y^0 y\right] e^{-i\beta z}, & 0 < y < a \\ B(i\beta)k_y^1 \sin\left[\frac{m\pi}{w}\left(x+\frac{w}{2}\right)\right] \sin\left[k_y^1 (b-y)\right] e^{-i\beta z}, & a < y < b \end{cases} \tag{3.64}$$

$$H_x = \begin{cases} -A\omega\epsilon_0\beta \sin\left[\frac{m\pi}{w}\left(x+\frac{w}{2}\right)\right] \cos\left[k_y^0 y\right] e^{-i\beta z}, & 0 < y < a \\ -B\omega\epsilon_r\epsilon_0\beta \sin\left[\frac{m\pi}{w}\left(x+\frac{w}{2}\right)\right] \cos\left[k_y^1 (b-y)\right] e^{-i\beta z}, & a < y < b \end{cases} \tag{3.65}$$

$$H_y = 0 \tag{3.66}$$

$$H_z = \begin{cases} A(i\omega\epsilon_0)\frac{m\pi}{w} \cos\left[\frac{m\pi}{w}\left(x+\frac{w}{2}\right)\right] \cos\left[k_y^0 y\right] e^{-i\beta z}, & 0 < y < a \\ B(i\omega\epsilon_r\epsilon_0)\frac{m\pi}{w} \cos\left[\frac{m\pi}{w}\left(x+\frac{w}{2}\right)\right] \cos\left[k_y^1 (b-y)\right] e^{-i\beta z}, & a < y < b \end{cases} \tag{3.67}$$

where ${k_c}^2 = (m\,\pi/w)^2 + \beta^2$. At the dielectric-vacuum interface, $y = a$, the tangential electric and magnetic field components must be continuous [93]. Evaluating E_z and H_x at $y = a$ for both regions, the constant relations are obtained

$$-Ak_y^0 \sin[k_y^0 a] = Bk_y^1 \sin[k_y^1 (b-a)], \tag{3.68}$$

$$A\cos[k_y^0 a] = B\epsilon_r \cos[k_y^1 (b-a)]. \tag{3.69}$$

Dividing the Equations 3.68 and 3.69, the dispersion relation yields

$$k_y^1 \sin[k_y^1 (b-a)] \cos[k_y^0 a] = -\epsilon_r k_y^0 \sin[k_y^0 a] \cos[k_y^1 (b-a) \tag{3.70}$$

which is a function of frequency. In conjunction with Equation 3.60 and 3.61, the dispersion relation is solved numerically at each frequency, and the allowed values of β, k_y^0 and k_y^1 are determined. From Equation 3.68/3.69, the ratio of the coefficients A and B may be obtained.

Odd modes

For the odd modes ($n = 1, 3, 5, ...$), the EM field components are obtained by substituting Equation 3.59 into Equation 3.52 and 3.53

$$E_x = \begin{cases} A\frac{m\pi}{w}k_y^0 \cos\left[\frac{m\pi}{w}\left(x+\frac{w}{2}\right)\right] \cos\left[k_y^0 y\right] e^{-i\beta z}, & 0 < y < a \\ B\frac{m\pi}{w}k_y^1 \cos\left[\frac{m\pi}{w}\left(x+\frac{w}{2}\right)\right] \sin\left[k_y^1 (b-y)\right] e^{-i\beta z}, & a < y < b \end{cases} \tag{3.71}$$

$$E_y = \begin{cases} A{k_c}^2 \sin\left[\frac{m\pi}{w}\left(x+\frac{w}{2}\right)\right] \sin\left[k_y^0 y\right] e^{-i\beta z}, & 0 < y < a \\ B{k_c}^2 \sin\left[\frac{m\pi}{w}\left(x+\frac{w}{2}\right)\right] \cos\left[k_y^1 (b-y)\right] e^{-i\beta z}, & a < y < b \end{cases} \tag{3.72}$$

$$E_z = \begin{cases} A(-i\beta)k_y^0 \sin\left[\frac{m\pi}{w}\left(x+\frac{w}{2}\right)\right] \cos\left[k_y^0 y\right] e^{-i\beta z}, & 0 < y < a \\ B(-i\beta)k_y^1 \sin\left[\frac{m\pi}{w}\left(x+\frac{w}{2}\right)\right] \sin\left[k_y^1 (b-y)\right] e^{-i\beta z}, & a < y < b \end{cases} \tag{3.73}$$

$$H_x = \begin{cases} -A\omega\epsilon_0\beta \sin\left[\frac{m\pi}{w}\left(x+\frac{w}{2}\right)\right] \sin\left[k_y^0 y\right] e^{-i\beta z}, & 0 < y < a \\ -B\omega\epsilon_r\epsilon_0\beta \sin\left[\frac{m\pi}{w}\left(x+\frac{w}{2}\right)\right] \cos\left[k_y^1 (b-y)\right] e^{-i\beta z}, & a < y < b \end{cases} \tag{3.74}$$

$$H_y = 0 \tag{3.75}$$

$$H_z = \begin{cases} A(i\omega\epsilon_0)\frac{m\pi}{w} \cos\left[\frac{m\pi}{w}\left(x+\frac{w}{2}\right)\right] \sin\left[k_y^0 y\right] e^{-i\beta z}, & 0 < y < a \\ B(i\omega\epsilon_r\epsilon_0)\frac{m\pi}{w} \cos\left[\frac{m\pi}{w}\left(x+\frac{w}{2}\right)\right] \cos\left[k_y^1 (b-y)\right] e^{-i\beta z}. & a < y < b \end{cases} \tag{3.76}$$

Applying the boundary condition at $y = a$, the constant relations yield

$$Ak_y^0 \cos[k_y^0 a] = Bk_y^1 \sin[k_y^1 (b-a)], \tag{3.77}$$

$$A \sin[k_y^0 a] = B\epsilon_r \cos[k_y^1 (b-a)], \tag{3.78}$$

with the corresponding dispersion relation

$$k_y^1 \sin[k_y^1 (b-a)] \sin[k_y^0 a] = \epsilon_r k_y^0 \cos[k_y^0 a] \cos[k_y^1 (b-a)]. \tag{3.79}$$

The phase and group velocity cannot be written with an analytic expression, as in the case of a hollow metallic waveguide, but the general relation still applies

$$v_p = \frac{\omega}{\beta}, \tag{3.80}$$

$$v_g = \frac{\partial\,\omega}{\partial\beta}, \tag{3.81}$$

with the characteristic impedance given by [96]

$$Z_{\mathrm{LSM}} = \begin{cases} \dfrac{k_y^0}{\epsilon_0\omega}, & 0 < y < a \\ \dfrac{k_y^1}{\epsilon_r\epsilon_0\omega}, & a < y < b. \end{cases} \tag{3.82}$$

3.4 Terahertz-electron interaction

In this section, the interaction of travelling charged particles, particularly electrons, with co-propagating THz EM waves is discussed.

Particles of charge q, and mass m_0 in an EM field, experience the Lorentz force given by [97, 98]

$$\frac{d\mathbf{p}}{dt} = m_0\boldsymbol{\alpha} = q\left(\mathbf{E} + \mathbf{v} \times \mathbf{B}\right), \tag{3.83}$$

where $\boldsymbol{\alpha}$ is the acceleration of the particle, and $\mathbf{v}$ the particle velocity. In the relativistic regime, as the particle velocity gets closer to the speed of light, the expression for the Lorentz force is modified. The particle velocity can be expressed in terms of the relativistic momentum and the particle energy. A relativistic electron of total energy K, has a velocity amplitude of [97]

$$v = c\sqrt{1 - \frac{1}{\gamma^2}}, \tag{3.84}$$

where c is the speed of light and γ the Lorentz factor, given by

$$\gamma = \frac{K}{m_0c^2} = \frac{1}{\sqrt{1-\beta^2}}, \tag{3.85}$$

where $\beta = v/c$, not to be confused with the propagation constant discussed in §3.3. The total energy of the particle of the particle can be expressed in terms of the relativistic momentum

$$K^2 = (\gamma m_0c^2)^2 = (m_0c^2)^2 + \mathbf{p}\cdot\mathbf{p}c^2 \tag{3.86}$$

where

$$\mathbf{p} = \gamma m_0 c\beta. \tag{3.87}$$

The correction of the relativistic acceleration of a charged particle can be ob-

tained from the equation of motion [98]

$$\frac{d\mathbf{p}}{dt} = \frac{d(m_0\gamma\mathbf{v})}{dt} = \frac{d(m_0\gamma)}{dt} + m_0\gamma\frac{d\mathbf{v}}{dt} = m_0\gamma^3(\boldsymbol{\alpha}\cdot\beta)\beta + m_0\gamma\boldsymbol{\alpha}. \tag{3.88}$$

Combining Equation 3.88 and Equation 3.83, then the acceleration experienced by some charged particle of charge q yields [98]

$$\boldsymbol{\alpha} = \frac{q}{m_0\gamma}\left(\mathbf{E} + c\beta\times\mathbf{B} - (\mathbf{E}\cdot\beta)\beta\right). \tag{3.89}$$

The acceleration of a charged particle is inversely proportional to the Lorentz factor, and there is an extra term that accounts for the EM field transformation from the EM reference to the particle reference. For the classical model, where $\beta^2 \to 0$ and $\gamma \to 1$, the classical acceleration written in Equation 3.83 is recovered.

Chapter 4

Experimental and simulation techniques

In this chapter, an overview of the different ultrafast laser systems and electron beam facilities is provided. Moreover, a description of the experimental techniques, equipment and DLW structures employed is included as well as the simulation techniques and tools used for the numerical solution of the dispersion relation and for the simulation of the THz-electron interaction.

4.1 Experimental techniques

4.1.1 Ultrafast laser systems

1 mJ regenerative amplifier

The 1 mJ regenerative amplifier system was composed of several lasers, including a continuous-wave Diode-Pumped Solid-State (DPSS) pump laser (Millenia, Spectra-Physics), a Q-switched pump laser (Empower, Spectra-Physics), a low pulse-energy oscillator laser (Tsunami, Spectra-Physics) and a regenerative amplifier (Spitfire Pro, Spectra-Physics).

The output of the regenerative amplifier produces 100 fs FWHM pulses with a centre wavelength of 800 nm, a maximum pulse energy of 1 mJ at a 1 kHz repetition rate. A frequency-doubled, continous-wave Nd:YAG laser, emitting at 532 nm (Millenia, Spectra-Physics) acts as an optical pump for a Ti:sapphire (Ti:Al_2O_3) oscillator laser (Tsunami, Spectra-Physics). After successful mode-locking [56, 99],

low-energy ultrafast light pulses with 100 fs FWHM duration emerge from the oscillator laser, centered at 800 nm with a repetition rate of approximately 80 MHz.

The output of the oscillator laser acts as seed for the regenerative amplifier (Spitfire Pro, Spectra-Physics). Regenerative amplifiers use chirped pulse amplification (CPA). This technique exploits the dispersion where component frequencies are separated in time, thus chirped. In that way, before the light pulse passes through the gain medium of the amplifier, it first gets dispersed and temporally stretched by a dispersive delay line consisting of a diffraction-grating pair arrangement. Therefore, the peak power is much lower as the same pulse energy is now spread out over a longer period of time. The stretched pulse is then amplified and recompressed by a second grating pair. CPA allows light amplification that would normally cause damage to the optical components involved. CPA takes place in the regenerative amplifier enclosure with the pump laser (Empower, Spectra-Physics) used as the optical pump as depicted in Figure 4.1.

The output from the regenerative amplifier is linearly polarised ultrafast laser pulses with 100 fs FWHM duration, a centre wavelength of 800 nm, with approximately 1 mJ pulse energy at a repetition rate of 1 kHz. This laser system is housed in the Photon Science Institute (PSI), in the Alan Turing Building of The University of Manchester.

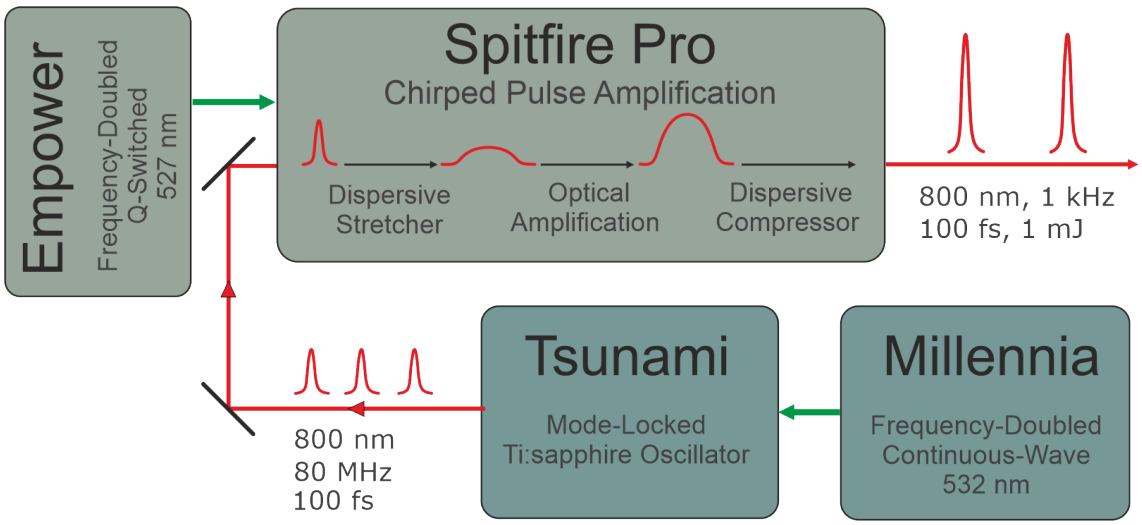

Fig. 4.1: Schematic diagram of the laser system. A continuous-wave laser (Millennia) pumps the mode-locked Ti:sapphire oscillator (Tsunami). The generated 100 fs long pulses get amplified by CPA in a regenerative amplifier (Spitifire Pro) pumped by a Q-switched laser (Empower).

Terawatt laser system

This laser system is housed at the Laser, Terahertz and Terawatt Experiments (LATTE) laboratory, located in Daresbury. The LATTE lab houses a customised terawatt (TW) laser system [100] that is capable of producing up to 800 mJ laser pulses at 10 Hz repetition rate with a centre wavelength of 800 nm and Fourier-limited pulse duration of 60 fs FWHM. The TW laser system employed a Ti:sapphire oscillator (Micra, Coherent) which produced 800 nm, 30 fs, 4 nJ pulses at a repetition rate of 83 MHz. These pulses acted as a seed to a Ti:sapphire based regenerative amplifier (Legend, Cohrent) providing 800 nm 50 fs, 2 mJ pulses at a 1 kHz repetition rate. The output of the regenerative amplifier was stretched and routed through a multipass Ti:sapphire amplifier (MPA). Two frequency-doubled Nd:YAG lasers (Continuum Powerlite II), producing 532 nm, 10 ns, 1.5 J pulses at 10 Hz repetition rate acted as a pump for amplification, which, following recompression to 60 fs, resulted in TW peak powers at 10 Hz repetition rate. The compressor for the MPA was located in a separate vacuum chamber, in order to prevent the breakdown of air when the pulses undergo compression. The output of the MPA was then delivered to the electron-beam experimental test user facility area via a metallic beam transport line under vacuum.

Cockcroft laser system

The Cockcroft laser system is a dual-stage regenerative amplifier, delivering ultrafast laser pulses of 35 fs FWHM duration, centre wavelength of 800 nm with an average pulse energy of 11 mJ at a tunable repetition rate. This system consists of a Ti:Sapphire oscillator (Synergy, Spectra-Physics) which generates the initial pulse train. Two regenerative amplification stages within the Spitfire ACE then amplify one pulse out of this train. Each amplification is pumped by a Q-switched laser system emitting at 527 nm (Ascend-60, Spectra-Physics). The Synergy and the two Ascend lasers are cooled with a closed-loop chiller system, for greater condition stability within the laboratory. The output beam is a horizontally polarised, TEM_{00} mode beam with a 12 mm $1/e^2$ diameter.

The Cockcroft laser system is housed at the LATTE laboratory, located in Daresbury. This laser system was dedicated to the 100 keV experimental programme. A

small fraction of the laser beam was used for photo-excitation of 100 keV electrons after Second Harmonic Generation (SHG), while the rest of the laser beam was used for THz generation and detection.

4.1.2 THz time-domain spectroscopy

Terahertz Time-Domain Spectroscopy (THz-TDS) is a non-contact technique used for characterising the far-infrared response of materials and devices over a wide frequency spectrum. THz-TDS is based on measuring the transmitted electric field as a function of time. This is realised using the experimental pump-probe technique as depicted in Figure 4.2. The pulse is split in two beams, the pump and the probe. The more intense pump beam is used to generate the THz radiation which is then mapped in the time-domain by the much weaker probe beam. By introducing a delay to either the pump or probe laser pulse, it is possible to vary the path length, thus temporally sample the electric field of the THz pulse. The distance, d, the delay stage can travel and the minimum step size are the only mechanical limitations.

By measuring the changes in both the amplitude and the phase of electric field of the broadband THz pulse induced by the sample, THz-TDS provides information

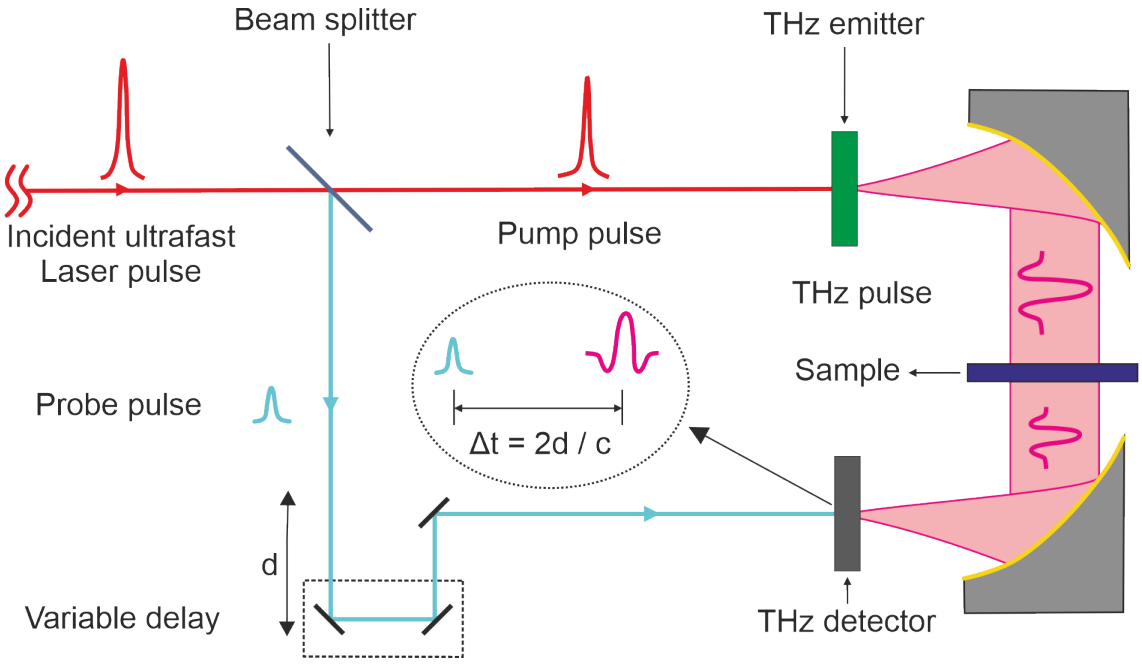

Fig. 4.2: Schematic diagram of a THz time-domain spectroscopy set up, using the pump-probe experimental technique for the generation and detection of THz pulses using ultra-fast laser pulses.

to determine the absorption and the dispersion of the sample over a wide frequency bandwidth. A comparison of the free space reference THz waveform (where no sample is present in the beam path) and the waveform transmitted through the sample allows the determination of the absorption coefficient and the refractive index of the sample as a function of frequency. THz spectroscopy can cover the spectral region from 0.1 to 20 THz (1-0.015 mm), with the majority of work being focused between 0.01 to 3 THz (1 mm to 0.1 mm).

4.1.3 Electro-optic detection

Balanced Electro-Optic (EO) detection was used to map out the electric field component of the THz waveform by exploiting the birefringence in an EO crystal such as ZnTe or GaP. A typical balanced EO detection scheme consists of an EO crystal, a quarter ($\lambda/4$) waveplate, a Wollaston prism and two photodiodes as illustrated in Figure 4.3.

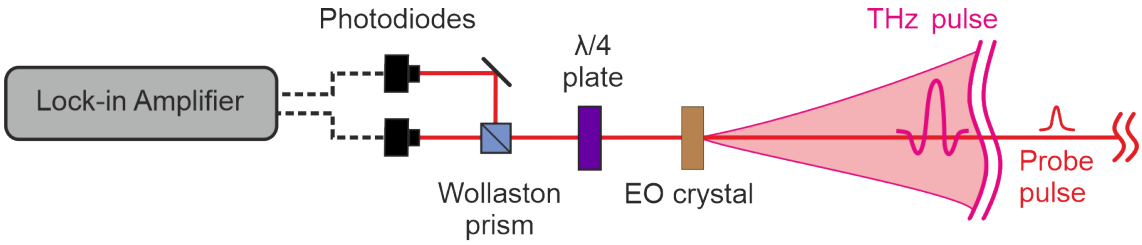

Fig. 4.3: Schematic diagram of a typical EO detection scheme, consisting of an EO crystal, a quarter waveplate, a Wollaston prism and two photodiodes.

The incident THz electric field induces birefringence in the EO crystal, through the Pockels' effect. As a result, the polarisation state of the optical probe beam that is co-propagating with the THz pulse in the EO crystal, is modified. This phase modulation of the probe beam is proportional to the THz electric field amplitude. The refractive indices n_1, n_2, for light polarised along two different axes of the EO crystal are

$$n_1 = n_0 + \frac{1}{2}\left({n_0}^3\, r E_{\mathrm{THz}}\right); \qquad n_2 = n_0 - \frac{1}{2}\left({n_0}^3\, r E_{\mathrm{THz}}\right), \tag{4.1}$$

where n_0 is the refractive index of the probe beam in the EO crystal, r the electro-optic coefficient of the crystal and E_{THz} the THz electric field amplitude. Polarised

light propagating through a crystal of thickness L, will experience phase shift of

$$\phi_1 = \frac{2\pi}{\lambda} n_1 L; \qquad \phi_2 = \frac{2\pi}{\lambda} n_2 L, \tag{4.2}$$

with a relative phase shift $\Gamma = \phi_1 - \phi_2$. Here λ is the wavelength of the probe beam. With no THz radiation applied on the EO crystal, the probe beam, which is initially linearly polarised, would pass through with no phase shift. Consequently, upon the the $\lambda/4$ waveplate, which is set with the optic axis at 45° to incident polarisation, it becomes circularly polarised. The probe beam then gets separated into two orthogonally polarised components by the Wollaston prism. The two components are measured by the two photodiodes after the Wollaston prism. The measured signal is the difference between the two photodiodes readings, which is equal to zero when THz radiation is absent, hence balanced.

However, when THz radiation is propagating through the EO crystal, the probe beam would be elliptically polarised and this will have as a result two unequal components emerging from the Wollaston prism. This measured difference is proportional to the applied THz electric field, E_{THz}. Planken *et al.* [76] have demonstrated that the relative phase shift Γ is related by the ratio of the difference in measured intensities of the two photodiodes, ΔI, and with the total intensity of the probe beam, I_0. Therefore, rearranging Equations (4.1) and (4.2), the E_{THz} is given by

$$E_{\mathrm{THz}} = \frac{\Delta I}{I_0} \frac{\lambda}{2\pi\, {n_0}^3\, r\, L} \frac{1}{t}, \tag{4.3}$$

where t is the Fresnel transmission coefficient which for normal incidence is equal to

$$t = \frac{2\, n_i}{n_i + n_{\mathrm{THz}}}, \tag{4.4}$$

where n_i and n_{THz} are the refractive indices of air and of the EO crystal respectively, at THz frequencies. This correction factor takes into account the losses arising from the refractive index mismatch between the crystal-air interface, resulting in reflections of the THz radiation.

4.2 Electron beam facilities

4.2.1 The Compact Linear Accelerator for Research and Applications

The Compact Linear Accelerator for Research and Applications (CLARA) is a research facility based at Daresbury Laboratory [101]. The accelerator had an experimental area, Beam Area 1 (BA1), in which experiments could be performed during the exploitation time. At the time, January 2019, CLARA provided electron bunches with energy of 35 MeV. A block diagram of the user area BA1 can be seen in Figure 4.4, with the main optics and diagnostics illustrated.

A copper cathode is excited by 266 nm, 2 ps FWHM photoinjector laser pulses at a repetition rate of 10 Hz, producing electron bunches that are initially accelerated in a 3 GHz RF gun to 5 MeV. Subsequently, the bunches are transported to a Linear Accelerator (LINAC) for further acceleration up to 35 MeV. The relativistic electron bunches are transported to BA1 using a magnetic dog leg. The phase of the RF LINAC is configurable, so that the energy chirp of the bunch is adjusted accordingly. BA1 is isolated from the rest of the beamline by a concrete shield wall.

In Figure 4.4, the beam optics and diagnostics along with the vacuum chamber are illustrated. The chamber was provided to the user to install the necessary optical

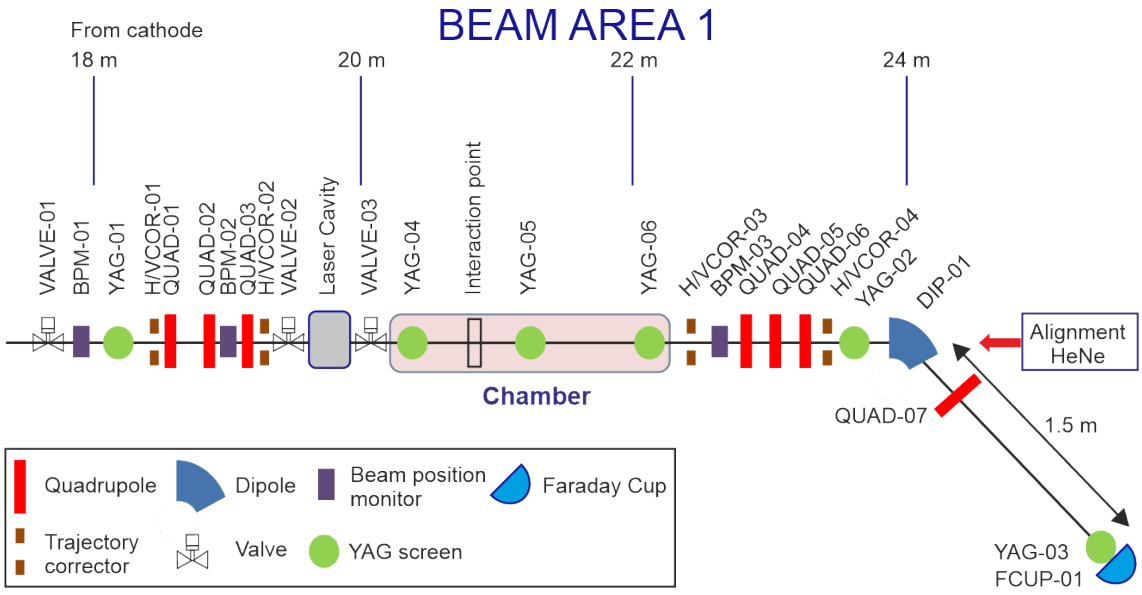

Fig. 4.4: Block diagram of beam area 1, the experimental area used during the exploitation time of the CLARA electron accelerator.

components and structures, for the undergoing experiment. A number of quadrupole magnets allowed for focussing or imaging of the electron bunches through the interaction region and onto the energy spectrometer. At the exit of the chamber, a downstream quadrupole triplet was used to match the beam into the energy spectrometer. The energy spectrometer consists of the dipole, a final quadrupole magnet (QUAD-07) and a YAG screen (YAG-03). The charge of the electron beam could be varied by adjusting the intensity of the photo-injector laser (not shown). Next to the chamber, an optical table was installed, giving the option of having an optical set up for the ongoing experiment. The diagram of the optical set up for the work on CLARA, is given in Chapter 6.

4.2.2 100 keV electron gun

The 100 keV electron gun system employed a commercial electron gun, EGH-8121A from Kimball Physics. This system was capable of producing electron bunches with an energy range of between 10 keV and 100 keV with an increment of 10 keV. The gun consisted of two main sections; a tetrode-configured electron source and a focus-deflection system as can be seen in Figure 4.5.

The first section comprises a bootstrap cathode, a control grid aperture (Wehnelt), a variable first anode and a grounded second anode. The particles are generated and accelerated to their final kinetic energy in this section of the gun, which is contained in the High Voltage (HV) shield. The HV shield is a pod-shaped structure, supplied by high voltage and it is mounted on a large tapered insulator.

The cathode used was a 200 μm by 200 μm lanthanum hexaboride (LaB6) crystal. The electron gun had the capability of being operated in either thermionic emission mode or photo-emission mode or in a combination of the two. For initial set-up and alignment, the thermionic mode was used, and for the generation of a few-picoseconds electron bunches, photo-emission mode was used by employing ultrashort laser pulses with photon energy higher than the bandgap of the crystal ($<$460 nm). The Wehnelt cylinder acted as a control grid, adjusting the amount of charge that would eventually reach the accelerating stage of the gun. A negative bias voltage with respect to the bootstrap cathode would eventually suppress the extraction field from the first anode and photo-emitter.

The first anode consisted of a short tube with an aperture at the end. A variable

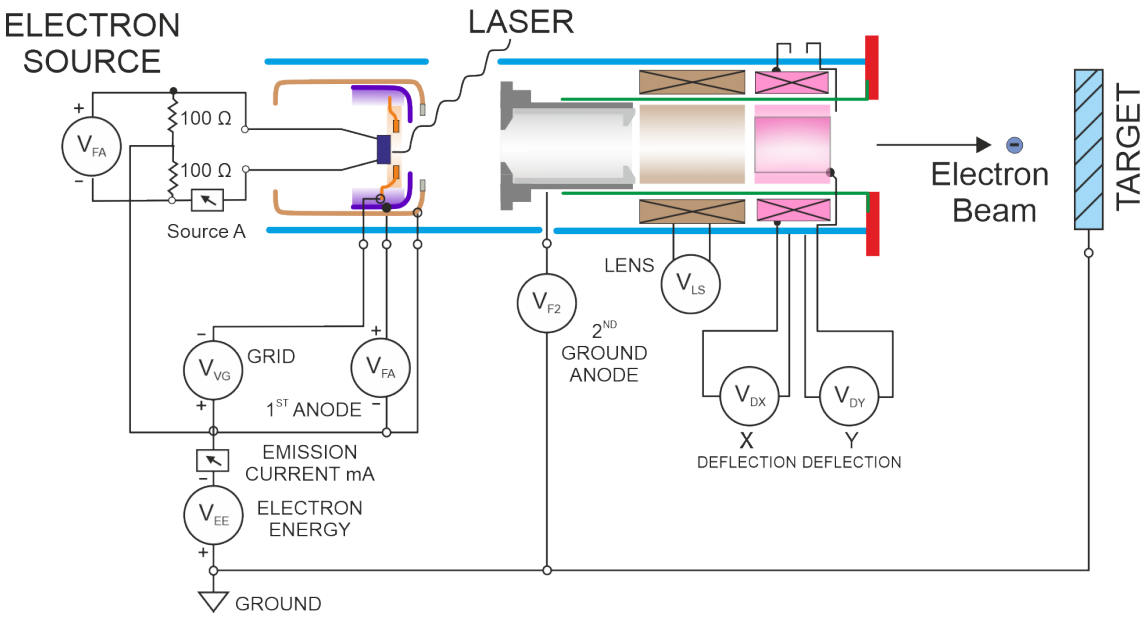

Fig. 4.5: Block diagram of the 100 keV electron gun taken from [102].

potential was applied on the first anode, creating a potential difference between the cathode and the photo-emitter, also known as extraction field. The extraction field would determine the number of electrons getting extracted from the cathode thus the emission current. The extraction field would also determine the path of the electrons and the resulting divergence of the beam. The second anode is a separate grounded tube, with an aperture at both ends. The potential difference between the cathode and the second anode would determine the final kinetic energy of the electrons.

The particle beam is further focused and positioned in the second section of the gun. Built-in magnetic focusing lens and deflecting element were used for the imaging of the electron beam onto the detector. A solenoid magnet was used as the focussing element, and two deflecting coil magnets to steer the beam in the vertical and horizontal direction, respectively. The lens current required to produce a focus at a certain distance is dependent on the beam energy. The same applied for the positioning of the beam using the deflecting coils.

The electron gun system is attached to a vacuum chamber and kept under vacuum. The electron gun system and the chamber could be isolated from each other by manual-driven gate valves, so the chamber could be vented while the electron gun system was kept under vacuum. On the other end of the chamber, a Microchannel Plate (MCP) detector was attached to detect the electrons. The MCP acted as

an amplifier of the number of electrons through secondary electron emission, which was then detected on a phosphor screen with a CCD camera (mvBlueCOUGAR-X, MatrixVision). The MCP plate was kept at a bias voltage of 1 kV, in order to accelerate the secondary electrons onto the phosphor screen, which was kept at a bias voltage of 5 kV. The voltage potential difference between the MCP exit to the screen, resulted in gaining factors of up to 10^4 within a single plate. The electron gun system was operated at photo-emission mode, driven by a UV pulse at 400 nm, producing electrons at energy of 100 keV, unless stated otherwise.

4.2.3 DLW structures

The DLW structures were designed to manipulate 100 keV and 35 MeV electron beams, driven with THz pulses at central frequency of approximately 0.5 THz. As illustrated in Figure 4.6, the structure consisted of two major sections, the coupler and the waveguide. The structures were manufactured by the Millimetre-Wave Technology (MMT) Group of the Rutherford Appleton Laboratory (RAL)-Space.

The coupler is a copper linearly tapered horn with an entrance aperture width w_c, height b_c and length L_c. The coupler flares down to aperture width of w and aperture height of $2b$. The purpose of the coupler was to efficiently couple the vertically polarised free space THz pulse into the desired LSM_{nm} waveguide mode.

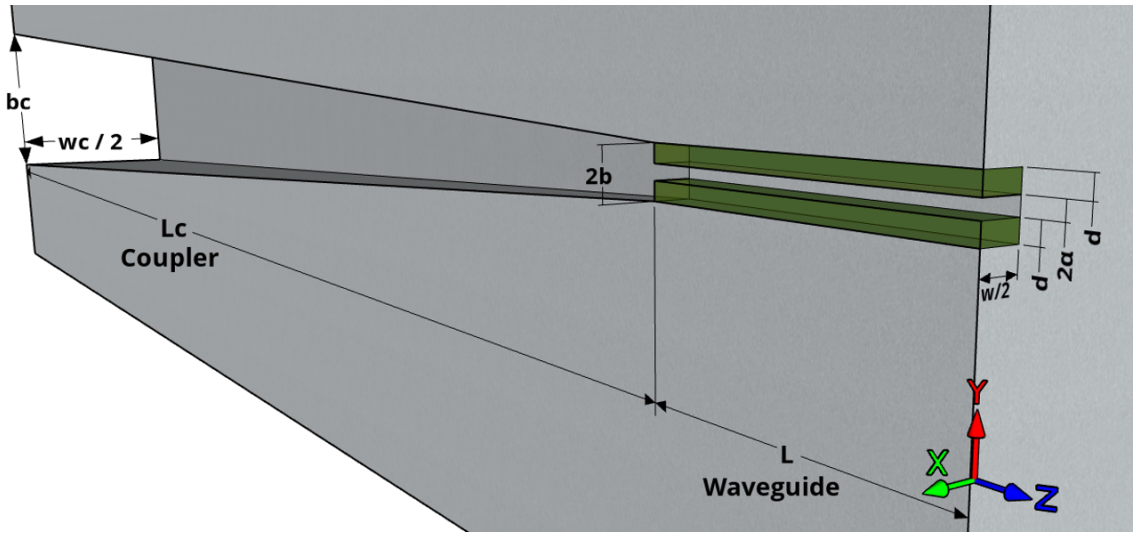

Fig. 4.6: Cross-sectional view about the y-axis of the DLW structure consisted of the linearly tapered coupler and the waveguide lined at the top and bottom with dielectric leaving free space aperture for electron beam propagation along the z-direction.

This also reduced reflections arising from the mismatch between the transverse field distribution of the free space TEM_{mn} Gaussian mode and the LSM_{nm} waveguide mode [103]. The coupler was designed and modelled for the transmission of a broadband THz pulse into the correct mode of the waveguide, centred at approximately 0.5 THz [104]. For the optimisation of the coupler design, pulse propagation simulations through the horn and a small section of the waveguide were performed using the Time Domain Solver in CST Studio Suite [104]. For fixed transverse dimensions, w_c and b_c, mainly limited to manufacturing tolerances, the length of the coupler was investigated in order to maximise the transmission of the LSM_{nm} mode, and minimising the reflections. A collimated broadband THz pulse, centred at 0.5 THz, was considered for the simulations. The simulations were performed in the frequency range from 0.01 to 2 THz in order to cover the relevant spectrum of the excitation pulse. The structure was not designed to couple out the THz radiation, as an additional coupler at the exit would have been required.

The structure was milled with the coupler and the waveguide incorporated in the copper block. The waveguide design was hollow, rectangular copper cavity with the dielectric lining of thickness d, bonded on the top and bottom waveguide walls with glycol phthalate (Crystalbond adhesive). The particular adhesive has been investigated in THz spectroscopic studies [105], showing negligible absorption in the THz regime (0.01 - 6 THz). The dielectric of choice was fused quartz, and it was purchased in sheets of fixed thickness and width with a manufacturing tolerance of $\pm 10\,\mu$m. The relative permittivity ϵ_r of fused quartz in the THz regime has been reported to be 3.81 [106, 107], and this value was considered for all the calculations and data analysis. A free space aperture of height 2α was left for particle-beam propagation. The transverse dimensions of the waveguide w and b as well as the dielectric-thickness d, were tailored to match the phase velocity of the LSM_{nm} mode to the velocity of the copropagating electrons at approximately 0.5 THz. The parameters of the two manufactured DLW structures are summarised in Table 4.1.

Table 4.1: Parameter list of the DLW structures manufactured, designed for the manipulation of 100 keV and 35 MeV electron beams, respectively.

	DLW structure design	
Parameter	100 keV streaking	35 MeV acceleration
2α (μm)	200	575
w (mm)	1	1.2
d (μm)	240	60
L (mm)	5, 10	30
ϵ_r	3.81	3.81
b_c (mm)	5	3.25
w_c (mm)	10	3.18
L_c (mm)	44	23
Operating mode	LSM_{01}	LSM_{11}

4.3 Simulation techniques

In this section, the simulation techniques and modelling tools employed throughout the thesis are described. The numerical solution of the dispersion relation for the LSM_{mn} modes is outlined as well as the evolution of the EM fields inside the DLW. Upon evaluating the transient EM fields inside the transmission line, the THz-electron interaction was modelled, by tracking and updating the 6D phase space evolution of the electron beam.

4.3.1 Propagation constant solver

In a hollow metallic waveguide, for a propagating wave, where $f > f_c$, the phase velocity is typically greater than the speed of light, as Equation 3.48 denotes. The limit of v_p as f approaches f_c equals to infinity, and as f approaches infinity, $v_p = c$. Moreover, the cut-off frequency depends solely on the geometry of the waveguide. The implementation of dielectric slabs, modifies the evaluation of the propagation constant, depending on the choice and the thickness of the dielectric material. Therefore, the v_p of a supported LSM_{nm} mode can be tuned at sub-luminal velocities,

matching the velocity of co-propagating electrons at a certain frequency. Consequently, by implementing dielectric slabs to a metallic waveguide, and tweaking the geometry of the structure, the THz-electron interaction can be optimised.

As discussed in §3.3.2, the longitudinal propagation constant β_{nm}, for the supported LSM_{nm} modes in a DLW, do not have an analytical expression. The dispersion relation has to be solved numerically at every frequency, and then an interpolation is used over a frequency range. A root finding routine was developed in MATLAB, in order to find the solution to the characteristic equations

$$g(f,\beta_{nm}) = k_y^1 \sin[k_y^1(b-a)]\cos[k_y^0 a] + \epsilon_r k_y^0 \sin[k_y^0 a]\cos[k_y^1(b-a)], \quad \text{for } n = 0,2,4,...$$
$$q(f,\beta_{nm}) = k_y^1 \sin[k_y^1(b-a)]\sin[k_y^0 a] - \epsilon_r k_y^0 \cos[k_y^0 a]\cos[k_y^1(b-a)], \quad \text{for } n = 1,3,5,...$$

are function of the transversal wavenumbers k_y^0 and k_y^1, which are functions of f and β_{nm} as denoted in Equations 3.60 and 3.61, respectively. The function $g(f,\beta_{nm})$ corresponds to the even solutions of the LSM_{nm} modes, whereas $q(f,\beta_{nm})$ corresponds to the odd solutions of the LSM_{nm} modes.

Due to the transcendental form of the characteristic equations, for certain given input parameters, n discrete solutions exist, with the higher n-th harmonics appearing at higher frequencies. In this thesis, only the fundamental LSM_{nm} modes are of interest, where $n = 0$, $m = 1$ for the case of the even modes and $n = 1$, $m = 1$ for the case of the odd modes. Therefore, a custom-written root search routine was employed, which tracks the solution of the n-th mode.

The root searching routine uses as input parameters the geometry of the waveguide, namely, the width w, half-vacuum aperture a, the dielectric thickness d, the relative permittivity of the dielectric ϵ_r, the mode index m, and the enquired frequency f. For every set of input parameters, the characteristic equations are evaluated as a function of β. In Figure 4.8, a block diagram illustrating the flowchart of the propagation constant solver algorithm is depicted.

Here as an example, the parameters of the 100 keV structure outlined in Table 4.1 are used, evaluated at $f = 1\,\mathrm{THz}$, and $m = 1$ for each symmetry. The evaluation of the characteristic equations $g(\beta_{n1})$ and $q(\beta_{n1})$ are shown in Figure 4.7(a) and 4.7(b), respectively. In general, the characteristic equations have a real and an imaginary component. However, for the given geometry, $g(\beta_{n1})$ has only a real non-

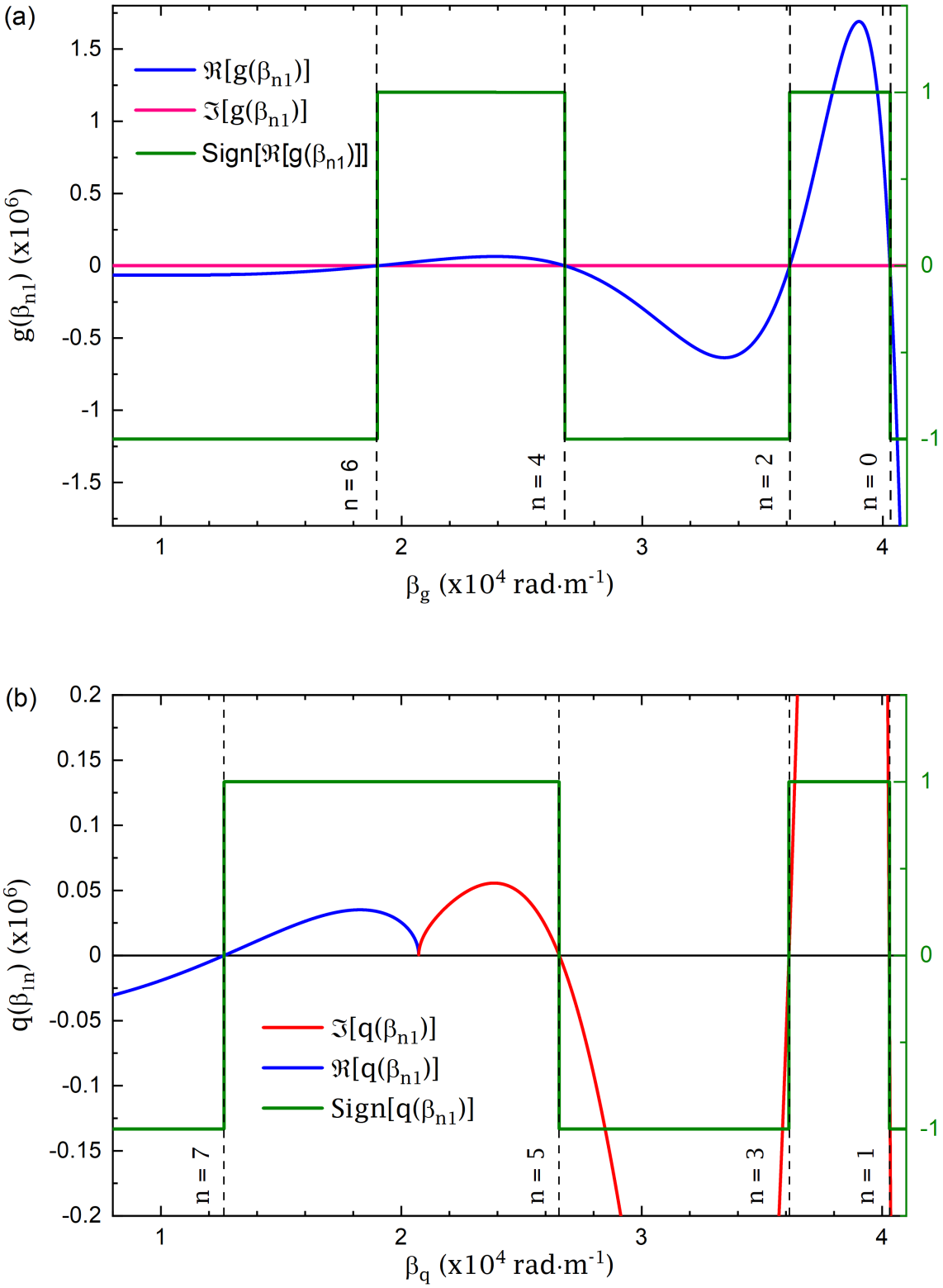

Fig. 4.7: The real (blue) and imaginary part (red) of the characteristic equation (a) $g(\beta_{nm})$ and (b) $q(\beta_{nm})$, evaluated as a function of β_{n1}, at $f = 1\,\mathrm{THz}$. The waveguide geometry of the 100 keV DLW structure, summarised in Table 4.1, was used as input parameters. In green solid line, the sign function of the characteristic equation is shown and in dashed lines, the n-th roots are denoted for each symmetry.

zero component. The characteristic equation $g(\beta_{n1})$ is evaluated at trial range of β_g, and a resolution of $\delta\beta_g$. The maximum value of β_g is set to $2\pi f\sqrt{\epsilon_r}/c$, and $\delta\beta_g$ is arbitrarily chosen. The first solution, where $g(\beta_g) = 0$, corresponds to the fundamental mode of the enquired symmetry, whereas the higher harmonics appear at smaller values of β_g. The analysis here will focus on the solution of the even modes, where similar analysis applies for the odd modes, but with different notation.

To estimate the number of roots and the range in which each root lies, the signum function of $\Re[g(\beta_{n1})]$ is calculated, as depicted in green line in Figure 4.7(a). The signum function returns an array the same size as β_g, where each element is equal to 1 if $g(\beta_g(i)) > 0$, equal to 0 if $g(\beta_g(i)) = 0$ and equal to -1 if $g(\beta_g(i)) < 0$, where i is the index number of the array $\beta_g(i)$. Subsequently, the indices $i^{(n)}$, of which the derivative of the signum function has a non-zero value are found, $\mathrm{Sign}'[g(\beta_g(i^{(n)}))] \neq 0$, where $\beta_g(i^{(n)})$ correspond to an approximation of the n-th root. The interval in which the n-th root lies, is given by

$$\Delta\beta_g^{(n)} = \beta_g(i^{(n)} + 1) - \beta_g(i^{(n)} - 1) = A^{(n)} - B^{(n)},$$

where $A^{(n)}$ and $B^{(n)}$ define the upper and lower bound of $\Delta\beta_g^{(n)}$.

The Bisection method was then employed in order to numerically find the n-th root which is bracketed in the $\Delta\beta_g^{(n)}$ interval. The Bisection method is also known as the Bolzano's or Half Interval method, and it was chosen as it is a relatively simple to implement routine, it is always convergent, by increasing the number of iteration, N_{iter}, yields to more accurate solution and the error bound is controllable [108]. The Bisection method was also found to be computationally efficient in the case of multiple roots.

As illustrated in the flowchart in Figure 4.8, the principle behind the Bisection method is the intermediate theorem for continuous functions [109]. The midpoint of the interval $\Delta\beta_g^{(n)}$ is calculated, $C^{(n)}$, then if the product $g(A^{(n)}) \cdot g(C^{(n)})$ is negative, the root exists in the interval $[A^{(n)}, C^{(n)}]$. In the next iteration, the upper bound is replaced by $B^{(n)} = C^{(n)}$, and a new midpoint is evaluated. If the product is positive, then the lower bound of the interval is replaced by $A^{(n)} = C^{(n)}$, accordingly. At each iteration, the interval is divided, until the solution found is smaller than a user-defined tolerance, $g(C^{(n)}) < \mathrm{tol}$, or when the process reaches the maximum

number of iterations, N_{iter}. When a solution satisfies either of the two conditions, the value of the propagation constant is given as an output $\beta_{nm}(f) = C^{(n)}$. The Bisection method is repeated for all n intervals. The propagation constant solver algorithm was nested in a for-loop, executed for each inquired frequency.

In Figure 4.9, the propagation constant of the first 6 LSM_{n1} modes are plotted, as a function of frequency. The black dashed and dotted lines, indicate the

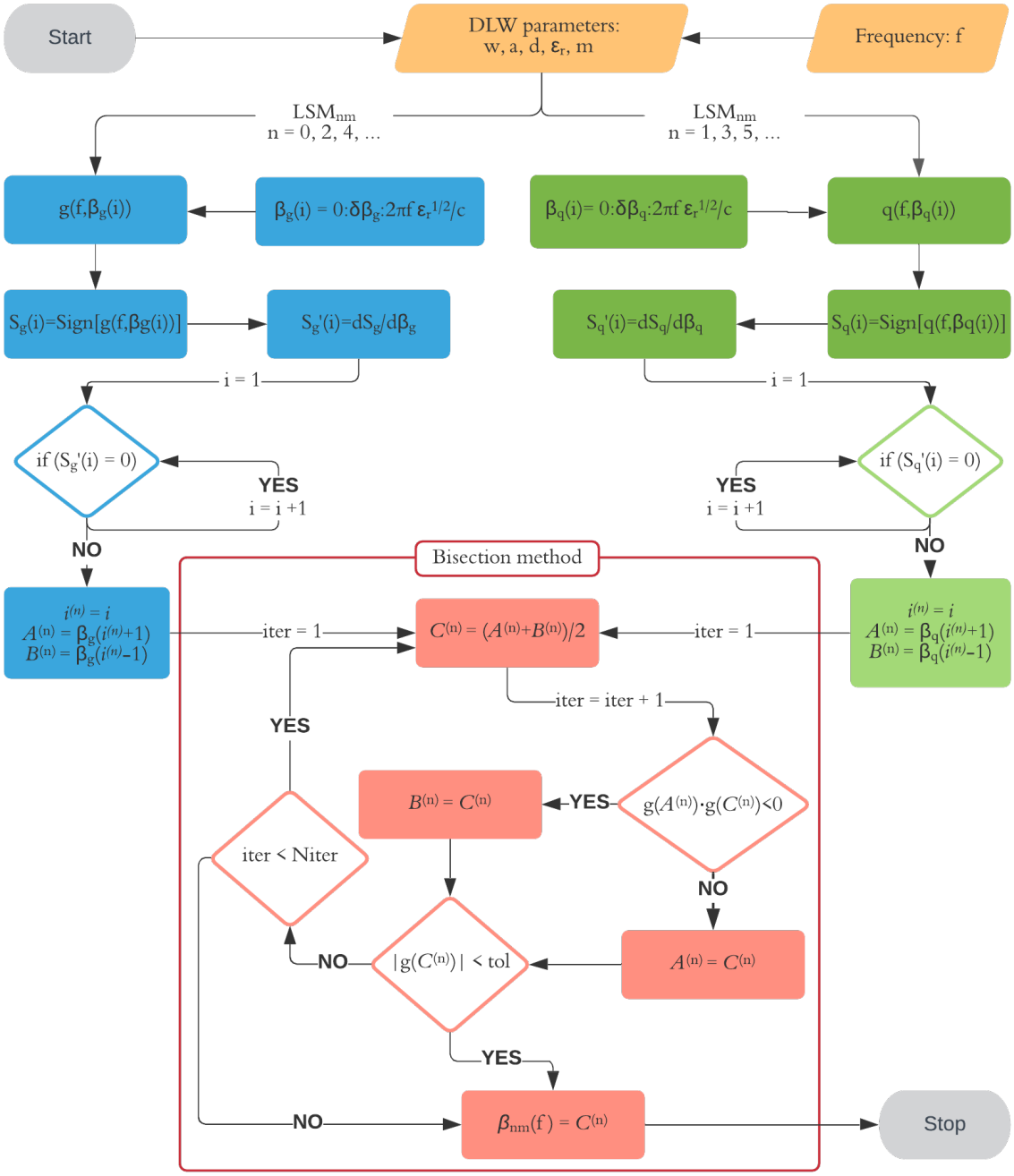

Fig. 4.8: Block diagram for the propagation constant solver routine, solving numerically the characteristic equations of the LSM_{nm} modes, for given structure geometry parameters and frequency.

wavenumbers of plane waves for a dielectric material $\epsilon_r = 3.81$, and for vacuum, respectively. As can be seen, the cut-off frequency is higher for higher harmonics. Unlike the TE/TM modes in a hollow metallic waveguide, the propagation constant can take values higher than the vacuum wavenumber, achieving sub-luminal phase velocities, whilst leaving a vacuum aperture channel for particle propagation. In this way, the propagating EM wave inside the DLW, can be phase velocity-matched with the propagating particles, enhancing the THz-particle interaction. The upper limit of the propagation constant is defined by the choice of dielectric, given by $\omega\sqrt{\epsilon_r}/c$, plotted in dashed line in Figure 4.9.

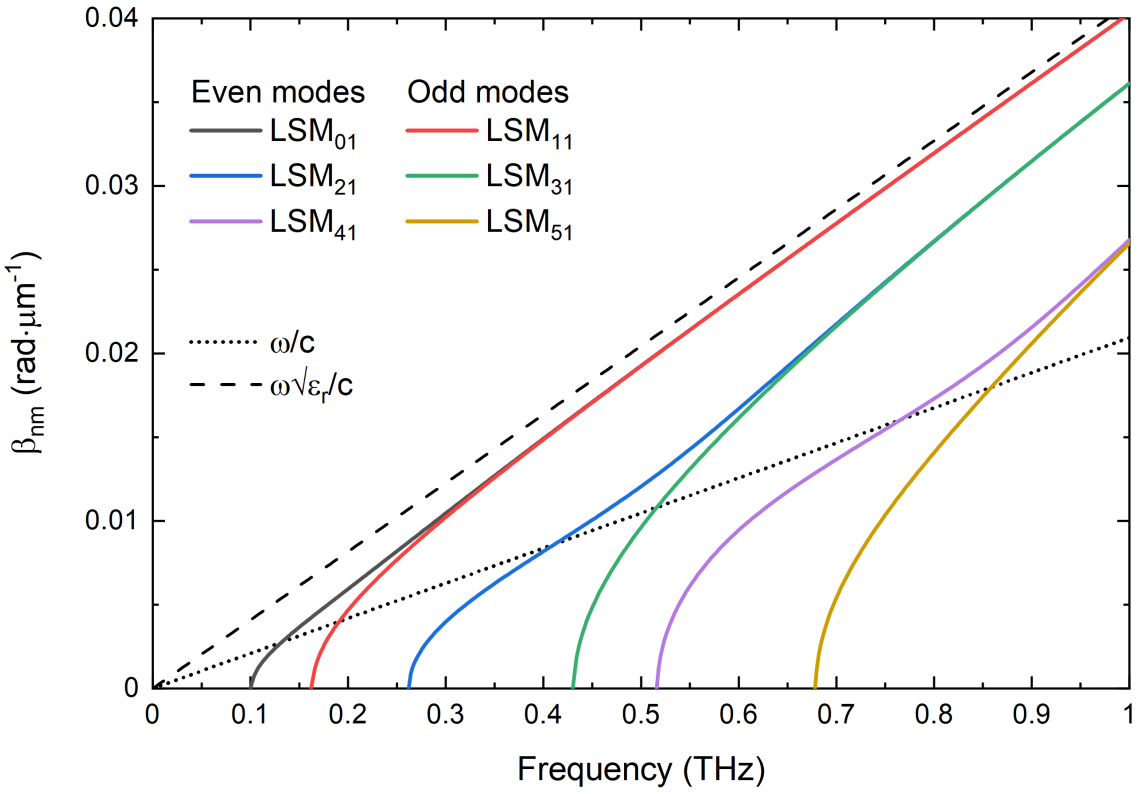

Fig. 4.9: Propagation constant of the LSM_{n1} modes, where $n = 0, 1, ..., 5$. The waveguide geometry of the 100 keV DLW structure, summarised in Table 4.1, was used. The black dotted and dashed lines indicate the wavenumbers for vacuum and for a dielectric material of $\epsilon_r = 3.81$, respectively.

4.3.2 THz-electron interaction

In order to simulate the interaction of the electrons with the EM fields, the equation of motion, described in Equation 3.89, needs to be solved. In the simulations, each particle is characterised by a 6-dimensional phase space, where its position and velocity is described in Cartesian coordinates, $p_{n,t_i}(x, y, z, \beta_x, \beta_y, \beta_z)$, where $\beta = v/c$, n the index number of the particle and t_i is the time instance index. An electron bunch propagating through a DLW structure, is a system consisted of N number particles, depending on the charge e.g. a 1 fC bunch corresponds to approximately 6x10^3 electrons.

The 6D phase space of a particle at t_i, can be expressed by the concatenation of a 3-dimensionsal position vector, $\boldsymbol{r}_{n,t_i}$, and and a 3-dimensional velocity vector, $\boldsymbol{\beta}_{n,t_i}$, to make a 6D vector given by

$$\begin{bmatrix} \boldsymbol{r} \\ \boldsymbol{\beta} \end{bmatrix}. \tag{4.5}$$

The phase space evolution of a particle can be simulated by solving the equation of motion described by Equation 3.89. Nevertheless, the evolution of a system consisted of N particles cannot be described with an analytical expression, as it depends on the initial phase space condition of each particle. Therefore, numerical methods are used in order to perform the particle dynamics simulations. Here, the particle index n will be omitted for conciseness.

Equation 3.89 is a second-order, non-linear, homogeneous, ordinary differential equation. However, Equation 3.89 can be written in the form of a first-order ordinary differential equation, by expressing it in terms of the first time-derivative [110]

$$f(t_i, \boldsymbol{\beta}) = \frac{d\boldsymbol{\beta}}{dt} = \frac{q}{m_0\gamma(\beta)} \left(\mathbf{E}_{t_i} + c\boldsymbol{\beta}_{t_i} \times \mathbf{B}_{t_i} - (\mathbf{E}_{t_i} \cdot \boldsymbol{\beta}_{t_i})\boldsymbol{\beta}_{t_i} \right). \tag{4.6}$$

Given the initial conditions, $\boldsymbol{\beta}_{t_i} = \boldsymbol{\beta}_0$ at the intial time t_0, the solution

$$\boldsymbol{\beta}_{t_{i+1}} = \boldsymbol{\beta}_{t_i} + h\, f(t_i, \boldsymbol{\beta}_{t_i}), \tag{4.7}$$

can then be approximated. Here $h = t_{i+1} - t_i$ is the time step, which is arbitrarily chosen and kept as a constant throughout the whole simulation process. Equation 4.7 describes 'the Euler method', which consists the simplest method of solving ordinary differential equations [110, 111]. A system is advanced by a sequence of small time intervals, h. Although, in each time step, the rate of change of the solution is treated as constant and is found at the beginning of the interval. As a result, the truncation error per time step associated with this method is greater than more advanced methods, making it prone to numerical instabilities [111, 112].

In this thesis, the Runge-Kutta 4th-order method (RK4) will be adapted. RK4 is a well known and widely used method for numerically integrating ordinary differential equations [110, 112]. Moreover, the RK4 method is easy to implement, stable and suitable for energy conversation which is essential for this model. The main principle behind the RK4 method is performing a more symmetric integration across the time interval, by using 4 trial steps per interval, resulting in a more accurate solution. The approached solution obtained using the RK4 method can be expressed as

$$\boldsymbol{\beta}_{t_{i+1}} = \boldsymbol{\beta}_{t_i} + h\,\xi(t_i, \boldsymbol{\beta}_{t_i}), \tag{4.8}$$

where $\xi(t_i, \boldsymbol{\beta}_{t_i})$ is the increment function, which is interpreted as the weighted slope over the interval h. The increment function formalism is [113, 114]

$$\xi(t_i, \boldsymbol{\beta}_{t_i}) = \frac{1}{6}\left(k_1 + 2k_2 + 2k_3 + k_4\right), \tag{4.9}$$

where the constants k, are given by [113, 114]

$$\begin{aligned} k_1 &= f(t_i, \boldsymbol{\beta}_{t_i}), \\ k_2 &= f(t_i + \frac{h}{2}, \boldsymbol{\beta}_{t_i} + \frac{h}{2}k_1), \\ k_3 &= f(t_i + \frac{h}{2}, \boldsymbol{\beta}_{t_i} + \frac{h}{2}k_2), \\ k_4 &= f(t_i + h, \boldsymbol{\beta}_{t_i} + hk_3). \end{aligned} \tag{4.10}$$

In each time step, the velocity vector of the particle is advanced using the RK4 in-

tegration method according to Equation 4.9, and the position vector is also updated by

$$\boldsymbol{r}_{t_{i+1}} = \boldsymbol{r}_{t_i} + h\,\boldsymbol{\beta}_{t_i}. \tag{4.11}$$

The EM fields inside the waveguide, are modelled by their analytic expressions described by the Equations 3.62-3.67 for the LSM_{01} mode, and Equations 3.71-3.76 for the LSM_{11} mode. For a given waveguide geometry, the propagation constant relation is obtained by using the propagation constant solver routine discussed in §4.3.1. Then, the transient profile of the injected pulse is either user-defined or an electro-optic measurement is used as an input. For the case of the user-defined waveform, the corresponding amplitude spectrum is modelled according to a modified Gaussian distribution

$$U(\omega) = \exp\left[-\left(\frac{(\omega-\omega_0)}{\sqrt{2}\,\sigma_\omega}\right)^2\left(\frac{\omega_0}{\omega}\right)^x\right], \tag{4.12}$$

where ω_0 is the centre frequency, σ_ω the standard deviation and x the source-dependant frequency-decay coefficient. For these simulations, the spectral Full Width at Half Maximum (FWHM) bandwidth is defined as $\Delta\omega = 2\sqrt{\ln(2)}\,\sigma_\omega$. The equivalent $1/e^2$ of the field width is given by $\tau = \mathrm{TBP}/(\ln(2)\sigma_\omega)$, where TBP is the Time-Bandwidth Product, which is approximately 0.441 for Gaussian distributions.

Only the EM fields inside the vacuum aperture channel were modelled, as it is where the interaction takes place. As an example here, the EM fields of the LSM_{01} mode are evaluated for a single-cycle pulse with $\omega_0 = 0.5\,\mathrm{THz}$ and $\tau = 3.5\,\mathrm{ps}$, which corresponds to a bandwidth of $\Delta\omega = 300\,\mathrm{GHz}$. In Figure 4.10, the transient excitation signal is plotted, along with the corresponding spectral amplitude used for the model.

The geometry parameters of the 100 keV DLW structure, summarised in Table 4.1, are used here. As can be seen from Equations 3.62-3.67, the electric and magnetic field components are function of the longitudinal propagation constant β_{01} and frequency. Therefore, Equations 3.62-3.67 are evaluated at each frequency, and the weighted mean is then obtained, using the amplitude spectrum as the weighting function. It should be noted, that the values for frequencies below the f_c are not

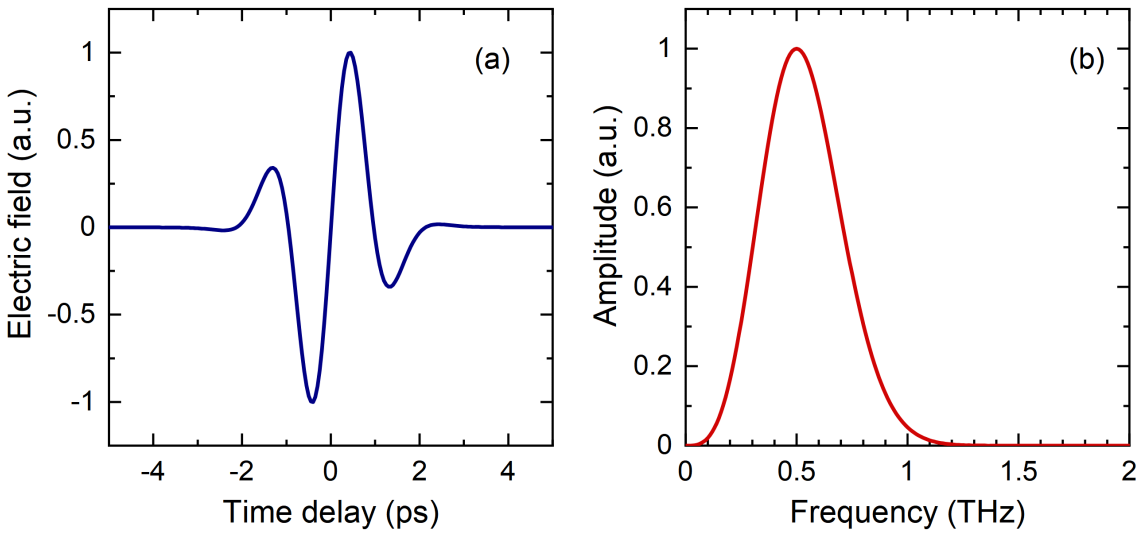

Fig. 4.10: (a) The waveform and (b) the corresponding amplitude spectrum used as the excitation signal for the modelling of the EM field pattern of the LSM_{01} mode.

considered, as this frequency range corresponds to evanescent waves.

In Figure 4.11, the electric field components of the LSM_{01} mode are depicted as a function of the horizontal and vertical position of the vacuum aperture. The intensity has been normalised so that the peak of the of the E_y-component is equal to 1 V/m on-axis, $E_y(x = 0, y = 0) = 1\,\mathrm{V/m}$. It should be noted, that E_z is plotted with a $\pi/2$ phase shift with regard to E_x and E_y in Figure 4.11. The phase shift between the peaks of the E_z and the E_y components, is evident from Equation 3.64. This can be illustrated in Figure 4.12, where the E_y and the E_z components are

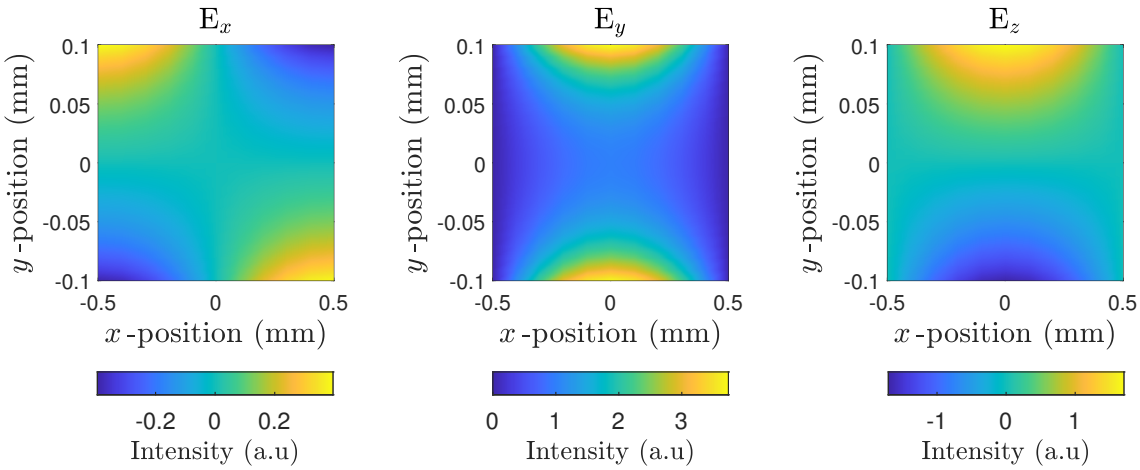

Fig. 4.11: The modelled electric field components of the LSM_{01} mode, in the vacuum region, as a function of the transversal positions. The E_z component is in a $\pi/2$ phase shift in respect with E_x and E_y.

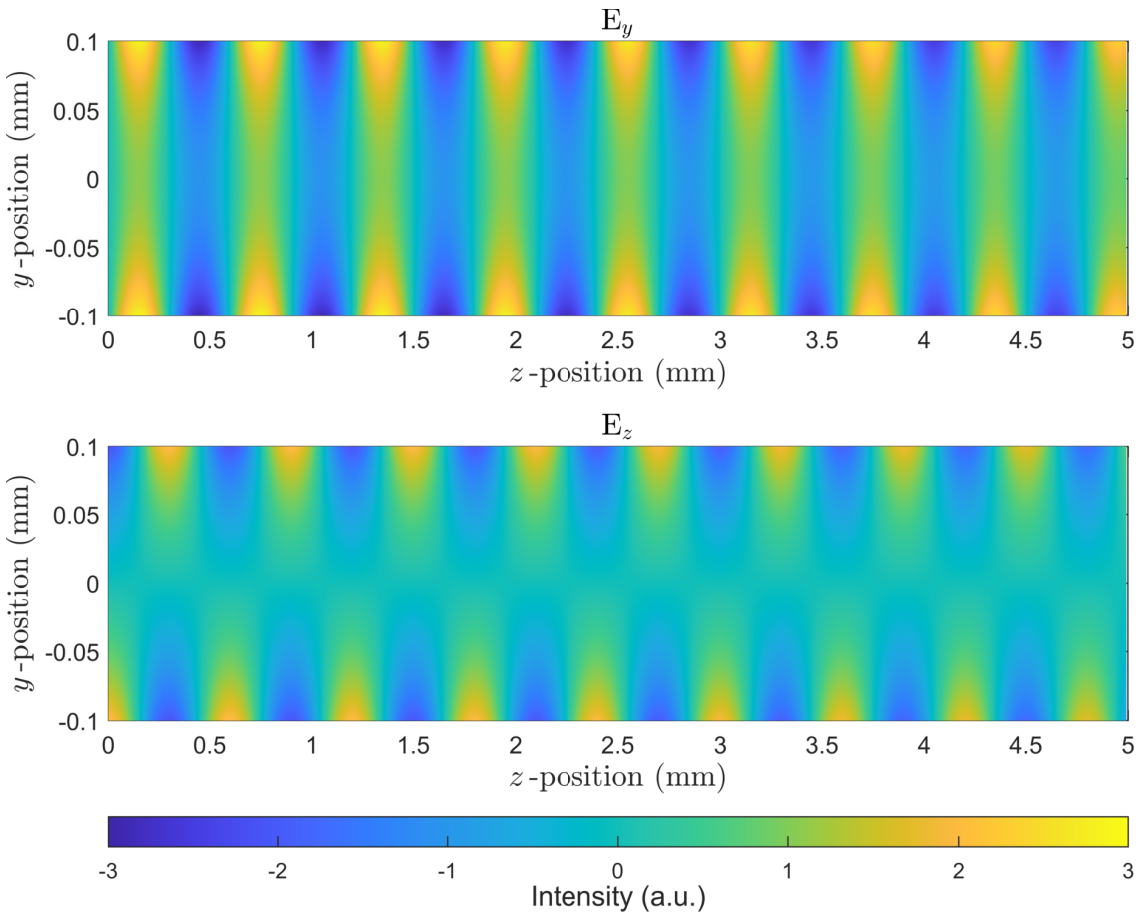

Fig. 4.12: The modelled E_y and E_z components of the LSM_{01} mode, in the vacuum region, as a function of the vertical and the longitudinal position, at $x = 0\,\text{mm}$.

plotted as a function of the vertical and longitudinal position on the $x = 0\,\text{mm}$ plane of the waveguide. The E_x is not plotted, as it has a zero-value at the $x = 0\,\text{mm}$ plane. For this illustration, a simple sine wave was used as the transient profile. The dependency of the electric components on the transversal directions can be observed from Figure 4.11. E_y is symmetrical about the $x = 0\,\text{mm}$ and $y = 0\,\text{mm}$ plane, whereas E_z is symmetrical only about the $x = 0\,\text{mm}$ plane and anti-symmetrical about the $y = 0\,\text{mm}$ plane. E_x is anti-symmetrical in both planes. Consequently, the E_z component has a zero-value along the XZ-plane. E_z rises along the dielectric-vacuum interface, $|y| = 0.1\,\text{mm}$. Therefore, the DLW structure could be employed as an ultrafast electron-streaker when operated in the LSM_{01} mode.

In order to simulate the THz-electron interaction, a script was developed in MATLAB, which encapsulated a number of sub-routines, each one assigned for the execution of a specific part of the simulation. The script was adapted using the

Particle-in-Cell (PIC) method, which is widely used in Plasma Physics [115–120]. PIC method is a class of numerical simulation methods used to model the time evolution of the EM fields and of virtual particles in the system phase space. A discretised representation of the EM fields over the simulation domain is obtained by a rectilinear grid, as depicted in Figure 4.13. Each mesh cell represents a small volume in space where the electric and magnetic field are computed. The accuracy of the simulation is proportional to the number of mesh cells, however, the total simulation time is directly impacted as well. Therefore, a good compromise between simulation speed and accuracy is reached. As a general-principle, the smallest wavelength of interest must be spatially sampled at a rate of 10 mesh cells per wavelength. Consequently, the longitudinal dimension of a mesh cell, dz, is constrained by the highest frequency sampled in the simulation, and according to the Nyquist rate theorem [121]

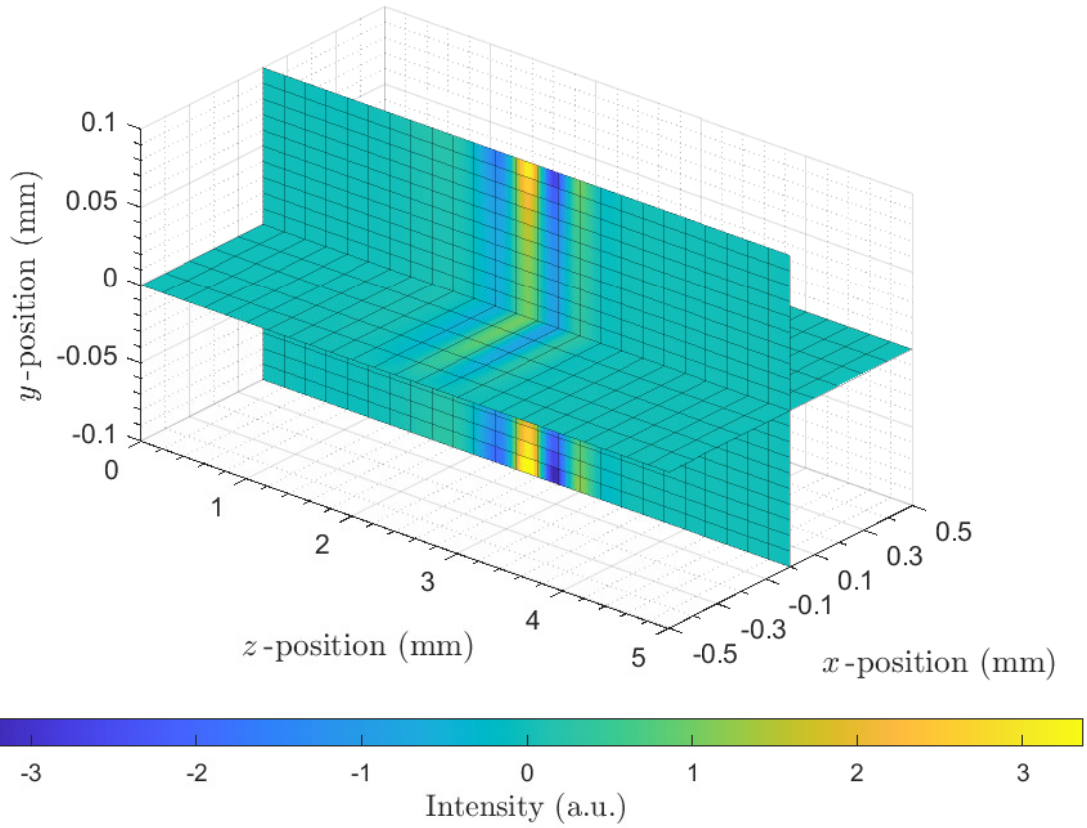

Fig. 4.13: Illustration of the calculation domain, discretised by a rectilinear grid, where the EM fields are computed. Slice planes of the E_y component at $x = 0\,\text{mm}$ and at $y = 0\,\text{mm}$.

$$dz \leqslant \frac{1}{10}\frac{\sqrt{\mu\epsilon}}{f_{\max}}, \tag{4.13}$$

where $f_{\max}$ is the sampling frequency.

The complete block diagram illustrating the flowchart of the THz-electron interaction algorithm based on the PIC method is depicted in Figure 4.14. The mesh generator subroutine, takes as input the physical size of the vacuum channel of the waveguide, and the cell size $\mathrm{d}x\times\mathrm{d}y\times\mathrm{d}z$. In Figure 4.13, the computational volume is depicted, discretised by the mesh grid lines. The slice planes of the $\mathrm{E}_y(x, y, z)$ component, orthogonal to the x-axis at $x = 0\,\mathrm{mm}$ and to the y-axis at $y = 0\,\mathrm{mm}$ are drawn, as an example. An interpolated colouring has been used for the face colour of the mesh surfaces. A less coarse mesh grid is illustrated, for clarity.

The particles are defined in continuum space in both position and velocity. The particle distribution with initial conditions, is either user-defined or imported from an external file generated by a commercial software package such as the General-Particle-Tracer (GPT) [122, 123]. An overview of the principles of GPT is given in the Appendix. Likewise, the excitation signal is either user-defined or imported from an external file. With the time step size and total transit time (TT) defined, the Phase Space Evolution (PSE) subroutine is executed. PSE is an iterative procedure where the EM fields and the particles are pushed in time. At each time point, the EM fields of the desired LSM_{nm} are computed on the mesh grid of the simulation domain. Subsequently, a grid-to-particle interpolation is performed in order to calculate the EM field value at each particle position. The intrinsic cubic interpolation MATLAB function *interp3()* was employed. Then the phase space of the particle bunch is evolved by solving the equation of motion with the RK4 method, following with a particle boundary condition inspection. If any particles escape from the boundaries of the simulation domain, then the particle is marked as out-of-bound. Finally, the waveform of the excitation signal is advanced one time step by using the propagation constant of the LSM_{nm} mode, until the total transit time is reached.

At each time point, the trajectories and momenta of the macroparticles are stored into matrices. The resultant particle distribution is then transported onto a screen, via a transfer matrix [98, 124], of drift length L. Then the imaged transverse profile of the particle bunch is tracked as a function of the relative time delay between

the bunch and the EM fields. Simulations supporting the experiments discussed in Chapter 7, were performed using this method, in order to interpret the experimental observables, and extract the longitudinal profile of the particle beam.

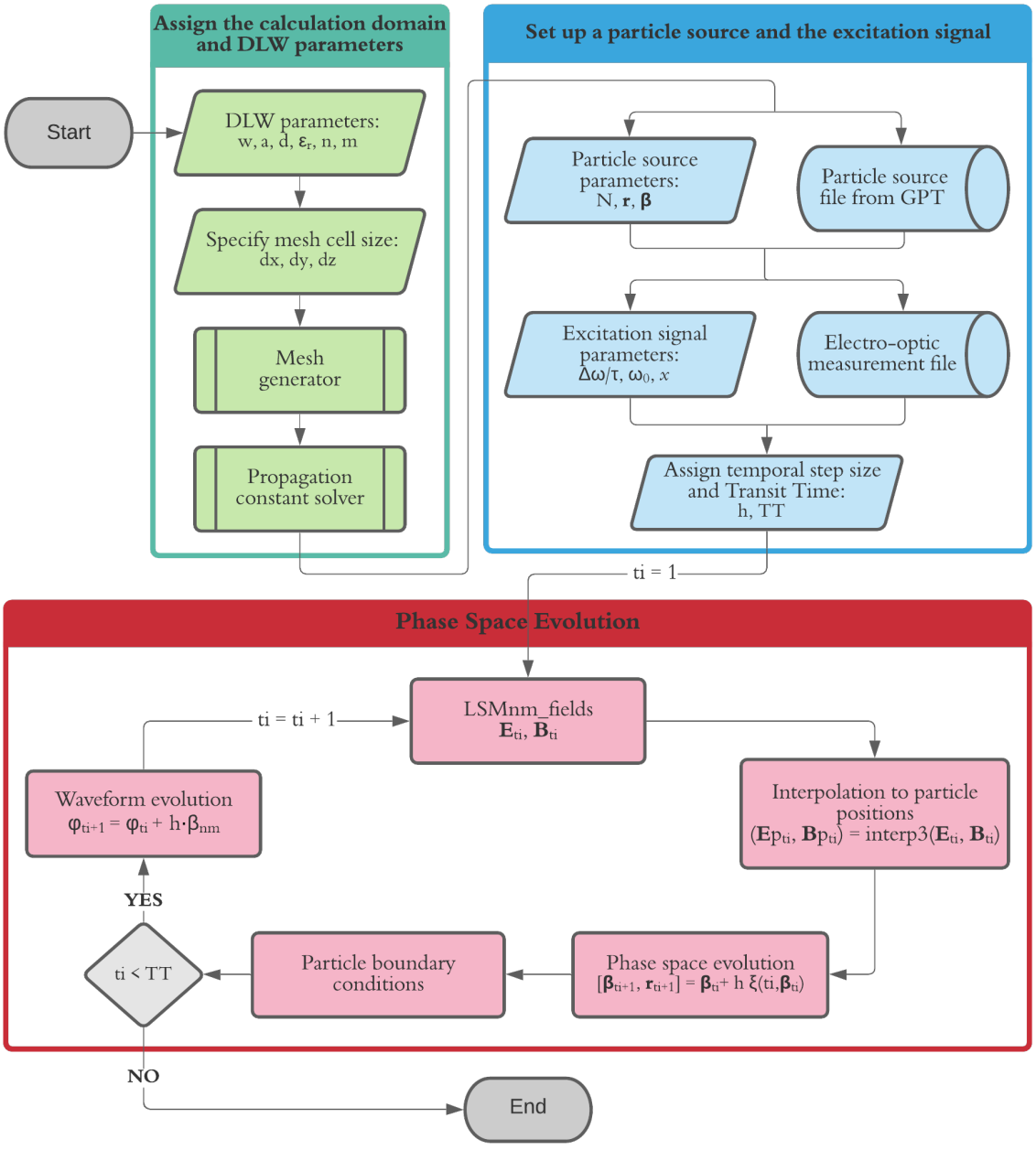

Fig. 4.14: Flowchart of the THz-electron simulation routine, by implementing the PIC method.

Chapter 5

Characterisation of the dispersion relation of a 100 keV DLW structure

5.1 Overview

In this chapter, the structure designed for manipulation of 100 keV electron beams, was experimentally characterised. The structure was designed to achieve THz phase velocity matching with co-propagating 100 keV electron bunches. In order to confirm the phase-matching capability, the propagation constant of the structure was measured.

The propagation constant of the DLW transmission line was determined by employing a custom-built THz time-domain spectrometer §4.1.2. Free space reference waveforms and transmitted through the DLW structures waveforms of the THz radiation were recorded and then analysed. From the analysis, the propagation characteristics of both the waveguide and the integrated coupler was determined. Moreover, the experimental results were then compared with the simulations and the operational frequency of the structure was experimentally determined.

5.2 Experimental method

5.2.1 Experimental apparatus

A schematic diagram of the experimental setup is illustrated in Figure 5.1. The experimental setup was based on a THz time-domain spectrometer (see §4.1.2). The input laser beam was produced by the 1 mJ regenerative amplifier system (§4.1.1), providing 100 fs FWHM long laser pulses with centre wavelength of 800 nm, 500 μJ pulse energy and at a repetition rate of 1 kHz. The incident laser beam was split into a pump beam for THz generation and a probe beam for THz detection with a 90:10 power ratio. The pump beam was expanded to a beam diameter of 20 mm, using a Galilean telescope, consisted of a plano-concave and a plano-convex lens configuration, f_1 =-100 mm and f_2 =200 mm respectively. The expanded pump beam was used to excite a 25 x 25 mm spintronic source with the residual transmitted 800 nm light beam blocked by a 800 nm filter which was a black card.

A 2 mm-thick, (110)-cut Zinc Telluride (ZnTe) crystal was used in this experiment for the EO detection. The EO crystal, ZnTe, was placed right at the exit

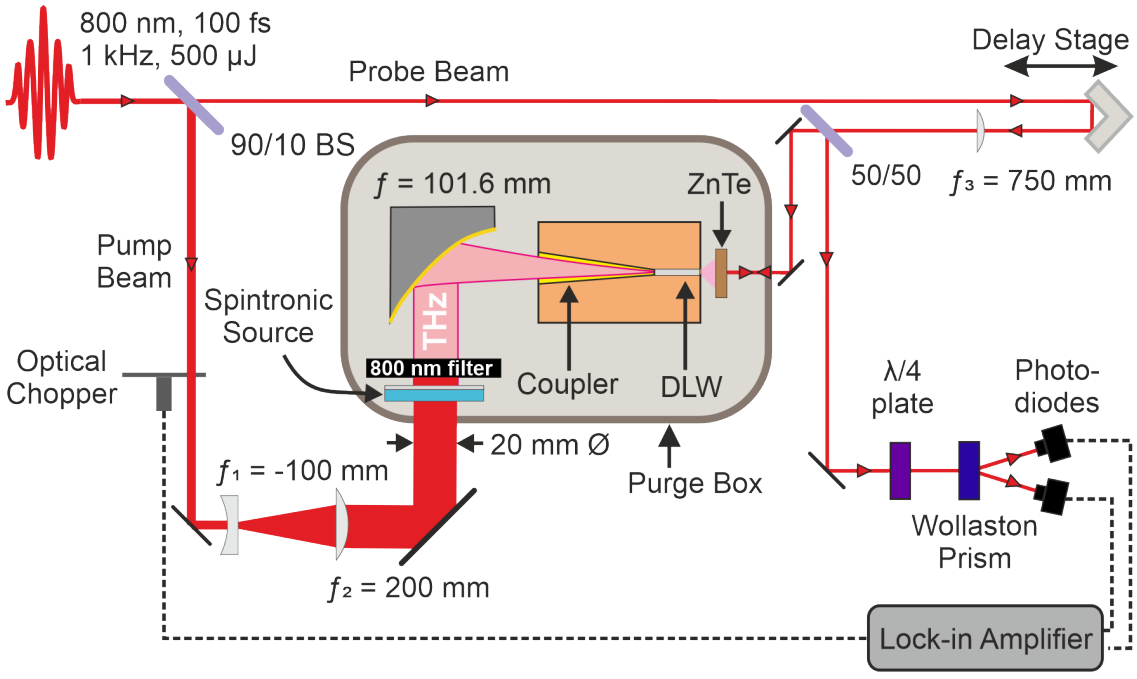

Fig. 5.1: Schematic diagram of the experimental THz-TDS setup showing the generation and coupling of the THz radiation into the DLW followed by a standard back-reflection geometry EO detection scheme.

of the DLW structure in order to maximise the output signal. To realise this, a back-reflection geometry was employed, with the probe beam sent through the back of the detection crystal and then reflected off the front face before co-propagating back through the crystal with the THz pulse. A plano-convex lens, with focal length of $f_3 = 750\,\text{mm}$, was used to focus the probe beam to a beam diameter of approximately $100\,\mu\text{m}$ at the EO crystal. For the transverse control of the position of the probe beam, two manual linear translation stages were used in conjunction.

In order to reduce the influence of water vapour absorption on the THz spectral measurements, the THz generation process and transmission measurements were contained in an enclosure as depicted in Figure 5.1. The air in the enclosure was purged down at a relative humidity of approximately 5 %, as monitored by a humidity probe. All measurements were carried out at room temperature.

The parameters of the DLW structure under investigation are summarised in Table 5.1. The 'cut-back' technique [125–127] was used to determine the propagation constant of the waveguide. In order to realise this, two identical structures were manufactured with waveguide lengths of 5 mm and 10 mm respectively. The rest of the parameters were the same. For the reference pulse measurement, the DLW structure was removed from the optical set up, with the EO crystal remaining at the same place.

Table 5.1: Parameter list of the DLW structure, designed for the manipulation of 100 keV electron beams. Manufacturing tolerances are of the order of $\pm 10\,\mu\text{m}$.

Waveguide		Coupler	
Parameter	Value	Parameter	Value
α (μm)	100	b_c (mm)	5
w (mm)	1	w_c (mm)	10
L (mm)	5, 10	L_c (mm)	44
d (μm)	240		
ϵ_r	3.81		
f_c (THz)	0.1		

5.2.2 THz source

The THz emitter employed was a bilayer metallic structure consisting of a 2 nm CoFeB layer and a 2 nm Pt layer, deposited on a 500 μm-thick MgO substrate by DC-magnetron sputtering. A horizontally magnetic field was applied on the spintronic source, by two 25 mm-diameter neodymium disc magnets as illustrated in Figure 5.2. This ensured that vertically polarised THz radiation was generated upon optical excitation. The residual optical pump beam was blocked by a 800 nm filter. The mount holder of the spintronic sample was plastic, with nylon screws, assuring that no magnetic distortions would be induced.

The magnetic field produced by the two magnets was approximately 100 mT as measured using a Hall probe. This was above the saturation level required for the particular spintronic sample [128]. The sample was excited at normal incidence, with the emitted THz radiation collected with a 2-inch diameter, gold coated, off-axis parabolic (OAP) mirror with a reflective focal length of 101.8 mm. The THz radiation was then propagated into the coupler of the DLW structure.

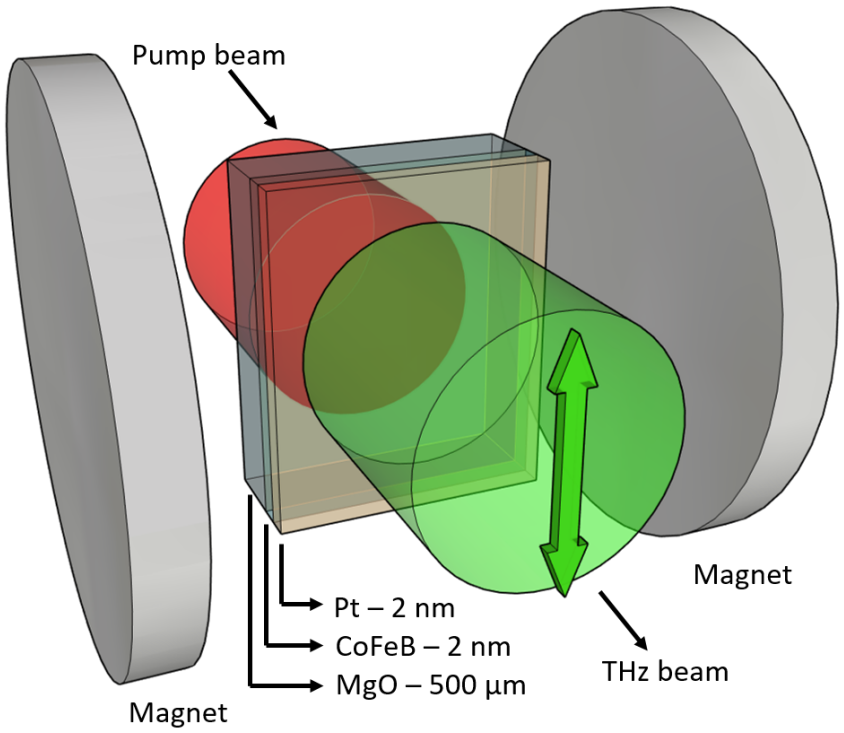

Fig. 5.2: Graphical representation of the vertically polarised THz radiation emission from the spintronic emitter via optical excitation. Dimensions not to scale.

5.3 Results and analysis

5.3.1 Modelling of the DLW structure

The dispersion relation of the two transmission lines composing the DLW structure, the coupler and the waveguide, was modelled by employing two different techniques.

The propagation constant of the waveguide was calculated using the method described in §4.3.1. Figure 5.3(a) shows the propagation constant of the LSM_{01} mode corresponding to the waveguide parameters listed in Table 5.1. Moreover, the propagation constant of the fundamental TE_{10} mode for the analogous hollow metallic waveguide, is plotted in Figure 5.3(a). The cut-off frequency, f_c of the LSM_{01} mode was calculated to be 0.11 THz, whereas for the TE_{10} mode, it was ascertained to be approximately 0.15 THz. The black dashed and solid lines depict the wavenumbers for vacuum and for a dielectric material of $\epsilon_r = 3.81$, respectively. The choice of the dielectric, sets an upper limit that the propagation constant of the LSM_{nm} mode can achieve. Similarly for the hollow waveguide, the propagation constant can be less than or equal to the vacuum wavenumber.

Figure 5.3(b) depicts the phase and group velocity of the LSM_{01} and TE_{10} mode.

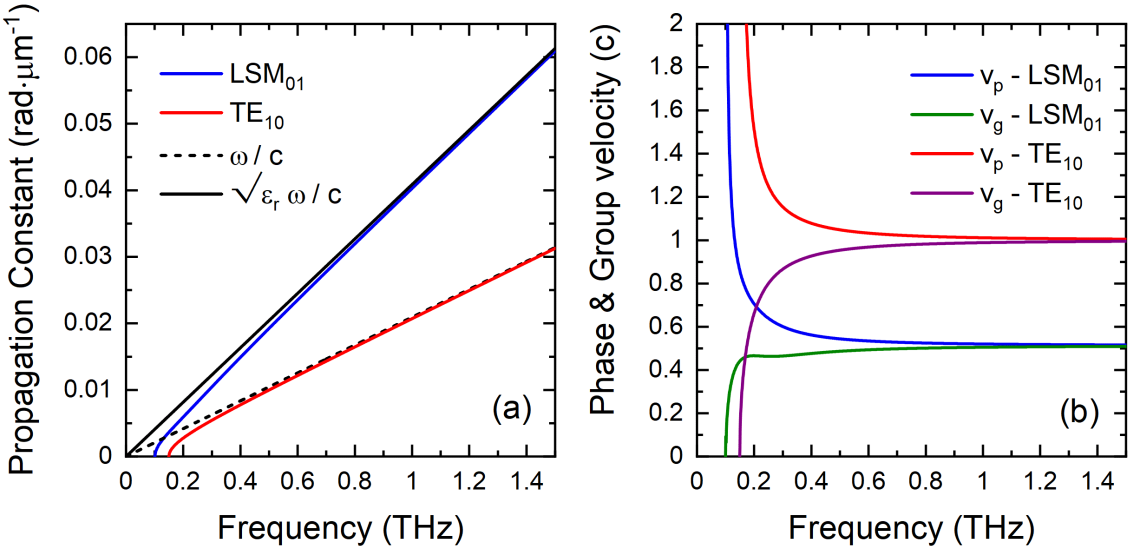

Fig. 5.3: (a) Calculated propagation constant of the LMS_{01} and TE_{10} mode for the waveguide parameters given in Table 5.1. The black dashed and solid lines indicate the wavenumbers for vacuum and for a dielectric material of $\epsilon_r = 3.81$, respectively. (b) Calculated phase and group velocity of the LSM_{01} and TE_{10} mode.

The effect of the dielectric linings in a waveguide is evident as with the addition of the dielectric-linings, sub-luminal phase velocities can potentially be achieved inside the transmission line. In the case of the hollow waveguide, the phase velocity is typically greater than the speed of light. The phase velocity approaches infinity to the limit of $f \to f_c$, while the group velocity is equal to zero for $f = f_c$.

The propagation constant of the LSM_{01} mode was calculated as a function of the waveguide parameters in order to investigate the effect of those parameters. The base parameters that have been used, are summarised in Table 5.1. As can be seen in Figure 5.4, the half vacuum aperture, α, the dielectric thickness, d, and the width, w, were the free variables for the parameter sweep. The phase velocity as a function of frequency was calculated, with the fixed variables displayed on the top of

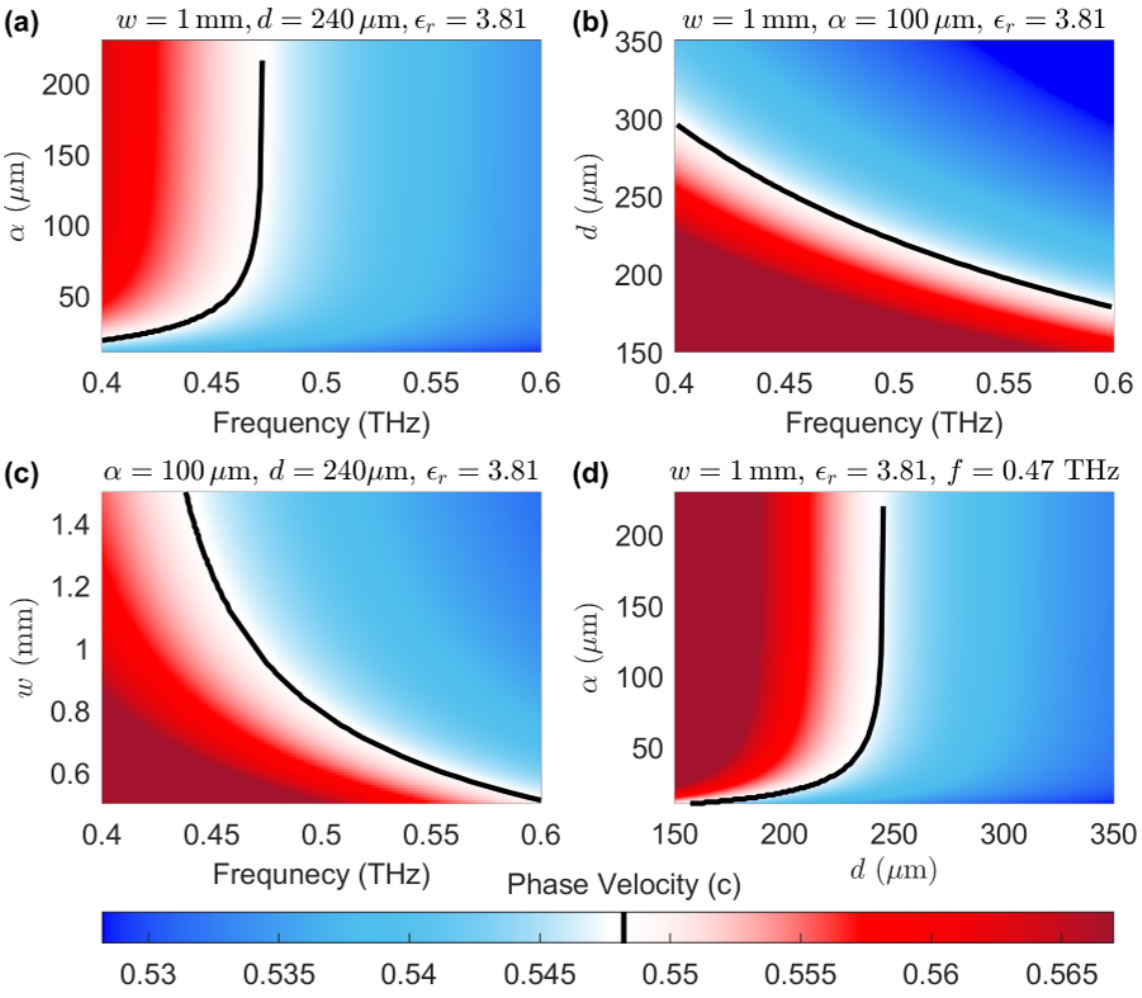

Fig. 5.4: Phase velocity of the LSM_{01} mode as a function of the (a) half vacuum aperture α , (b) the dielectric thickness d, (c) the width w, and (d) as a function of α and d at 0.47 THz. Solid black line shows the velocity of 100 keV electrons.

each parameter sweep. The solid black line depicts the parameter combinations for which the phase velocity of the LSM_{01} mode is matched to the velocity of 100 keV electrons.

The effect of the half vacuum height α, is outlined in Figure 5.4(a). As can be seen, the phase-matched operational frequency, f_{op}, is relatively constant as α increases, but decreases rapidly as α decreases. The dielectric thickness d, has a significant role in the tailoring of the phase velocity of the operating frequency as depicted in Figure 5.4(b). For thicker d, the phase velocity at a certain frequency drops, and increases as d decreases. The impact of the width of the waveguide, w, is less dominant as can be seen in Figure 5.4(c), considering that the manufacturing tolerances are three orders of magnitude smaller. Figure 5.4(d), shows how the phase velocity at 0.47 THz varies for different combinations of α and d. This is useful for tailoring the structure parameters for different particle beam energies whilst employing the same driving THz source.

The coupler comprises a linearly tapered horn, therefore the modelling could not be carried out analytically. The coupler can be approached as a rectangular metallic waveguide with variable transverse dimensions. The effect of the coupler cannot be described as propagation constant, as it does not consist of a constant cross-sectional transmission line. Therefore, the effect of the coupler will be addressed as 'effective propagation term', β_c.

A simple wave propagation algorithm was developed in order to model the propagation of a broadband pulse though a transmission line. In order to benchmark the algorithm, the simple example of a uniform transmission line was first examined. The transmission line comprised of a hollow rectangular waveguide, with transverse dimensions of $a = 1.5$ mm and $b = 1$ mm.

Considering that the TE_{mn} mode is excited, the transmission line is segmented into smaller transmission lines, dz, of propagation constant β_{mn}. A single-cycle, broadband THz pulse was then launched directly into the TE_{mn} mode and the evolution of the phase space was tracked. An iterative procedure takes position where the pulse is propagated N times, for a distance dz, for a total distance of $L = N \cdot dz$. The dispersion relation can then be obtained.

Figure 5.5 summarises the benchmark results of the algorithm, depicting the modelled propagation constant as well as the phase and group velocity for the first

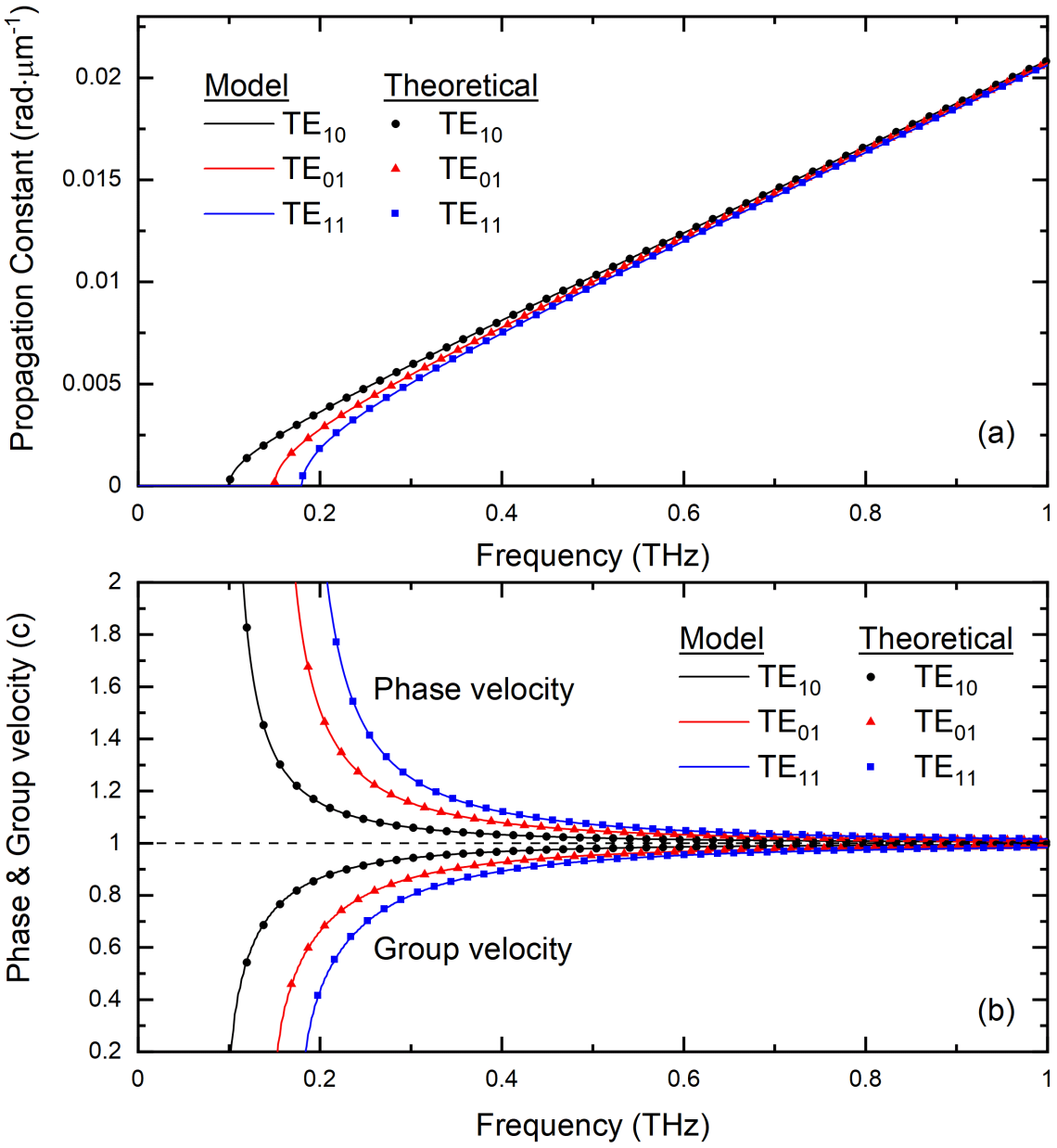

Fig. 5.5: Benchmark results of the wave propagation model developed to obtain (a) the propagation constant and the corresponding (b) phase and group velocity of the first three fundamental traverse modes. In scatter plot the theoretical expected values.

harmonic waveguide transverse modes TE_{10}, TE_{01} and TE_{11}. Here, the spatial step size was $dz = 200\,\mu$m, for a $L = 44$ mm-long transmission line. As can be seen from the benchmarking, the results from the model agree very well with the theoretical expected values.

For the modelling of β_c, the transmission line was segmented into N cascaded hollow rectangular waveguides, of length dz, with variable transverse dimensions. The fundamental TE_{10} mode was launched for a single-cycle, broadband pulse, cov-

ering a frequency range of 0.01-3 THz. The spatial step size was set to $dz = 200\,\mu$m, for a total length equal to the length of the coupler, $L_c = 44$ mm.

5.3.2 Electro-optic measurements

The free space waveform of the electric field obtained from the spintronic source can be seen in Figure 5.6. The main pulse, label (a), is a single-cycle THz pulse with a FWHM of the field envelope of 0.86 ps. More pulses appear on the right hand side, after the main pulse, labelled (b)-(d). The second pulse (b), arrived at approximately 6.7 ps, was attributed to a second THz emission. The optical pump pulse was reflected inside the MgO substrate of the source thus generating a second time-delayed THz pulse at a reduced amplitude. With given substrate thickness, 500 μm, and index of refraction, $n = 1.73$ of MgO at 800 nm [129], the expected time delay would be 5.76 ps. This suggested that the substrate was thicker, approximately to 575 μm. Subsequently, a third and a fourth pulse labelled (c) and (d), arrived at approximately 42.7 ps and 49.4 ps respectively. These two reflections were attributed to THz reflections within the EO crystal. This is in good agreement

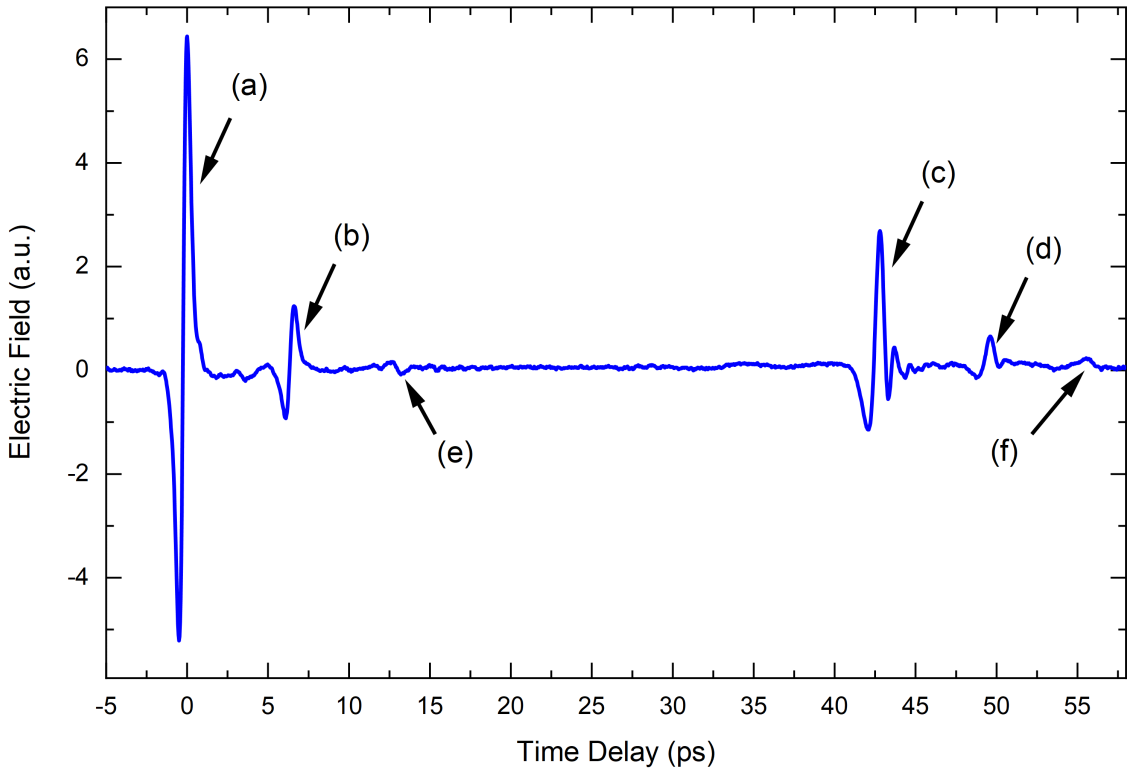

Fig. 5.6: Free space reference waveform generated by the spintronic source, detected using a 2 mm-thick ZnTe crystal. Labels (a)-(d) are explained in the text.

with a 2 mm-thick ZnTe with a refractive index of $n_{\mathrm{THz}} = 3.16$ at THz frequencies [130]. The time delay between pulses (a)-(b) and (c)-(d) was approximately the same.

The feature labelled (e) in Figure 5.6 found at 13.2 ps was attributed to a third THz emission, similar to pulse (b). A phase shift of π was noted on these pulses. This feature was also observed by Torosyan *et al.* [131] but without an explanation. The phase shift on pulses (e) and (f) has been attributed due to the MgO-metal layer interface, as the metal film is considered to have a higher refractive index than the substrate. The time delay between (e)-(b) and (b)-(a) was the same. The damage threshold of the spintronic source was found to be higher than the highest pump laser fluence available by the laser system. Therefore the sample was illuminated with the maximum pump laser fluence available.

To benchmark the spectrometer, the vapour water absorbance was measured and compared to the literature as shown in Figure 5.7. The spintronic emitter produced a single-cycle THz pulse, with a bandwidth extending up to 2 THz. The THz waveforms with purged and unpurged air were detected, depicted in Figure 5.7(a) with the corresponding amplitude spectra in 5.7(b). For the purged waveform, the air was purged to a relative humidity level of 5%-6% with Nitrogen at room temperature. The two waveforms were vertically offset for clarity. The amplitude spectra were then used to calculate the absorbance due to water vapour over the 0.1-2 THz frequency range as can be seen in 5.7(c). The rotational transitions in water vapour at THz frequencies have been extensively studied in the literature [132, 133] and was used as a reference for comparison. The main transitions have been labelled and marked with straight solid lines in Figure 5.7(c) along with the experimental results of the absorbance.

From the experimental results and analysis, it was suggested that the THz spectrometer was commissioned successfully, with the required frequency resolution.

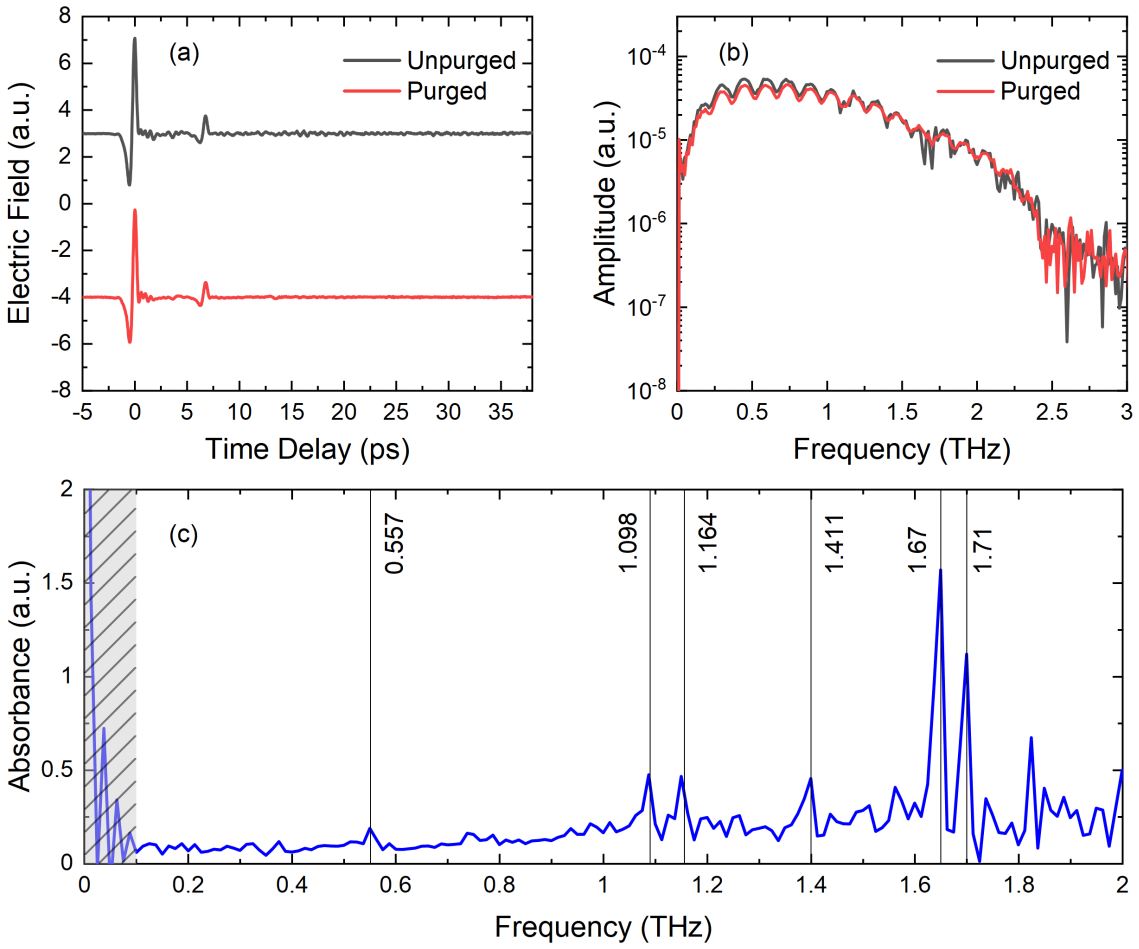

Fig. 5.7: (a) THz waveforms for purged (relative humidity of 6%) and unpurged air, with (b) the corresponding amplitude spectra. (c) The water vapour absorbance for 0.1-2 THz as measured from the THz time domain spectrometer, with comparison with the literature [132, 133] (solid lines). The waveforms in (a) are vertically offset for clarity.

Transmission measurements

Figure 5.8(a) and 5.8(b) show the THz waveforms measured before and after transmission through the DLW structures which incorporated the 5 mm and 10 mm long DLW, respectively. The spintronic emitter produced a single-cycle THz pulse with a duration of 1.9 ps ($1/e^2$ of the field envelope), which was stretched to approximately 16 ps and 29 ps in the 5 mm and 10 mm long DLW structures, respectively. The two transmitted pulses were also delayed in time.

The corresponding amplitude spectra and phase information are plotted in Figure 5.9. As can be seen in Figure 5.9(d), the spectra showed a sharp drop in amplitude at 0.11 ± 0.01 THz and 0.12 ± 0.01 THz for the pulses transmitted though the 5 mm and 10 mm long DLW structure, respectively. This was in good agreement

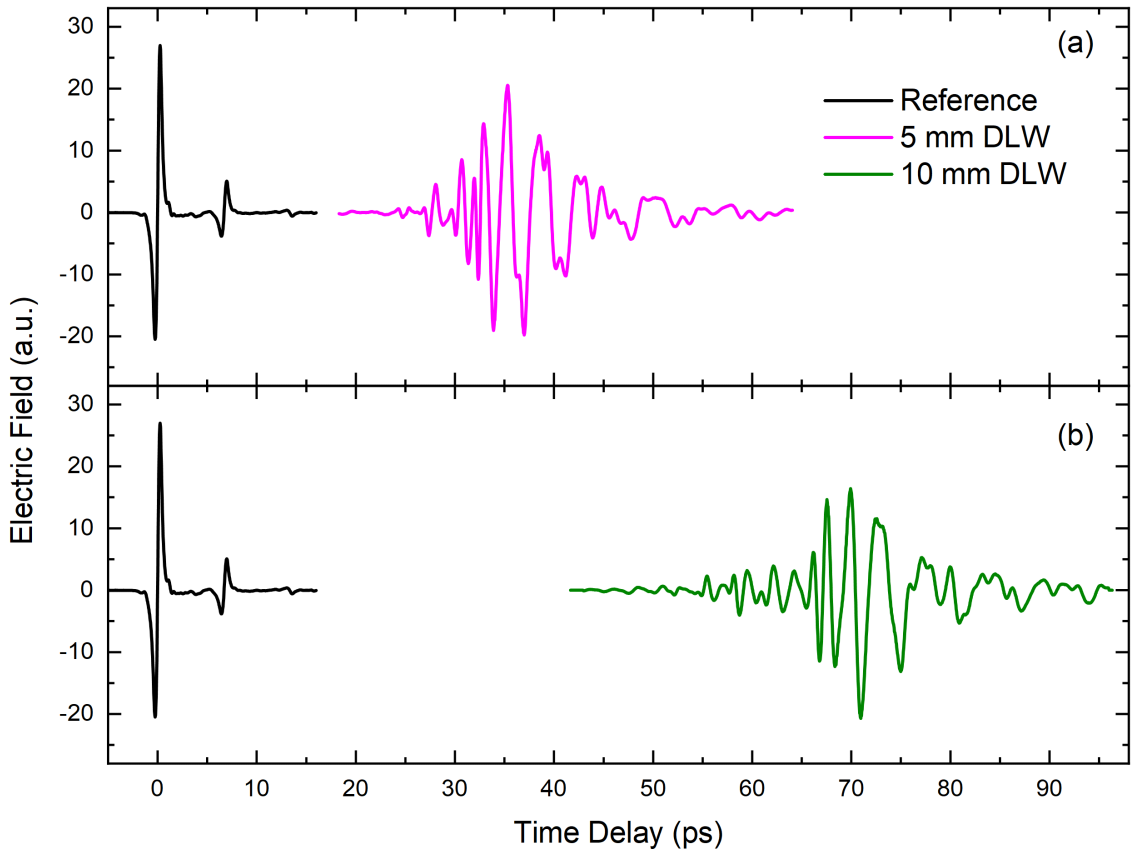

Fig. 5.8: THz waveforms transmitted through (a) the 5 mm long DLW structure and (b) the 10 mm long DLW structure, both with the free space reference. All waveforms were record with purged air.

with the waveguide cut-off frequency, f_c, calculated at 0.1 THz for the parameters listed in Table 5.1. The combination of the broadening of the pulse in time, after propagation through the DLW structure, and the cumulative phase, indicated the dispersive effect of the structures.

The second THz pulse produced by the spintronic emitter resulted in frequency oscillation artefacts, clearly observed in the amplitude spectrum shown in Figure 5.9(a) and 5.9(b). The modulation was measured to be 0.417 THz, which corresponds to the time-domain position of the reflection echoes, $\tau = 6.7$ ps. In the literature, the standard method of suppressing the distortion of reflection echoes is applying a time window on the main pulse [73, 134]. This technique can be applied for pulses shorter than τ. Nevertheless, for the pulses transmitted through the DLW structures, the main pulse was broadened and such that it overlapped with the reflection in time. This would make the use of a time window not suitable, as it would cut off the broadened pulse.

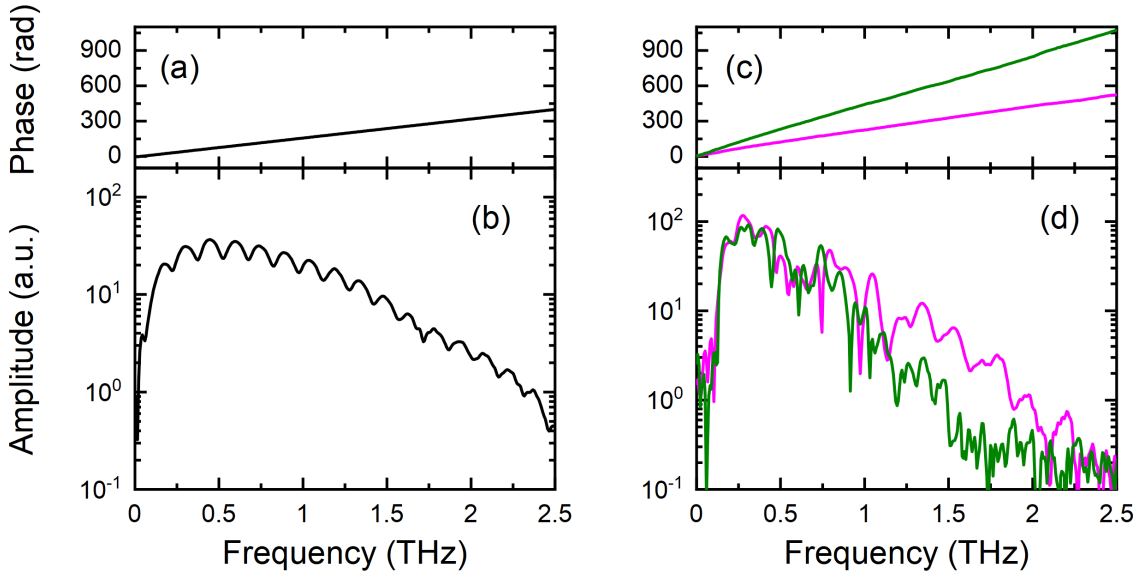

Fig. 5.9: Amplitude spectra for (b) the air reference and for (b) the DLW structures (d). The corresponding phase information in (a) and (c) respectively.

To remove the reflection effect from the analysis, a simple numerical algorithm was employed [135]. The method involves the numerical deconvolution of the reflection echoes in the frequency domain. The measured signal, $S(t)$, can be described by

$$S(t) = E(t) + r\,E(t-\tau), \tag{5.1}$$

where $E(t)$ is the primary THz pulse and the second term is the second pulse emission defined by a time delay τ and an attenuation factor r. The assumption made here was that the amplitude and phase spectra shape of the primary and the second pulse were the same. The Fourier transform of the convolution of two functions can be expressed as the product of their corresponding transforms, as stated by the Convolution theorem [136, 137]. Therefore, the Fourier transform of $S(t)$ yields

$$\widetilde{S}(\omega) = \widetilde{E}(\omega)\cdot(1 + r\,e^{-i\omega\tau}) = \widetilde{E}(\omega)\cdot\widetilde{H}(\omega), \tag{5.2}$$

where $\widetilde{H}(\omega)$ is considered the transfer function. With $\widetilde{H}(\omega)$ a known parameter, a deterministic deconvolution in the frequency domain may be applied on the recorded signal, thus recovering $\widetilde{E}(\omega)$. Subsequently, the free from reflection waveform can

be obtained by performing an inverse Fourier transform to $\widetilde{E}(\omega)$

$$E(t) = \mathfrak{F}^{-1}[\widetilde{E}(\omega)] = \mathfrak{F}^{-1}[\widetilde{S}(\omega)/\widetilde{H}(\omega)]. \tag{5.3}$$

This model can be scaled up and applied to a signal with N reflections

$$S(t) = E(t) + \sum_{n=1}^{N} r_n\, E(t - \tau_n). \tag{5.4}$$

The main benefit of this technique over other numerical methods is that it does not reduce the frequency resolution thus not introducing further artefacts/distortion to the spectrum as discussed by Naftaly *et al.* [135]. Nevertheless, the limitation is that it is not applicable for strongly absorbing and/or dispersive samples.

The reflection deconvolution algorithm was applied to the reference and transmit-

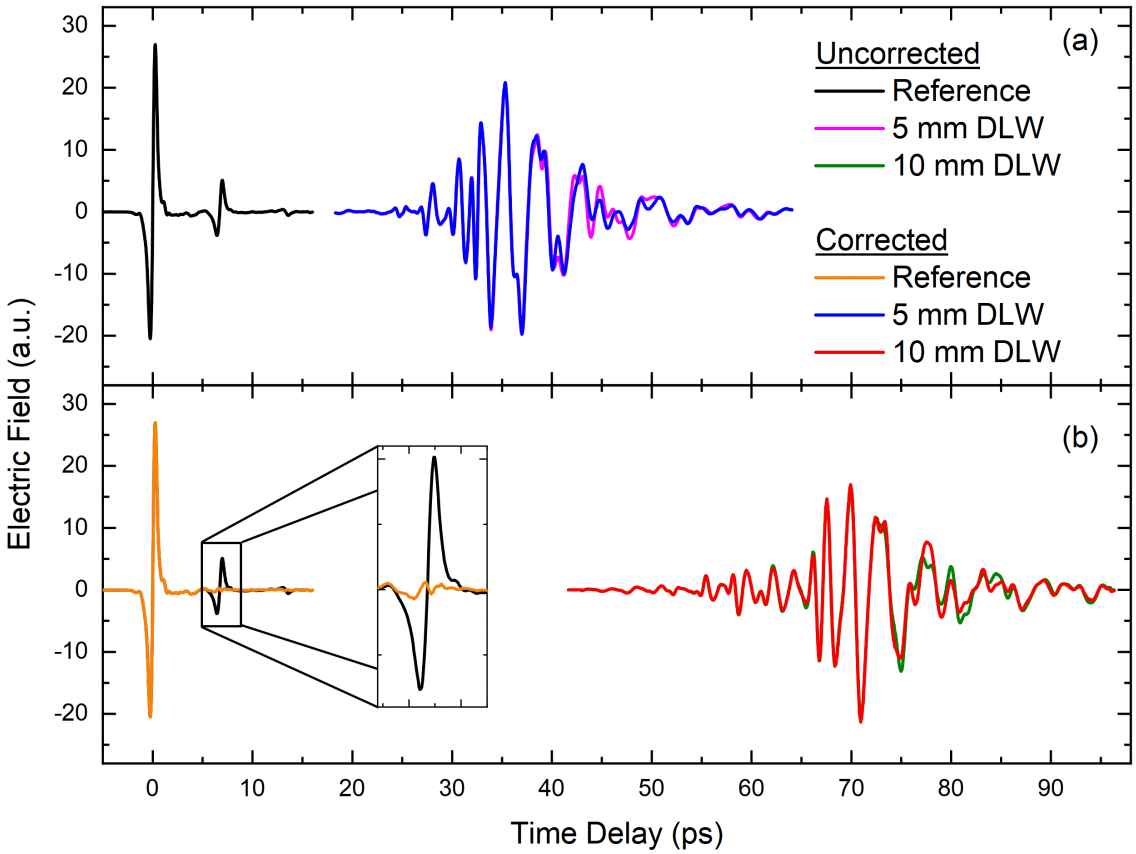

Fig. 5.10: Transmitted through (a) the 5 mm and (b) the 10 mm long DLW structure waveforms, with the reference waveform both with and without the reflection removal applied. Inset shows the effect of the deconvolution algorithm on the secondary pulse emission.

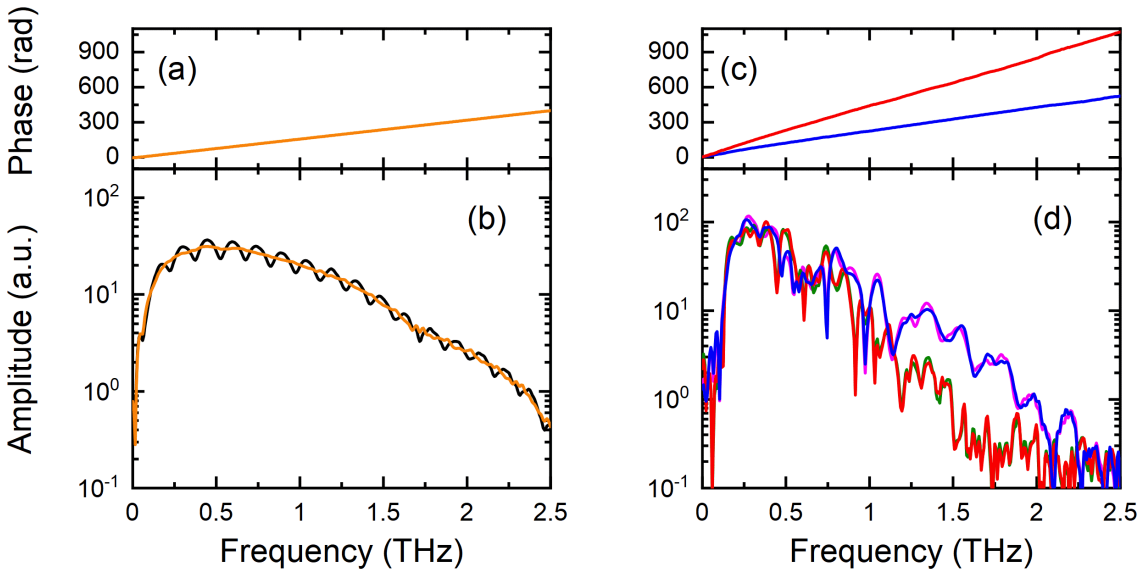

Fig. 5.11: Amplitude spectra for (b) the reference and for (d) the DLW structures both with (orange, blue and red) and without (black, magenta and green) the reflection pulse removal correction applied. The corresponding phase information in (a) and (c) respectively.

ted through the DLW structure waveforms, depicted in Figure 5.10. The parameters used for the reflection deconvolution were $r = 0.188$ and $\tau = 6.7\,\text{ps}$, taken from the experimentally measured reference waveform. The inset in Figure 5.10(b) shows the suppression of the second pulse emission in the time-domain. Figure 5.11(b) and (d) show the corrected amplitude spectra of the reference and the waveguide transmitted THz pulses with the effect of the reflection removed. It was evident from Figure 5.11(a), that the frequency modulation due to the second THz pulse emission was successfully suppressed, as the corrected amplitude spectrum was smooth spanning for a frequency range of 0.01-2 THz.

5.3.3 Dispersion relation

The electric field waveform emerging from the DLW structure was subject to dispersion from a number of transmission lines. The THz pulse propagates through free space of length of L_{fs}, the coupler of length L_c, and the dielectric-lined waveguide of length L_{wg}. Each transmission line is characterised from its corresponding propagation constant β. To obtain the dispersion due to the DLW alone, β_{wg}, the separation of the other components was required.

Here, the cut-back technique was employed, where two identical structures were used, one which incorporated a waveguide with shorter length, $L_{wg1} > L_{wg2}$. The frequency-domain of the transmitted electric field through the two DLW structure can be described by

$$\begin{aligned}\widetilde{E}_{wg1}(\omega) &= |\widetilde{E}_{wg1}(\omega)| \exp\left[-i(\beta_{fs}(\omega)L_{fs} + \beta_c(\omega)L_c + \beta_{wg}(\omega)L_{wg1})\right] \\ \widetilde{E}_{wg2}(\omega) &= |\widetilde{E}_{wg2}(\omega)| \exp\left[-i(\beta_{fs}(\omega)L_{fs} + \beta_c(\omega)L_c + \beta_{wg}(\omega)L_{wg2})\right].\end{aligned} \tag{5.5}$$

Dividing the two relations of Equation 5.5, and taking the argument yields

$$\arg\left[\frac{\widetilde{E}_{wg1}(\omega)}{\widetilde{E}_{wg2}(\omega)}\right] = \beta_{wg}(\omega)(L_{wg_1} - L_{wg_2}). \tag{5.6}$$

Rearranging Equation 5.6, the dispersion relation of the DLW is given as

$$\beta_{wg}(\omega) = \frac{1}{L_{wg_1} - L_{wg_2}} \arg\left[\frac{\widetilde{E}_{wg1}(\omega)}{\widetilde{E}_{wg2}(\omega)}\right]. \tag{5.7}$$

With the propagation constant of the waveguide defined, β_{wg}, the effect of the coupler can be obtained, using the reference pulse. The air reference electric field and the transmitted through the DLW structure can be expressed in the frequency-domain by

$$\begin{aligned}\widetilde{E}_{wg}(\omega) &= |\widetilde{E}_{wg}(\omega)| \exp\left[-i(k(\omega)L_{fs} + \beta_c(\omega)L_c + \beta_{wg}(\omega)L_{wg})\right] \\ \widetilde{E}_{ref}(\omega) &= |\widetilde{E}_{ref}(\omega)| \exp\left[-i(k(\omega)L_{fs} + k(\omega)L_c + k(\omega)L_{wg})\right],\end{aligned} \tag{5.8}$$

where $k(\omega) = \omega/c$, is the free space wavenumber, assuming that the free space would induce negligible dispersion to the travelling pulse. Following a similar procedure applied on Equations 5.6 and 5.7, the effective propagation term of the coupler, β_c, would be

$$\beta_c(\omega) = \frac{1}{L_c}\left(\arg\left[\frac{\widetilde{E}_{wg}(\omega)}{\widetilde{E}_{ref}(\omega)}\right] - \beta_{wg}(\omega)\, L_{wg} + k(\omega)(L_c + L_{wg})\right). \tag{5.9}$$

The dispersion relation of the waveguide was calculated by applying Equation 5.7 on the experimentally measured transmitted waveforms. The effective propagation

term of the coupler, β_c, was calculated by applying Equation 5.9 on the reference and the transmitted through the 10 mm-long DLW structure waveforms. In this analysis, reflection deconvolution has been applied to all the waveforms.

The experimental and modelled β_{wg} and β_c are shown in Figure 5.12. The grey shaded areas indicate regions of uncertainty in the experimental data due to low spectral amplitude. As can been seen, the model and the experimental results were in good agreement over the range 0.1-0.6 THz. In Figure 5.13, the experimentally determined phase velocity of the waveguide is outlined together with the modelled phase, v_p, and group v_g, velocities. At the operational frequency, $f_{op} = 0.47$ THz, v_p was measured to be, $v_p = 0.548 \pm 0.002c$ matching the $0.548c$ velocity of 100 keV electrons, indicated with the dashed black lines in Figure 5.13.

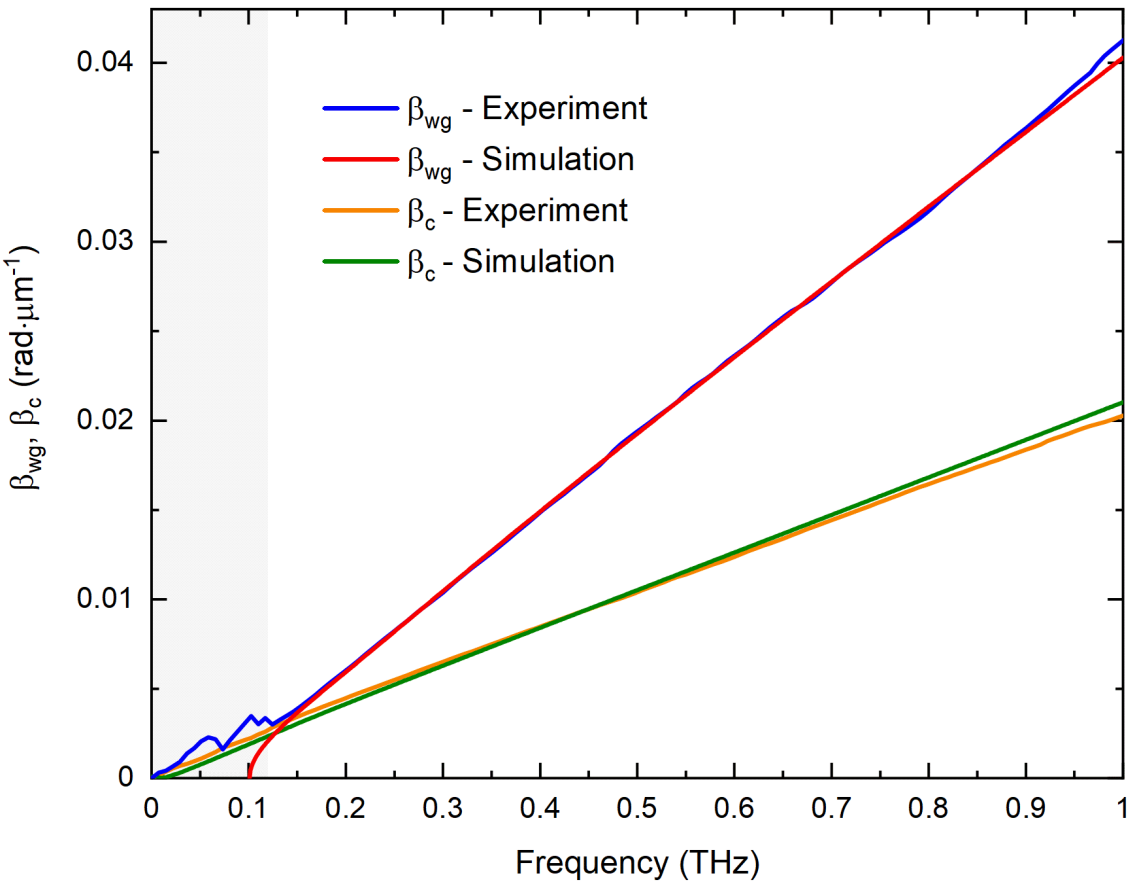

Fig. 5.12: Experimentally measured propagation constant for the waveguide, β_{wg}, and the effective propagation term for the coupler, β_c, compared with the model.

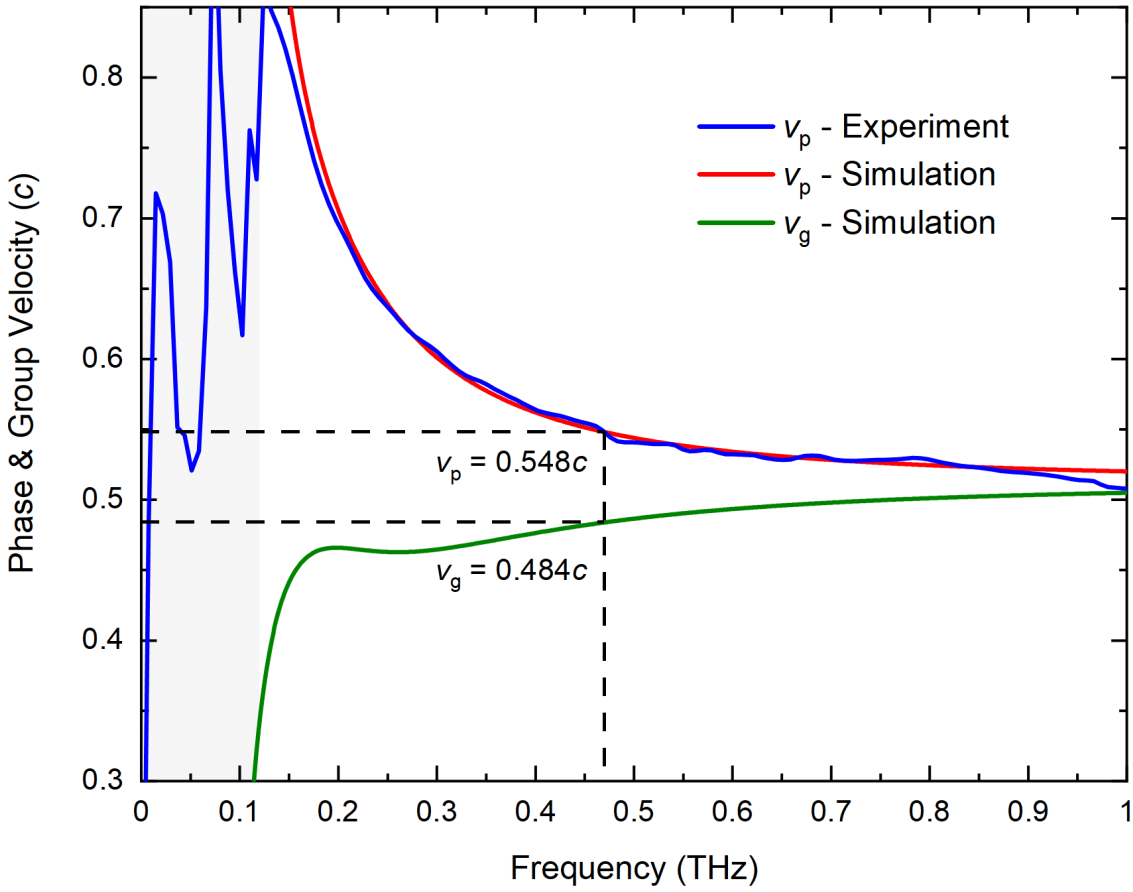

Fig. 5.13: Experimentally measured phase velocity for the waveguide, v_p, compared with the modelled v_p and v_g (see text for details). Dashed lines indicate the operational frequency which is phase velocity-matched with the velocity of 100 keV electrons.

5.3.4 Time-frequency analysis

The pulse transmitted through the DLW structure was subject to non-linear dispersion. This would make the pulse to be a non-stationary signal where the frequency content is dispersed over time. The DLW structure acts as a dispersive delay line, where the lower frequencies propagate slower than the higher frequencies. This may not be obvious at first, from neither the time-domain nor the frequency-domain of the signal. Therefore, a time-frequency (TF) analysis of the signal was carried out.

Here, the Wigner-Ville Distribution (WVD) [138, 139] was employed. WVD provides higher temporal and frequency resolution as it does not suffer from spectral leakage because no time-windows are applied like in other TF methods such as the

Short-Time Fourier Transform (STFT) [140, 141]. The WVD of a singal $S(t)$ is defined as [142]

$$W_S(t,\omega) = \int_{-\infty}^{\infty} S\left(t+\frac{\tau}{2}\right) S^*\left(t-\frac{\tau}{2}\right) e^{-i\omega\tau}\, d\tau, \tag{5.10}$$

where $S^*(t)$ is the complex conjugate of $S(t)$. The first two terms of Equation 5.10 could be described as the local autocorrelation function of $S(t)$, Fourier transformed at all time points τ. In this manner, WVD may describe how the spectral density evolves over time.

The WVD of the free space reference pulse and the pulse transmitted through the 10 mm-long DLW structure are illustrated in Figure 5.14(a) and 5.14(b), respectively. For the reference waveform in Figure 5.14(a), the WVD revealed a sub-ps long distribution with zero dispersion, as expected. All the frequency components of the broadband pulse travel in phase, temporally overlapped in free space. The red dashed line visualises the TEM_{00} mode, with zero group velocity dispersion.

For the transmitted pulse in Figure 5.14, the WVD revealed a distribution temporally stretched, with the higher frequency components arriving earlier in time, corresponding to negative chirp. The stretching and the consequent chirping of the transmitted pulse was due to the strong group-velocity dispersion of the DLW. As can be seen, the broadening of the pulse is stronger near the cut-off frequency, $f_c = 0.12$ THz. The dashed black line in Figure 5.14, visualises the combined model for the DLW structure. The model considered the propagation of the TE_{10} mode through the 44 mm-long tapered coupler. Subsequently, the pulse is propagated into the LSM_{01} mode for a total length of 10 mm. The cumulative group-velocity dispersion is visualised as the dashed black line, plotted along with the experimentally measured WVD of the transmitted pulse. As can be seen, there was a good agreement between the model and the experimental measurements for the 0.1-0.6 THz frequency range. Single-mode excitation was realised, as can been confirmed from the TF analysis.

Although WVD may provide higher time-frequency resolution, it has some other limitations when the signal has multiple components [138,142,143]. The main downside is the interference cross terms between a pair of signal components, and between negative and positive frequencies which would make the interpretation of the anal-

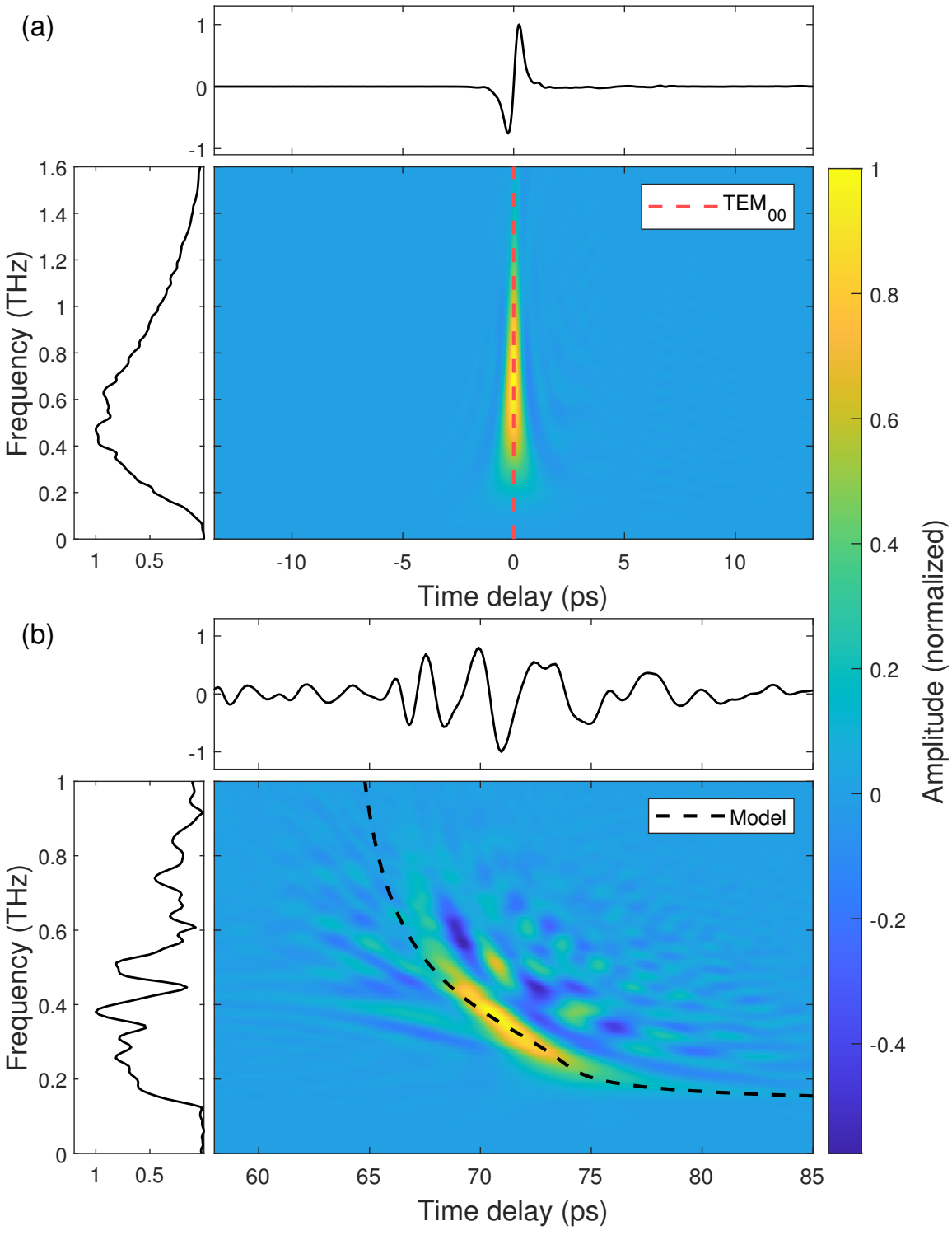

Fig. 5.14: Wigner-Ville distribution for (a) the reference pulse and (b) the transmitted through the 10 mm-long DLW structure pulse with the corresponding waveform and amplitude spectrum on the top and left, respectively. The red and black dashed lines show the TEM_{00} mode and the DLW structure model.

ysis very difficult. The latter can be simply solved by applying a Hilbert transform on the signal S(t) in Equation 5.10 [143]. In this way, the solution for the negative frequencies are neglected in the analysis. In Figure 5.14, Hilbert transformation has been applied on both signals. Therefore, the cross-terms observed in Figure 5.14(b), are due to the signal itself. Negative-amplitude components are present as a result of the cross-terms, leading to non-physical artefacts.

5.4 Conclusions

In this chapter, the deflecting mode of the DLW structure, LSM_{01}, was successfully excited and then measured by employing a custom-built THz time-domain spectrometer and using the cut-back technique. A linearly-polarised, single-cycle, broadband THz pulse was generated using a spintronic sample, which was then coupled into the DLW structure. The emerging transmitted electric field was then detected with a back-reflected geometry EO detection scheme. The DLW structure was characterised in terms of the dispersion relation of the comprised components of the device as a function of frequency. The operational frequency which is velocity phase-matched with 100 keV electrons was experimentally determined. Single-mode propagation was confirmed from the TF analysis of the results.

A simple model was developed to simulate the influence of the coupler, taking into account the assumption that the TE_{10} mode coupled into the tapered coupler. Combined with the dispersion relation of the LSM_{01} mode, the model had a good agreement with the experimental results. A deconvolution algorithm of numerically suppressing the reflection echoes due to the secondary pulse emission induced by the substrate of the THz source was also utilised. In this way, the transmitted through the DLW structure waveforms were corrected, and the frequency-modulation was removed from the spectra without introducing further artefacts or at the expense of reducing the frequency resolution.

Chapter 6

THz-driven acceleration of relativistic electrons using a DLW structure

6.1 Overview

This chapter is split into two parts. In the first part, the dielectric-lined waveguide (DLW) structure designed for the manipulation of 35 MeV electron beams was experimentally characterised. The accelerating mode of the DLW structure, LSM_{11} was studied over a broad range of frequencies, by employing a custom-built THz time-domain spectrometer. The operational frequency of the structure was subsequently experimentally determined. Free space reference and transmission measurements were required in order to determine the propagation constant of the LSM_{11} mode. The experimental results were then compared with a model.

In the second part, experimental demonstration of THz-driven acceleration of relativistic electron beams is reported. Exploitation time was allocated using the Compact Linear Accelerator for Research and Applications (CLARA) at Daresbury Laboratory [101], providing electron beams with energy of 35 MeV. The electron beam interacted with high-power multicycle THz pulses inside the DLW structure. The optical radiation was produced by a laser facility, housed at the same site §4.1.1, providing ultrafast pulses of 50 mJ energy. In this chapter, description of the implementation of the experiment, followed with results for different electron bunch parameters and THz source parameters are included.

6.2 Characterisation of the DLW structure

The DLW structure consisted of the dielectric-lined waveguide and a linearly tapered horn metallic coupler, without a dielectric lining. The DLW structure was manufactured in two parts, with the top and bottom sections joined together with the aid of alignment pins. Microscope images of the coupler entrance, Figure 6.1(a) and waveguide exit 6.1(b) indicate the measured dimensions, with a 60 μm-thick fused-quartz dielectric lining at the top and the bottom of the waveguide. The photographs were taken using a Leica DMC4500 camera [144]. In Table 6.1, the parameters of the DLW structure under investigation, are summarized.

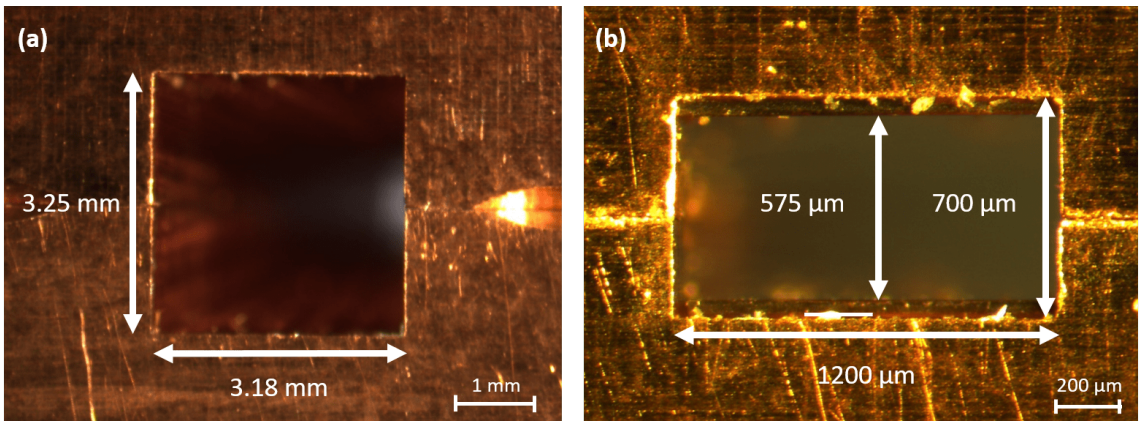

Fig. 6.1: Microscope photograph of the DLW structure (a) the entrance of the coupler and (b) the exit of the DLW waveguide.

Table 6.1: Parameter list of the DLW structure, designed for the manipulation of 35 MeV electron beams. Manufacturing tolerances are of the order of $\pm 10\,\mu$m.

Waveguide		Coupler	
Parameter	Value	Parameter	Value
2α (μm)	575	b_c (mm)	3.25
w (mm)	1.2	w_c (mm)	3.18
L (mm)	30	L_c (mm)	23
d (μm)	60		
ϵ_r	3.81		
f_c (THz)	0.24		

The structure was optically characterised by employing a custom-built THz-TDS §4.1.2, with a novel THz emitter. In order to excite the accelerating mode of the structure, LSM_{11}, a THz beam profile with a transverse polarity inversion was required. Subsequently, measurements of a broadband THz pulse transmitted through the DLW structure were performed to determine the propagation characteristics, and to identify the operational frequency of the device. The DLW structure was designed to accelerate electron beam of 35 MeV energy, corresponding to velocity of $0.999c$.

6.2.1 Experimental apparatus

A schematic diagram of the experimental setup is illustrated in Figure 6.2. The experimental setup was based on a THz time-domain spectrometer (see §4.1.2). The experimental set up was based on §5.2.1, with some modifications. The incident 800 nm beam was split into a pump beam for THz generation and a probe beam for THz detection with a 90/10 power ratio. The pump beam was expanded to a beam diameter of 20 mm, using a Galilean telescope. The expanded pump beam was used to excite a combined spintronic source with the residual transmitted 800 nm light

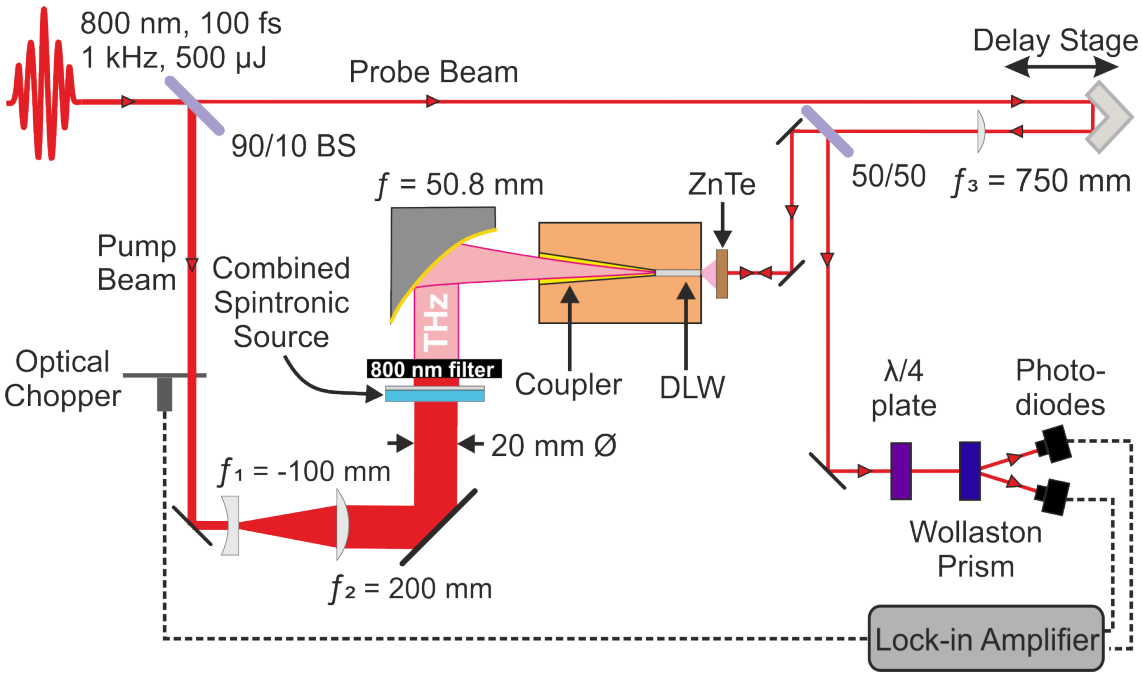

Fig. 6.2: Schematic diagram of the experimental THz-TDS setup illustrating the generation and coupling of the THz radiation into the DLW followed by a standard back-reflection geometry EO detection scheme.

beam blocked by a 800 nm filter which was a black card.

For the excitation of the accelerating mode of the waveguide, LSM_{11}, a free space THz field pattern shape similar to the TEM_{01} mode was required. Moreover, a broadband source was also necessary in order to determine the propagation constant of the LSM_{11} mode over a broad range of frequencies. In the literature, previous works have demonstrated the generation of this particular mode. Cliffe *et al.* [75] have achieved high field single-cycle THz pulses by vertically stacking two polarity-inverted $LiNO_3$ crystals, and Hibberd *et al.* [73] by patterning the magnetic field applied on a single spintronic source, with both demonstrating the generation of a quasi-TEM_{01} mode in free space.

Here, a combined spintronic source was proposed. The proposed THz emitter consisted of two vertically stacked spintronic sources with opposite ordering of the magnetic (CoFeB) and non-magnetic (Pt) layers, as illustrated in Figure 6.3. The two samples originated from the same fused-silica substrate, which was cleaved in two before separate sputtering of the spintronic layers onto each piece, allowing for alignment along the cleaved edges when combined back together. An MgO layer was used as a cap to the non-substrate side, in order to prevent oxidisation of the metallic layers. The two samples were mounted on a perspex plate, and nylon screws were used for clamping. A horizontal magnetic field was applied to the combined source by two 2 inch-diameter neodymium disc magnets, as shown in Figure 6.3, and it was measured to be 130 mT at the source center.

The emerging quasi-TEM_{01} THz beam was collected with a 2-inch diameter, gold coated, OAP mirror with a reflective focal length of 50.6 mm, into the coupler of the DLW structure. Measurements of the THz radiation transmitted through the DLW were performed using an electro-optic detection scheme, as illustrated in Figure 6.2. The electro-optic crystal was placed at the exit of the DLW structure to detect the transmitted THz electric field, using a back-reflection geometry. Two different ZnTe crystals were employed, a (110)-cut and a (100)-cut, in order to detect the transverse and longitudinal components of the electric field, respectively. All measurements were carried out at room temperature and ambient humidity.

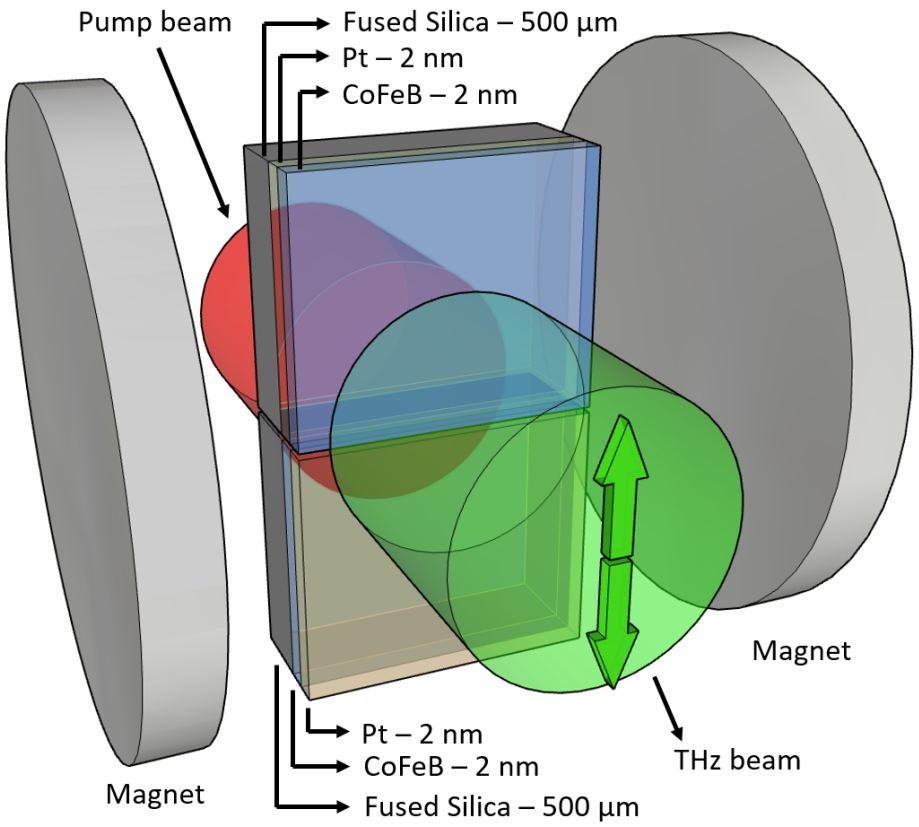

Fig. 6.3: Schematic diagram of the TEM_{01} mode-shaped THz radiation emission from a combined spintronic THz source, consisting of two vertically stacked spintronic sources with opposite ordering of the magnetic CoFeB and non-magnetic Pt layers, excited by optical radiation. Dimensions not in scale.

6.2.2 Results and analysis

The THz source was characterised first in free space, without the inclusion of the DLW structure. Both the transverse and the longitudinal components were measured by employing a different detection crystal each time. Waveforms were recorded as a function of the sampling position on the EO detection crystal.

A (110)-cut, 500 μm-thick, AR coated ZnTe crystal was used to detect the transverse field components of the combined source. The probe beam was vertically translated at the focal point of the THz beam for a range of 3.2 mm, using a computer-controlled translation stage. Figure 6.4(a) shows the spatial profile of the transverse THz electric field components as a function of time delay, with the corresponding amplitude spectra in Figure 6.4(b). A polarity flip in the field observed along the vertical sampling axis is observed, as expected for a TEM_{01}-shape beam. On the mirror

symmetry axis, the transverse fields cancel, resulting to a zero on-axis transverse electric field as it can be observed from the spectral components in Figure 6.4(b).

An approximately equal splitting into negative and positive lobes was observed. Depicted in Figure 6.5(a), the waveforms at 0.5mm from the centre of the focal point (blue and red dashed lines in Figure 6.4(a)), show the opposite polarity emerging from the two samples. The asymmetry in the field strength was attributed to a misalignment in the THz beam focusing and the detection crystal. As seen in Figure 6.5(b), the corresponding spectra with a measured bandwidth extending up to approximately 2 THz. The amplitude spectra emerging from the two samples were very similar, up to the noise level.

A model was used in order to verify the experimental results. For the model, the evolution of the transversal size and the radius of curvature of a Gaussian beam was calculated by incorporating in the system a focussing element, modelling the OAP mirror. The propagation of the Gaussian beam was performed using the ABCD matrices, used for geometric ray tracing [145–149].

To simplify the analysis of the Gaussian beam propagation, the complex beam parameter $q(z)$, was introduced, given by [150]

$$\frac{1}{q(z)} = \frac{1}{R(z)} - i\frac{\lambda}{n\pi w(z)^2}, \tag{6.1}$$

where $w(z)$ is the beam width, $R(z)$ the radius of curvature, n the refractive index of the medium the beam propagates through, c the speed of light, λ the wavelength and z the direction of propagation. The initial beam width was set to $w_0 = 10\,\text{mm}$, same as the beam width of the incident optical pump beam. The initial radius of curvature was set to $R_0 = \infty$, as a collimated beam was assumed.

The OAP mirror was treated as a focussing element with a ray transfer matrix of

$$\mathbf{M}_f = \begin{bmatrix} A & B \\ C & D \end{bmatrix} = \begin{bmatrix} 1 & 0 \\ -1/f & 1 \end{bmatrix}, \tag{6.2}$$

where f is the parental focal length of the OAP mirror. The ray transfer matrix of propagation in free space or in a medium of constant refractive index n, and distance d, can be expressed as

$$\mathbf{M}_d = \begin{bmatrix} A & B \\ C & D \end{bmatrix} = \begin{bmatrix} 1 & n\,d \\ 0 & 1 \end{bmatrix}. \tag{6.3}$$

For the model, a combined matrix of $\mathbf{M}_f\mathbf{M}_d$, with $n = 1$, $f = 50.8\,\text{mm}$ and $d = [0, 120]\,\text{mm}$ was applied to q_0 of R_0 and w_0. As Equation 6.1 denotes, different frequencies will feature different beam parameters, namely the radius of curvature and beam width for the same ray transformation matrices.

The bandwidth of the source was approximated with a modified Gaussian distribution, given by

$$U(\omega) = \exp\left[-\left(\frac{(\omega-\omega_0)}{\sqrt{2}\,\sigma_\omega}\right)^2\left(\frac{\omega_0}{\omega}\right)^x\right], \tag{6.4}$$

where ω_0 is the center frequency, σ_ω the standard deviation and x the source-dependant frequency-decay coefficient. The amplitude spectrum which was used for the model was with $\omega_0 = 0.5\,\text{THz}$, $x = 0.5$ and $\sigma_\omega = 0.42\,\text{THz}$ which corresponds to a single-cycle pulse of $1.5\,\text{ps}$ $1/e^2$ width of the field. The amplitude spectrum is depicted in Figure 6.7(a).

In Figure 6.7(b), the evolution of the beam width as a function of the drift length, is depicted for this system, at different frequencies. At higher frequencies, the beam width may reach shorter beam waist for the same focussing element, as expected. The beam waist was found to be inversely proportional to the frequency. Moreover, the foci form at different longitudinal positions for different frequencies, introducing an optical aberration.

The field pattern of the TEM_{01} mode was modelled by using the Hermite-Gaussian functions of complex argument [149, 151]. In Cartesian coordinates, the electric field pattern of the TEM_{lm} mode is given by

$$\begin{aligned} E_{l,m}(x,y,z) =& E_0\frac{w_0}{w(z)}\,H_l\left[\frac{\sqrt{2}x}{w(z)}\right]H_m\left[\frac{\sqrt{2}y}{w(z)}\right]\exp\left[-\frac{x^2+y^2}{w^2(z)}\right] \\ & \exp\left[-i\left(kz + k\frac{x^2+y^2}{2R(z)} - \psi(z)\right)\right] \end{aligned} \tag{6.5}$$

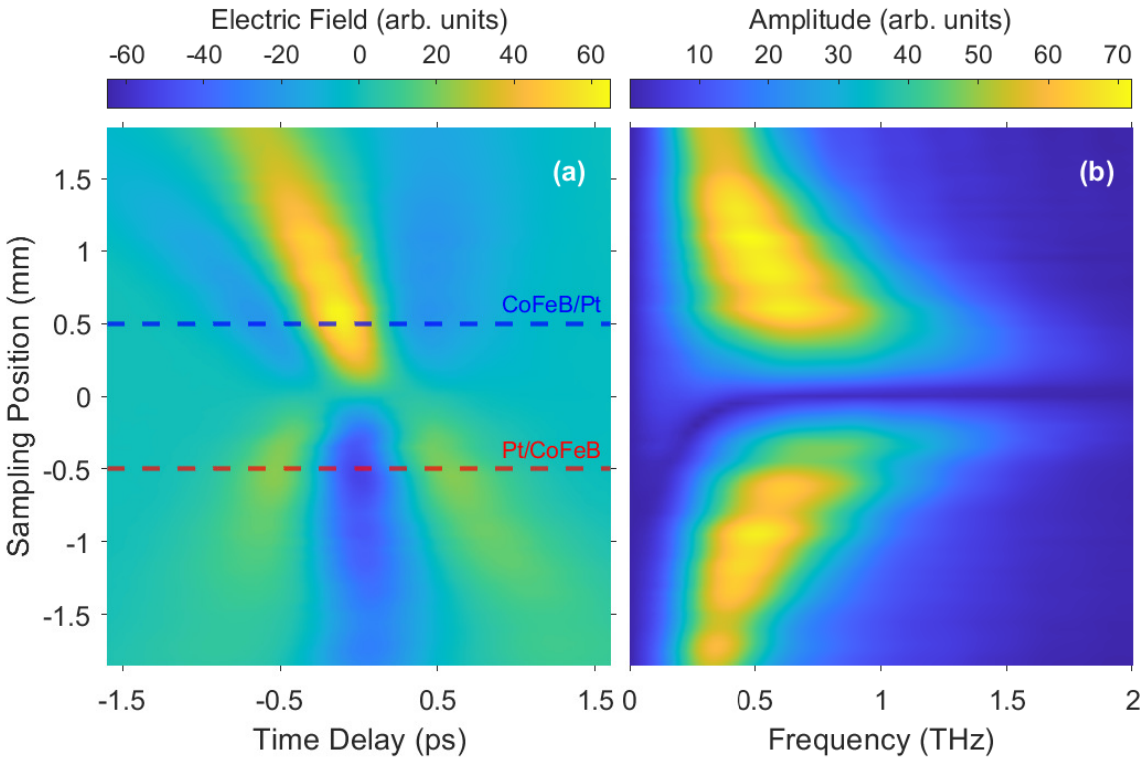

Fig. 6.4: (a) Transverse THz waveforms measured at the THz beam focus, as a function of vertical sampling position on the ZnTe (110)-cut detection crystal for the combined THz source with (b) the corresponding amplitude spectra. The waveforms outlined in blue and red dashed lines are plotted in Figure 6.5.

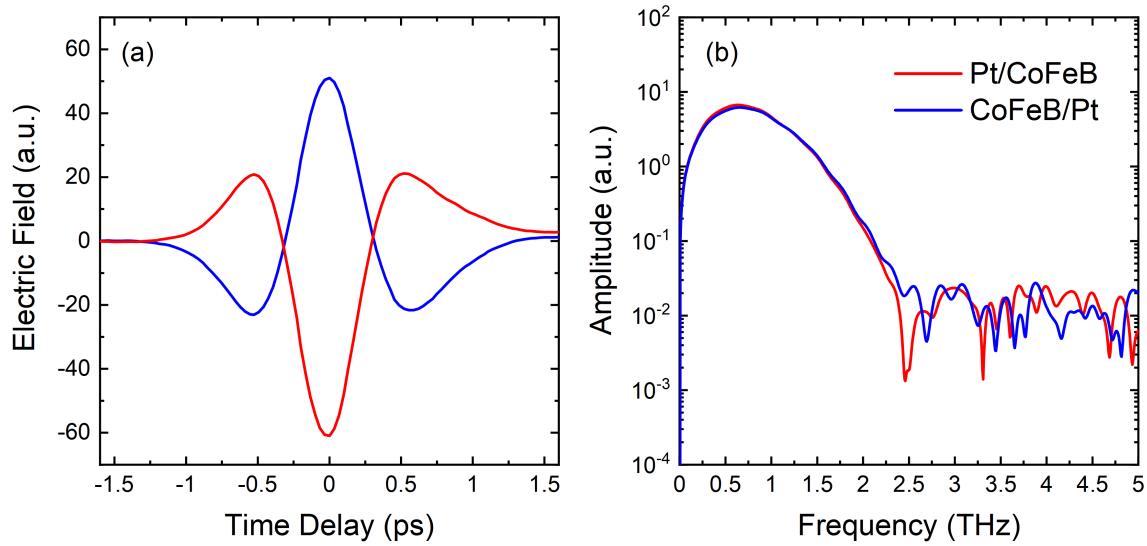

Fig. 6.5: (a) Transverse electric field waveforms obtained at sampling positions ±0.5 mm from the center of the focal point with (b) the corresponding amplitude spectra. The blue and red line correspond to the blue and red dashed lines in Figure 6.4, respectively.

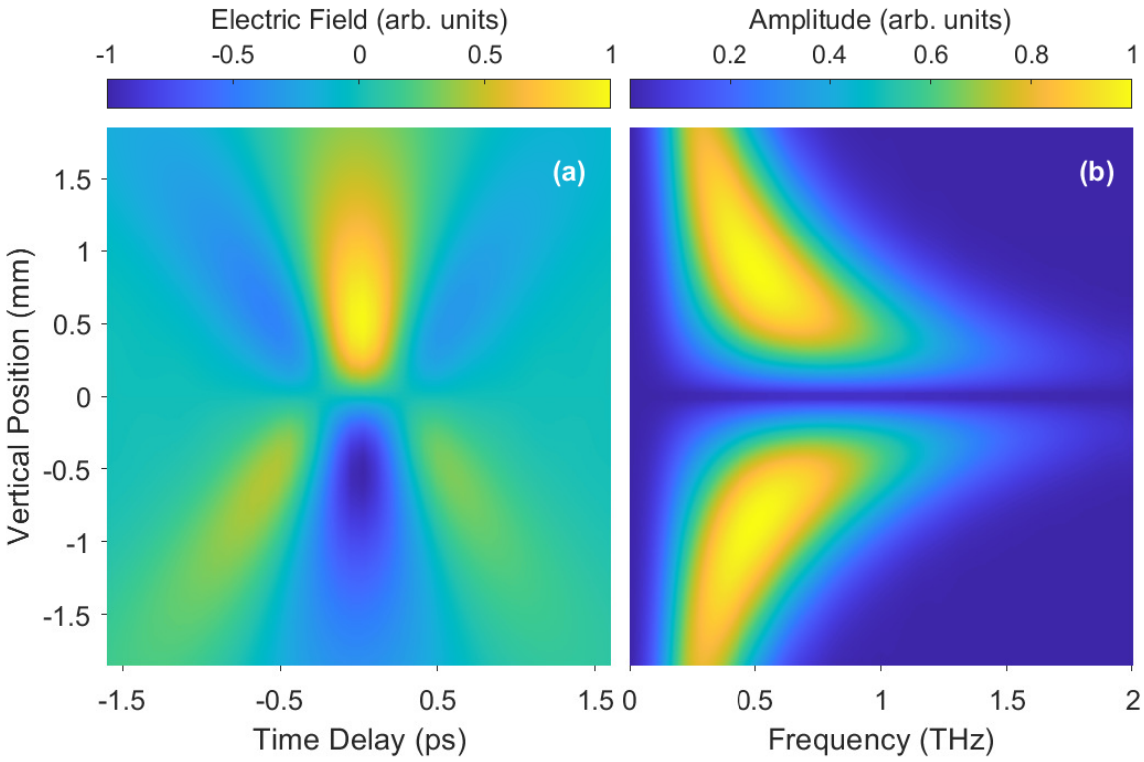

Fig. 6.6: (a) Modelled transverse THz waveforms for a TEM_{01} mode, as a function of the vertical position, at the focal point, with (b) the corresponding amplitude spectra. An initial beam width $w_0 = 10\,\text{mm}$, intial radius of curvature $R_0 = \infty$, and a focussing element of focal length $f = 50.8\,\text{mm}$, was used for the model.

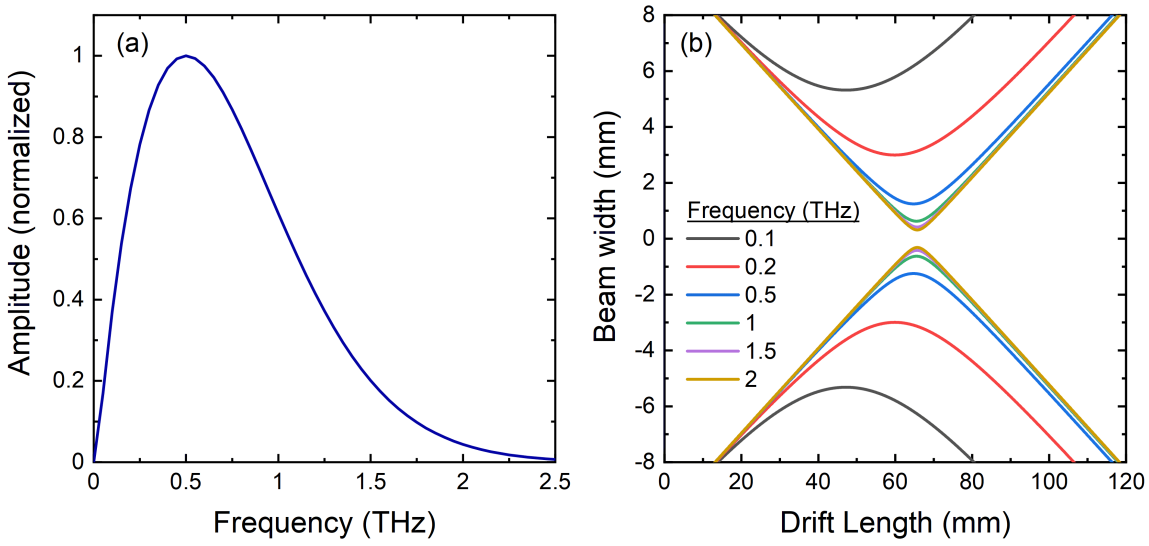

Fig. 6.7: (a) Normalised amplitude spectrum used for the TEM_{01} mode beam model. (b) The modelled beam width as a function of drift length, calculated for different frequencies.

where E_0 is the amplitude, $\psi(z)$ the Gouy phase, k the wavenumber and H_i the i-th order Hermite polynomial. For $l = m = 0$, the fundamental TEM_{00} mode is obtained.

In Figure 6.6(a), the modelled TEM_{01} mode transverse electric field pattern is plotted, as a function of the vertical position and time delay. The time and position range were selected as such, to be the same to Figure 6.4, for easier comparison. The electric field pattern was modelled by using Equation 6.5, for l=0, m=1, solving for every frequency and eventually superimposing across the whole bandwidth for the final result. For every frequency, the amplitude E_0 and beam width $w(z)$ was extracted from Figure 6.7(a) and 6.7(b), respectively. By Fourier transforming the waveforms at each position, the corresponding amplitude spectra are obtained and plotted in Figure 6.7(b).

As can be seen, the experimental results agree very well with the model. The characteristic flip polarity of the electric field is evident in both occasions, as well as the beam size at the focal point, for the corresponding bandwidth. The only difference noticed at the experimental results, is the skewing of the upper half of the electric field, which has been attributed to some slight misalignment of the EO detection crystal in respect to the probe beam. The amplitude spectra show a zero on-axis component, as expected for a TEM_{01} mode beam. The experimental results in conjunction with the model, have validated that the proposed combined spintronic source successfully produced a TEM_{01} mode-shaped broadband THz beam, necessary for the excitation of the accelerating LSM_{11} mode of the waveguide.

Subsequently, the longitudinal components of the electric field were measured. For these further measurements, a (100)-cut, 500 μm-thick, AR coated ZnTe crystal was employed as a detection crystal. Figure 6.8 depicts the longitudinally polarised THz waveform and spectral amplitude as a function of the sampling position on the EO detection crystal.

As can be seen, the peak of the longitudinally polarised radiation was measured to be on-axis, where there is zero transverse component. This was due to the transverse field gradient, arising from the polarity flip in the transverse polarisation by the interferometric combination of two reverse-order grown spintronic samples, as explained by Cliffe *et al.* [75]. The waveform measured on-axis (sampling position at 0 mm) with the corresponding spectral amplitude is plotted in Figure 6.9.

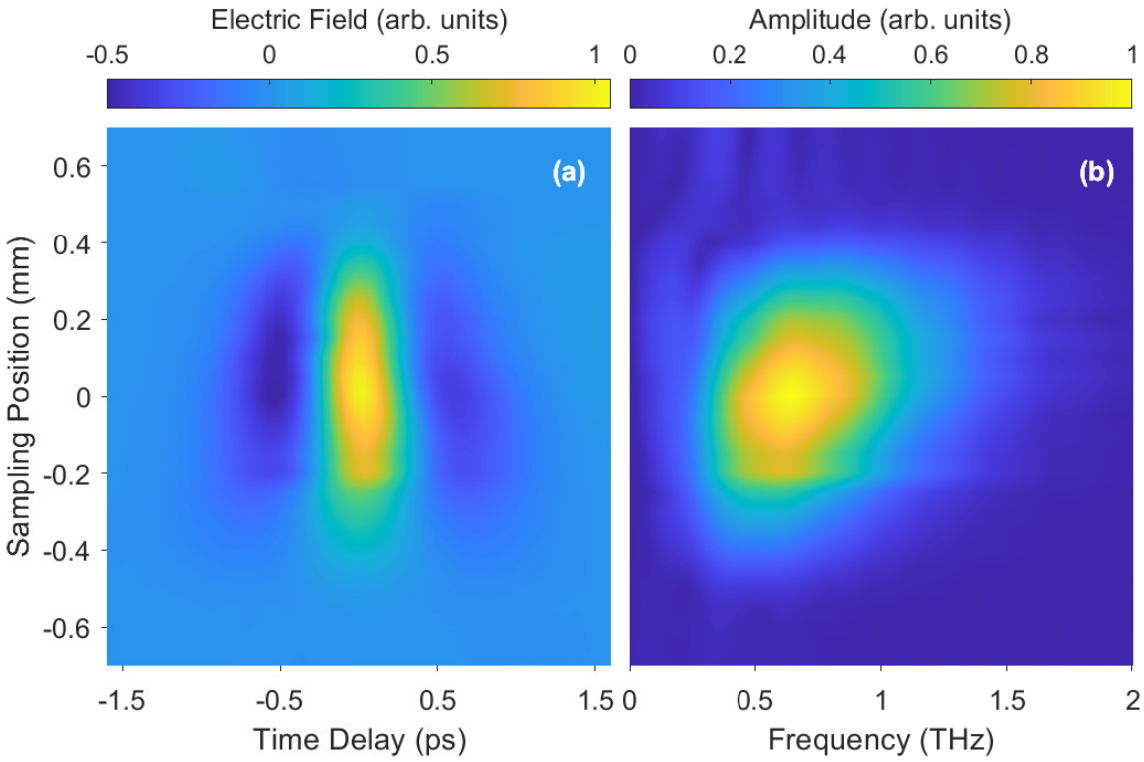

Fig. 6.8: (a) Longitudinal THz waveforms measured at the beam focus, as a function of vertical sampling position on the ZnTe (100)-cut detection crystal for the combined THz source with (b) the corresponding amplitude spectra.

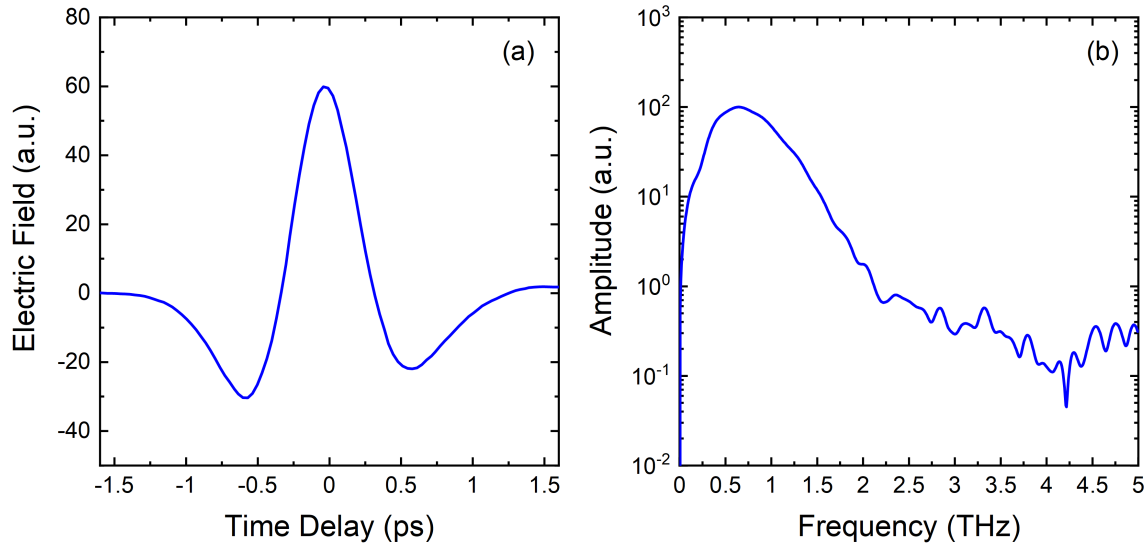

Fig. 6.9: (a) Longitudinal electric field waveform obtained at sampling position 0 mm, employing a (100)-cut ZnTe as a detection crystal. (b) The corresponding spectral amplitude.

A single-cycle, broadband longitudinally polarised pulse was measured, extending up to 2 THz bandwidth.

As the proposed combined source was characterised, and supported by a model, a TEM_{01} mode broadband THz pulse was produced. The generated pulse was then transmitted through the DLW structure. For the transmission measurements, the coupler of the DLW structure was placed approximately at the focal point, and the EO crystal was placed at the exit of the waveguide. A (100)-cut, 2 mm-thick ZnTe crystal was employed for the EO detection of longitudinally polarised radiation.

Free space and transmitted through the DLW structure waveforms were measured in order to determine the dispersion effect of the structure. In Figure 6.10, the measured free space and transmitted waveforms are depicted, with the corresponding

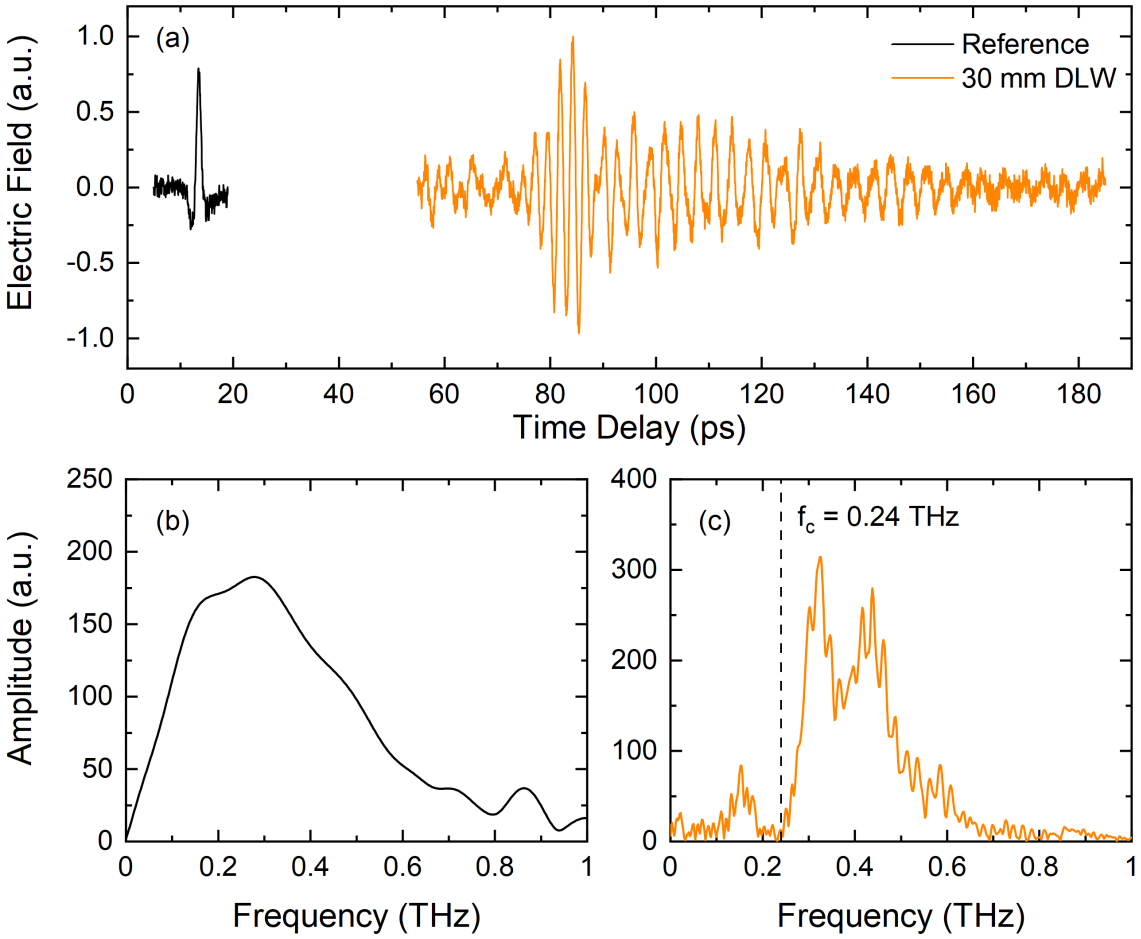

Fig. 6.10: (a) Longitudinally polarised reference free space waveform and transmitted through the 30 mm-long DLW structure waveform, measured with a (100)-cut, 2 mm-thick ZnTe detection crystal. Corresponding amplitude spectra of (b) the reference and (c) the transmitted pulse with the calculated cut-off frequency, f_c, for the LSM_{11} mode.

amplitude spectra. The reference pulse, which had a duration of approximately 1 ps, has been stretched to approximately 90 ps. Moreover, the peak-to-peak time delay of the reference and the transmitted pulse was roughly 70 ps. This indicated the strong group-velocity dispersion dispersion of the structure. The reason that the reference pulse looked different from Figure 6.9, was because the detection crystal remained where the exit of the structure was, and that was not at the focal point of the source. In addition, a thicker detection crystal was used.

A cut-off frequency was observed in the spectral amplitude of the transmitted through the DLW structure pulse, shown in Figure 6.10(c). The cut-off frequency was experimentally measured at 0.23 ± 0.05 THz, which was is in a good agreement with the calculated for the LSM_{11} mode, 0.24 THz. The spectral content measured before the cut-off frequency was believed to be due to misalignment of the source with respect to the entrance of the structure, allowing a lower mode to couple, but at significantly lower coupling efficiency. The immediately lower waveguide available mode is the LSM_{01} mode, with a calculated $f_c = 0.12$ THz, for the given structure geometry.

The cut-back technique used in Chapter 5, could not be applied here. The reason is that there was no availability of a secondary structure with the same geometry as the one under investigation. Therefore, the effect of the coupler could not be eliminated from the analysis. The effect of the coupler was instead modelled as explained in §5.3.1. The dispersion relation of the waveguide was then calculated by deconvolving the effect of the coupler from the transmitted pulse.

The reference free space and the transmitted through the DLW structure electric field can be expressed in the frequency-domain by

$$\begin{aligned} \widetilde{E}_{wg}(\omega) &= |\widetilde{E}_{wg}(\omega)| \exp\left[-i(k(\omega)L_{fs} + \beta_c(\omega)L_c + \beta_{wg}(\omega)L_{wg})\right] \\ \widetilde{E}_{ref}(\omega) &= |\widetilde{E}_{ref}(\omega)| \exp\left[-i(k(\omega)L_{fs} + k(\omega)L_c + k(\omega)L_{wg})\right], \end{aligned} \tag{6.6}$$

where $k(\omega) = \omega/c$, is the free space wavenumber, L_{fs} the free space length, L_c the length of the coupler, L_{wg} the length of the waveguide, β_c the effective propagation constant of the coupler and β_{wg} the propagation constant of the waveguide. Dividing the two expressions in Equation 6.6, taking the argument and rearranging, the propagation of the waveguide is given as

$$\beta_{wg}(\omega) = \frac{1}{L_{wg}} \left(\arg \left[\frac{\widetilde{E}_{wg}(\omega)}{\widetilde{E}_{ref}(\omega)} \right] - \beta_c(\omega) L_c + k(\omega)(L_c + L_{wg}) \right). \tag{6.7}$$

For the modelling of β_c, the transmission line was segmented into N cascaded hollow rectangular waveguides, of length dz, with variable transverse dimensions. The TM_{11} mode was launched for a single-cycle, broadband pulse, covering a frequency range of 0.01-3 THz. The spatial step size was set to $dz = 50\,\mu$m, for a total length equal to the length of the coupler, $L_c = 23$ mm.

The dispersion relation of the waveguide was determined by applying Equation 6.7 on the experimentally measured reference and transmitted waveforms. The experimental and modelled β_{wg} as well as the modelled β_c are shown in Figure 6.11. The grey shaded areas indicate regions of uncertainty in the experimental data due to low spectral amplitude. Because of the lower frequency content, a residual offset

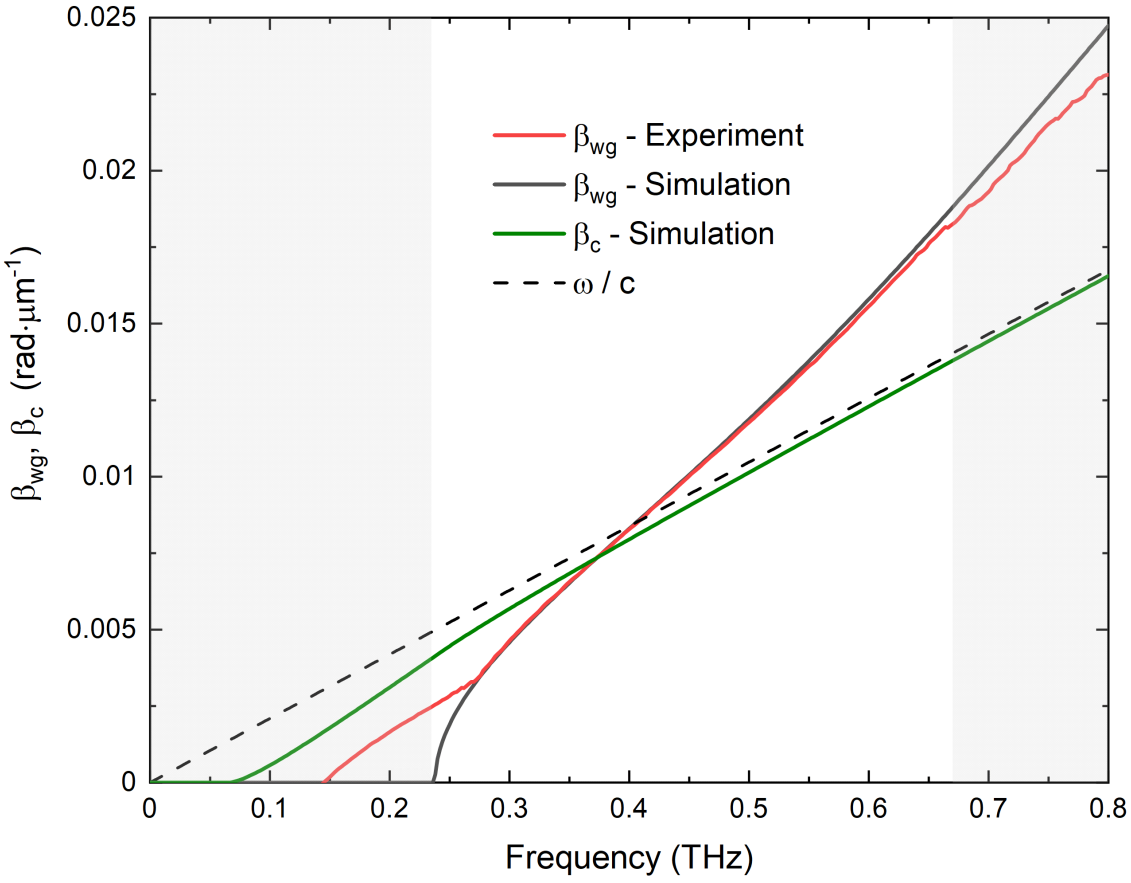

Fig. 6.11: Experimentally measured propagation constant for the waveguide, β_{wg}, and the effective propagation term for the coupler, β_c, compared with the model. The black dashed line denotes the speed of light in vacuum, ω/c.

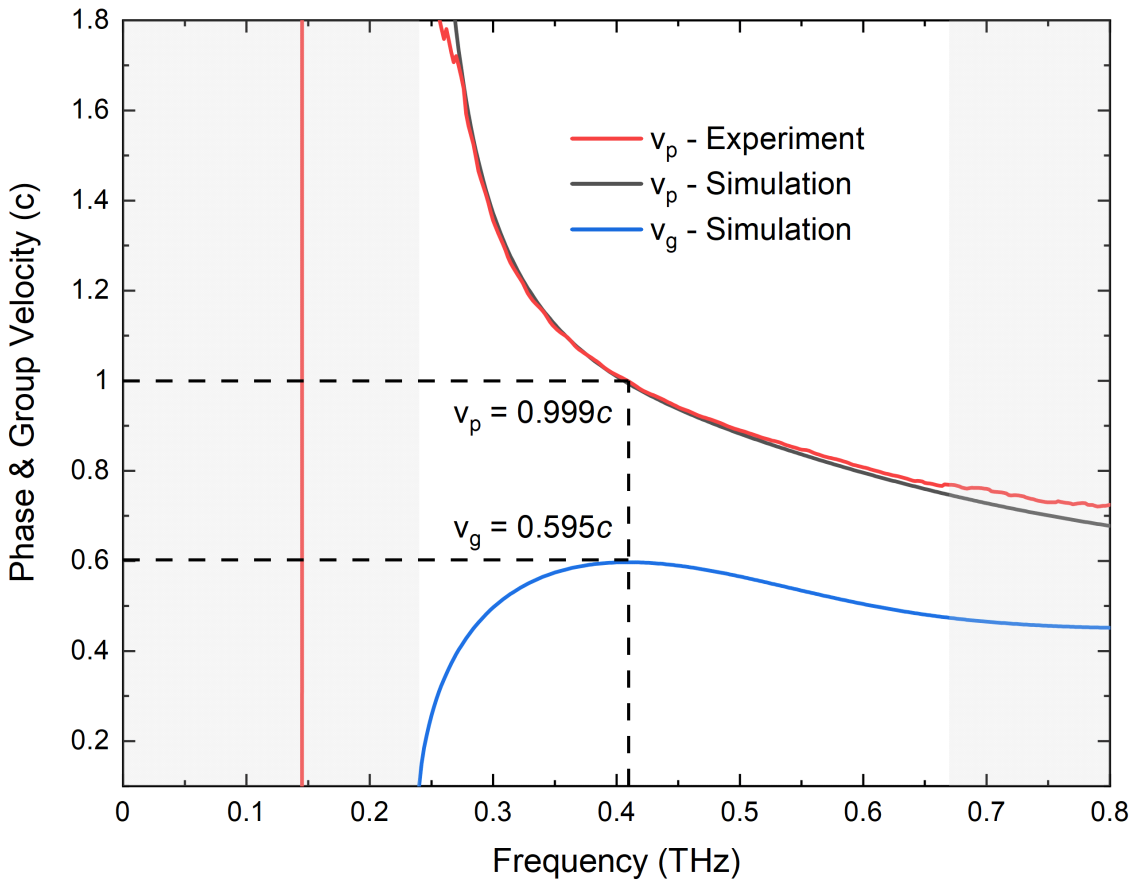

Fig. 6.12: Experimentally measured phase velocity for the waveguide, v_p, compared with the modelled v_p and v_g. The dashed lines indicate the operational frequency which is phase velocity-matched with the velocity of 35 MeV electrons.

was remained in β_{wg}, which was manually removed from the analysis. The experimentally phase velocity of the waveguide is outlined together with the modelled phase v_p and group v_g, velocities for the LSM_{11} mode. The operational frequency was experimentally determined $f_{op} = 0.41 \pm 0.02$ THz, where v_p is matched to the velocity of 35 MeV electrons, $0.999c$, indicated with the dashed black lines in Figure 6.12. The group velocity at the operational frequency was calculated to be $v_g = 0.595c$, for the LSM_{11} mode.

A time-frequency analysis has been carried out, on the measured waveforms. The Wigner-Ville Distribution (WVD) was employed, as explained in §5.3.4. The WVD of the free space and transmitted through the 30 mm-long DLW structure waveforms are illustrated in Figure 6.13(a) and 6.13(b), respectively. The transient signal and the amplitude spectrum of the signals are plotted on the top and at the left, respectively.

For the free space pulse, the WVD revealed a ps-long distribution with all the frequency components temporally overlapped, as expected. For the transmitted pulse, the WVD revealed a distribution temporally stretched, with the higher frequency components arriving earlier in time, corresponding to negative chirp. The stretching and the consequent chirping of the transmitted pulse was due to the strong group-velocity dispersion of the waveguide. The broadening of the pulse is stronger close to the cut-off frequency, $f_c = 0.24\,\mathrm{THz}$.

The dashed orange line in Figure 6.13(b), depicts the model for the DLW structure, consisted of the tapered coupler and the DLW. The model considered the propagation of the TM_{11} mode through the 23 mm-long tapered coupler and the propagation of the LSM_{11} mode for a total length of 30 mm. The cumulative group-velocity dispersion is visualised as the dashed orange line, plotted along with the experimentally measured WVD of the transmitted pulse. As can be seen, there was a good agreement between the model and the experimental measurements for the

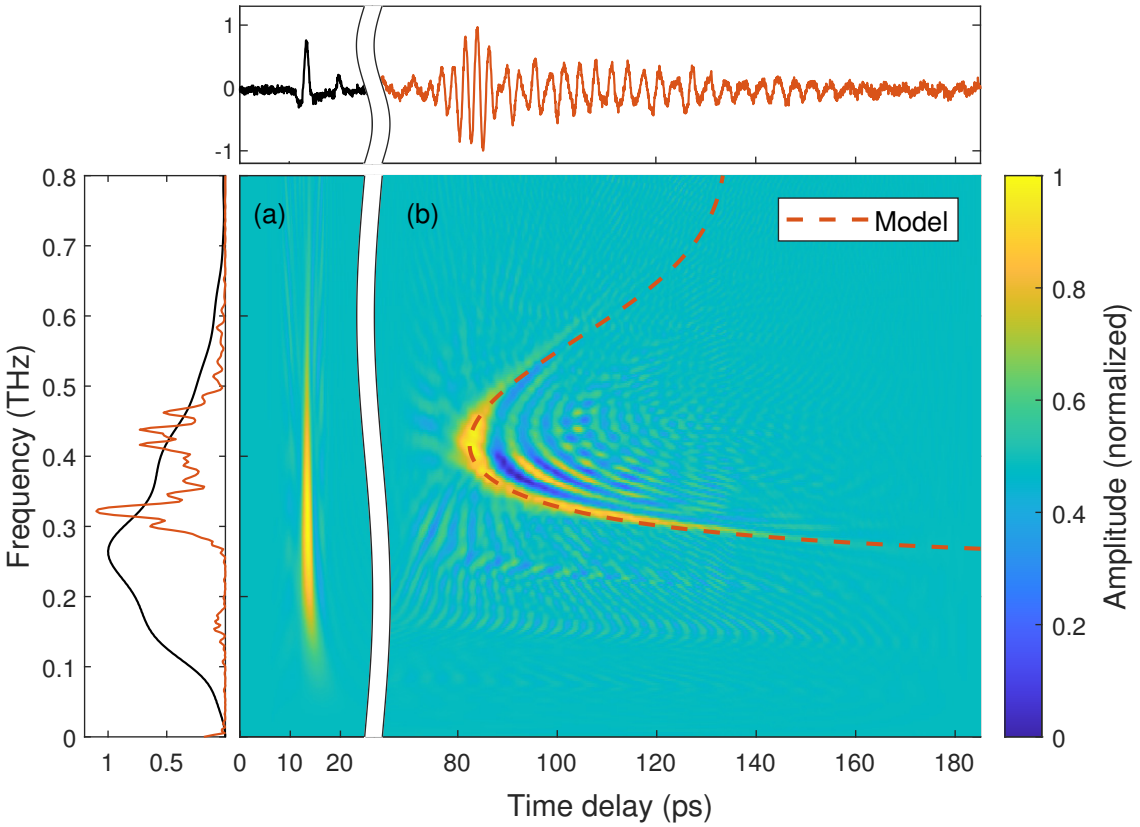

Fig. 6.13: Wigner-Ville distribution for (a) the reference pulse and (b) the transmitted through the 30 mm-long DLW structure pulse with the corresponding waveform and amplitude spectrum on the top and the left, respectively. The orange dashed line in (b) shows the modelled group velocity dispersion of the DLW structure.

0.24-0.6 THz frequency range.

6.2.3 Summary

A proposed THz emitter was manufactured and then characterised, producing broadband THz pulses into the TEM_{01} mode. The electric field pattern generated by the source was measured in free space, at the focal point, verifying the generation of the desired mode with a model. The model made use of Gaussian beam propagation for a broadband pulse. The generated THz radiation was subsequently coupled into the DLW structure in order to excite the accelerating mode of the waveguide. The transmitted pulse, emerging from the DLW structure, was measured in order to determine the propagation constant of the LSM_{11} mode. From the analysis, the operational frequency of the structure was experimentally determined, $f_{op} = 0.41$ THz, which is phase velocity matched with the velocity of 35 MeV electron beams.

6.3 Experimental demonstration of electron acceleration

Exploitation time using the CLARA facility at Daresbury Laboratory was allocated for THz-driven acceleration of relativistic electron beams testing. Electron beams with an energy of 35 MeV were provided by the CLARA test facility, and the optical radiation from the LATTE lab, both located at the same site but in separated rooms. The interaction of relativistic electron beams and high field THz pulses co-propagating through a DLW structure was investigated.

6.3.1 Experimental apparatus

The optical experimental setup was installed in BA1 on an optical table, next to the vacuum chamber. Because of the limited allocation time in BA1, the optical apparatus was pre-assembled and tested in the LATTE lab on optical breadboards, and then moved into the BA1. A schematic diagram of the experimental setup is illustrated in Figure 6.14. Only the optical table and the vacuum chamber of BA1 are depicted here.

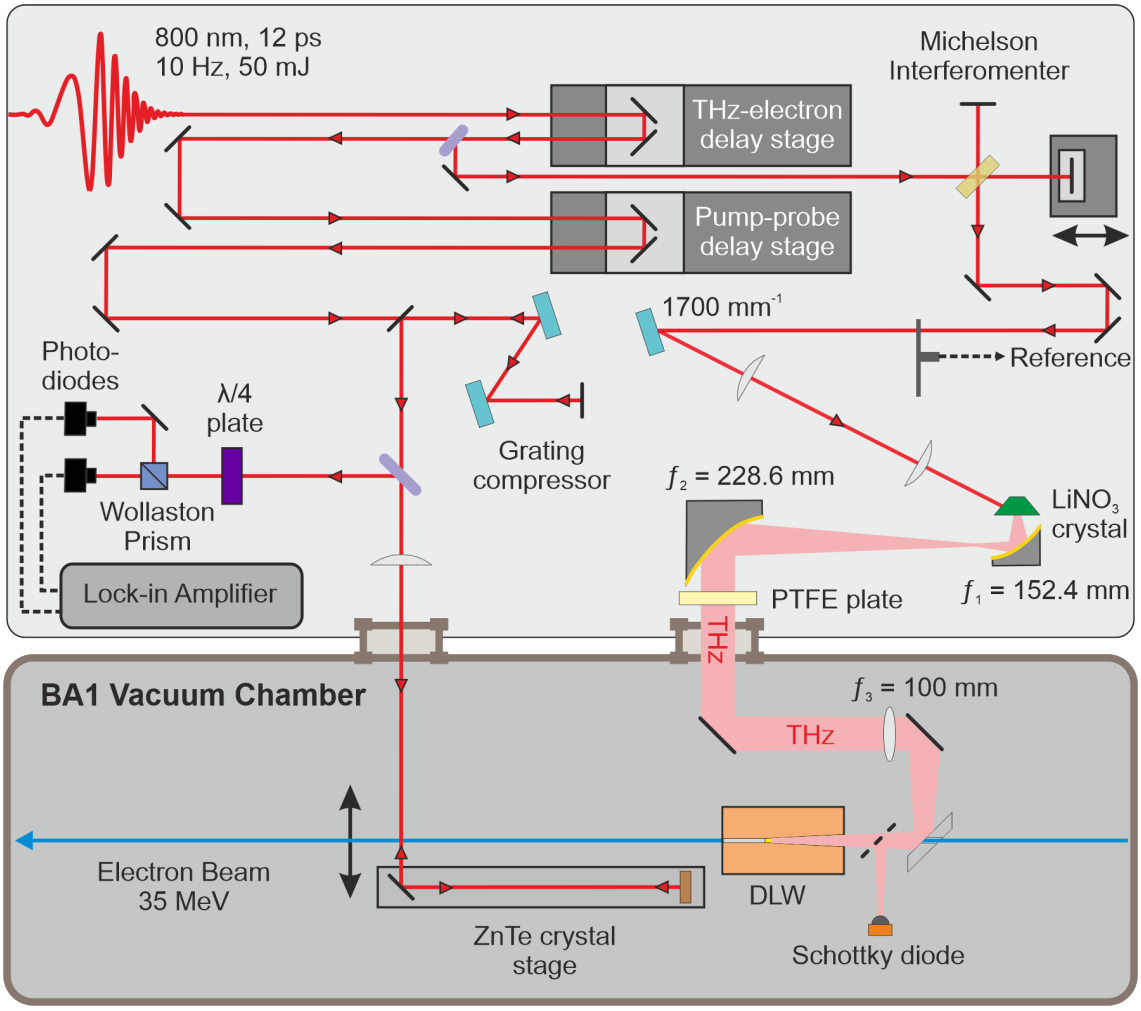

Fig. 6.14: Schematic diagram of the optical experimental setup outside the interaction vacuum chamber in BA1, CLARA test facility. Narrowband THz pulses were generated using a chirped pulse beating scheme combined with tilted pulse-front pumping on a $LiNbO_3$ srystal. The THz pulses were transported and coupled in the DLW structure, in the vacuum chamber. Relativistic electron beams co-propagated and interacted with the THz pulses in the DLW structure, and then transported onto an energy spectrometer. An electro-optic detection scheme was used in atmosphere, with the probe beam compressed.

The input laser beam was produced by the TW laser system in the LATTE lab, and delivered to the BA1 user facility via a metallic beam transport line under vacuum. The laser beam was 800 nm center wavelength, with 50 mJ pulse energy and 10 Hz repetition rate. For the requirements of the experiment, an added phase chirp was added to the laser pulse by adjusting the final compressor grating pair of the TW laser, resulting to a pulse duration of approximately 12 ps FWHM. Two delay stages (Newport) were then used, in order to vary the THz-electron timing and the THz-probe beam delay, respectively. The laser beam was split into a pump

beam for THz generation and a probe beam for EO detection with a reflective 95:5 ratio beam splitter after the THz-electron delay stage.

Narrowband THz pulses of a 100 GHz FWHM bandwidth with tunable center frequency were generated through chirped pulse beating (CPB) in a 0.6% MgO-doped stoichiometric $LiNbO_3$ (LN) crystal. The phase chirp was introduced by adjusting the grating separation of the TW laser compressor. The chirped pump pulse was then split into two pulses by a 50:50 beam splitter, and a time delay was induced to one of the pulses by a variable manual stage, with respect to the other by a Michelson interferometer arrangement.

The two propagating pulses were then spatially recombined, and transported to a pulse-front-tilt (PFT) configuration. A holographic grating (Spectrogon) of groove density of 1700 mm^{-1} was used to achieve the PFT in the -1 diffraction order, and a $4f$ lens configuration consisting of two cylindrical lenses with focal lengths of 130 mm and 75 mm was used to image the grating surface onto the LN crystal. The diffracted and incident angles as well as the choice of the two cylindrical lenses were determined as discussed in §3.2.3, for efficient THz generation in a LN crystal. As depicted in Figure 6.15, the incident angle was set at $\theta_i = 31.1°$ with a corresponding diffracted angle $\theta_d = 57.5°$ for a pump-pulse front angle of $\gamma = 63°$. The group, n_g, and the phase, n_ϕ, refractive indices at 800 nm were not measured for the particular LN crystal, but taken from the literature [152]. Because of the different growing technique of the LN crystal from the one of the literature, a 5% uncertainty was included in the determination of the aforementioned refractive indices. The deviation of the appropriate magnification for efficient THz generation was explored, as shown in filled areas in Figure 6.15. The deviation from the center incident and diffracted angle was considered negligible or within the precision of the rotational stage that the diffraction grating was mounted on. The horizontal magnification factor provided by the $4f$ lens geometry was 0.577, which was within the calculated range $\beta_1 = \beta_2 = 0.58 \pm 0.02$.

The resulting pump beam of 18 mJ energy and with a spot size of 5 mm x 10 mm $1/e^2$, excited the LN crystal, generating THz pulses of approximately 2.1 μJ pulse energy, as measured at the crystal surface with a pyroelectric detector (THz-I-BNC, Gentec). The attachable cone coupler of the detector was used to collect the diverging THz radiation, with the sensor covered with a black plastic film in order to

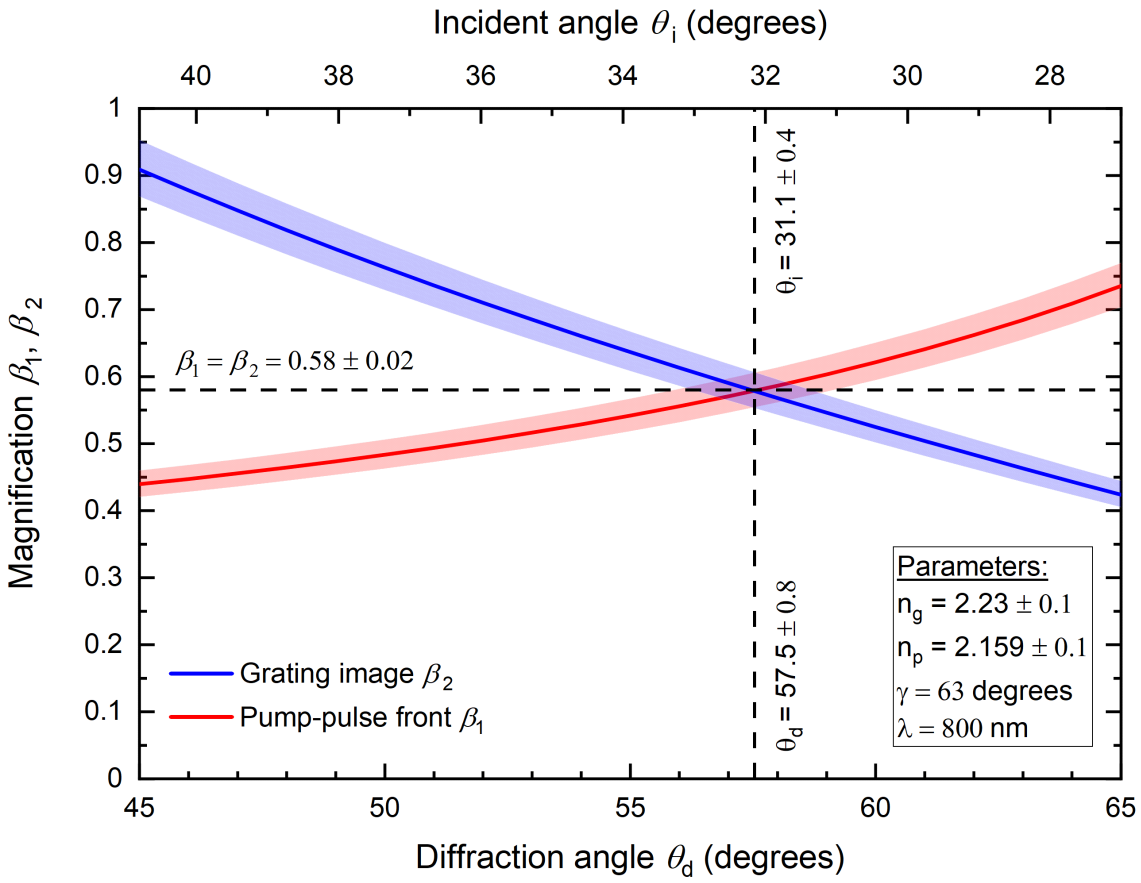

Fig. 6.15: Calculated magnifications of the pump-pulse front β_1, and the grating image β_2 as a function of the diffraction θ_d and incident angle θ_i for a 1700 mm^{-1} diffraction grating. The dashed lines indicate the combination of angles that $\beta_1 = \beta_2$. The filled area indicates the uncertainty in the magnification due to the uncertainty of the refractive index of $LiNbO_3$ at 800 nm.

block any residual optical radiation.

The THz radiation was then collected and transported into the vacuum chamber through a quartz window. An initial pair of OAP mirrors of parental focal lengths of $f_1 = 152.4$ mm and $f_2 = 228.6$ mm was used to collect and collimate the emerging THz radiation, which was then routed with silver mirrors to the interaction point in the vacuum chamber. Focusing of the THz radiation was achieved using a third TPX lens of focal length $f_3 = 100$ mm, resulting in a $1/e^2$ spot size of approximately 3 mm at the DLW structure coupler entrance. In Figure 6.16, the modelled beam width as a function of the drift length, calculated for different frequencies is depicted. The beam transport was designed to deliver a THz beam of spot size smaller than the entrance of the coupler with the minimum chromatic dispersion. For the model,

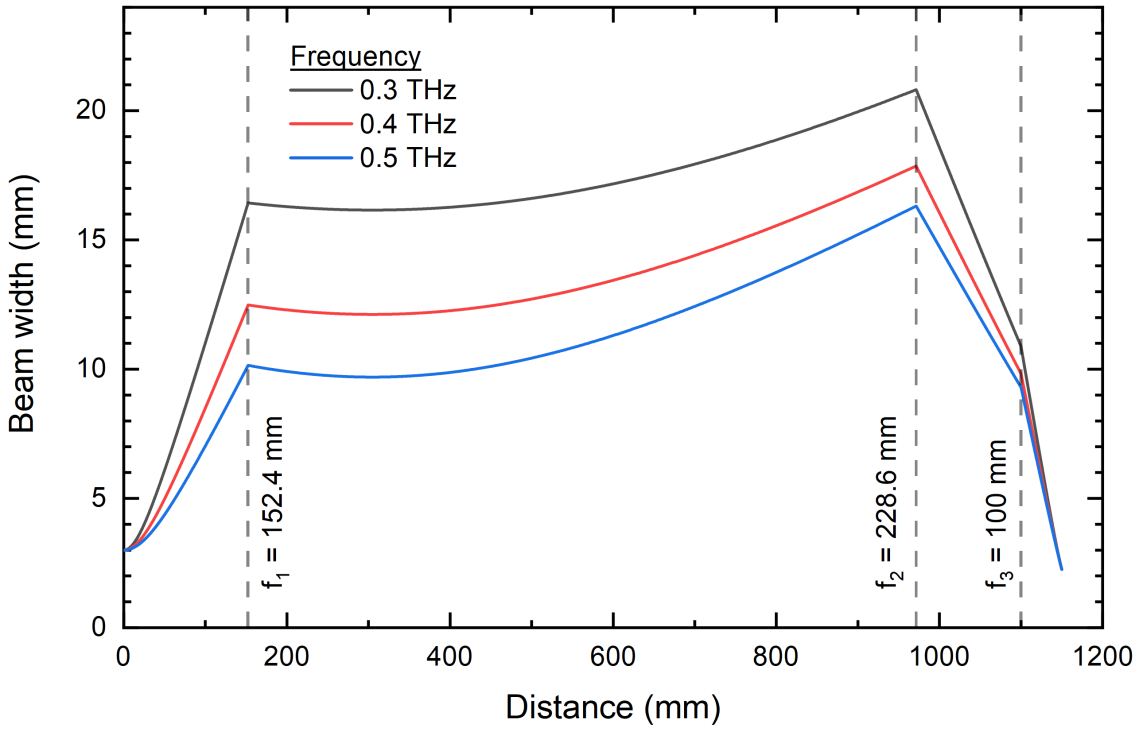

Fig. 6.16: Modelled beam width of the THz beam as a function of the drift length, calculated for different frequencies. The dashed lines indicate the position of each focusing element along the THz beam transport.

an initial beam width of $w_0 = 3\,\text{mm}$ and a radius of curvature of $R_0 = \infty$ was considered. The model had a good agreement with the experimentally measured spot size at the entrance of the coupler, measured with a knife edge. The spot size of the pump beam was also measured using a knife-edge. The pulse energy measured at the coupler entrance of the DLW structure was $0.79\,\mu\text{J}$, as half of the energy was expected to be reflected from the quartz window, and further 25-30% loss from the TPX lens.

For exciting the accelerating LSM_{11} mode of the DLW structure, a quasi-TEM_{01} THz mode in free space was required. The intial plan, was to vertically stack two LN crystal with inverted polarity, as it was demonstrated by Cliffe *et al.* [75]. However, the two crystals could not be fixed so that the path length of the 800 nm laser beam was the same, resulting in a time delay between the emerging waveforms. Moreover, the two LN crystals were not performing with the same efficiency, resulting to an uneven intensity between the top and the bottom portions of the THz intensity pattern. A different approach was followed, by employing only one LN crystal and introducing a phase shift delay of half a cycle between the top and bottom halves

of the THz beam. This approach was proposed as the generated THz pulse was narrowband, where for a broadband pulse this approach would not have been ideal. The phase delay was applied with a 40 mm-diameter polytetrafluoroethylene (PTFE) plate, which was made with a thickness difference between the top and the bottom halves of $d = \lambda_0/(2(n-1)) \approx 900\,\mu$m, where λ_0 is the center wavelength of the THz pulse and $n = 1.4$ the refractive index of PTFE [153].

For the EO detection, a small fraction of the chirped laser pulse was recompressed to the Fourier-limited 60 fs beam duration with a grating pair compressor, to be used as the probe beam. The grating compressor comprised of an identical diffraction grating pair (Spectrogon) with groove density of $1200\,\text{mm}^{-1}$ and a roof metallic mirror. The perpendicular separation of the grating pair was dependent on the incident angle on the diffraction grating and the stretched pulse duration, as discussed in §3.2.4. The pulse duration of the probe beam was optimised by employing a commercial GRENOUILLE device, capable of measuring the pulse duration live. After compression, the probe beam was focussed onto a 500 μm-thick (110)-cut ZnTe crystal in a back reflection geometry for EO sampling measurements of the THz electric field at the entrance of the coupler. The EO measurements were performed in atmosphere, as the ZnTe crystal was not vacuum compatible. The optical components for the EO measurements were installed on a translational stage, which was moved in the THz path when needed.

The spatial and temporal overlap of the THz pulse and the electron beam at the interaction point was crucial. For the synchronisation, a commercial phase-lock-loop electronics module (Synchrolock, Coherent) integrated into the CLARA PI laser system and a translation delay stage on the THz beam line were employed. For the coarse synchronisation, the time of arrival (TOA) of the electron beam and the THz pulse was measured from a fixed point, using the same sensor, a Schottky diode [154]. The TOA of the electron beam was measured by detecting the coherent transition radiation (CTR) emitted when the electron beam hit a metal target [155] whereas the THz pulse was directly detected. The metal target was a metallic mirror, which was mounted on a translational stage, and would also route the THz beam onto the Schottky diode. The diode was connected to a 6 GHz digital oscilloscope (DPO70604, Tektronix), and triggered by the PI laser reference frequency. The relative time of arrival of the CTR and the THz pulses was resolved

on the oscilloscope, and was brought closer to within a 1 ns by adjusting the phase-lock-loop electronics module. For the final, fine control of the temporal overlap, the translational stage with step size of 33 fs and total range of 1 ns, was used. M. Hibberd, D. Lake and D. Walsh helped with the operation and the alignment of the TW laser system, as well with the synchronisation set up.

6.3.2 Results and analysis

The electric field of the narrowband THz pulses was measured with EO detection at atmosphere and room temperature. In Figure 6.17, the measured waveforms transmitted through the top and the bottom of the phase-shifter plate are depicted, with the corresponding amplitude spectra. The waveforms were recorded at the coupler entrance of the DLW structure, in free space. As can be seen, the phase-shifter plate induced a half a cycle relative phase shift between the two waveforms, confirming the polarity inversion of the THz beam, known for a quasi-TEM_{01} mode field pattern. The bandwidth of the THz source was measured to be 100 GHz FWHM, centered at 0.4 THz with minimal differences between the top and the bottom halves.

The electron beam parameters and beam optics settings could be changed remotely from the Control Room. The position and focussing of the beam through the DLW structure was achieved by tuning the optics as discussed in §4.2.1. A transverse size of 100 μm rms was achieved at the interaction point. The bunch charge was varied between 10-70 pC which was within the threshold of the camera monitoring the energy spectrometer. Varying the phase of the RF LINAC would essentially change the longitudinal profile of the electron beam. The CLARA machine was primarily operated by Y. Saveliev, T. Pacey and J. Jones, providing the BA1 diagnostics of the CLARA particle beamline.

Two main accelerator configurations were primarily explored here. The first was with a longer bunch and with a bigger energy spread, and the second was with a shorter bunch and lower energy spread. In Figure 6.18, examples of single-shot energy spectra obtained at the energy spectrometer for the long bunch configuration are depicted with 6.18(a) THz-off and 6.18(b) THz-on. The corresponding energy spectral density was obtained by integrating the shots across the transverse position dimension, as depicted in Figure 6.18(c). Subsequently, the measured modulation

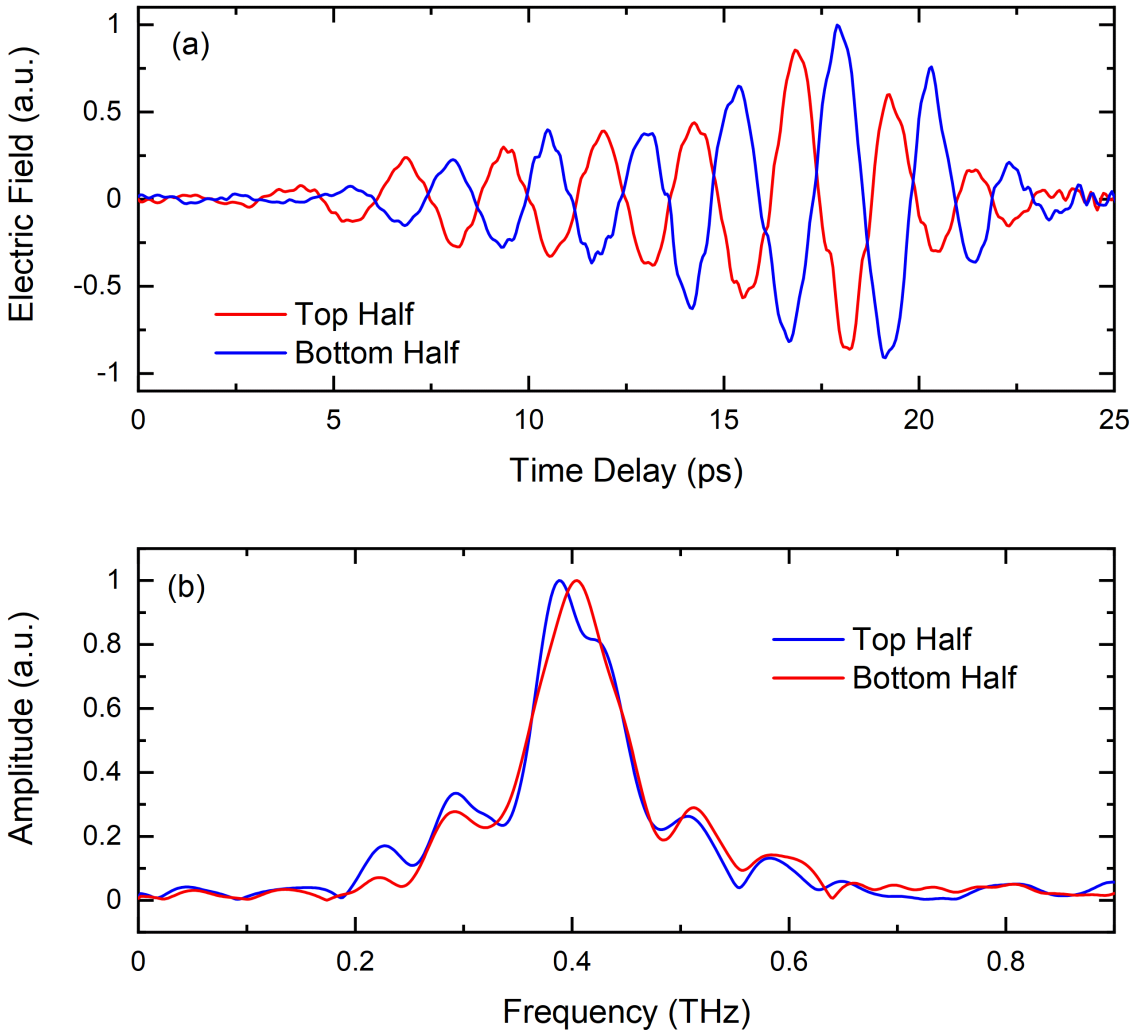

Fig. 6.17: EO sampling measurements of the temporal (a) and spectral (b) profiles of the THz pulse transmitted through the top and bottom half of the phase-shifter plate, measured at the entrance of the DLW structure coupler. [156]

was extracted from the difference between the energy density spectra, as can be seen in Figure 6.18(d).

The modulation observed in the energy spectrum for the long-bunch electron beam configuration, arose from the temporally sinusoidal interaction with the multicycle THz pulse. The electron bunch was sufficiently longer than the wavelength of the driving THz pulse resulting in a quasi-sinusoidal energy gain and loss, as the electron bunch interacted with more than one cycles. Temporally localised change of the chirp was imposed in the phase space of the bunch, which correspond to the positive and negative peaks in the modulated energy density spectrum.

To quantify the acceleration achieved from the THz-driven DLW structure δE_{THz}, the measured single-shot modulation was compared with a model. A sinusoidal

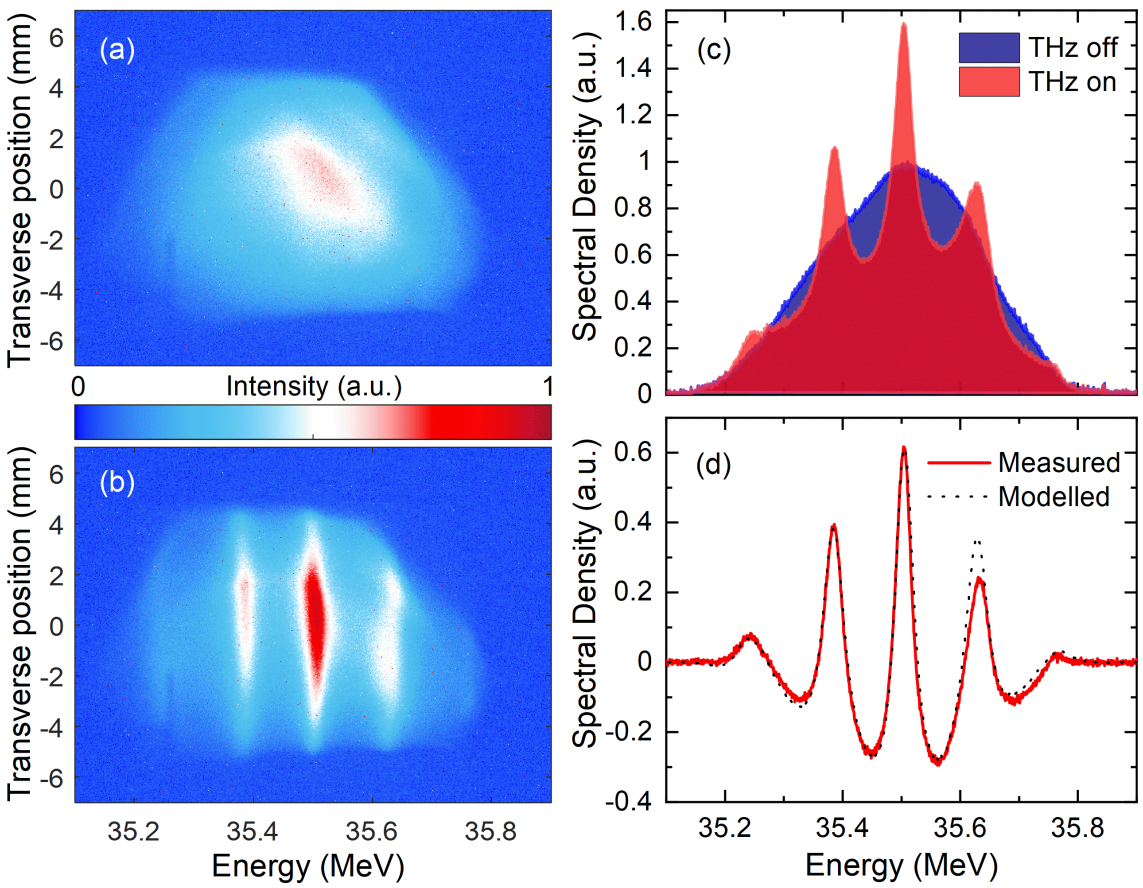

Fig. 6.18: Single-shot energy spectrometer images captured for the long-duration, high-energy spread electron beam configuration with (a) THz off and (b) THz on and (c) the corresponding energy density spectra. (d) Measured modulation extracted from (c), with the model depicted in dotted black line. [156]

modulation with a frequency of 0.4 THz was applied on a modelled electron bunch with linear chirp. To account the spatial resolution limitation of the spectrometer due to the beam emittance and uncorrelated time-slice energy spread, an effective energy spread δE_{eff}, was included in the model. An iterative fitting routine was developed to fit the model with the measured results, with independent variables the acceleration gradient, δE_{THz}, δE_{eff}, beam duration and the linear and cubic chirp components. The effective interaction length of the THz pulses and the electron beam inside the DLW structure was estimated to be approximately 4.3 mm, limited by the group velocity walk-off and the THz pulse duration.

From the model, the peak acceleration achieved was estimated to be $\delta E_{\mathrm{THz}} = 8.8\,\mathrm{keV}$, with an average acceleration gradient of 2 MV/m, which was an order of magnitude greater than what Curry *et al.* reported with the IFEL-coupled

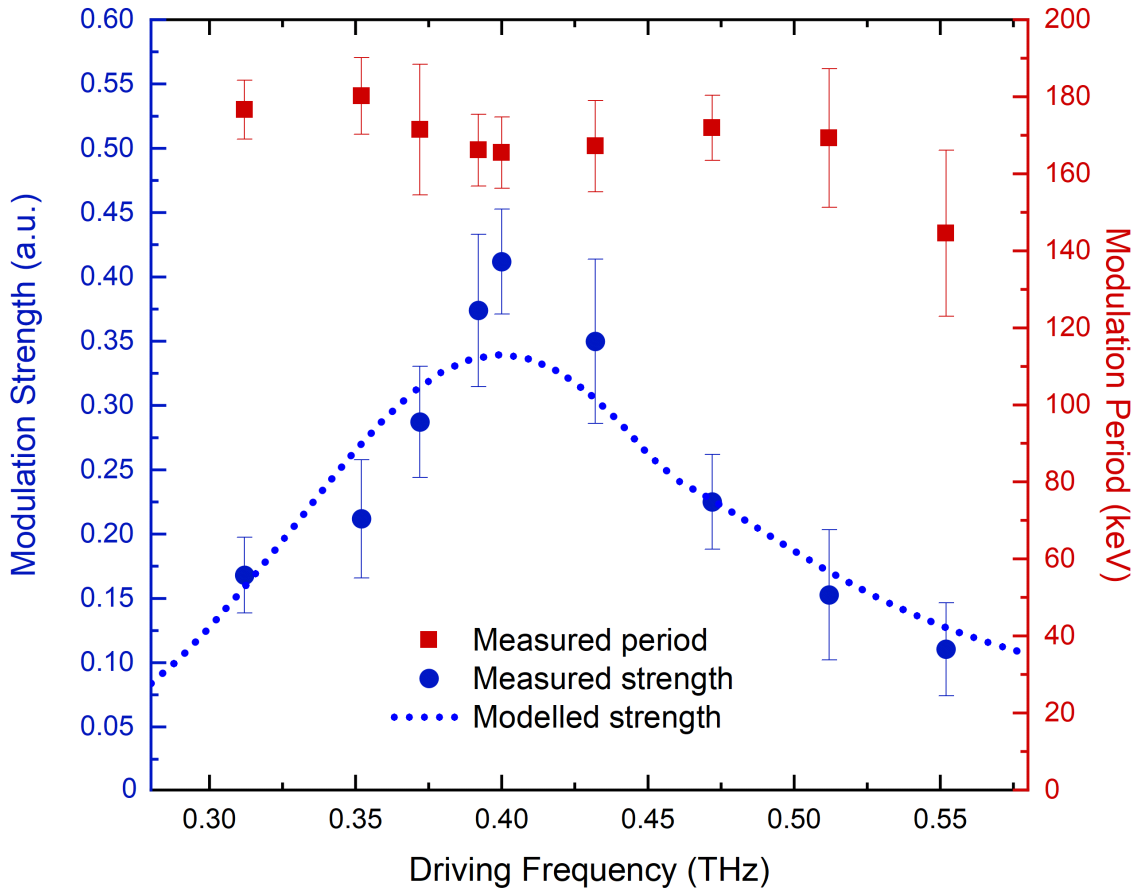

Fig. 6.19: Measured and modelled modulation strength and modulation period as a function of the center frequency of the driving THz pulses for the long-duration electron beam configuration. [156]

scheme [46]. The model depicted as a dotted line in Figure 6.18(d), also considered a value of δE_{eff}=7.9 keV, beam duration of approximately 6 ps FWHM and linear and cubic coefficients of 47.3 keV/ps and 0.4 keV/ps^3, respectively. As can be seen, the modelled modulation had a good agreement with the measured modulated energy density spectrum. The measured linear chirp was of comparable magnitude with the value, 53 keV/ps, predicted by beam dynamics simulations conducted by the ASTEC staff team.

The center frequency of the THz pulse driving the DLW structure could be tuned by adjusting the relative time delay between the two chirped pulses in the Michelson interferometer arrangement. The relative delay was introduced by a manual stage on which one of the zero-degree mirror was mounted on. The modulation strength and modulation period was explored as a function of the center THz frequency as shown in Figure 6.19. The modulation strength was extracted as explained in

Figure 6.18. The error bars indicate the standard deviation from 100 consecutive single-shot measurements.

The strongest interaction was observed at 0.40 THz, corresponding to the operational frequency of the DLW structure. As explained in §6.2, the DLW structure was designed to mediate a phase velocity matched to 35 MeV electron beams at 0.41±0.02 THz. For frequencies greater or lower than the operational frequency, the modulation strength decreases, following a trend according to the model. For the modelled frequency dependent modulation strength, plotted as a dotted blue line in Figure 6.19, the acceleration voltage throughout the DLW structure was calculated using the dispersion relation of the LSM_{11} mode, for a range of center frequencies and an effective bandwidth of 100 GHz. Over the THz frequency range explored, the modulation period induced on the bunch was primarily dictated by the efficiency of the interaction. The modulation period was observed to be relatively constant at the value 165±10 keV. This study showcased the importance of experimentally characterising the DLW structure, and by measuring the dispersion relation, the operational frequency could then be identified.

The other electron beam configuration studied was the short-bunch of approximately 2 ps FWHM bunch duration, with low energy spread. The aim was to achieve pure acceleration of the entire bunch, also known as single-bucket acceleration. This was only possible if the longitudinal size of the bunch was significantly smaller than half of the wavelength of the THz electric field. This was one of the main advantages of THz-driven acceleration over the DLA structures [38], which are powered by 800 nm laser pulses, meaning the operating wavelength is at least 2 orders of magnitude shorter than the electron bunch. Moreover, because of the operating wavelength and the cavity dimensions, only 2.2% electron beam transmittance through the DLA structure was reported, whereas in this work the whole bunch would potentially interact with the THz pulses.

At the time of the experiment, CLARA was between development stages, with the beam properties not being fully optimised. A bunch duration on the scale of 100 fs was initially expected, however a bunch duration comparable to the THz period was eventually delivered. Single-shot electron energy density spectra measured with THz-off and THz-on are shown in Figure 6.20, with the corresponding fitted model. Depending on the timing of the electron bunch relative to the phase of the

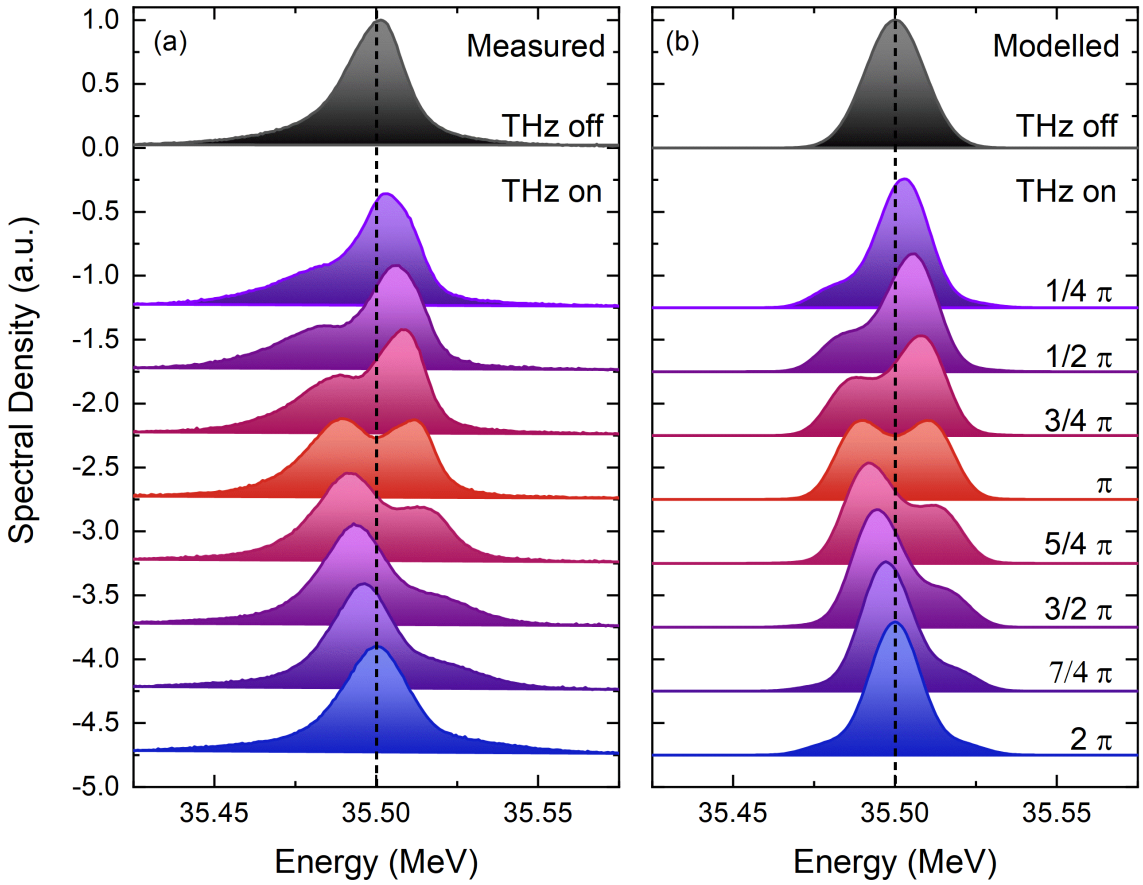

Fig. 6.20: (a) Single-shot electron energy spectra measured for the shot-duration, low-energy spread configuration for a phase range of 2π relative to the THz pulse, with (b) the corresponding modelled electron energy spectra. [156]

THz-pulse, the measured spectral profile was changed accordingly. For a relative phase delay of π, the beam energy spread was symmetrically doubled from 21 keV (THz-off) to 42 keV (THz-off). In this configuration, the bunch was equally decelerated and accelerated, resulting in the maximum increase of the beam energy spread. Asymmetric acceleration was realised for phase delays below π, whereas deceleration for greater than π.

The same fitting routine was employed in order to fit the model with the measured results for the short-bunch configuration, over the full 2π phase range between the electron beam and the THz pulse. From the model, an effective energy spread of $\delta E_{eff} = 5.9\,\text{keV}$ was deduced, with a linear chirp component of 7.8 keV and a peak THz acceleration of $\delta E_{\text{THz}} = 10\,\text{keV}$. The acceleration achieved was of the same scale observed for the long-bunch configuration. From this analysis, the rms timing jitter between the two seed oscillators of the PI and TW laser systems, was ascertained to

be approximately 100 fs. Despite of a non-optimal compressed bunch duration, the analysis revealed a single-bunch acceleration of a relativistic, high charge electron bunch, measured from a single-shot. The data analysis as well as the fitting of the model with the measured results were primarily conducted by A. Healy, E. Smith and O. Finlay.

6.3.3 Summary

An optical apparatus was set up in BA1 to generate narrowband, frequency-tunable, high-field THz pulses through CPB in a LN crystal, and by employing a phase-shifter midline of the THz beam, a quasi-TEM_{01} mode was achieved in free space. The THz radiation was transported and then coupled into the DLW structure, exciting the accelerating LSM_{11} mode and then successfully interacting with copropagating 35 MeV electrons. The temporal synchronisation of the THz pulse and the electron beam was realised by detecting the CTR emitted from the electron beam from a metal target and the THz radiation directly onto a Schottky diode connected on a high-bandwidth oscilloscope. THz-driven acceleration was demonstrated, with two electron beam configurations being explored. Moreover, a model was developed, able to fit the experimentally measured results, extracting properties of the electron beam provided by CLARA such as bunch duration, the linear and the cubic chirp components and the effective energy spread due to the emittance and uncorrelated time-slice energy spread of the particle beam.

6.4 Conclusions

In this chapter, a DLW structure designed to support the accelerating mode LSM_{11}, tailored to phase velocity-match electron beams of energy 35 MeV, was optically characterised through transmission measurements in a custom-built THz-TDS set up. A broadband TEM_{01} mode generated from a novel combined spintronic source, was characterised in free space and used to excite the LSM_{11} mode of the waveguide. Through the analysis of the transmitted through the DLW structure waveform, the propagation constant of the LSM_{11} mode was measured and the operating frequency was experimentally ascertained at $f_{op} = 0.41 \pm 0.02$ THz. Exploitation time at the CLARA test facility was allocated, in order to benchmark the DLW structure for

THz-driven acceleration and manipulation of relativistic electron beams. The DLW structure was driven by narrowband, frequency-tunable, polarisation-tailored THz pulses produced through CPB in a LN crystal. The energy spectra of copropagating electrons was measured on an energy spectrometer before and after interaction with the THz pulses. Long and short bunch electron bunch duration were explored, where the bunch chirp was experimentally determined.

For the long-bunch configuration, the cubic chirp component revealed from the experimental data, was not expected from the beam dynamics simulations of the CLARA beamline. This was a direct measurement, often inaccessible unless RF-driven transverse deflecting structures and dedicated electron-beams optics are available. The DLW structure was thus proven to explore the picosecond temporal structure of high-energy, high charge electron beams, while preserving the transverse beam quality.

For the short-bunch configuration, preferential acceleration and deceleration was observed as a function of the relative phase of the electron bunch with the THz pulse. For a bunch duration comparable with the period of the THz pulse, single bucket acceleration was demonstrated, with the DLW structure enabling transmittance of bunch charges of up to 60 pC, which was over three orders of magnitude higher than in the previous THz-driven acceleration works in the literature [41, 42, 46]. Furthermore, it was shown through simulations, that in scheme the transverse beam quality is conserved [156].

From the proof-of-principle results, the DLW structure was demonstrated to serve as a compact THz-driven linear particle accelerator as well as an ultrafast diagnostics device for relativistic subpicosecond-long charged particles. With the use of narrower-bandwidth, higher energy THz pulses, the interaction would proportionally increase. Moreover, the interaction would further increase with multiple stages, in a cascaded configuration, marking a route of scaling down the size of future particle accelerators.

Chapter 7

THz-driven streaking of sub-relativistic electrons using a DLW structure

7.1 Overview

In this chapter, experimental demonstration of THz-driven manipulation of sub-relativistic electrons is described, followed with relevant simulations. A 100 keV electron gun system was assembled in the LATTE lab at Daresbury, UK (§4.2.2), powered by a high-power laser system (§4.1.1), providing ultrafast 800 nm laser pulses with 11 mJ pulse energy. This work aimed to characterise the temporal profile of a short electron bunch, using a DLW structure, driven by single-cycle THz pulses as a streaking device, in an all-optical control and metrology concept. The DLW structure was designed to match the phase velocity of the supported LSM_{01} mode at approximately 0.5 THz with the velocity of 100 keV electrons. As a result, the THz-electron interaction length can be increased.

The propagation constant of the DLW structure was experimentally measured in §5 [157]. Upon interaction of the electron beam with the THz pulse, the modulation of the transverse profile of the electron bunch detected on a downstream detector, was measured as a function of the relative time delay between the two. The longitudinal profile of the particle bunch was extracted from the comparison of the experimental observables to the simulations. The time evolution of the electromagnetic (EM) fields and of the particles inside the DLW structure was modelled

as explained in 4.3.2.

7.2 Experimental apparatus

The schematic diagram of the optical apparatus and the vacuum chamber used in this Chapter is illustrated in Figure 7.1. The experimental set-up can be divided into three sections; electron generation section, the THz radiation generation transport section, and the vacuum chamber where the THz-electron interaction took place. The Cockroft laser system powered the whole experiment, providing up to 11 mJ of 35 fs FWHM long pulses with a center wavelength of 800 nm at an adjustable repetition rate (§4.1.1).

7.2.1 Electron generation and alignment

The experiment consisted of a 100 keV electron gun system, mounted onto a cuboid vacuum chamber. An MCP detector was attached on the other end of the vacuum chamber. The MCP detector enabled the monitoring of the transverse profile of the electron bunch with a CCD camera (mvBlueCOUGAR-X, MatrixVision). The electron gun system, vacuum chamber and MCP detector could be isolated with manual-driven gate valves, maintaining the vacuum level in each section. Separate Penning vacuum gauges were employed for the electron gun and the vacuum chamber. Two side CF flanges were replaced with fused silica windows, for the transport of the THz radiation and of the visible alignment laser, respectively.

The electron gun was able to operate in either thermionic or photo-excitation electron emission mode. For the generation of short electron bunches, the gun was operated in the photo-emission mode. As can be seen in Figure 7.1(b), a beam sampler was used in order to reflect a small fraction of the incident laser pulse (1 %) which was later used for the photo-excitation of electrons. The beam was routed through a translational stage, in order to vary the arrival time of the electron bunch relative to the THz pulses. The beam was then telescoped down to reduce the beam size with a pair of lenses, $f_a = 300$ mm and $f_b = -50$ mm, resulting in a beam of approximately 2 mm $1/e^2$ diameter.

The beam went through a β-BaB_2O_4 (BBO) non-linear crystal, where Second Harmonic Generation (SHG) occurred, generating 400 nm radiation. The residual

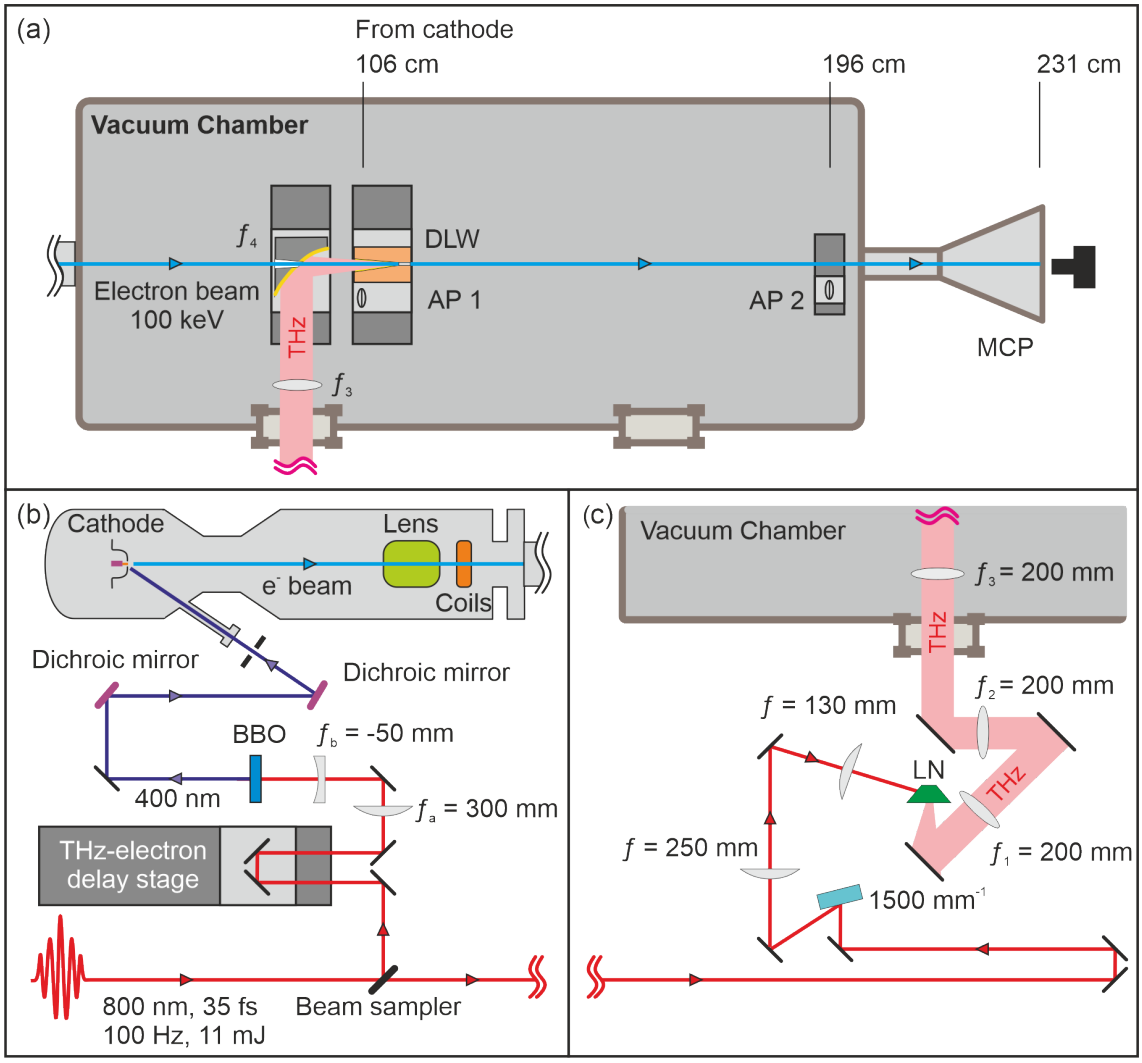

Fig. 7.1: Schematic diagram of the 100 keV experimental setup; (a) the vacuum chamber containing the DLW structure where the electrons interact with the THz pulses, and then getting detected on an MCP detector with a CCD camera, (b) the generation of electrons via photo-emission where a small percentage of the incident laser pulse undergoes SHG for UV generation and the rest is used for (c) THz generation using the PFT scheme on a LN crystal. Vacuum compatible apertures (AP) were employed as well as an alignment laser, for the alignment of the electron beam and the optical components in the vacuum chamber.

800 nm radiation was separated from the 400 nm radiation with a pair of dichroic mirrors, and then safely dumped onto a target. The 400 nm radiation was eventually routed onto the photo-cathode, through a quartz-window. Despite using a telescope to reduce the beam size, an additional aperture was used. This helped suppressing the illumination of the surrounding apertures, like the grid and the 1st anode, which was responsible for the 'fringe' photo-electrons detected on the MCP. An example

of these fringe electrons can be seen in Figure 7.2(a), before the final alignment of the UV beam. The fringe electrons appear as a series of haloes around the main central beam, and can be limited by optimising the UV alignment, as depicted in Figure 7.2(b).

The grid aperture was used to limit or suppress electron emission from the cathode when a negative potential was applied with respect to the bootstrap cathode (500 V). The grid was therefore pulsed to a voltage between 0 and 500 V which allowed electron emission in a 5 μs window. To synchronise the various electrical components, namely the grid, the electron gun controller, the camera and the electron photo-emission process, a commercial pulse generator (Quantum Composer 9530) was employed. The 1 kHz reference signal from the laser oscillator of the laser system was used as the input trigger, with the various outputs used to the rest of the electrical components.

The built-in solenoid lens in conjunction with the deflecting coils were used for the imaging of the electron beam onto the MCP detector. For the coarse alignment, the electron gun was operated in thermionic emission, with a non-focussed beam.

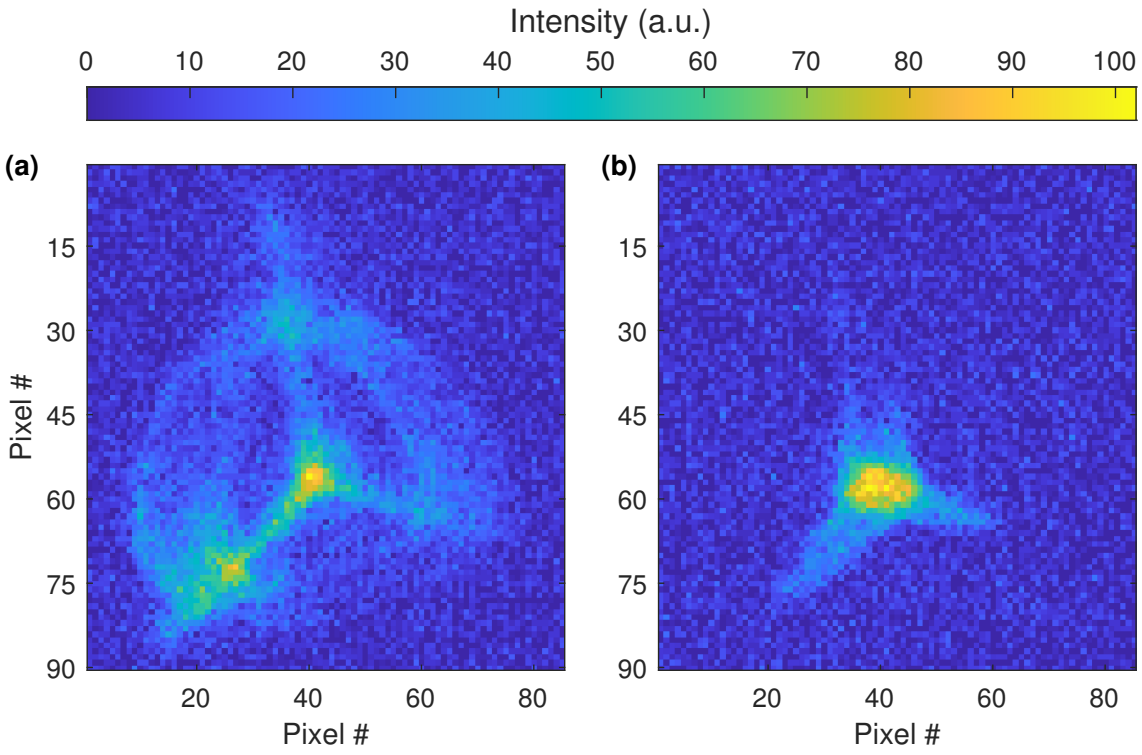

Fig. 7.2: An example of a typical electron beam spot detected on the MCP phosphor screen (a) with and (b) without the 'fringe' electrons produced due to incorrect UV beam alignment.

Then it was transitioned to photo-emission mode, where the UV beam was aligned until the beam formed from the thermionic and photo emission was almost identical. To ensure that the electron beam was collimated, two apertures (AP) mounted on translational stages were used before the MCP detector and next to the interaction point. Horizontal and vertical copper coils around the whole experimental enclosure, covering the electron gun, the vacuum chamber and the MCP detector, were installed in order to obtain an additional control of the electron beam alignment. In Figure 7.3, the compensator coils are indicated with yellow arrows. The custom-made compensator coils were used for the angling of the beam whereas the built-in steering coils were used for the positioning of the beam.

It was found, that the 100 keV electrons were very sensitive to local magnetic fields, resulting in distortion of the beam. This was observed when the apertures were brought into the beamline. After more investigation, magnetic fields of the order of 1 mT were measured with a Hall probe, emerging from the grub screws and the posts the apertures were mounted on. These components were replaced with ones with negligible magnetic field. Deflection of the beam was also observed while the translational stages were moving, or when high voltage electrical equipment was being used or moved in the LATTE lab, making alignment of the beam a standard routine procedure, using the two apertures.

The DLW structure as well as the OAP mirror were placed on linear translational stages in the vacuum chamber. The DLW structure consisted of the dielectric-

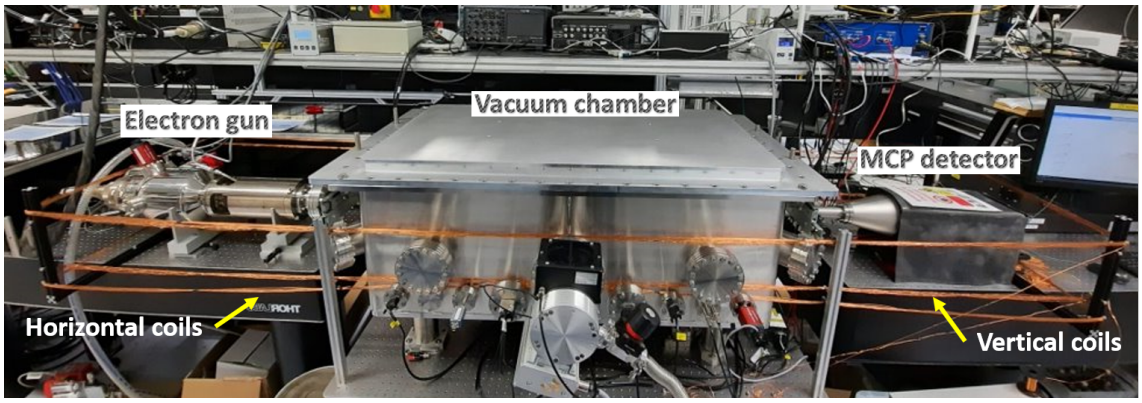

Fig. 7.3: Wide-angle photograph of the experimental apparatus, including the electron gun, the vacuum chamber and the MCP detector. The custom-made horizontal and vertical compensator coils surrounding the whole electron beam path, are indicated with yellow arrows.

lined waveguide and a linearly tapered horn metallic coupler, without a dielectric lining and it was mounted on a computer-controlled 5-tilt axis mechanical stage (8081M-UHV, Newport) for further alignment. The structure was optically characterised as described in Chapter 5, measuring the phase velocity to be $v_p = 0.548 \pm 0.002c$ at 0.47 THz after exciting the LSM_{01} waveguide mode, matched to the velocity of 100 keV electrons. The OAP mirror was 2-inch diameter with gold coating and with a through hole for particle propagation. Inside the chamber, the positioning of the components with respect to the electron beam used an alignment laser which counter-propagated with the beam.

7.2.2 THz generation

After the beam sampler, the laser beam was transported to the THz generation section, as illustrated in Figure 7.1(c). The laser pulse was sent to a pulse-front-tilt (PFT) configuration which consisted of a holographic diffraction grating (Spectrogon) with a groove density of 1500 mm^{-1}, and a $4f$ lens configuration, incorporating two cylindrical lenses with focal lengths of 250 mm and 130 mm, respectively. The PFT was achieved in the -1 diffraction order, with diffracted and incident angles determined as discussed in §3.2.3, for efficient THz generation in a LN crystal. As shown in Figure 7.4, the incident angle was set at $\theta_i = 19.8°$ with a corresponding diffracted angle $\theta_d = 59.4°$ for a pump-pulse front angle of $\gamma = 63°$. Because the two LN crystals employed here were of different growing technique and doping from the one in the literature [152], a 5% uncertainty was included in the determination of the refractive indices. The margin of error of the incident and diffracted angle as shown in filled areas in Figure 7.4, was within the precision of the rotational stage where the diffraction grating was mounted on. The horizontal magnification factor provided by the $4f$ lens geometry was 0.52, which was within the calculated range $\beta_1 = \beta_2 = 0.54 \pm 0.02$.

Two different LN crystals were employed for the THz generation. The two crystals were of different dimensions and of different crystal growing technique. The bigger crystal was an MgO-doped congruent LN crystal whereas the smaller crystal was an MgO-doped stoichiometric LN crystal. During the optimisation process of the PFT, the bigger crystal was replaced with the smaller one, as it was required to be used in a different experiment.

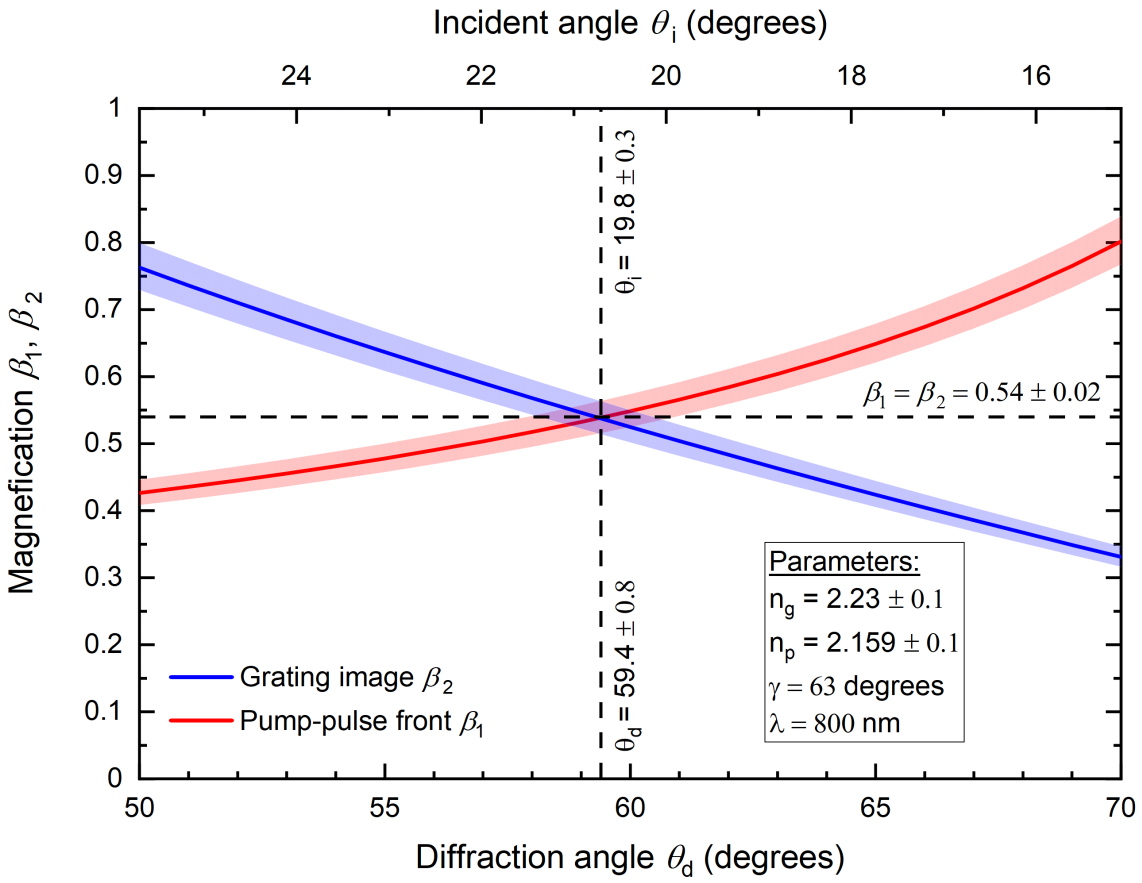

Fig. 7.4: Calculated magnifications of the pump-pulse front β_1, and the grating image β_2 as a function of the diffraction θ_d and incident angle θ_i for a 1500 mm^{-1} diffraction grating. The dashed lines indicate the combination of angles that $\beta_1 = \beta_2$. The filled area indicates the uncertainty in the magnification due to the uncertainty of the refractive index of LN at 800 nm.

A pyroelectric detector (THz-I-BNC, Gentec) was used to measure the pulse energy emerged from the LN crystal and determine the divergence of the THz beam. The attachable coupler of the detector was used, with the sensor covered with a black plastic film in order to block any residual optical radiation. The sensor had an active area of 4 mm^2. To determine the beam width and the divergence of the beam, power measurements as a function of the transverse horizontal and vertical position of the detector relative to the LN crystal were taken, at several longitudinal positions.

The THz radiation was then collected and transported into the vacuum chamber through a fused silica window with metal coated mirrors. An imaging setup consisting of 3 TPX lenses of focal length $f_{1,2,3} = 200$ mm, and 1 OAP mirror of parental focal length $f_4 = 101.6$ mm, was used to image the THz beam from the LN crystal

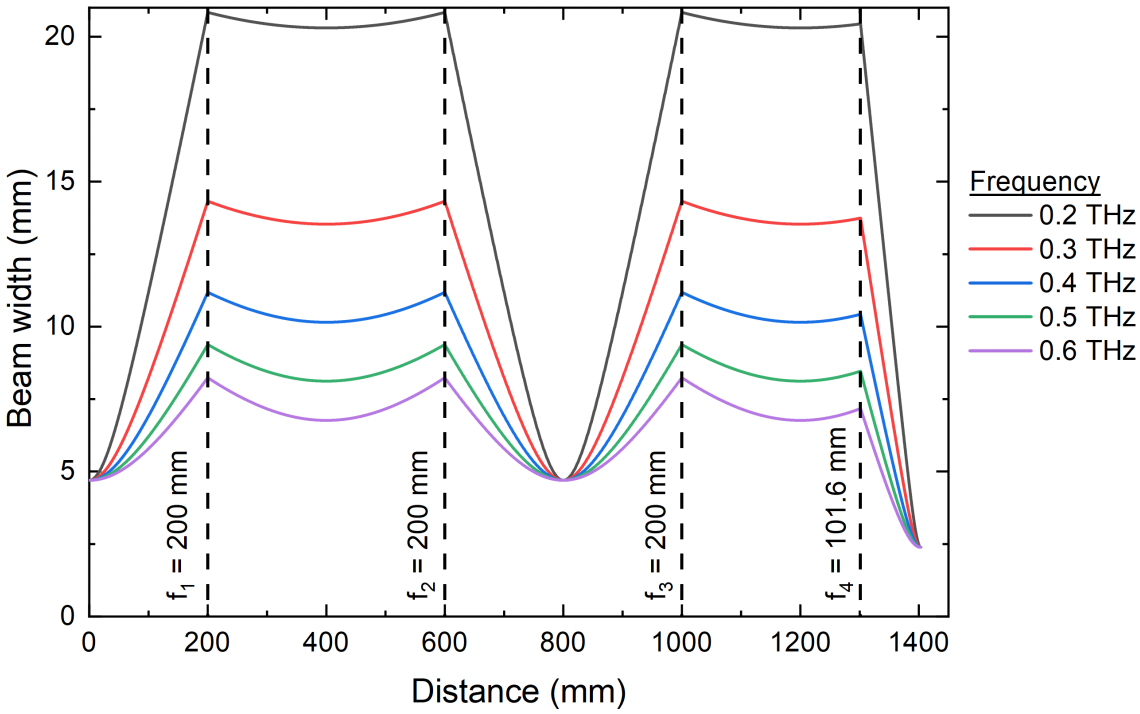

Fig. 7.5: Modelled beam width of the THz beam as a function of the distance, calculated for different frequencies. The dashed lines indicate the position of each focusing element along the THz beam transport line.

to the interaction point with a de-magnification factor of 2. In Figure 7.5, the modelled beam width as a function of the distance, calculated for different frequencies is shown. For the model, an initial beam width of $w_0 = 4.6\,\text{mm}$ and a radius of curvature of $R_0 = \infty$ was considered. The spot size was measured at the entrance of the coupler with a knife edge, agreeing with the model. A pulse energy of approximately $1\,\mu\text{J}$ was measured with the pyroelectric detector. The temporal synchronisation of the electrons and the THz pulse was achieved by matching the path lengths of the two, considering that the electron bunch was travelling at sub-luminal velocity, and then fine-tuning of the timing was achieved with the translational stage. All power and EO detection measurements were carried out at room temperature (RT) and at relative ambient humidity inside the vacuum chamber.

To convert the image obtained from the camera, from number of pixels to distance, a calibration process was followed. As the deflection was expected to be predominantly in the vertical direction, the camera was set such that the vertical bounds of the phosphor screen were visible. The transverse dimensions of the screen were measured separately, with a height of approximately 3.2 cm. The pixel to dis-

tance conversion factor was ascertained by calculating the ratio of the total number of pixels with the screen height.

7.3 Results and analysis

7.3.1 Electro-optic measurements

The waveform of the linearly polarised electric field of THz pulse generated from the LN crystal, was measured with EO detection inside the vacuum chamber, at the interaction point. For the EO measurements, a 500 μm-thick (110)-cut ZnTe crystal was employed, in a standard EO detection geometry, carried out in atmosphere and at room temperature (RT). In Figure 7.6, the measured waveform in free space can be seen, (a) before and (b) after the reflection deconvolution, with (c) the corresponding amplitude spectra. The main pulse, label (1), is a single cycle THz pulse with a 2.65 ps FWHM of the field envelope. More pulses appear later in time, labelled (2) and (3). The second and third pulse, arrived at approximately 10 ps and 21 ps after the main pulse respectively, were attributed to a first and second reflection of the main THz pulse in the ZnTe crystal. This agreed, given the thickness of the crystal was 500 μm and the refractive index of ZnTe at THz frequencies, $n_{\mathrm{THz}} = 3.16$ as reported by Gallot *et al.* [130].

The deconvolution algorithm of numerically suppressing the reflection echoes, discussed in Chapter 5, was applied on the measured waveform, with the results depicted in Figure 7.6(b). The parameters used for the reflection deconvolution were $r_{i=1,2} = [0.3, 0.11]$ and $\tau_{i=1,2} = [10.17, 20.7]$, taken from the measured EO signal. The residual oscillations following the main pulse was due to the strong water absorption at 0.557 THz and 0.75 THz. The effect of the reflection removal can also be seen in Figure 7.6(c), where the amplitude spectra with and without the reflection echoes, are plotted. A FWHM bandwidth of 260 GHz was measured from the generated THz pulse, with a center frequency of 0.38 THz.

A larger (3 cm height) congruent LN crystal (cLN) was first employed for THz generation, which was then replaced with a smaller (1 cm height) stoichiometric LN crystal (sLN). The damage threshold for a sLN crystal was expected to be close to 20 mJ/cm^2, as mentioned in the literature [75]. Depicted in Figure 7.7,

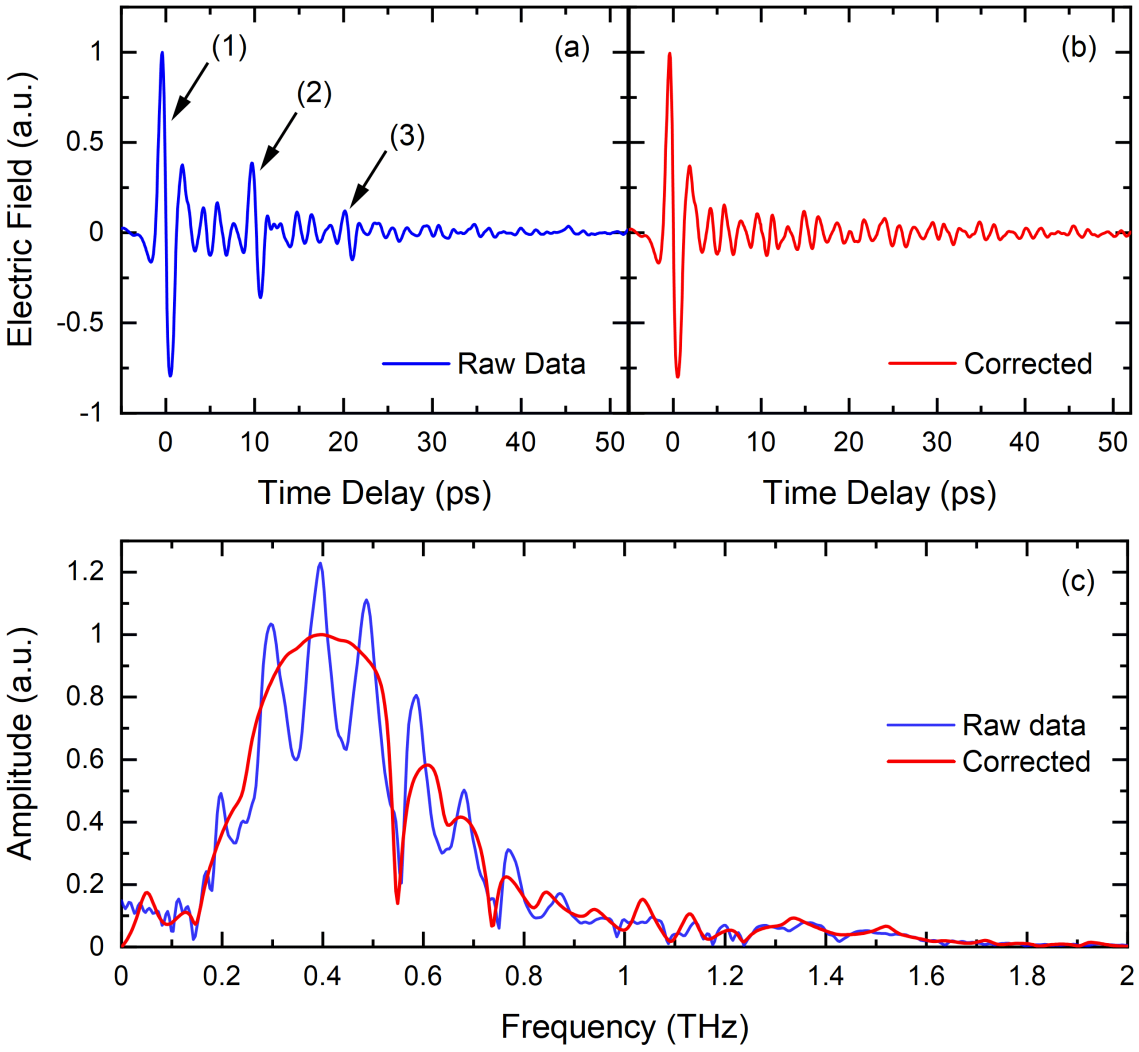

Fig. 7.6: (a) Raw data of the EO sampling measurement of the THz waveform measured at the entrance of the DLW structure coupler, inside the vacuum chamber. (b) The results of the reflection deconvolution applied on (a). (c) The corresponding amplitude spectra of (a) and (b). Labels (1)-(3) are discussed in the text.

power measurements of the emerging THz radiation as a function of the incident laser fluence were performed, with the calculated pump to THz energy conversion efficiency depicted on the same figure. For pump fluence up to 8 mJ/cm^2, the THz energy scaled up quadratically, with the conversion efficiency scaling linearly. For higher pump fluence, the generated THz pulse energy was scaling linearly, with the conversion efficiency reaching a plateau, indicating that it was close to the damage threshold. The sLN crystal was then used, tested at higher pump fluence, up to 20 mJ/cm^2, scaling with the same trend. The discrepancy of the generated pulse energy at 12.6 mJ/cm^2 between the two crystals was because of a small re-alignment performed after the swap of the two crystals.

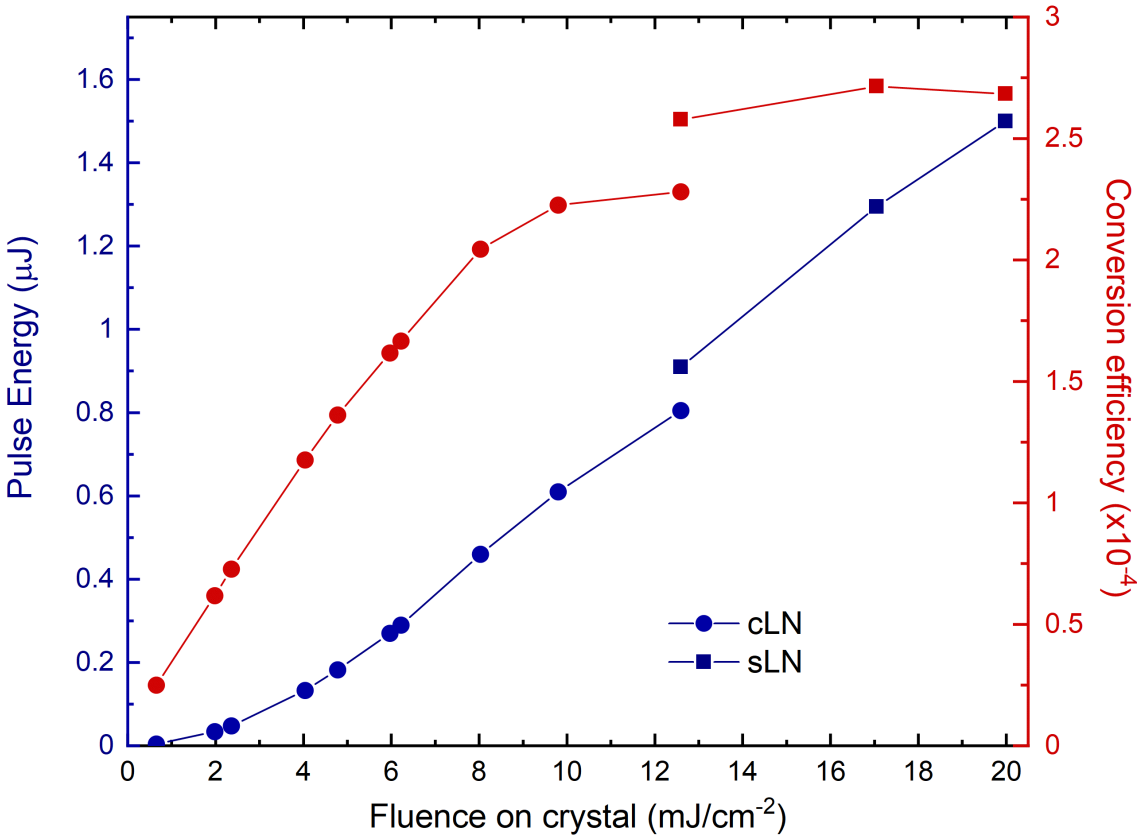

Fig. 7.7: Generated THz pulse energy as a function of the incident pump fluence (blue) with the calculated pump-to-THz energy conversion efficiency (red). Two crystals were investigated at different pump fluence; in bullets the congruent LN crystal and in squares the stoichiometric LN crystal.

Neither visible damage on the crystal nor a decrease in the generated pulse energy over a long period of time was observed, after exciting it at maximum fluence. The highest pulse energy recorded was approximately 1.5 μJ, with a corresponding energy conversion efficiency of 2.7x10^{-4}. The same order of magnitude of optical-to-THz energy conversion efficiencies have been reported in the literature with similar laboratory parameters [79,158,159]. The THz emitter was operated at the maximum fluence, allowing a pulse energy measurement of 1 μJ, at the entrance of the coupler, inside the vacuum chamber.

The total distance of the THz beam from the LN crystal to the interaction point was approximately 140 cm. In order to preserve the beam quality and limit the losses throughout the beam transport, an imaging setup was designed. For the design of the beam transport, determining the beam waist and the divergence emerging from the THz source was crucial, as it would govern the beam width as it propagates.

For the extraction of the initial beam waist, the horizontal and vertical profile of the emerging intensity pattern was measured at several propagation distances. The pyroelectric detector, with an active sensor of 2 x 2 mm, was employed, mounted on a XYZ manual-driven stage of a total travel range of 25 mm in each direction.

In Figure 7.8(a) and 7.8(b), power measurements across the horizontal and the vertical direction relative to the LN crystal surface, are depicted in scattered plot, for several propagation distances. A Gaussian distribution fit was applied on the experimental measurements, obtaining the horizontal and vertical beam width as a function of the propagation distance, as depicted in Figure 7.8(c). As it can be seen, the beam was skewed for the horizontal case, indicating that the stage was

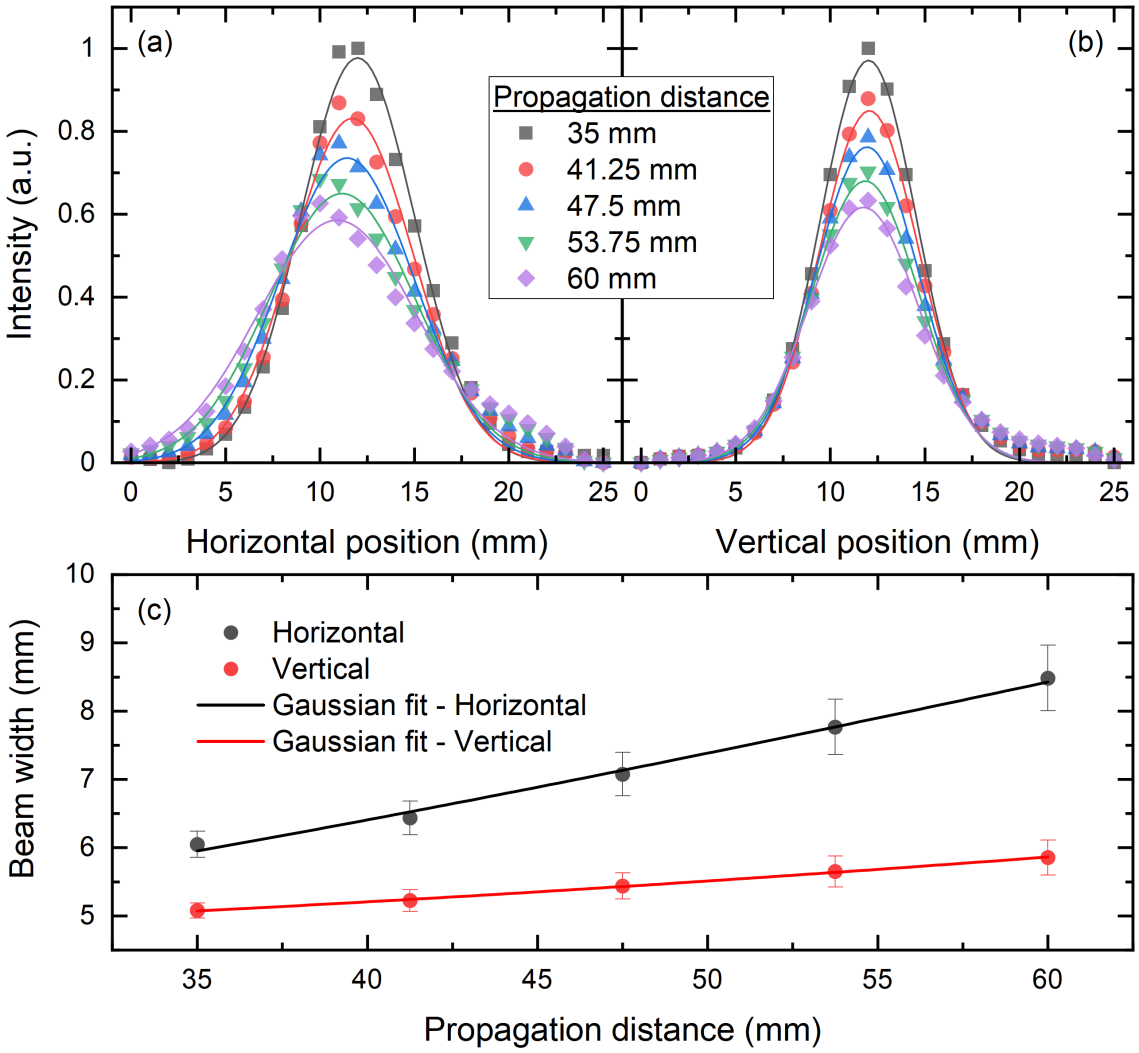

Fig. 7.8: Measured (a) horizontal and (b) vertical THz beam profile at different propagation distances (scattered plot), with the Gaussian distribution fit (line plot). (c) Horizontal and vertical beam width as a function of the propagation distance, extracted from (a) and (b), with the corresponding Gaussian beam propagation fit (line plot).

not misaligned, relative to the LN crystal. A Gaussian beam propagation fit was applied for the evolution of the beam width, given by [146]

$$w(z) = w_0 \sqrt{1 + \left(\frac{\lambda z}{\pi w_0^2} \right)^2}, \tag{7.1}$$

where $w(z)$ is the beam width, z the propagation distance, λ the central wavelength and w_0 the beam waist. The fit results for the horizontal and vertical beam width can be seen as the black and red line plot in Figure 7.8(c), respectively. The beam waist and the wavelength were the fitting coefficients, with z the independent variable. From the results of the fitting curves, the beam waist was ascertained, with a value of $w_0 = 4.6 \pm 0.1$ mm for the vertical profile and $w_0 = 4.1 \pm 1.2$ mm for the horizontal profile. The fitting model also predicted a centre frequency of $f_0 = 0.34 \pm 0.02$ THz, which was in a good agreement with the measured amplitude spectrum, depicted in Figure 7.6(c).

The value of the beam waist was used for the design of the beam transport, consisted of four focussing elements, and metallic mirrors. The THz radiation was transported to the interaction point, inside the vacuum chamber, imaged with a de-magnification factor of 2.

7.3.2 Deflectogram

The spatial overlap of the electron beam and the THz beam was a relatively easy task, as the interaction took place in a structure which comprised of a coupler. The coupler was of great importance in order to couple the deflecting LSM_{01} mode from the free space TEM_{00} THz pulse. The coupler also facilitated the alignment of the THz pulse through the structure. The alignment of the electron beam proved to be more challenging, as external magnetic fields originating from either the LATTE lab or even the Earth magnetic field, were inducing distortion to the beam. At the time, only the built-in focussing lens and two steering coils were available, corresponding to the correction of the beam position and angle. Image of the electron beam aligned though the structure and the OAP, without the THz field, can be seen in Figure 7.9(a).

With the matching of the THz and electron beam path lengths up to the entrance

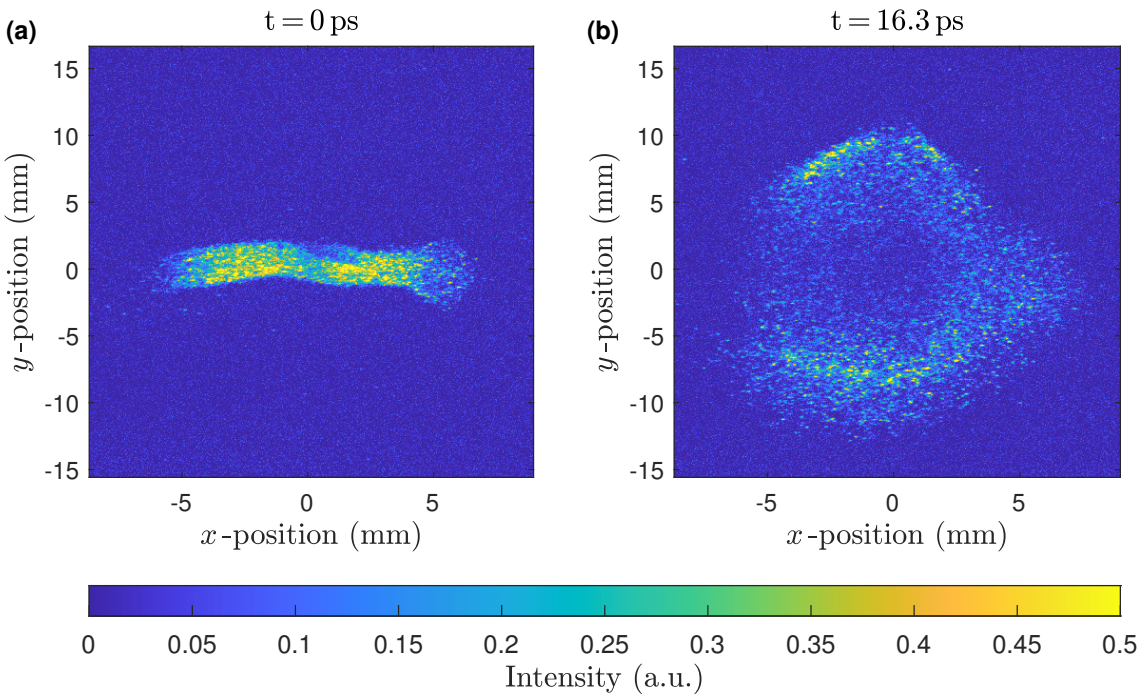

Fig. 7.9: Images of the electron beam aligned through the DLW structure, detected on the MCP screen, (a) without and (b) with the THz field on.

of the structure, the temporal overlap was roughly achieved. The final synchronisation stage involved a trial and error method, where the THz-electron delay stage was driven, until a modulation of the electron beam would be observed. In Figure 7.9(b), a modulation of the transverse profile of the beam can can be seen, following the translation of the delay stage. The vertical profile of the beam was modulated, as expected from simulations.

The bunch duration was expected to be dependent on the excitation laser pulse duration and the pulse broadening caused during the acceleration process. The electron gun system was simulated by C. Shaw in GPT [122], where the settings of the gun were explored, namely the first and second anode voltage, grid voltage, and focussing lens. The settings were set such as the shortest electron bunch with maximal brightness and transmittance through the structure could be delivered. The first anode was set to 5 kV, whereas the grid and the second anode were set to 0 V.

From the MCP images, the horizontal and vertical line profiles of the beam were obtained, by summing the pixel intensities at each direction. As can be seen in Figure 7.10(a), the beam spot becomes vertically larger when the temporal overlap is met, and the electron beam interacts with the THz radiation inside the DLW. The

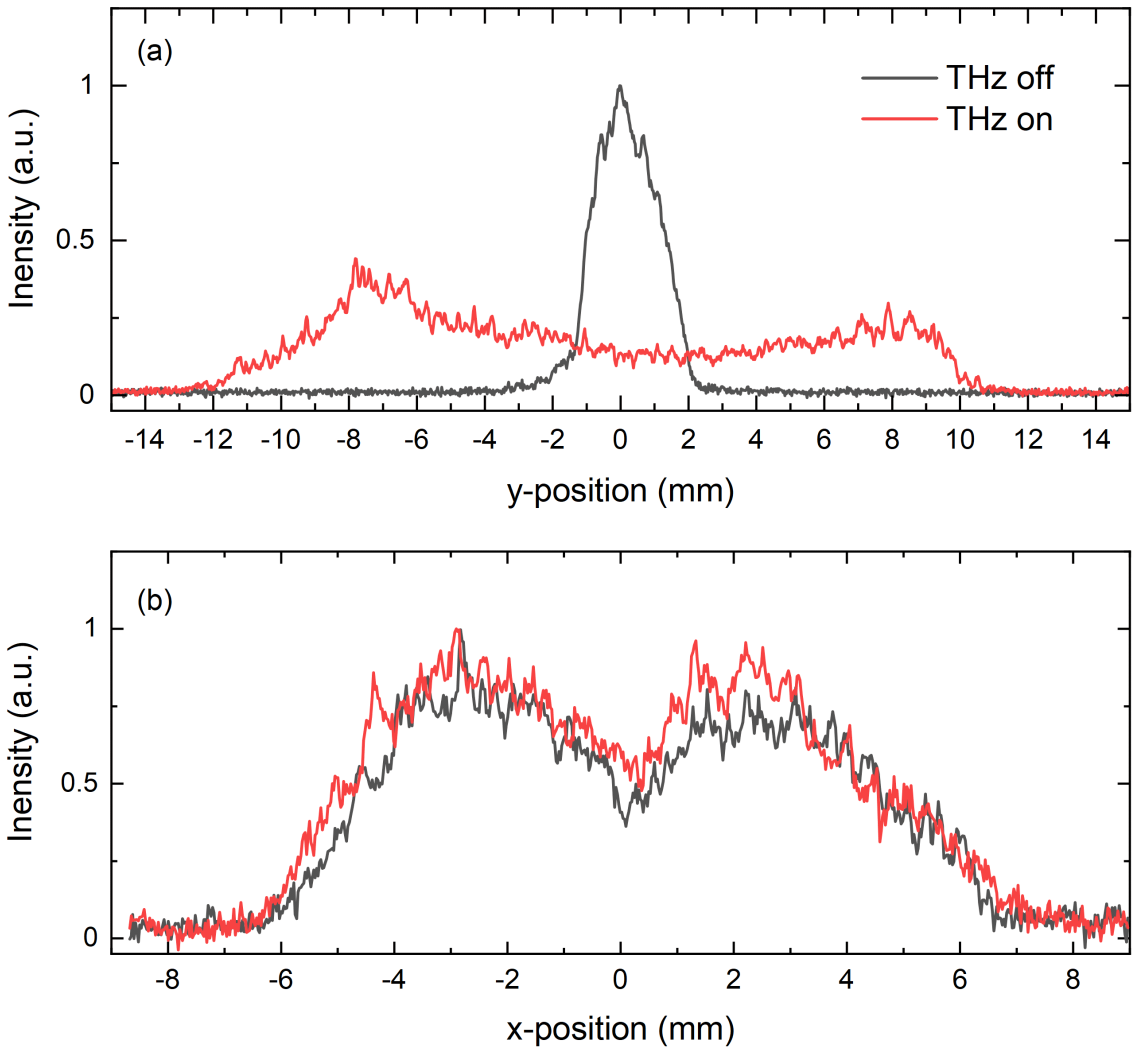

Fig. 7.10: (a) Vertical and (b) horizontal line profiles of the electron beam detected on the MCP, with THz off (black line) and THz on (red line).

beam becomes up to 10 times bigger. This was an indication of deflection of the electrons in the y-direction, as it was predicted by the simulations. The modulation on the x-direction was negligible as depicted in Figure 7.10(b).

With the temporal synchronisation established, electron beam images were taken as a function of the THz-electron relative time delay. A time window of 55 ps was scanned, with a time step equal to approximately 133 fs. This corresponds to resolution of approximately 20 steps per wavelength, if considered the centre frequency of the driving THz pulse is 0.38 THz. Post-processing of the time scan involves the extraction of the vertical and horizontal line profiles, and merging them into one figure, producing a deflectogram. Essentially, a deflectogram depicts the deflection evolution of the electron beam, in the plane of deflection.

Figure 7.11 depicts the deflectogram obtained from the time scan. At each time

point, 10 shots were taken, and then averaged. A background image was also obtained with the electron beam blocked, in order to subtract the noise originating from the MCP and the camera. The electron beam in the deflectogram follows a quasi-sinusoidal trend. It is proportional to the integral of the Lorentz force along the electron trajectory inside the DLW structure. The zero-crossing is considered the time point where the spreading of the beam is the strongest, and it is where the $t_0 = 0\,\text{ps}$ is set. Streaking speed is a figure of merit, quantifying the deflection rate the electron beam undergoes. This figure of merit is usually used to benchmark ultrafast streaking devices and it is also used for comparison. For the measurement of a short duration electron bunch, the temporal resolution is proportional to the streaking speed strength [53].

Before and mainly after t_0, there are trailing oscillations, arising from the dispersion of the THz pulse in the DLW structure. Another explanation for the oscillations that appear after $t = 15\,\text{ps}$, is water absorption of the THz radiation, when it was transported from the optical table to the vacuum chamber. The amplitude of the

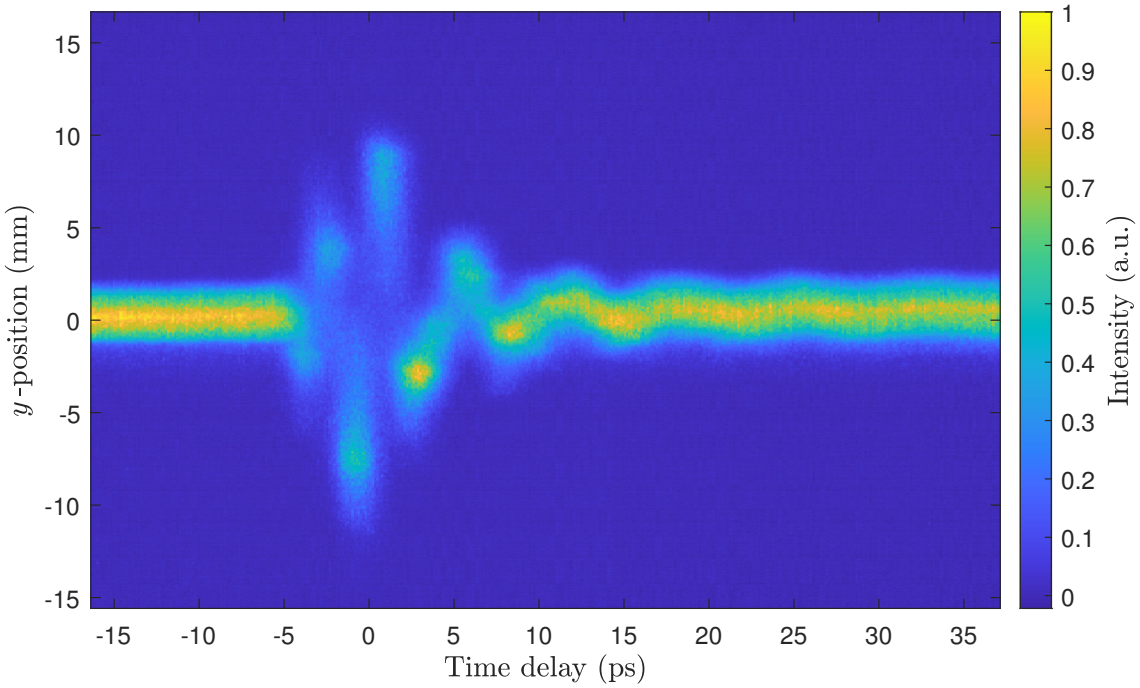

Fig. 7.11: Deflectogram (time-dependent deflection) measured by varying the delay between the electron beam and the THz pulse. Images of the electron beam were integrated along the x-position.

deflection after t_0 rapidly decreases. The peak-to-peak amplitude of the vertical displacement was approximately 19 mm. The streaking speed at t_0 was experimentally ascertained from the deflectogram in Figure 7.11. It was measured to be 11.01 mm/ps, corresponding to approximately 28 mrad/ps. This figure exceeds the streaking speeds demonstrated in the literature where metallic slits or resonator structures were employed [47, 50, 53].

Figure 7.12 illustrates the deflectogram along the horizontal direction. As can be seen, the modulation is smaller than what has been observed for the vertical deflection. A modulation was observed at t_0, with small trailing oscillations. It was a focussing effect on the x-direction, and it was expected since the electron beam was filling the whole DLW aperture. Weak horizontal electric field field arise on the edges of the DLW as can be seen in Figure 4.11, leading to focussing and defocussing of the beam as a function of time. Nevertheless, the horizontal modulation was weaker than the vertical, without introducing any complications. Furthermore, the horizontal and vertical components of the modulation are decoupled, and can be analysed independently.

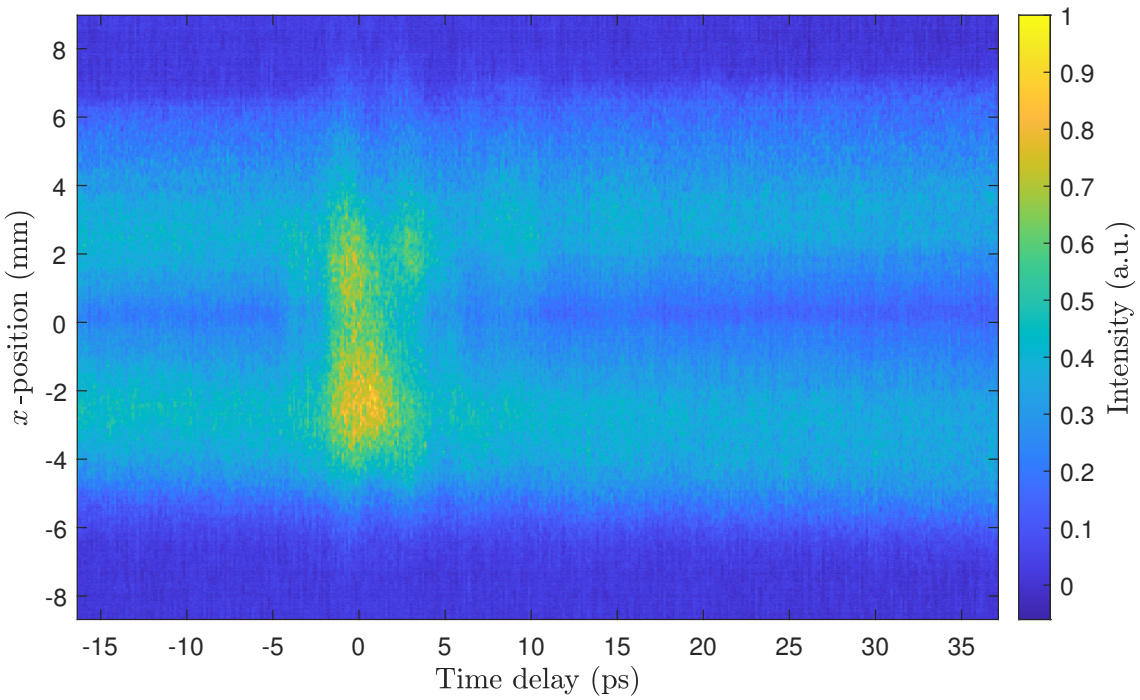

Fig. 7.12: Deflectogram (time-dependent deflection) measured by varying the delay between the electron beam and the THz pulse. Images of the electron beam were integrated along the y-position.

7.3.3 Simulations

For a sufficiently short electron bunch, the determination of the bunch duration can be determined with a single-shot method, as demonstrated by Li *et al.* [53]. In this method, the streaking speed is first measured experimentally, by varying the relative delay between the electrons and the THz pulse, and from the resulting deflectogram, the deflection rate is ascertained. Then, the injection time of the electron bunch is set to the zero-crossing, where the spread of the electrons is at maximum. The bunch duration is then proportional to the spread measured on the camera sensor.

For the single-shot method to work and give accurate results, the electron bunch duration, should be shorter than half cycle of the driving THz pulse. For the case where the electron bunch duration is longer, then the electron bunch overlaps and interacts with more than one cycle, thus a different analysis is required. This would look like the smearing observed in the deflectogram in Figure 7.11, and it was also demonstrated by Kealhofer *et al.*, for the uncompressed beam configuration [47].

In order to extract and determine the electron pulse duration, the interaction was simulated and fitted to the data of Figure 7.11. The simulation technique described in §4.3.2 was used. The details of the simulations are described, following the order in the flowchart illustrated in Figure 4.14. The geometry parameters of the 100 keV DLW structure were used as input parameters for the generation of the mesh grid, and the calculation of the propagation constant. Spatial step sizes equal to $dx = 100\,\mu$m, $dy = 10\,\mu$m and $dz = 15\,\mu$m were chosen, discretising the simulation domain to approximately $77{\times}10^3$ mesh cells. The dz step size assured that a sampling frequency of 2 THz was sufficiently sampled in the calculation domain. The dy and dx step sizes were determined after a convergence scan, reaching a good computational time and accuracy balance. Only the vacuum region of the DLW was considered here.

For the THz source, the LSM_{01} was directly excited into the waveguide. The excitation signal was a single-cycle THz pulse, with a center frequency of 0.38 THz. The option of using the EO scan measurement directly to the simulations was available. However, the oscillations in the measured waveform due to the water absorption, introduced strong artefacts. Furthermore, the THz pulse EO measurement was obtained inside the vacuum chamber, following a propagation of more than 2 m

in ambient atmosphere. For the deflectogram measurements, the THz pulse only travelled approximately 0.5 m in ambient atmosphere, and then carried on in vacuum. Therefore, the transient excitation signal was modelled based on the measured data. The amplitude spectrum was modelled by fitting Equation 4.12 on the measured amplitude spectrum. The transient excitation signal was then obtained by inverse-Fourier transforming the amplitude spectrum. The excitation transient signal and the corresponding amplitude spectrum used in the simulation are depicted in Figure7.13 along with the measured data.

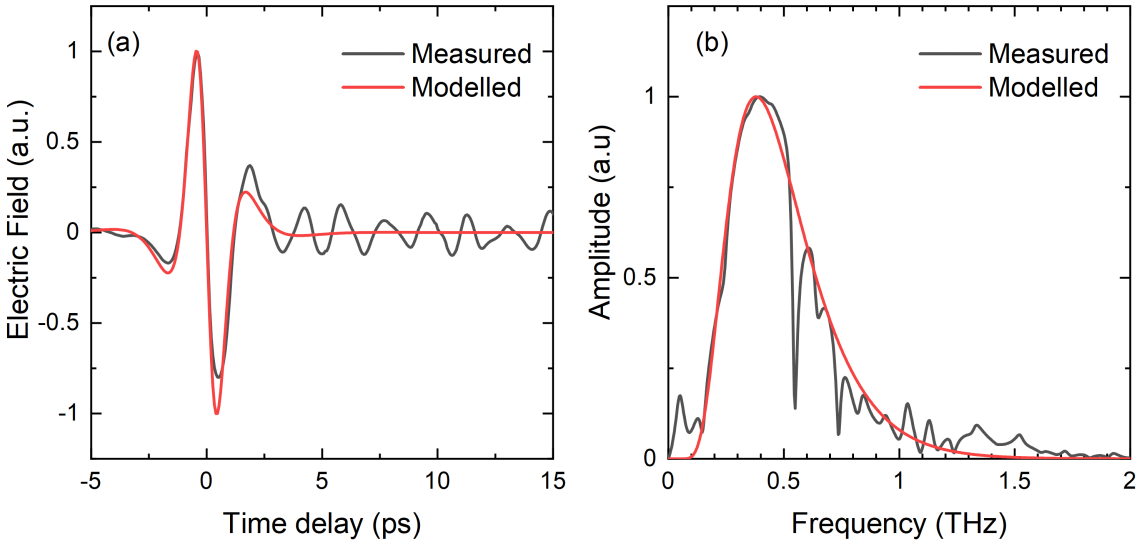

Fig. 7.13: (a) The modelled waveform (red) and (b) the modelled corresponding amplitude spectrum (red) of the measured electric field waveform (black) and amplitude spectrum (black), respectively.

The particle source was simulated with a commercial software, GPT, from the electron gun up to the entrance of the waveguide. The particle source was then directly inserted into the simulation. The GPT file was produced and provided by C. Shaw. In Figure 7.14, the particle source distribution is depicted. The mean energy of the electron bunch was approximately 100 keV, with a small energy spread. The transverse size was on the order of 200 μm diameter and 4 mrad divergence in both transverse planes. This electron distribution was used as the initial condition, a starting point of the fitting process.

Finally, the Phase Space Evolution (PSE) algorithm, would simulate the THz-electron interaction based upon the set parameters. PSE is an iterative procedure where the particle equation of motion is solved with numerical methods for each

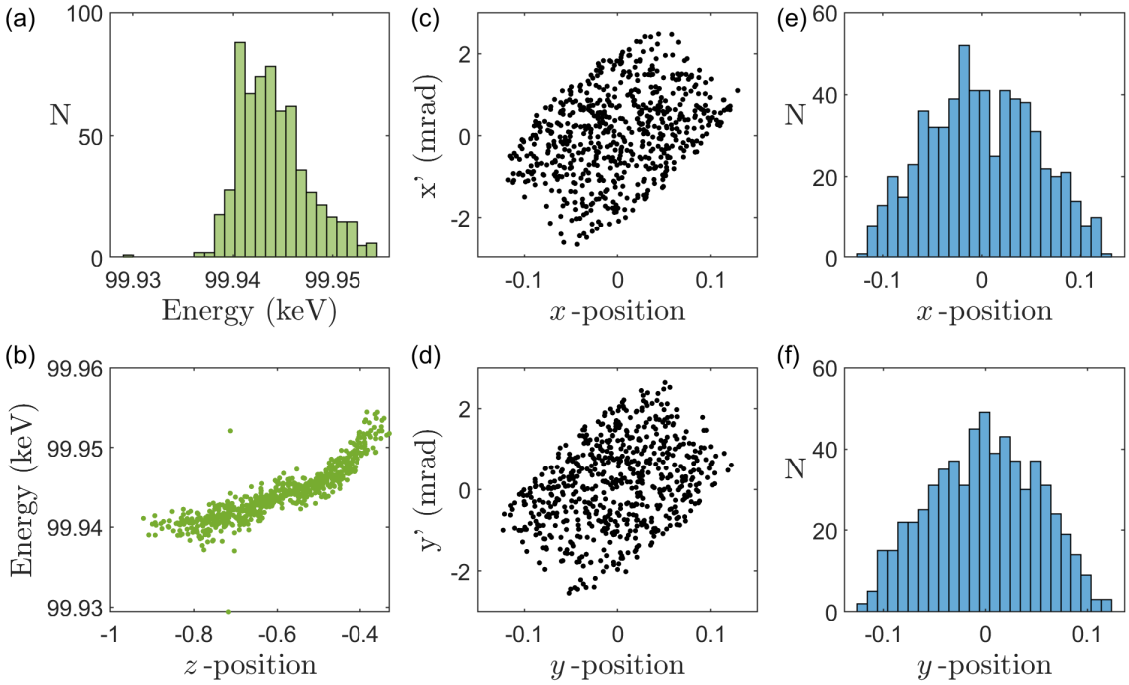

Fig. 7.14: The electron beam distribution used for the simulations. (a) The energy spectrum with the (b) energy spread as a function of the longitudinal position. (c) Horizontal and (d) divergence along with the histograms of the (e) horizontal and (f) vertical positions.

particle, and then the phase space of the electron bunch is evolved as well as the EM fields. The simulation terminates when the particles exit the simulation bounds, or the Transit Time is reached. The temporal step size of the PSE algorithm was set to $h = 30\,\mathrm{fs}$. The script tracks the boundary condition of the particles, monitoring whether they are still within the calculation domain, hence a transmittance was provided for each simulation run.

In order to simulate a deflectogram, the PSE algorithm was iterated over a sequence, varying the injection time of the electron pulse relatively to the THz field. Then in post-processing, the beam was transported onto a screen, via a transfer matrix, where the transverse profile of the beam was extracted. Similarly to the experimental data, a deflectogram was produced, by plotting the line profiles of the beam as a function of the injection time. In Figure 7.15(b) the simulated deflectogram is depicted along with the measured 7.15(a).

As can be seen, similar trends appear in the simulated deflectogram, at the zero-crossing, and then the smaller oscillations match as well. The small oscillations were

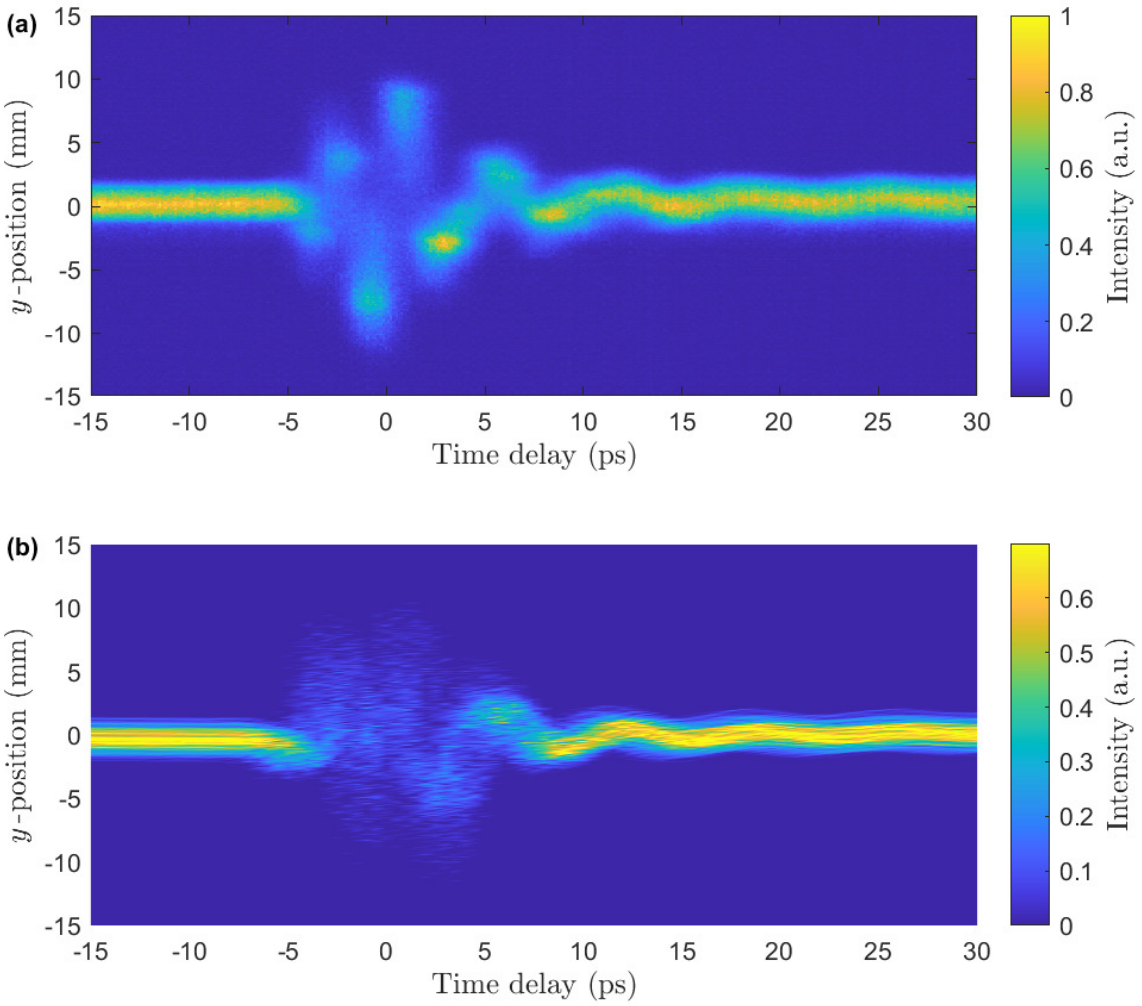

Fig. 7.15: (a) Measured and (b) simulated deflectogram. The simulated deflectogram was produced by using the electron beam distribution in Figure 7.14.

attributed due to the dispersion of the broadband THz pulse in the DLW. However, it was hard to distinguish any useful features from the diagram. This was mainly due to the small number of particles that have been simulated. In the laboratory, the electron gun operated at 10 Hz or higher, and the response time of the camera is finite. Therefore, what is measured by the MCP is the accumulation of electrons, whereas in the simulation, only one bunch is modelled, with a number of particles of approximately 600.

The simulation was repeated, with a higher number of virtual particles, in the order of 10^4, for the same time range. The electron beam distribution extracted from GPT was used as a reference, interpolating more particle within the same dis-

tribution. A parameter sweep was performed, where the electron beam parameters such as divergence, transverse size and beam duration were scanned, in order to find the best fitting. This fitting routine is scalable to more parameters, such as the THz field strength, beam energy, energy spread and vertical or horizontal offset inside the waveguide. However, in order to investigate all the parameters, considerably more computational power would be required. The simulation time increases linearly with the number of particles, and its proportional to the number of parameters in the scan. Here the THz source, DLW geometry and propagation constant were kept constant.

Figure 7.16(b) depicts the final deflectogram from the fitting parameter sweep. The results from the THz-electron simulation agree very well with the experimentally measured data. For the final deflectogram, an electron beam of 3.5 ps beam duration, 160 μm $1/e^2$ diameter and divergence of 7 mrad was used. In Figure 7.16, the features are more distinct and clearer which was evidence that the model developed and used for the THz-electron interaction was accurate. From the simulations, the transmittance of the particles would decrease before and after the zero-crossing, where the deflection maximises. As the electrons interact with the THz field, they start deflecting inside the structure, colliding with the dielectric slabs. However, in the simulations more than 60% of the beam was transmitted at maximum deflection.

Furthermore, from the simulations it was deduced that the peak deflecting electric field, on-axis, inside the waveguide, was $\mathrm{E}_y = 1.1\,\mathrm{MV/m}$. This was in line with other works in the literature, where Kealhofer *et al.* have employed a 1.3 MV/m THz source [47], Zhao *et al.* 17 MV/m [50], both with moderate THz pulse energies. Other works have mentioned higher figures like Li *et al.* where a 20 μJ pulse energy and field strength of up to 55 MV/m was used and Zhang *et al.* have used $2\times6\,\mu$J sources.

It should be noted that the shot-to-shot timing jitter was small enough so it would not make the analysis of the measurements challenging. Furthermore, the relative timing jitter between the THz pulse and the electron pulse was also negligible as the same laser system was used for the generation of electron and the driving THz pulse. The noise originating from other electronic devices within the laboratory or sometimes the facility, was greater than the machines responsible for the experiment.

In Figure 7.17 the deflectograms for a range of bunch durations is depicted

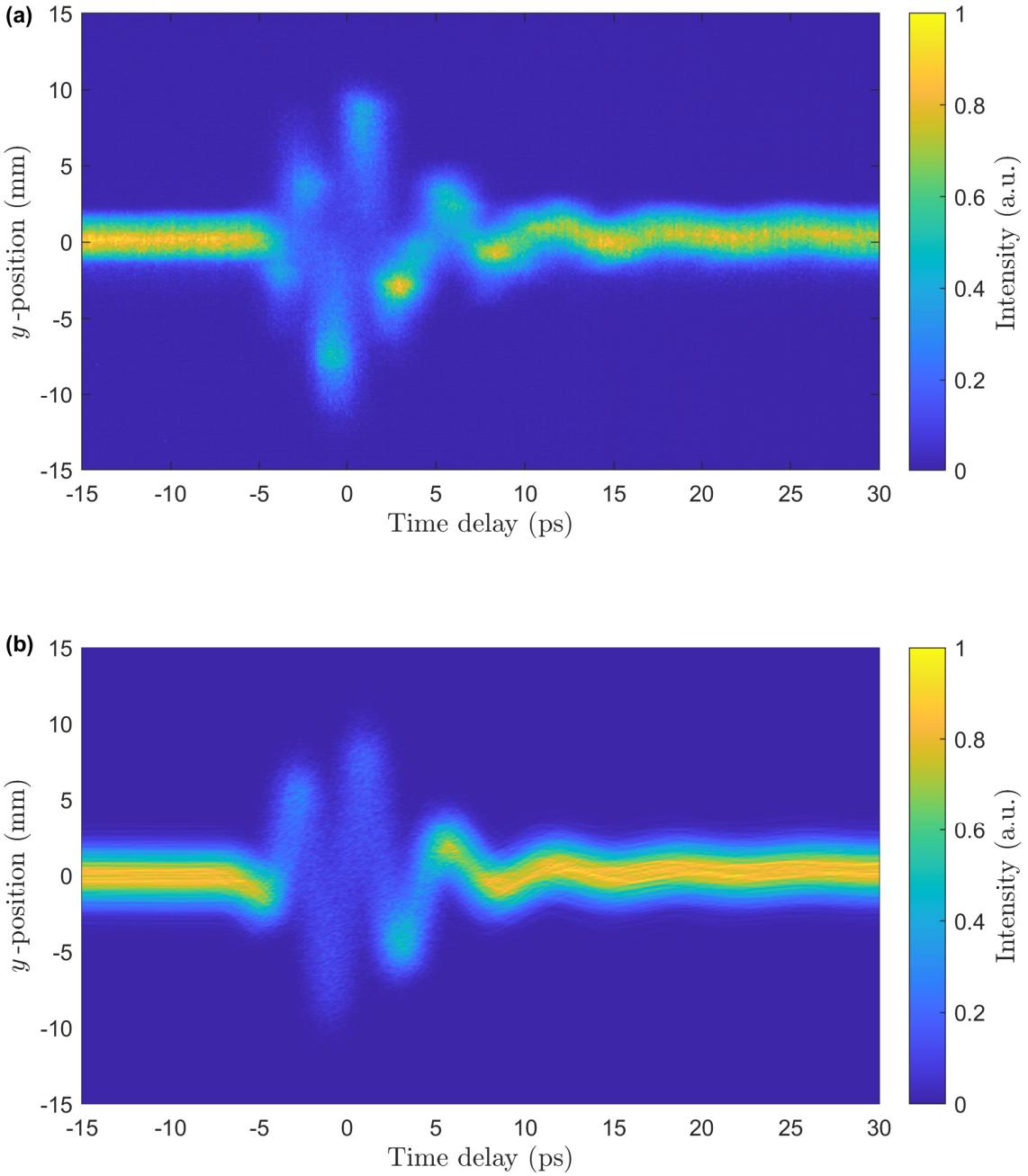

Fig. 7.16: (a) Measured and (b) simulated deflectogram. The simulated deflectogram was produced by using an interpolation of the electron beam distribution in Figure 7.14.

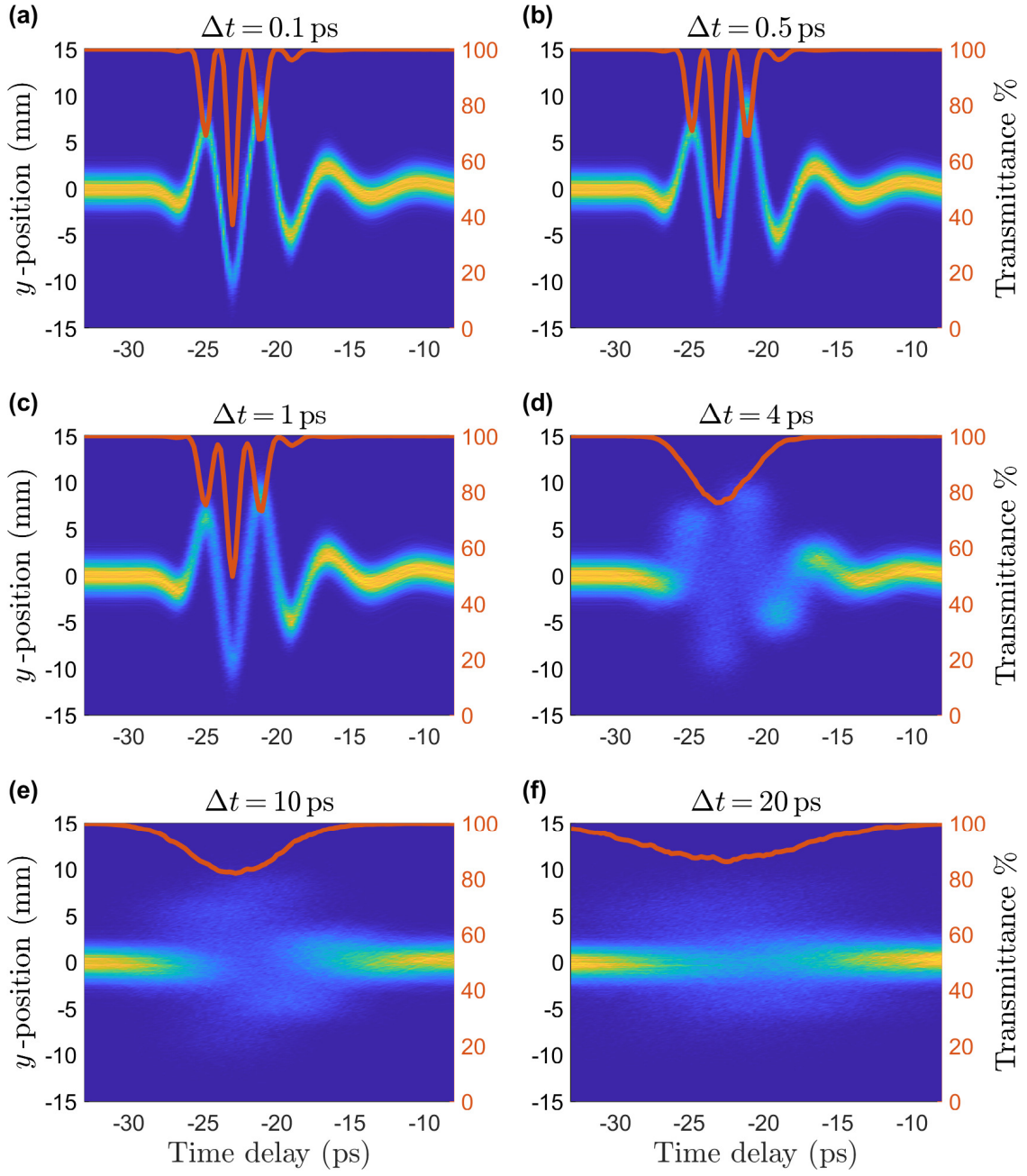

Fig. 7.17: Simulated deflectograms, for a range of electron bunch durations. For each deflectogram the bunch duration is written on the title, and in orange line, the transmittance is depicted as a function of the time delay.

for the same THz source parameters. As can be seen, the traces for shorter duration like in Figure 7.17(a) and 7.17(b) are sharper, as the bunch length is shorter than the half cycle of the driving THz pulse. However, at the maximum deflection, before and after the zero-crossing, the particle transmittance dropped as low as 40%, as the particles were more temporally localised and a bigger portion of the bunch would deflect and eventually collide on the dielectric slabs. As the bunch duration increases, the trace is clearly temporally smeared, as the electron bunch interacts with more than one cycle of the driving THz pulse. Furthermore, the transmittance increases for longer bunch durations. Here, only one set of electron beam parameters has been experimentally investigated. For shorter bunch durations, a bunch compressor would be required.

7.4 Conclusions

In this chapter, an all-optical concept for the control and characterisation of ultrafast electron bunches has been demonstrated. A 100 keV electron gun was installed in the LATTE lab, along with a high-power laser system, delivering 35 fs long, 800 nm centered laser pulses of 11 mJ energy. The laser system was used for the generation of electrons through photo-excitation of the cathode, and for the generation of THz radiation via optical rectification in a LN crystal.

The aim of the experiment was to generate ultrafast electron bunches and characterise the corresponding temporal content, using a THz-driven streaking scheme. Here, the streaking device was a DLW structure, designed to support the deflecting LSM_{01} mode, and it was tailored to phase velocity-match electron beams of 100 keV energy. The operating frequency was experimentally ascertained at $f_{op} = 0.47 \pm 0.02$ THz [157]. The DLW structure was driven by single-cycle THz pulses. The generated THz pulse had a lower centre frequency than the design frequency, however, because of the broad frequency content of the driving THz pulse, the DLW device was still operational.

The THz pulse and the electron bunch were spatially and temporally overlapped inside the DLW structure. The modulation of the transverse profile of the electron beam was monitored on a downstream MCP detector, as a function of the relative time delay. A deflectogram was obtained from the experimental results, where the

trace of the deflection as a function of time was deduced. The DLW structure was for the time demonstrated to operate as a THz-driven streaking device. The streaking speed was estimated to be approximately 28 mrad/ps, exceeding of what has been demonstrated in the literature for similar electron energy regime and THz sources.

The interaction was modelled using the simulation technique described in §4.3.2. A simulated deflectogram was obtained and through a parameter sweep process, the electron bunch parameters were fitted to the measured deflectogram. From the fitting routine, a bunch duration of 3.6 ps was ascertained. However, the fitting routine can be scaled up in order to investigate more experimental parameters. The fitting routine was only tested for one set of experimental results. Experiments were still ongoing at the time of compiling this work.

By the time the experiment was conducted, there were only two steering coils available and one electron beam lens. In future experiments, more controls for the beam alignment would be beneficial for the transmittance of the beam through the DLW structure. Ideally the beam would have been focussed through the structure and then focussed again onto the detector.

Chapter 8

Conclusions and further work

In this thesis, the work undertaken implementing a novel THz-driven particle accelerator and manipulator is detailed. The device was a rectangular-shaped dielectric-lined waveguide (DLW) structure, employed for either acceleration or deflection of relativistic and sub-relativistic electron beams. The DLW structures were tailored to support the Longitudinal Magnetic Section (LSM) modes with a phase velocity matched to the velocity of the electron beams at a specific frequency. The aim of this concept was to increase the THz-electron interaction length, in order to realise more efficient THz-driven particle acceleration and manipulation.

The propagation constant of the LSM_{01} mode was measured, using the cut-back technique, in a THz time-domain spectroscopy experiment. The DLW structure was designed for THz-driven streaking of 100 keV electron beams, at a center frequency of 0.47 THz. Linearly polarised, broadband THz pulses were coupled into the DLW structure in order to excite the deflecting mode. The propagation constant was measured by deconvolving the measured phase data of the electric field emerging from two identical structures of different length. At the operational frequency, the phase velocity was measured $v_p = 0.548 \pm 0.002c$ matching the $0.548c$ velocity of 100 keV electrons. A simple model was also developed to simulate the influence of the coupler and also remove the reflection echoes from the measured waveform.

In separate experiment, the propagation constant of the accelerating LSM_{11} mode of a different DLW structure was measured. The DLW structure was designed for acceleration of 35 MeV energy at center frequency of 0.4 THz. A TEM_{01} broadband THz pulse was coupled into the DLW structure in order to excite the accelerating mode. The operating frequency was experimentally ascertained at

$f_{op} = 0.41 \pm 0.02\,\mathrm{THz}$. In both cases, the coupling coefficient of the structure was not measured, as there was no output coupler at the time. Different coupler geometries could be explored such as an exponentially-tapered coupler as demonstrated by Othman *et al.* [160]. The current DLW structures were designed taking into account an incident plane wave THz pulse, however for the next generation structures the Gaussian shape of the incident THz beam should be taken into account. Another advantage of an output coupler, would be the realisation of cascaded acceleration of an electron beam, using the same THz pulse.

Exploitation time at the CLARA test facility was allocated, in order to benchmark the DLW structure for THz-driven acceleration of electron beams of 35 MeV energy. The DLW structure was driven by narrowband, polarisation-tailored THz pulses. The DLW structure facilitated the acceleration of up to three orders of magnitude higher charge than previous THz-driven acceleration works [42]. The peak acceleration achieved was estimated to be $\delta E_{\mathrm{THz}} = 10\,\mathrm{keV}$, with an average acceleration gradient of 2 MV/m, which was an order of magnitude greater than what Curry *et al.* have reported [46]. Although this figure cannot directly compete with current radio frequency accelerating cavities. However, this demonstration was directly applicable to both scaled-up and multi-staged acceleration, marking a key milestone in the development of future high-energy, high-charge THz-driven accelerators.

This scheme could be applied for any energy regime, by tailoring the dielectric thickness and vacuum aperture. For future experiments, a more powerful THz source would be employed, in order to scale the acceleration to the order of 1 MeV. Bringing the THz source to cryogenic temperatures, as well as tuning the bandwidth and the centre frequency of the source with a different scheme [161] could improve the interaction. Moreover, in order to compensate the group velocity walk-off of the THz pulse, a tapered DLW structure could be designed.

An all-optical concept for the control and characterisation of ultrafast electron bunches has been demonstrated in the LATTE lab, where a 100 keV electron gun system was installed along with a high-power laser system. Ultrafast electron bunches were generated via photo-excitation and the pulse duration was measured using a THz-driven streaking scheme. The DLW structure was employed as the streaking device, driven by single-cycle THz pulses. Streaking speed up to 28 mrad/ps was measured, exceeding of what has been demonstrated in the literature for similar

electron energy regime and THz sources [47, 50, 53]. The bunch duration of the electron beam was determined to be 3.6 ps. Experiments were still ongoing at the time of compiling this work.

The control of the beam was found to be limited at the time of the experiment, therefore aligning the beam through the structure and focussing it onto the screen was challenging. Magnetic isolation of the whole apparatus would be beneficial, as it was proven to be very sensitive to external magnetic fields. In future work, the energy spectrum of the beam would also be measured, by employing an energy spectrometer. In conjunction with the streaking device, the energy chirp of the electron beam could be experimentally determined. Moreover, a second DLW structure could be used, operating in the accelerating mode, where it could be used for compression or acceleration of the beam, depending on the relative phase. When varying the electron beam to higher charges, the alignment through the structure was not possible. This was attributed to charging up of the dielectrics as the electrons would collide on them. As a result, a static electric field would build up, acting as a gate. Therefore, a collimator ensuring an electron beam of diameter less than then vacuum aperture of the structure would be advantageous.

A model simulating the interaction of the particles with electromagnetic (EM) fields was developed, based on the Particle-In-Cell method. In the simulation, the relativistic particle equation of motion was solved with numerical methods, and then the phase space of the electron bunch was evolved as well as the EM fields. The LSM_{01} was directly injected and the analytical EM field pattern was evaluated on a discretised mesh grid. A fitting routine was developed in order to match the simulations with the experimental results, concluding to the corresponding electron beam parameters. The fitting routine was not fully optimised and has not been tested with experimental results of different beam parameters. Further optimisation would consider the implementation of more fitting parameters. Future work using this simulation, would be the investigation of THz-electron interaction for a range of THz bandwidths. Moreover, since the script was developed in MATLAB, it could be easily deployed on computers clusters and cloud servers, where more computational power is available.

Appendix

General Particle Tracer

The General Particle Tracer (GPT) is a software package developed by Pulsar Physics [122, 123]. GPT consists of computer-based simulation tools used for the study of the 3-dimensional charged-particles dynamics in electromagnetic fields . It is mainly employed for the design and modelling of accelerators and beam lines. In this thesis, GPT was used for the modelling of the 100 keV electron gun system in Chapter 7. The relativistic equation of motion for the macro-particles is solved in the time domain using a 5th order embedded Runge-Kutta integrator with an adaptive stepsize control. A 3D space-charge model is also available and it was considered for the beam modelling in §7.3.3. The elements of the 100 keV electron gun system, namely the cathode, the 1st and 2nd anode, the control grid aperture and the focussing lens were modelled. The settings of the gun were explored such as the shortest electron bunch with maximal brightness and transmittance through the structure could be delivered. The 1st anode was set to 5 kV, whereas the control grid and the 2nd anode were set to 0 V. The resulting particle distribution was then extracted as an output file and used as an input in MATLAB for post-processing.

References

[1] F. Wang, C. Adolphsen, and C. Nantista, "Performance limiting effects in X-band accelerators," *Physical Review Special Topics-Accelerators and Beams*, vol. 14, no. 1, p. 010401, 2011.

[2] Y.-S. Lee, *Principles of terahertz science and technology*, vol. 170. New York: Springer Science & Business Media, 2009.

[3] S. L. Dexheimer, *Terahertz spectroscopy: Principles and Applications*. New York: CRC press, 2007.

[4] X.-C. Zhang and J. Xu, *Introduction to THz wave photonics*, vol. 29. New York: Springer, 2010.

[5] H. Zhao, Y. Tan, L. Zhang, R. Zhang, M. Shalaby, C. Zhang, Y. Zhao, and X.-C. Zhang, "Ultrafast hydrogen bond dynamics of liquid water revealed by terahertz-induced transient birefringence," *Light: Science & Applications*, vol. 9, no. 1, pp. 1–10, 2020.

[6] W. Zouaghi, M. Thomson, K. Rabia, R. Hahn, V. Blank, and H. Roskos, "Broadband terahertz spectroscopy: principles, fundamental research and potential for industrial applications," *European Journal of Physics*, vol. 34, no. 6, p. S179, 2013.

[7] R. A. Lewis, "A review of terahertz sources," *Journal of Physics D: Applied Physics*, vol. 47, no. 37, p. 374001, 2014.

[8] S. Dhillon, M. Vitiello, E. Linfield, A. Davies, M. C. Hoffmann, J. Booske, C. Paoloni, M. Gensch, P. Weightman, G. Williams, *et al.*, "The 2017 terahertz science and technology roadmap," *Journal of Physics D: Applied Physics*, vol. 50, no. 4, p. 043001, 2017.

[9] G. P. Gallerano, S. Biedron, *et al.*, "Overview of terahertz radiation sources," in *Proceedings of the 2004 FEL Conference*, vol. 1, pp. 216–221, 2004.

[10] D. Faries, K. Gehring, P. Richards, and Y. Shen, "Tunable far-infrared radiation generated from the difference frequency between two ruby lasers," *Physical Review*, vol. 180, no. 2, p. 363, 1969.

[11] J. Morris and Y. Shen, "Far-infrared generation by picosecond pulses in electro-optical materials," *Optics Communications*, vol. 3, no. 2, pp. 81–84, 1971.

[12] Köhler, Rüdeger and Tredicucci, Alessandro and Beltram, Fabio and Beere, Harvey E and Linfield, Edmund H and Davies, A Giles and Ritchie, David A and Iotti, Rita C and Rossi, Fausto, "Terahertz semiconductor-heterostructure laser," *Nature*, vol. 417, no. 6885, pp. 156–159, 2002.

[13] P. Shumyatsky and R. R. Alfano, "Terahertz sources," *Journal of Biomedical Optics*, vol. 16, no. 3, p. 033001, 2011.

[14] Z. Wang, "Generation of terahertz radiation via nonlinear optical methods," *IEEE Transactions on Geoscience and Remote Sensing*, vol. 1, no. 1, pp. 1–5, 2001.

[15] D. A. Deacon, L. Elias, J. M. Madey, G. Ramian, H. Schwettman, and T. I. Smith, "First operation of a free-electron laser," *Physical Review Letters*, vol. 38, no. 16, p. 892, 1977.

[16] H. Wiedemann, *Particle accelerator physics*. New York: Springer Nature, 2015.

[17] L. Evans and P. Bryant, "LHC machine," *Journal of Instrumentation*, vol. 3, no. 08, p. S08001, 2008.

[18] R. Bhandari and M. K. Dey, "Applications of accelerator technology and its relevance to nuclear technology," *Energy Procedia*, vol. 7, pp. 577–588, 2011.

[19] M. Silindir and A. Y. Özer, "Sterilization methods and the comparison of e-beam sterilization with gamma radiation sterilization," *Fabad Journal of Pharmaceutical Sciences*, vol. 34, no. 1, p. 43, 2009.

[20] A. Grudiev, S. Calatroni, and W. Wuensch, "New local field quantity describing the high gradient limit of accelerating structures," *Physical Review Special Topics-Accelerators and Beams*, vol. 12, no. 10, p. 102001, 2009.

[21] A. Grassellino, A. Romanenko, Y. Trenikhina, M. Checchin, M. Martinello, O. Melnychuk, S. Chandrasekaran, D. Sergatskov, S. Posen, A. Crawford, *et al.*, "Unprecedented quality factors at accelerating gradients up to 45 mvm-1 in niobium superconducting resonators via low temperature nitrogen infusion," *Superconductor Science and Technology*, vol. 30, no. 9, p. 094004, 2017.

[22] V. D. Shiltsev, "Accelerator physics and technology challenges of very high energy hadron colliders," *International Journal of Modern Physics A*, vol. 30, no. 23, p. 1544001, 2015.

[23] C. Joshi and V. Malka, "Focus on laser-and beam-driven plasma accelerators," *New Journal of Physics*, vol. 12, no. 4, p. 045003, 2010.

[24] E. R. Colby and L. Len, "Roadmap to the future," in *Reviews of Accelerator Science and Technology: Volume 9: Technology and Applications of Advanced Accelerator Concepts*, pp. 1–18, World Scientific, 2016.

[25] T. Tajima and J. M. Dawson, "Laser electron accelerator," *Physical Review Letters*, vol. 43, no. 4, p. 267, 1979.

[26] A. Modena, Z. Najmudin, A. Dangor, C. Clayton, K. Marsh, C. Joshi, V. Malka, C. Darrow, C. Danson, D. Neely, *et al.*, "Electron acceleration from the breaking of relativistic plasma waves," *nature*, vol. 377, no. 6550, pp. 606–608, 1995.

[27] X. Wang, R. Zgadzaj, N. Fazel, Z. Li, S. Yi, X. Zhang, W. Henderson, Y.-Y. Chang, R. Korzekwa, H.-E. Tsai, *et al.*, "Quasi-monoenergetic laser-plasma acceleration of electrons to 2 GeV," *Nature Communications*, vol. 4, no. 1, pp. 1–9, 2013.

[28] E. Esarey, C. Schroeder, and W. Leemans, "Physics of laser-driven plasma-based electron accelerators," *Reviews of Modern Physics*, vol. 81, no. 3, p. 1229, 2009.

[29] P. Chen, J. Dawson, R. W. Huff, and T. Katsouleas, "Acceleration of electrons by the interaction of a bunched electron beam with a plasma," *Physical Review Letters*, vol. 54, no. 7, p. 693, 1985.

[30] J. B. Rosenzweig, D. Cline, B. Cole, H. Figueroa, W. Gai, R. Konecny, J. Norem, P. Schoessow, and J. Simpson, "Experimental observation of plasma wake-field acceleration," *Physical Review Letters*, vol. 61, no. 1, p. 98, 1988.

[31] P. Muggli and M. J. Hogan, "Review of high-energy plasma wakefield experiments," *Comptes Rendus Physique*, vol. 10, no. 2-3, pp. 116–129, 2009.

[32] E. Gschwendtner and P. Muggli, "Plasma wakefield accelerators," *Nature Reviews Physics*, vol. 1, no. 4, pp. 246–248, 2019.

[33] B. Naranjo, A. Valloni, S. Putterman, and J. Rosenzweig, "Stable charged-particle acceleration and focusing in a laser accelerator using spatial harmonics," *Physical Review Letters*, vol. 109, no. 16, p. 164803, 2012.

[34] J. Breuer and P. Hommelhoff, "Laser-based acceleration of nonrelativistic electrons at a dielectric structure," *Physical Review Letters*, vol. 111, no. 13, p. 134803, 2013.

[35] J. Rosenzweig, A. Murokh, and C. Pellegrini, "A proposed dielectric-loaded resonant laser accelerator," *Physical Review Letters*, vol. 74, no. 13, p. 2467, 1995.

[36] B. M. Cowan, "Three-dimensional dielectric photonic crystal structures for laser-driven acceleration," *Physical Review Special Topics-Accelerators and Beams*, vol. 11, no. 1, p. 011301, 2008.

[37] X. E. Lin, "Photonic band gap fiber accelerator," *Physical Review Special Topics-Accelerators and Beams*, vol. 4, no. 5, p. 051301, 2001.

[38] E. Peralta, K. Soong, R. England, E. Colby, Z. Wu, B. Montazeri, C. McGuinness, J. McNeur, K. Leedle, D. Walz, *et al.*, "Demonstration of electron acceleration in a laser-driven dielectric microstructure," *Nature*, vol. 503, no. 7474, pp. 91–94, 2013.

[39] D. Cesar, S. Custodio, J. Maxson, P. Musumeci, X. Shen, E. Threlkeld, R. England, A. Hanuka, I. Makasyuk, E. Peralta, *et al.*, "High-field nonlinear optical response and phase control in a dielectric laser accelerator," *Communications Physics*, vol. 1, no. 1, pp. 1–7, 2018.

[40] M. Shalaby and C. P. Hauri, "Demonstration of a low-frequency three-dimensional terahertz bullet with extreme brightness," *Nature Communications*, vol. 6, no. 1, pp. 1–8, 2015.

[41] E. A. Nanni, W. R. Huang, K.-H. Hong, K. Ravi, A. Fallahi, G. Moriena, R. D. Miller, and F. X. Kärtner, "Terahertz-driven linear electron acceleration," *Nature Communications*, vol. 6, p. 8486, 2015.

[42] D. Zhang, A. Fallahi, M. Hemmer, X. Wu, M. Fakhari, Y. Hua, H. Cankaya, A.-L. Calendron, L. E. Zapata, N. H. Matlis, *et al.*, "Segmented terahertz electron accelerator and manipulator (STEAM)," *Nature photonics*, vol. 12, no. 6, pp. 336–342, 2018.

[43] W. R. Huang, E. A. Nanni, K. Ravi, L. J. Wong, K.-H. Hong, and F. X. Kärtner, "Electron acceleration in a single-cycle terahertz field," in *2014 39th International Conference on Infrared, Millimeter, and Terahertz waves (IRMMW-THz)*, pp. 1–1, IEEE, 2014.

[44] W. R. Huang, A. Fallahi, X. Wu, H. Cankaya, A.-L. Calendron, K. Ravi, D. Zhang, E. A. Nanni, K.-H. Hong, and F. X. Kärtner, "Terahertz-driven, all-optical electron gun," *Optica*, vol. 3, no. 11, pp. 1209–1212, 2016.

[45] D. Zhang, M. Fakhari, H. Cankaya, A.-L. Calendron, N. H. Matlis, and F. X. Kärtner, "Cascaded multicycle terahertz-driven ultrafast electron acceleration and manipulation," *Physical Review X*, vol. 10, no. 1, p. 011067, 2020.

[46] E. Curry, S. Fabbri, J. Maxson, P. Musumeci, and A. Gover, "Meter-scale terahertz-driven acceleration of a relativistic beam," *Physical Review Letters*, vol. 120, no. 9, p. 094801, 2018.

[47] C. Kealhofer, W. Schneider, D. Ehberger, A. Ryabov, F. Krausz, and P. Baum, "All-optical control and metrology of electron pulses," *Science*, vol. 352, no. 6284, pp. 429–433, 2016.

[48] D. Ehberger, A. Ryabov, and P. Baum, "Tilted electron pulses," *Physical Review Letters*, vol. 121, no. 9, p. 094801, 2018.

[49] D. Ehberger, K. J. Mohler, T. Vasileiadis, R. Ernstorfer, L. Waldecker, and P. Baum, "Terahertz compression of electron pulses at a planar mirror membrane," *Physical Review Applied*, vol. 11, no. 2, p. 024034, 2019.

[50] L. Zhao, Z. Wang, C. Lu, R. Wang, C. Hu, P. Wang, J. Qi, T. Jiang, S. Liu, Z. Ma, *et al.*, "Terahertz streaking of few-femtosecond relativistic electron beams," *Physical Review X*, vol. 8, no. 2, p. 021061, 2018.

[51] L. Zhao, Z. Wang, H. Tang, R. Wang, Y. Cheng, C. Lu, T. Jiang, P. Zhu, L. Hu, W. Song, *et al.*, "Terahertz oscilloscope for recording time information of ultrashort electron beams," *Physical Review Letters*, vol. 122, no. 14, p. 144801, 2019.

[52] L. Zhao, H. Tang, C. Lu, T. Jiang, P. Zhu, L. Hu, W. Song, H. Wang, J. Qiu, C. Jing, *et al.*, "Femtosecond relativistic electron beam with reduced timing jitter from THz driven beam compression," *Physical Review Letters*, vol. 124, no. 5, p. 054802, 2020.

[53] R. Li, M. Hoffmann, E. Nanni, S. Glenzer, M. Kozina, A. Lindenberg, B. Ofori-Okai, A. Reid, X. Shen, S. Weathersby, *et al.*, "Terahertz-based subfemtosecond metrology of relativistic electron beams," *Physical Review Accelerators and Beams*, vol. 22, no. 1, p. 012803, 2019.

[54] J. A. Fülöp, S. Tzortzakis, and T. Kampfrath, "Laser-driven strong-field terahertz sources," *Advanced Optical Materials*, vol. 8, no. 3, p. 1900681, 2020.

[55] K. Yang, P. Richards, and Y. Shen, "Generation of far-infrared radiation by picosecond light pulses in linbo3," *Applied Physics Letters*, vol. 19, no. 9, pp. 320–323, 1971.

[56] A. Othonos, "Probing ultrafast carrier and phonon dynamics in semiconductors," *Journal of Applied Physics*, vol. 83, no. 4, pp. 1789–1830, 1998.

[57] J. Hebling, G. Almasi, I. Z. Kozma, and J. Kuhl, "Velocity matching by pulse front tilting for large-area THz-pulse generation," *Optics Express*, vol. 10, no. 21, pp. 1161–1166, 2002.

[58] X.-j. Wu, J.-l. Ma, B.-l. Zhang, S.-s. Chai, Z.-j. Fang, C.-Y. Xia, D.-y. Kong, J.-g. Wang, H. Liu, C.-Q. Zhu, *et al.*, "Highly efficient generation of 0.2 mj terahertz pulses in lithium niobate at room temperature with sub-50 fs chirped ti:sapphire laser pulses," *Optics Express*, vol. 26, no. 6, pp. 7107–7116, 2018.

[59] J. A. Fülöp, Z. Ollmann, C. Lombosi, C. Skrobol, S. Klingebiel, L. Pálfalvi, F. Krausz, S. Karsch, and J. Hebling, "Efficient generation of thz pulses with 0.4 mj energy," *Optics Express*, vol. 22, no. 17, pp. 20155–20163, 2014.

[60] S.-W. Huang, E. Granados, W. R. Huang, K.-H. Hong, L. E. Zapata, and F. X. Kärtner, "High conversion efficiency, high energy terahertz pulses by optical rectification in cryogenically cooled lithium niobate," *Optics Letters*, vol. 38, no. 5, pp. 796–798, 2013.

[61] J. Fülöp, L. Pálfalvi, G. Almási, and J. Hebling, "Design of high-energy terahertz sources based on optical rectification," *Optics Express*, vol. 18, no. 12, pp. 12311–12327, 2010.

[62] M. I. Bakunov and S. B. Bodrov, "Terahertz generation with tilted-front laser pulses in a contact-grating scheme," *JOSA B*, vol. 31, no. 11, pp. 2549–2557, 2014.

[63] L. Pálfalvi, J. Fülöp, G. Almási, and J. Hebling, "Novel setups for extremely high power single-cycle terahertz pulse generation by optical rectification," *Applied Physics Letters*, vol. 92, no. 17, p. 171107, 2008.

[64] L. Pálfalvi, G. Tóth, L. Tokodi, Z. Márton, J. A. Fülöp, G. Almási, and J. Hebling, "Numerical investigation of a scalable setup for efficient terahertz generation using a segmented tilted-pulse-front excitation," *Optics Express*, vol. 25, no. 24, pp. 29560–29573, 2017.

[65] J. A. Fülöp, G. Polónyi, B. Monoszlai, G. Andriukaitis, T. Balciunas, A. Pugzlys, G. Arthur, A. Baltuska, and J. Hebling, "Highly efficient scalable monolithic semiconductor terahertz pulse source," *Optica*, vol. 3, no. 10, pp. 1075–1078, 2016.

[66] C. Vicario, A. Ovchinnikov, S. Ashitkov, M. Agranat, V. Fortov, and C. Hauri, "Generation of 0.9-mJ THz pulses in DSTMS pumped by a Cr: Mg 2 SiO 4 laser," *Optics Letters*, vol. 39, no. 23, pp. 6632–6635, 2014.

[67] C. Vicario, B. Monoszlai, and C. P. Hauri, "Gv/m single-cycle terahertz fields from a laser-driven large-size partitioned organic crystal," *Physical Review Letters*, vol. 112, no. 21, p. 213901, 2014.

[68] B. Monoszlai, C. Vicario, M. Jazbinsek, and C. Hauri, "High-energy terahertz pulses from organic crystals: Dast and dstms pumped at ti: sapphire wavelength," *Optics Letters*, vol. 38, no. 23, pp. 5106–5109, 2013.

[69] C. Bull, S. M. Hewett, R. Ji, C.-H. Lin, T. Thomson, D. M. Graham, and P. W. Nutter, "Spintronic terahertz emitters: Status and prospects from a materials perspective," *APL Materials*, vol. 9, no. 9, p. 090701, 2021.

[70] T. Seifert, S. Jaiswal, U. Martens, J. Hannegan, L. Braun, P. Maldonado, F. Freimuth, A. Kronenberg, J. Henrizi, I. Radu, *et al.*, "Efficient metallic spintronic emitters of ultrabroadband terahertz radiation," *Nature photonics*, vol. 10, no. 7, p. 483, 2016.

[71] N. Laman and D. Grischkowsky, "Terahertz conductivity of thin metal films," *Applied Physics Letters*, vol. 93, no. 5, p. 051105, 2008.

[72] E. T. Papaioannou, G. Torosyan, S. Keller, L. Scheuer, M. Battiato, V. K. Mag-Usara, J. L'huillier, M. Tani, and R. Beigang, "Efficient Terahertz Generation Using Fe/Pt Spintronic Emitters Pumped at Different Wavelengths," *IEEE Transactions on Magnetics*, no. 99, pp. 1–5, 2018.

[73] M. T. Hibberd, D. S. Lake, N. Johansson, T. Thomson, S. P. Jamison, and D. M. Graham, "Magnetic-field tailoring of the terahertz polarization emitted from a spintronic source," *Applied Physics Letters*, vol. 114, no. 3, p. 031101, 2019.

[74] R. W. Boyd, *Nonlinear optics*. New York: Academic press, 2008.

[75] M. Cliffe, D. Graham, and S. Jamison, "Longitudinally polarized single-cycle terahertz pulses generated with high electric field strengths," *Applied Physics Letters*, vol. 108, no. 22, p. 221102, 2016.

[76] P. C. Planken, H.-K. Nienhuys, H. J. Bakker, and T. Wenckebach, "Measurement and calculation of the orientation dependence of terahertz pulse detection in ZnTe," *JOSA B*, vol. 18, no. 3, pp. 313–317, 2001.

[77] G. Gaborit, F. Sanjuan, and J.-L. Coutaz, "Second order nonlinear optical processes in [111] cubic crystals for terahertz optoelectronics," *Lithuanian Journal of Physics*, vol. 58, no. 1, 2018.

[78] L. Tokodi, J. Hebling, and L. Pálfalvi, "Optimization of the tilted-pulse-front terahertz excitation setup containing telescope," *Journal of Infrared, Millimeter, and Terahertz Waves*, vol. 38, no. 1, pp. 22–32, 2017.

[79] H. Hirori, A. Doi, F. Blanchard, and K. Tanaka, "Single-cycle terahertz pulses with amplitudes exceeding 1 MV/cm generated by optical rectification in LiNbO3," *Applied Physics Letters*, vol. 98, no. 9, p. 091106, 2011.

[80] A. Weling, B. Hu, N. Froberg, and D. Auston, "Generation of tunable narrow-band THz radiation from large aperture photoconducting antennas," *Applied physics letters*, vol. 64, no. 2, pp. 137–139, 1994.

[81] S. Backus, C. G. Durfee III, M. M. Murnane, and H. C. Kapteyn, "High power ultrafast lasers," *Review of scientific instruments*, vol. 69, no. 3, pp. 1207–1223, 1998.

[82] A. S. Weling and D. H. Auston, "Novel sources and detectors for coherent tunable narrow-band terahertz radiation in free space," *JOSA B*, vol. 13, no. 12, pp. 2783–2792, 1996.

[83] R. Yano and H. Gotoh, "Tunable terahertz electromagnetic wave generation using birefringent crystal and grating pair," *Japanese Journal of Applied Physics*, vol. 44, no. 12R, p. 8470, 2005.

[84] T. Kampfrath, M. Battiato, P. Maldonado, G. Eilers, J. Nötzold, S. Mährlein, V. Zbarsky, F. Freimuth, Y. Mokrousov, S. Blügel, *et al.*, "Terahertz spin current pulses controlled by magnetic heterostructures," *Nature Nanotechnology*, vol. 8, no. 4, p. 256, 2013.

[85] K. Uchida, S. Takahashi, K. Harii, J. Ieda, W. Koshibae, K. Ando, S. Maekawa, and E. Saitoh, "Observation of the spin Seebeck effect," *Nature*, vol. 455, no. 7214, p. 778, 2008.

[86] G. E. Bauer, E. Saitoh, and B. J. Van Wees, "Spin caloritronics," *Nature materials*, vol. 11, no. 5, p. 391, 2012.

[87] M. Battiato, K. Carva, and P. M. Oppeneer, "Superdiffusive spin transport as a mechanism of ultrafast demagnetization," *Physical Review Letters*, vol. 105, no. 2, p. 027203, 2010.

[88] D. Wei, M. Obstbaum, M. Ribow, C. H. Back, and G. Woltersdorf, "Spin Hall voltages from ac and dc spin currents," *Nature Communications*, vol. 5, p. 3768, 2014.

[89] A. Hoffmann, "Spin Hall effects in metals," *IEEE transactions on magnetics*, vol. 49, no. 10, pp. 5172–5193, 2013.

[90] E. Saitoh, M. Ueda, H. Miyajima, and G. Tatara, "Conversion of spin current into charge current at room temperature: Inverse spin-Hall effect," *Applied physics letters*, vol. 88, no. 18, p. 182509, 2006.

[91] S. Maekawa, S. O. Valenzuela, E. Saitoh, and T. Kimura, *Spin current*, vol. 22. Oxford University Press, 2017.

[92] D. Yang, J. Liang, C. Zhou, L. Sun, R. Zheng, S. Luo, Y. Wu, and J. Qi, "Powerful and tunable THz emitters based on the Fe/Pt magnetic heterostructure," *Advanced Optical Materials*, vol. 4, no. 12, pp. 1944–1949, 2016.

[93] D. J. Griffiths, *Introduction to electrodynamics*. American Association of Physics Teachers, 2005.

[94] R. E. Collin, *Field theory of guided waves*, vol. 5. John Wiley & Sons, 1990.

[95] D. M. Pozar, *Microwave engineering*. John Wiley & sons, 2011.

[96] L. Xiao, W. Gai, and X. Sun, "Field analysis of a dielectric-loaded rectangular waveguide accelerating structure," *Physical Review E*, vol. 65, no. 1, p. 016505, 2001.

[97] T. P. Wangler, *RF Linear accelerators*. John Wiley & Sons, 2008.

[98] S.-Y. Lee, *Accelerator physics*. World Scientific, 2004.

[99] H. A. Haus, "Mode-locking of lasers," *IEEE Journal of Selected Topics in Quantum Electronics*, vol. 6, no. 6, pp. 1173–1185, 2000.

[100] G. Priebe, D. Laundy, M. Macdonald, G. Diakun, S. Jamison, L. Jones, D. Holder, S. Smith, P. Phillips, B. Fell, *et al.*, "Inverse Compton backscattering source driven by the multi-10 TW laser installed at Daresbury," *Laser and Particle Beams*, vol. 26, no. 4, p. 649, 2008.

[101] P. McIntosh, D. Angal-Kalinin, J. Clarke, L. Cowie, B. Fell, A. Gleeson, S. Jamison, T. Jones, B. Militsyn, Y. Saveliev, *et al.*, "The VELA and CLARA test facilities at Daresbury Laboratory," *Proc. LINAC'16*, pp. 734–739, 2016.

[102] Kimball-Physics, *EGH-8121A Electron Gun Technical Manual*, 2017.

[103] K. Iwaszczuk, A. Andryieuski, A. Lavrinenko, X.-C. Zhang, and P. U. Jepsen, "Terahertz field enhancement to the MV/cm regime in a tapered parallel plate waveguide," *Optics Express*, vol. 20, no. 8, pp. 8344–8355, 2012.

[104] A. Healy, *Energy modulation of electron bunches using a terahertz-driven dielectric-lined waveguide*. PhD thesis, Lancaster University, 2020.

[105] S. E. Ralph, S. Perkowitz, N. Katzenellenbogen, and D. Grischkowsky, "Terahertz spectroscopy of optically thick multilayered semiconductor structures," *JOSA B*, vol. 11, no. 12, pp. 2528–2532, 1994.

[106] C. Randall and R. Rawcliffe, "Refractive indices of germanium, silicon, and fused quartz in the far infrared," *Applied Optics*, vol. 6, no. 11, pp. 1889–1895, 1967.

[107] E. Dadrasnia, S. Puthukodan, V. V. Thalakkatukalathil, H. Lamela, G. Ducournau, J.-F. Lampin, F. Garet, and J.-L. Coutaz, "Sub-THz characterisation of monolayer graphene," *Journal of Spectroscopy*, vol. 2014, 2014.

[108] K. F. Riley, M. P. Hobson, and S. J. Bence, *Mathematical Methods for Physics and Engineering*. Cambridge University Press, 3 ed., 2006.

[109] K. F. Riley, M. P. Hobson, and S. J. Bence, *Mathematical methods for physics and engineering*. Cambridge University Press, 1999.

[110] G. James, P. P. Dyke, J. Searl, M. Craven, and Y. Wei, *Modern engineering mathematics*. Pearson UK, 2020.

[111] W. H. Press, S. A. Teukolsky, W. T. Vetterling, and B. P. Flannery, *Numerical Recipes : The Art of Scientific Computing*. Cambridge: Cambridge University Press, 2007.

[112] G. B. Arfken and H.-J. Weber, *Mathematical methods for physicists*. Academic Press Harcourt Brace Jovanovich, San Diego, 1967.

[113] J. C. Butcher, "A history of Runge-Kutta methods," *Applied numerical mathematics*, vol. 20, no. 3, pp. 247–260, 1996.

[114] J. H. Cartwright and O. Piro, "The dynamics of Runge–Kutta methods," *International Journal of Bifurcation and Chaos*, vol. 2, no. 03, pp. 427–449, 1992.

[115] C. K. Birdsall and A. B. Langdon, *Plasma physics via computer simulation*. CRC press, 2018.

[116] D. Wu, X. He, W. Yu, and S. Fritzsche, "Particle-in-cell simulations of laser–plasma interactions at solid densities and relativistic intensities: the role of atomic processes," *High Power Laser Science and Engineering*, vol. 6, 2018.

[117] C. K. Birdsall, "Particle-in-cell charged-particle simulations, plus Monte Carlo collisions with neutral atoms, PIC-MCC," *IEEE Transactions on plasma science*, vol. 19, no. 2, pp. 65–85, 1991.

[118] G. Stantchev, W. Dorland, and N. Gumerov, "Fast parallel particle-to-grid interpolation for plasma pic simulations on the gpu," *Journal of Parallel and Distributed Computing*, vol. 68, no. 10, pp. 1339–1349, 2008.

[119] A. Sävert, S. Mangles, M. Schnell, E. Siminos, J. Cole, M. Leier, M. Reuter, M. Schwab, M. Möller, K. Poder, *et al.*, "Direct observation of the injection dynamics of a laser wakefield accelerator using few-femtosecond shadowgraphy," *Physical Review Letters*, vol. 115, no. 5, p. 055002, 2015.

[120] A. Pukhov, "Particle-in-cell codes for plasma-based particle acceleration," *arXiv preprint arXiv:1510.01071*, 2015.

[121] A. V. Oppenheim, *Discrete-time signal processing*. Pearson Education India, 1999.

[122] M. De Loos and S. Van Der Geer, "General Particle Tracer: A new 3D code for accelerator and beamline design," in *5th European Particle Accelerator Conference*, p. 1241, 1996.

[123] S. Van der Geer, M. De Loos, and D. Bongerd, "General Particle Tracer: A 3D code for accelerator and beam line design," in *Proc. 5th European Particle Accelerator Conf., Stockholm*, 1996.

[124] A. W. Chao, K. H. Mess, *et al.*, *Handbook of accelerator physics and engineering*. World scientific, 2013.

[125] S. Atakaramians, S. Afshar, T. M. Monro, and D. Abbott, "Terahertz dielectric waveguides," *Advances in Optics and Photonics*, vol. 5, no. 2, pp. 169–215, 2013.

[126] M. Nagel, A. Marchewka, and H. Kurz, "Low-index discontinuity terahertz waveguides," *Optics Express*, vol. 14, no. 21, pp. 9944–9954, 2006.

[127] L.-J. Chen, H.-W. Chen, T.-F. Kao, J.-Y. Lu, and C.-K. Sun, "Low-loss subwavelength plastic fiber for terahertz waveguiding," *Optics Letters*, vol. 31, no. 3, pp. 308–310, 2006.

[128] Private communication with A.Shorrock, 12/04/2018.

[129] R. Stephens and I. Malitson, "Index of refraction of magnesium oxide," *Journal of Research of the National Bureau of Standards*, vol. 49, p. 249, oct 1952.

[130] G. Gallot, J. Zhang, R. McGowan, T.-I. Jeon, and D. Grischkowsky, "Measurements of the THz absorption and dispersion of ZnTe and their relevance to the electro-optic detection of THz radiation," *Applied Physics Letters*, vol. 74, no. 23, pp. 3450–3452, 1999.

[131] G. Torosyan, S. Keller, L. Scheuer, R. Beigang, and E. T. Papaioannou, "Optimized spintronic terahertz emitters based on epitaxial grown Fe/Pt layerf structures," *Scientific Reports*, vol. 8, no. 1, p. 1311, 2018.

[132] C. NASA, Molecular Spectroscopy, Jet Propulsion Laboratory and Institute of Technology, "Catalog Directory for H20 Vapour."

[133] X. Xin, H. Altan, A. Saint, D. Matten, and R. Alfano, "Terahertz absorption spectrum of para and ortho water vapors at different humidities at room temperature," *Journal of Applied Physics*, vol. 100, no. 9, p. 094905, 2006.

[134] M. Hibberd, V. Frey, B. Spencer, P. Mitchell, P. Dawson, M. Kappers, R. Oliver, C. Humphreys, and D. Graham, "Dielectric response of wurtzite gallium nitride in the terahertz frequency range," *Solid State Communications*, vol. 247, pp. 68–71, 2016.

[135] M. Naftaly and R. Miles, "A method for removing etalon oscillations from THz time-domain spectra," *Optics Communications*, vol. 280, no. 2, pp. 291–295, 2007.

[136] R. Bell, *Introductory Fourier transform spectroscopy*. Elsevier, 2012.

[137] V. Tomaselli, D. Edewaard, P. Gillan, and K. Möller, "Far-infrared bandpass filters from cross-shaped grids," *Applied Optics*, vol. 20, no. 8, pp. 1361–1366, 1981.

[138] Y. Wu and X. Li, "Elimination of cross-terms in the Wigner–Ville distribution of multi-component LFM signals," *IET Signal Processing*, vol. 11, no. 6, pp. 657–662, 2017.

[139] T. Claasen and W. Mecklenbrauker, "Time-frequency signal analysis by means of the wigner distribution," in *ICASSP'81. IEEE International Conference on Acoustics, Speech, and Signal Processing*, vol. 6, pp. 69–72, IEEE, 1981.

[140] P. M. Oliveira and V. Barroso, "Uncertainty in the time-frequency plane," in *Proceedings of the Tenth IEEE Workshop on Statistical Signal and Array Processing (Cat. No. 00TH8496)*, pp. 607–611, IEEE, 2000.

[141] L. Cohen, "Time-frequency distributions-a review," *Proceedings of the IEEE*, vol. 77, no. 7, pp. 941–981, 1989.

[142] L. Stankovic and S. Stankovic, "Wigner distribution of noisy signals," *IEEE Transactions on Signal Processing*, vol. 41, no. 2, pp. 956–960, 1993.

[143] W. Martin and P. Flandrin, "Wigner-Ville spectral analysis of nonstationary processes," *IEEE Transactions on Acoustics, Speech, and Signal Processing*, vol. 33, no. 6, pp. 1461–1470, 1985.

[144] E. Leica, "www. leica-microsystems. com," *Wetzlar, Germany*, 2014.

[145] P. Bélanger, "Beam propagation and the ABCD ray matrices," *Optics Letters*, vol. 16, no. 4, pp. 196–198, 1991.

[146] R. Iffländer, "Gaussian optics," in *Solid-State Lasers for Materials Processing*, pp. 45–68, New York: Springer, 2001.

[147] A. Forbes, *Laser beam propagation: generation and propagation of customized light*. CRC Press, 2014.

[148] A. Gerrard and J. M. Burch, *Introduction to matrix methods in optics*. Courier Corporation, 1994.

[149] R. Paschotta *et al.*, *Encyclopedia of laser physics and technology*, vol. 1. Wiley Online Library, 2008.

[150] H. Kogelnik, "Propagation of laser beams," *Applied optics and optical engineering*, vol. 7, pp. 155–190, 2012.

[151] A. Siegman, "Hermite–Gaussian functions of complex argument as optical-beam eigenfunctions," *JOSA*, vol. 63, no. 9, pp. 1093–1094, 1973.

[152] J. Hebling, A. Stepanov, G. Almási, B. Bartal, and J. Kuhl, "Tunable THz pulse generation by optical rectification of ultrashort laser pulses with tilted pulse fronts," *Applied Physics B*, vol. 78, no. 5, pp. 593–599, 2004.

[153] M. Naftaly, R. Miles, and P. Greenslade, "Thz transmission in polymer materials—a data library," in *2007 Joint 32nd International Conference on Infrared*

and Millimeter Waves and the 15th International Conference on Terahertz Electronics, pp. 819–820, IEEE, 2007.

[154] N. Daghestani, K. Parow-Souchon, D. Pardo, H. Liu, N. Brewster, M. Frogley, G. Cinque, B. Alderman, and P. G. Huggard, "Room temperature ultrafast InGaAs Schottky diode based detectors for terahertz spectroscopy," *Infrared Physics & Technology*, vol. 99, pp. 240–247, 2019.

[155] B. Schmidt, S. Wesch, C. Behrens, T. Koevener, E. Hass, S. Casalbuoni, and P. Schmüser, "Longitudinal bunch diagnostics using coherent transition radiation spectroscopy. Physical principles, multichannel spectrometer, experimental results, mathematical methods," tech. rep., Deutsches Elektronen-Synchrotron (DESY), 2018.

[156] M. T. Hibberd, A. L. Healy, D. S. Lake, V. Georgiadis, E. J. Smith, O. J. Finlay, T. H. Pacey, J. K. Jones, Y. Saveliev, D. A. Walsh, *et al.*, "Acceleration of relativistic beams using laser-generated terahertz pulses," *Nature Photonics*, pp. 1–5, 2020.

[157] V. Georgiadis, A. Healy, M. Hibberd, G. Burt, S. Jamison, and D. Graham, "Dispersion in dielectric-lined waveguides designed for terahertz-driven deflection of electron beams," *Applied Physics Letters*, vol. 118, no. 14, p. 144102, 2021.

[158] J. Hebling, K.-L. Yeh, M. C. Hoffmann, and K. A. Nelson, "High-power THz generation, THz nonlinear optics, and THz nonlinear spectroscopy," *IEEE Journal of Selected Topics in Quantum Electronics*, vol. 14, no. 2, pp. 345–353, 2008.

[159] A. Stepanov, S. Henin, Y. Petit, L. Bonacina, J. Kasparian, and J.-P. Wolf, "Mobile source of high-energy single-cycle terahertz pulses," *Applied Physics B*, vol. 101, no. 1, pp. 11–14, 2010.

[160] M. A. Othman, M. C. Hoffmann, M. E. Kozina, X. Wang, R. K. Li, and E. A. Nanni, "Parallel-plate waveguides for terahertz-driven mev electron bunch compression," *Optics Express*, vol. 27, no. 17, pp. 23791–23800, 2019.

[161] S. Carbajo, J. Schulte, X. Wu, K. Ravi, D. N. Schimpf, and F. X. Kärtner, "Efficient narrowband terahertz generation in cryogenically cooled periodically poled lithium niobate," *Optics Letters*, vol. 40, no. 24, pp. 5762–5765, 2015.